High Speed Nonlinear Optical Components for Next-Generation Optical Communications

A thesis presented to the
National University of Ireland, Cork
for the degree of
Doctor of Science

by

Ciaran Cleary

Supervisor: Dr. Robert J. Manning
Advisor: Dr. Roderick P. Webb
Head of the Department: Prof. John McInerney

Coláiste na hOllscoile Corcaigh, Éire
University College Cork, Ireland

Photonic Systems Group
Tyndall National Institute, Department of Physics
University College Cork
Ireland

August 2013

Contents

Abstract

Electronic signal processing systems currently employed at core internet routers require huge amounts of power to operate and they may be unable to continue to satisfy the consumer demand for more bandwidth without an inordinate increase in cost, size and/or energy consumption. In the future, optical signal processing techniques may be implemented for simple tasks such as wavelength conversion, demultiplexing and format conversion at high speed ($\geq$100Gb.s^{-1}) to alleviate the pressure on core router infrastructure. For these simple tasks, nonlinear optical (NLO) components such as semiconductor optical amplifiers (SOAs), electroabsorption modulators (EAMs) and silicon nanowires should be able to compete with complementary metal oxide semiconductor (CMOS) electronics in terms of device size and total power consumption. We present the amplitude and phase dynamics in a range of configurations containing SOAs, EAMs and/or silicon nanowires to support the design of all-optical switching elements for deployment in next-generation optical networks. All of the NLO device configurations investigated are compact and suitable for monolithic and/or hybrid integration.

Firstly, the gain and phase dynamics of a long, highly nonlinear SOA with strong wavelength dependence were investigated and it was found that, under certain operating conditions, the device behaved in a similar manner to the Turbo-Switch. These requirements included a high current bias ($\geq$400mA), the CW probe wavelength had to be close to the small signal gain peak wavelength (1565nm), the pump wavelength had to be to blue-shifted relative to the CW probe wavelength, and the pump-probe wavelength separation had to be 20 to 30nm. When these conditions were fulfilled, the gain evolution had a full recovery time as low as 9ps and there was a long-lived recovery tail of low magnitude. However, the corresponding phase evolution had a much longer full recovery time of 60ps.

Secondly, the amplitude and phase dynamics of a concatenated SOA-EAM-SOA (CSES) configuration were investigated and it was found that the behaviour of the system was reminiscent of the behaviour of the conventional Turbo-Switch. Under specific operation conditions, the CSES amplitude response consisted of a predominant ultrafast component with a

full recovery time of 10ps without any appreciable overshoot. The fastest amplitude recovery rates were achieved when the CW probe was at the longest wavelength that could be detected by the optical sampling oscilloscope (1565nm), the current bias applied to the SOAs was moderate ($\geq$300mA for SOA1, $\geq$200mA for SOA2), and the EAM bias was within the range $2.1 \leq V_{EAM} \leq 2.5$V. However, the corresponding CSES phase response remained long (~150ps) for all of the measurements.

Thirdly, the amplitude and phase dynamics of silicon nanowires embedded in SU8 polymer were studied and it was found that the free carrier lifetime was relatively long (7.5 to 16.2ns) due to surface passivation by the SU8 polymer. An impulse response formalism was employed to fit the experimental data and to obtain values for the two photon absorption coefficient β_{tpa}, the Kerr coefficient n_2 and TPA figure of merit. The impulse response model indicated that the blue wavelength chirp had the same order of magnitude as the red wavelength chirp for input pulses with a pulsewidth of 3.5ps. Two-copy wavelength conversion via XPM at a data rate of 80Gb.s^{-1} was demonstrated in silicon nanowires embedded in SU8 polymer by exploiting the wavelength chirp on both the red-shifted and blue-shifted sidebands of the modulated CW probe.

Finally, the amplitude dynamics in an EAM with a custom epitaxy design were measured and an impulse response model was used to extract the lifetimes associated with each stage in the amplitude response. It was found that the device had good power handling capability (there was a linear relationship between photocurrent and optical input power up to 12.5dBm) and a 1/e fast recovery time of 3.0ps at a moderate reverse bias of 4.5V, which corresponded to a 10/90 recovery time of 9ps. The EAM had such a good power handling capability and a fast response time due to the fact that the MQW was offset from the centre of the intrinsic region, carbon was employed as a p-type dopant in layers close to the MQW section, and the valence band discontinuity was minimized by means of a graded potential step at the heterojunction between the p-type region and the intrinsic region.

Declaration

I, Ciaran Cleary, declare that this PhD thesis is my own work and I have not submitted this PhD thesis for another degree, either in University College Cork or elsewhere.

_____

Ciaran Cleary

11th June 2013

Acknowledgements

During the course of my PhD project, I have been supported by many people to whom I would like to extend my gratitude. I am particularly grateful to my supervisor Dr Bob Manning for sharing his expertise, for his encouragement and support over the past four years and for proof-reading this thesis. Moreover, I would like to acknowledge the financial support that I received from Science Foundation Ireland (SFI). I would like to thank Dr Rod Webb, Dr James Dailey, Mark Power and Dr Chris Daunt for the opportunity to have numerous valuable discussions on various aspects related to my PhD project, all of whom were always willing to offer any assistance they could provide whenever I approached them. In particular, I would like to single out Dr Rod Webb for special mention for proof-reading this thesis in great detail and for helpful comments in this regard.

During my PhD studies I had the opportunity to collaborate with partners from the Danish Technical University (DTU), Karlsruhe Institute of Technology (KIT) and the Technical University of Eindhoven (TU/e) to conduct experiments under the umbrella of the EURO-FOS project. I wish to thank Dr Hua Ji and Dr Leif Oxenlowe from DTU for deciding to initiate the collaborative experiments on the silicon nanowires. Furthermore, I would like to express my gratitude for being afforded the opportunity to work with Simon Schneider, Wolfgang Heni and Benedikt Bauerle from KIT, all of whom were excellent colleagues in the workplace and good friends. Also, special thanks to Karen Solis Trapala from TU/e for her hard work, patience and friendship during her all-too-brief visit to Tyndall National Institute.

I would like to say thank you to all the current and former members from Photonic Systems Group (PSG) in Tyndall National Institute – it was a pleasure and a privilege to be able to conduct my research in such a warm and hospitable working environment. I wish to thank Martina Connolly, Olivia Coleman, Grace McHugh, Gretchen Werner and Kate McSweeney for their kind assistance in relation to administrative issues. I am immensely grateful to all of my

Glossary of terms

AMZI	Asymmetric Mach-Zehnder Interferometer
ASE	Amplified Spontaneous Emission
AWG	Arrayed Waveguide Grating
B2B	Back-to-Back
BER	Bit Error Rate
BPF	Bandpass Filter
BPSK	Binary Phase Shift Keying
BtB	Back-to-Back
CMOS	Complementary Metal Oxide Semiconductor
CSES	Concatenated SOA-EAM-SOA
CW	Continuous Wave
CWDM	Coarse Wavelength Division Multiplexing
DBR	Distributed Bragg Reflector
DEMUX	Demultiplexer
DFB	Distributed Feedback
DFG	Difference-Frequency Generation
DF-HNLF	Dispersion-Flattened Highly Nonlinear Fibre
DI	Delay Interferometer
DPSK	Differential Phase Shift Keying
DUT	Device Under Test
DWDM	Dense Wavelength Division Multiplexing
EAM	Electroabsorption Modulator
EDFA	Erbium-Doped Fibre Amplifier
ERFO	Erbium-Doped Glass Oscillator
FBG	Fibre Bragg Grating
FC	Format Conversion
FCA	Free Carrier Absorption
FCPE	Free Carrier Plasma Effect

FEC	Forward Error Correction
FKE	Franz-Keldysh Effect
FOM	Figure Of Merit
FTTH	Fibre-to-the-Home
FWM	Four-Wave Mixing
HNLF	Highly Nonlinear Fibre
IP	Internet Protocol
MOVPE	Metal Organic Vapour Phase Epitaxy
MQW	Multiple Quantum Well
MUX	Multiplexer
MZM	Mach-Zehnder Modulator
NLO	Nonlinear Optical
NOLM	Nonlinear Optical Loop Mirror
NRZ	Non-Return-To-Zero
OOK	On-Off Keying
OSA	Optical Spectrum Analyzer
OSNR	Optical-Signal-to-Noise-Ratio
OSO	Optical Sampling Oscilloscope
OSP	Optical Signal Processing
OTDM	Optical Time Division Multiplexing
PC	Polarization Controller
PDA	Personal Digital Assistant
PDM	Polarization Division Multiplexing
PIC	Photonic Integrated Circuit
PLC	Planar Lightwave Circuit
PMF	Polarization Maintaining Fibre
PPLN	Periodically Poled Lithium Niobate
PRBS	Pseudo-Random Bit Sequence
QAM	Quadrature Amplitude Modulation
QCSE	Quantum Confined Stark Effect
QDot	Quantum Dot

QDash	Quantum Dash
QPSK	Quadrature Phase Shift Keying
REAM	Reflective Electroabsorption Modulator
RF	Radio Frequency
RZ	Return-To-Zero
SAM	Self-Amplitude Modulation
SEM	Scanning Electron Microscope
SFG	Sum-Frequency Generation
SGM	Self-Gain Modulation
SHG	Second Harmonic Generation
Si	Silicon
SIMS	Secondary Ion Mass Spectroscopy
SM	Switching Mechanism
SOI	Silicon-On-Insulator
SMF	Single Mode Fibre
SMZI	Symmetric Mach-Zehnder Interferometer
SOA	Semiconductor Optical Amplifier
SPM	Self-Phase Modulation
SRS	Stimulated Raman Scattering
TE	Transverse Electric
THG	Third Harmonic Generation
TM	Transverse Magnetic
TOAD	Terahertz Optical Asymmetric Demultiplexer
TPA	Two Photon Absorption
UNI	Ultrafast Nonlinear Interferometer
WC	Wavelength-Converted
WDM	Wavelength Division Multiplexing
XAM	Cross-Absorption Modulation
XGM	Cross-Gain Modulation
XPM	Cross-Phase Modulation
XPolM	Cross-Polarization Modulation

Publications by the author

First author:

- "Dynamic characterization and impulse response modelling of amplitude and phase response of silicon nanowires," Ciaran S. Cleary, Hua Ji, James M. Dailey, Roderick P. Webb, Robert J. Manning, Michael Galili, Palle Jeppesen, Minhao Pu, Kresten Yvind, Leif K. Oxenlowe, *IEEE Photonics Journal*, vol. 5 (2013)

- "Amplitude and phase dynamics in silicon nanowires embedded in SU8 polymer waveguides," Ciaran S. Cleary, Hua Ji, Leif K. Oxenlowe, K. Yvind, James M. Dailey, Roderick P. Webb, Robert J. Manning, *Proceedings of Photonics Ireland (Belfast, Northern Ireland)*, To be presented (2013)

- "High speed cross-amplitude modulation in concatenated SOA-EAM-SOA," Ciaran S. Cleary, Robert J. Manning, *Optics Express*, vol. 20, pp. 14338-14349 (2012)

- "Amplitude and phase dynamics of concatenated SOA-EAM-SOA configuration," Ciaran S. Cleary, Robert J. Manning, *Proceedings of European Conference on Optical Communication (Amsterdam, Netherlands)*, paper P2.04 (2012)

- "Wavelength dependent fast gain recovery in a non-linear SOA," Ciaran S. Cleary, Mark J. Power, Simon Schneider, Roderick P. Webb, Robert J. Manning, *Proceedings of Photonics Ireland (Dublin, Ireland)*, paper A68 (2011)

- "Fast gain recovery with strong wavelength dependence in a non-linear SOA," Ciaran S. Cleary, Mark J. Power, Simon Schneider, Roderick P. Webb, Robert J. Manning, *Optics Express*, vol. 18, pp. 25726-25737 (2010)

Contributing author:

- "Sub 10ps carrier response times in electroabsorption modulators using quantum well offsetting," Chris L.M. Daunt, <u>Ciaran S. Cleary</u>, Robert J. Manning, Kevin Thomas, Robert J. Young, Emanuele Pelucchi, Brian Corbett, Frank H. Peters, *IEEE Journal of Quantum Electronics*, vol. 48, pp. 1467-1475 (2012)

- "Two-copy wavelength conversion of an 80Gbit/s serial data signal using cross-phase modulation and Detailed Pump-Probe Characterization," Hua Ji, <u>Ciaran S. Cleary</u>, James M. Dailey, Ju Wang, Hao Hu, Roderick P. Webb, Robert J. Manning, Michael Galili, Palle Jeppesen, Minhao Pu, Kresten Yvind, Leif K. Oxenlowe, *Proceedings of European Conference on Optical Communication (Amsterdam, Netherlands)*, paper We.2.E.3 (2012)

- "Dynamic characterization of silicon nanowires using a terahertz optical asymmetric demultiplexer-based pump-probe scheme," Hua Ji, <u>Ciaran S. Cleary</u>, James M. Dailey, Roderick P. Webb, Robert J. Manning, Michael Galili, Palle Jeppesen, Minhao Pu, Kresten Yvind, Leif K. Oxenlowe, *Proceedings of IEEE Photonics Conference (Burlingame, USA)*, paper WQ6 (2012)

- "Sub 10ps carrier response times in electroabsorption modulators using quantum well offsetting," Chris L.M. Daunt, <u>Ciaran S. Cleary</u>, Robert J. Manning, Frank H. Peters, *Proceedings of Frontiers in Optics (San Jose, USA),* paper PDPC2 (2011)

Introduction

1.1   Overview of fibre optic communications

Over the course of recent years, there has been a steady increase in the volume of data transmitted throughout optical fibre networks, which is primarily due to the continuous rise in internet usage worldwide [1]. Based on information provided by the website "www.internetworldstats.com", both the total number of people and the percentage of the world's population with internet access have climbed rapidly during the past twenty years, as illustrated by the graphs in Fig. 1.1.1 .
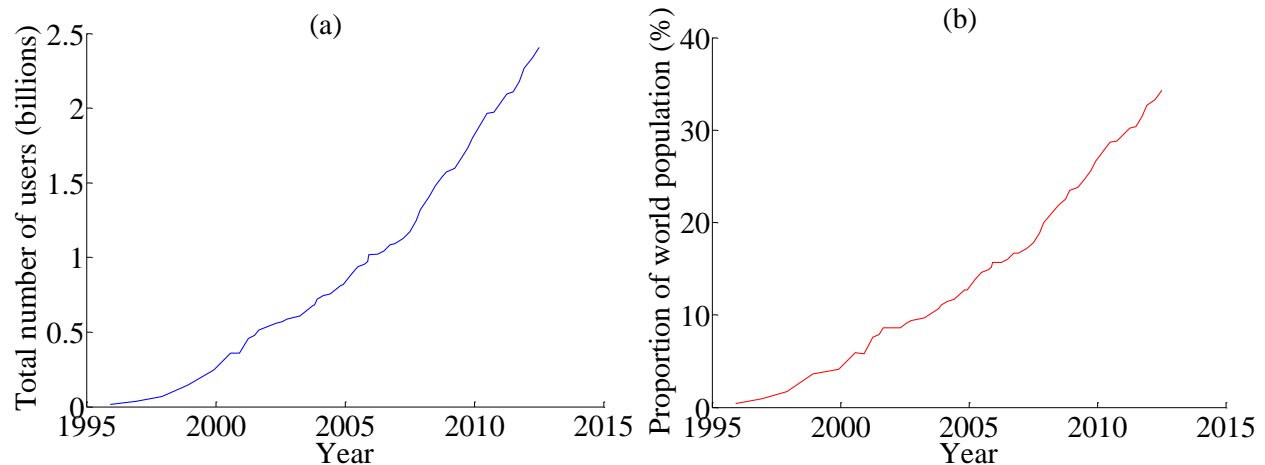
Fig. 1.1.1: (a) Total number of internet users worldwide and (b) the proportion of the world's population with internet access.

Moreover, in addition to the rise in the total number of internet users worldwide, there has been a dramatic ascent in the amount of data consumed per user, which has further contributed to the rise in internet traffic over the same period of time. Estimates vary about the annual increase in the volume of internet traffic, but the consensus suggests that the growth rate in traffic has been more than 40% each year since 1997 [3-6]. According to research conducted by Cisco Systems Inc. , global internet protocol (IP) traffic has soared since 1988 (see Fig. 1.1.2) [8].
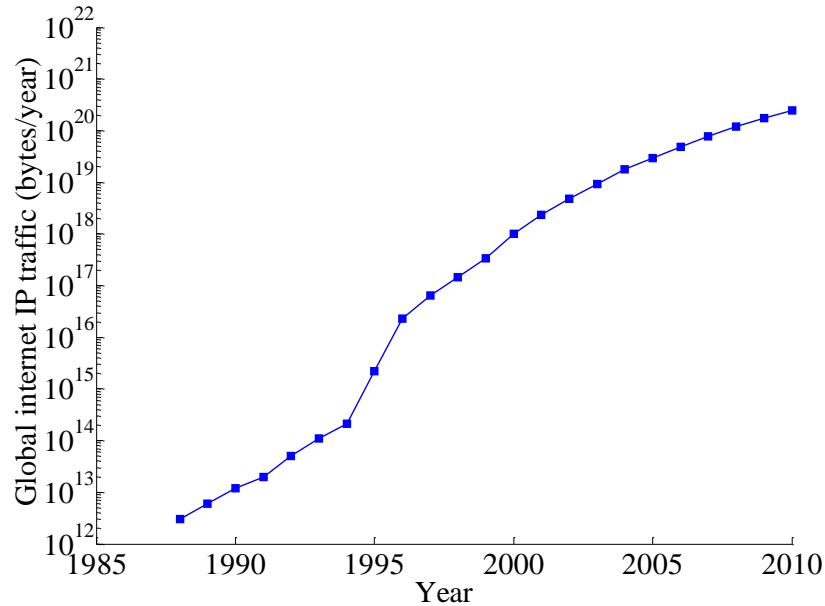
Fig. 1.1.2: Annual global IP traffic between 1988 and 2010 in exabytes per year.

Fig. 1.1.2 shows that there has been an upsurge in the volume of global IP traffic between 1988 and 2010. In 1998, global IP traffic stood at 3 terabytes/year but this rate climbed so rapidly global IP traffic surpassed 1 exabytes/year in 2000, and it stood at 245 exabytes/year in 2010.

The upward trend in internet usage is set to continue into the near future, driven by the increasingly widespread availability of high bandwidth internet services to consumers [9, 10]. These services include the provision of high definition video-on-demand [11], the growth in cloud computing services and e-commerce [12], the introduction of fibre-to-the-home (FTTH) technology [13, 14], and the expansion in sales of mobile devices with wireless internet access such as smartphones, tablet computers and personal digital assistants (PDAs) [15, 16].

To date, the optical communications industry has kept pace with this surge in demand for data by means of a variety of technological developments. Wavelength division multiplexing (WDM) and, to a lesser extent, optical time division multiplexing (OTDM) have enabled the transmission of immense quantities of information (in excess of 25Tb.s^{-1} [17]) over a single optical fibre. The basic concepts underlying WDM and OTDM networks will be outlined in Section 1.2 and Section 1.3 respectively. The major technological challenges which must be addressed in next-generation WDM, OTDM and hybrid OTDM/WDM optical networks will be discussed in Section 1.4. Finally, the concept of optical signal processing will be introduced in Section 1.5 as one possible solution to some of these technological challenges.

1.2   Wavelength division multiplexing (WDM)

One convenient property of optical fibre that has been exploited in optical communications is the ability to simultaneously transmit multiple data channels at different discrete wavelengths over a single fibre [18]. The process of combining all of these individual wavelength channels onto a single fibre is known as wavelength division multiplexing (WDM). WDM has been the key driving factor behind the development of high capacity transmission systems since the late 1980s [19]. The invention of the first commercially viable erbium doped fibre amplifier (EDFA) in 1987 was a major watershed in fibre optic communications [20]. An EDFA is ideal for simultaneous amplification of independent wavelength channels without crosstalk as it has a flat gain spectrum (when gain equalization techniques are utilized) throughout the C-band (1530 to 1565nm), where attenuation losses in an optical fibre are at a minimum. A simplified diagram of a WDM system is displayed in Fig. 1.2.1.
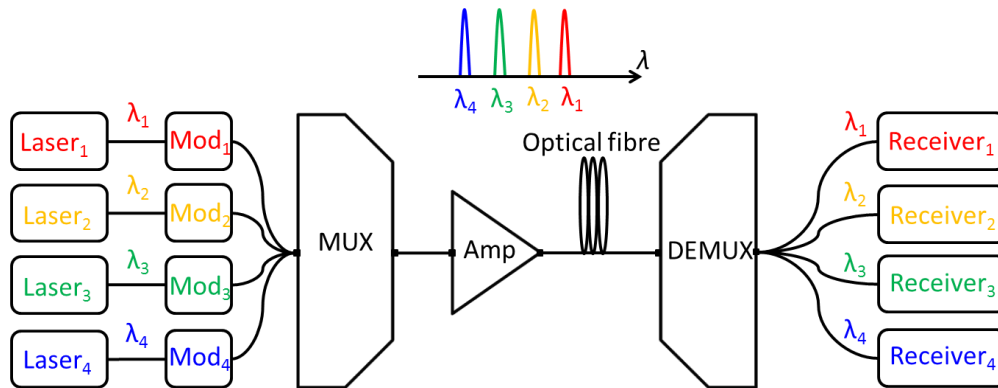
Fig. 1.2.1: Schematic diagram of WDM system with 4 wavelength channels (Mod=modulator, MUX=multiplexer, Amp=EDFA amplifier, DEMUX=demultiplexer).

In Fig. 1.2.1, there are 4 laser sources, which are typically distributed feedback (DFB) or distributed Bragg reflector (DBR) lasers with stable, narrow linewidths (≤0.1nm) operating in continuous wave (CW) mode at different wavelengths. The CW beams emitted by each laser are individually modulated by electro-optic modulators, typically Mach-Zehnder modulators (MZMs) based on lithium niobate (LiNbO$_3$). The modulated CW signals are aggregated onto single mode fibre (SMF) using a passive multiplexer such as a coupler or an arrayed waveguide grating (AWG). The multiplexed signals are transmitted over long lengths of fibre (hundreds or thousands of kilometres) and amplified by EDFAs at regularly spaced intervals (typically 80 to

100km) [21]. When signals reach their destination, they are split up into their constituent wavelengths using a demultiplexer, which generally takes the form of an AWG or multiple tunable filters. Finally, the data contained in each wavelength channel is detected by a receiver.

Fig. 1.2.1 only shows a single point-to-point link but in a real system, the network consists of a vast interconnected web of links which converge at points known as network nodes. Core routers direct traffic within the network by switching signals amongst the links at these nodes.

Furthermore, only 4 wavelength channels are shown in Fig. 1.2.1, which is a relatively low number of wavelength channels. There are two main types of WDM: coarse wavelength division multiplexing (CWDM) and dense wavelength division multiplexing (DWDM). CWDM refers to systems where there are 8 or fewer wavelength channels whereas DWDM refers to systems with 9 or more wavelength channels. CWDM systems are less complex and less expensive compared to DWDM systems. However, DWDM is preferred for long-haul transmission in the core network due to the higher data rates achievable using this technique. A typical DWDM system allows up to 160 channels separated by 25-100GHz to be multiplexed onto a single fibre [22].

Another feature absent from Fig. 1.2.1 is a method to mitigate linear and/or nonlinear impairments that accumulate in the SMF over long distances. In real systems, dispersion compensating systems counteract linear impairments such as chromatic dispersion, group velocity dispersion and adjacent channel crosstalk, and nonlinear impairments such as self-phase modulation (SPM), four-wave mixing (FWM), and stimulated Raman scattering (SRS) [23].

As well as multiplexing as many individual wavelength channels as possible onto a single fibre by spacing the channels closely together, advanced modulation techniques (which involve modulation of the intensity, phase and/or polarization of an optical carrier) are employed to improve the information spectral density in each wavelength channel. The combination of advanced modulation formats and WDM has led to impressive demonstrations of transmission capacity reported in the literature. For instance, G. Charlet *et al* utilized polarization division multiplexing (PDM) and quadrature phase shift keying (QPSK) to realize 16.4Tb.s^{-1} over 2550km of SMF [24]. Also, A. Sano *et al* demonstrated transmission at a bit rate of 69.1Tb.s^{-1} over 240km of silica core fibre using 21.4Gbaud PDM 16-ary quadrature amplitude modulation (QAM) [25]. Although these demonstrations were record-breaking experiments conducted in a research lab environment, data rates of approximately 1Tb.s^{-1} are readily achievable in modern commercial optical fibre links using these techniques [1].

1.3   Optical time division multiplexing (OTDM)

Another method of increasing the transmission capacity of an optical fibre is optical time division multiplexing (OTDM). The main idea underlying OTDM is that electrical non-return-to-zero (NRZ) data signals are modulated onto an optical pulse source to create optical return-to-zero (RZ) data signals before being multiplexed together (via bit interleaving) in the temporal domain. Each path contains a fixed optical delay line to ensure that every data channel is assigned a specific time slot [26]. A schematic diagram of a simple OTDM transmission system with 4 time slot channels is displayed in Fig. 1.3.1.
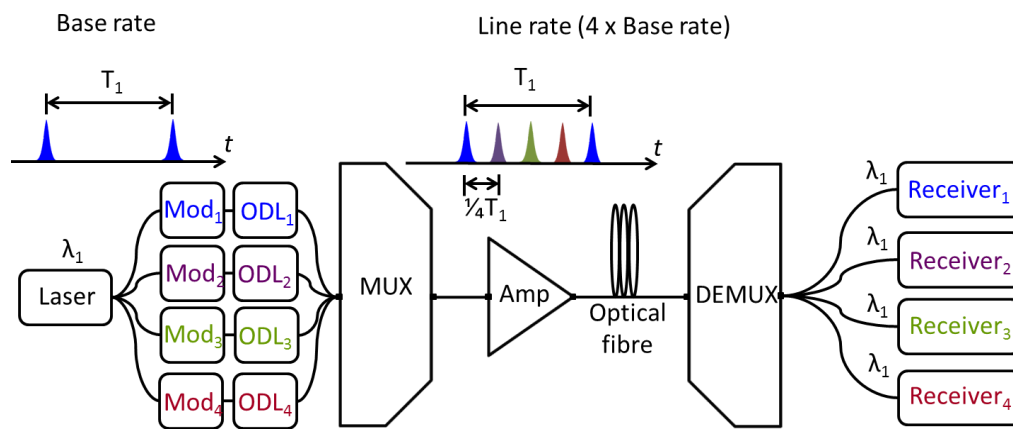
Fig. 1.3.1: Schematic diagram of TDM system with 4 time slot channels (ODL=optical delay line).

As RZ coding is necessary in OTDM systems, this means that optical sources which emit narrow pulses (pulsewidth ~3ps or less) are required at the transmitter. To avoid cross-talk between different time slot channels, it is necessary to utilize pulsed lasers with low pulsewidth (<5ps) and low timing jitter (<1ps) [27-30]. Suitable ultrafast pulse sources include mode-locked semiconductor laser diodes [31], mode-locked fibre ring lasers [32, 33], gain-switched DFB lasers [34], supercontinuum pulse generators [27, 35], and DFB lasers operated in conjunction with electroabsorption modulators (EAMs) or MZMs to act as pulse carvers [26, 36]. Using pulse compression techniques, record-breaking rates of single channel data transmission up to 1.28Tb.s^{-1} with the on-off keying (OOK) format and up to 10.2Tb.s^{-1} using advanced modulation formats [37, 38] have been demonstrated [39, 40]. However, transmission rates up to 170Gb.s^{-1} are achievable using commercially available laser sources without the need for additional pulse compression techniques or advanced modulation formats [41].

OTDM offers a number of advantages over WDM including simpler network management, bit rate transparency and a reduction in the component count, i.e. less transmitters and receivers are required [42]. However, there are several important disadvantages associated with OTDM such as strict requirements for accurate synchronization at the multiplexer and complicated clock-recovery systems at the demultiplexer, and the need to counteract effects such as polarization mode dispersion and nonlinear phenomena in fibre such as SPM and XPM between adjacent time slot channels [30, 43-47]. Due to these disadvantages, particularly the need for precise synchronization at the multiplexer and the requirement of precise compensation for dispersion in the fibre, the deployment of OTDM techniques in commercial optical communications has mainly been limited to access networks rather than core or metro networks.

1.4   Next-generation optical networks

To successfully deliver the bandwidth required to meet ever-increasing market demands without a commensurate increase in the cost and/or energy consumption associated with the installation and operation of optical communication systems, increased flexibility, reduced complexity and reduced power consumption on an energy-per-bit-basis will be key features in future next-generation optical networks [48-50].

Regarding increased flexibility, developments such as dynamic network reconfiguration by utilizing techniques such as wavelength conversion in WDM networks are expected to lead to more cost-effective systems [49, 51]. One possible solution to the complexity and cost associated with DWDM networks with >>8 channels is to replace these systems with hybrid OTDM/WDM transmission systems [52-54]. For a given total transmission capacity, hybrid OTDM/WDM would lead to a smaller number of wavelength channels operating at higher data rates compared to using DWDM alone.

Another priority issue is reduction in the energy consumption of the infrastructure of the internet. In 2007, J. Baliga *et al* established that the internet consumes at least 1% of the total electricity supply in countries where broadband is available and they estimate that it could potentially consume 7% of the total electricity supply if the average household access rate increases to 100Mb.s^{-1} [3, 55, 56]. Also, K. Hinton *et al* have studied the issue of energy consumption in depth and have concluded that as data rates continue to increase, the core network routers will begin to dominate the power consumption of the internet infrastructure [55].

To date, conventional electronic signal processing systems at core routers based on the principle of optical-electronic-optical (OEO) conversion and complementary metal oxide semiconductor (CMOS) electronic decision-making elements have been able to facilitate the expansion in data traffic [57, 58]. At the moment, the standard line rate for each individual wavelength channel in WDM networks is being upgraded from a rate of 40Gb.s^{-1} to a rate of 100Gb.s^{-1} and further increases in the standard line rate for each wavelength channel are expected [59]. However, the energy consumption of huge numbers of OEO converters (i.e. photodiodes and lasers), as well as energy density limitations and heat dissipation problems associated with high speed CMOS components are now significant problems that have created an "energy bottleneck" in the existing core router infrastructure [56, 60].

1.5 Nonlinear optical (NLO) devices and optical signal processing

In future, optical networks will be redesigned to employ fewer core routers and increased optical layer switching to deal with the "energy bottleneck". With regards to optical layer switching, it may be possible to utilize optical signal processing techniques to operate in parallel with electronic signal processing in next-generation optical fibre networks [61-63]. Optical signal processing involves switching signals in the optical domain without OEO conversion. This approach could offer benefits such as lower power consumption, smaller size and lower hardware costs compared to electronic signal processing [64, 65]. There is an on-going debate in the scientific community about the exact role that photonic switches can play in next-generation optical communications but it is likely that optical signal processing techniques will operate in parallel with electronic signal processing techniques rather than replacing them outright [55, 66].

The main potential application of optical signal processing in WDM systems is wavelength conversion in dynamically allocated wavelength-routed optical networks [67]. It has been established that optical wavelength conversion is an effective means to resolve contention issues and increase network throughput [68].

There are a wide range of potential applications for optical signal processing techniques in OTDM and hybrid OTDM/WDM networks. Although K. Hinton *et al* have shown that optical signal processing techniques are not suitable for complicated signal processing functions [69], they can perform relatively simple functions at high speed ($\geq$100Gb.s^{-1}) such as demultiplexing [39, 70, 71], format conversion [72, 73] and packet header recognition [74, 75].

Optical nonlinearities originate from the interaction of the electric field of incoming photons with charge carriers and phonons in a medium [76]. The electric field interacts with electrons in the outer shells in the atoms and this induces dielectric polarization in the medium. The polarization $P_e(\omega)$ of a medium through which an optical signal with angular frequency ω is propagating can be approximated by a power series function of the applied electric field E_ω in the frequency domain, as shown in Eq. 1.5.1 where ε_0 is the permittivity of free space and $\chi^{(i)}$ is the ith order susceptibility tensor of the medium [77].

$$P_e(\omega) = \varepsilon_0(\chi^{(1)}E_\omega + \chi^{(2)}E_\omega^2 + \chi^{(3)}E_\omega^3 + \chi^{(4)}E_\omega^4 + ...) \tag{1.5.1}$$

The susceptibility tensors $\chi^{(i)}$ determine whether the induced polarization is linear or nonlinear, whether the electric field of input optical signals induce phase shifts, whether the input optical signal experiences gain or loss, and whether signals at new frequencies are generated [76]. The first order susceptibility tensor is responsible for linear optical properties of the medium and the higher order susceptibility tensors are responsible for NLO effects. The linear component of the polarization $P_e^{(1)}(\omega)$ is given by Eq. 1.5.2.

$$P_e^{(1)}(\omega) = \varepsilon_0 \chi^{(1)}(\omega) E_\omega \tag{1.5.2}$$

The first-order susceptibility term $\chi^{(1)}$ is associated with dipole excitations with bound and free electrons induced by an individual photon. The real component of $\chi^{(1)}$ relates to the real part of the refractive index and the imaginary component of $\chi^{(1)}$ relates to loss or gain in the medium. The second-order nonlinear component of the polarization $P_e^{(2)}(\omega)$ is given by Eq. 1.5.3.

$$P_e^{(2)}(\omega) = \varepsilon_0 \chi^{(2)}(\omega; \omega_1, \omega_2) E_{\omega_1} E_{\omega_2} \tag{1.5.3}$$

The second-order nonlinearity leads to effects such as the Pockels effect, second-order harmonic generation (SHG), sum-frequency generation (SFG) and difference-frequency generation (DFG). Furthermore, the third-order nonlinear component of the polarization is given by Eq. 1.5.4, where K is a constant that depends on specific optical nonlinear effects.

$$P_e^{(3)}(\omega) = K\varepsilon_0 \chi^{(3)}(-\omega; \omega_1, \omega_2, \omega_3) E_{\omega_1} E_{\omega_2} E_{\omega_3} \tag{1.5.4}$$

The third-order nonlinearity is important in centrosymmetric crystals such as silicon and leads to effects such as the Kerr effect, FWM, SPM, and third-order harmonic generation (THG).

All of these NLO effects can be exploited to create logic gates which can realize signal processing functions in the optical domain. In principle, any NLO medium can be used in an all-optical switching element but a high nonlinear coefficient, a fast response time, polarization independence and a large bandwidth are desirable properties in the nonlinear material. Suitable materials include highly nonlinear fibre (HNLF), periodically poled lithium niobate (PPLN),

silicon (Si) waveguides, chalcogenide glasses (e.g. As_2S_3) and certain III-V compounds (e.g. GaInAsP or AlGaInAs). Regarding III-V compounds, they are generally formed into waveguides and either a forward current bias is passed through the waveguide (known as a semiconductor optical amplifier (SOA)) or a reverse bias voltage is applied across the waveguide (known as an electroabsorption modulator (EAM)).

NLO components can be classified as either active or passive devices. Active devices such as SOAs require a constant external electrical power supply in the form of a direct current bias to operate. Passive devices such as Si waveguides do not require a current bias to operate. However, a reverse bias can be applied to passive devices such as Si waveguides and EAMs to decrease the response time. An active device provides net gain to an input signal but it needs to be powered on at all times, even when there are no input signals. A passive device does not consume energy when there are no input signals but it does attenuate input signals so gain blocks are necessary to ensure cascadability.

Another important distinction between different types of NLO materials is whether the nonlinearity is resonant or non-resonant. In a resonant medium, the photon energy is similar to the transition energy of the material, e.g. an SOA has resonant nonlinearity at communications wavelengths as the photon energy is close to the bandgap energy for III-V compounds such as InGaAsP. However, in a non-resonant medium, the photon energy is far away from the transition energy in the material, e.g. HNLF has non-resonant nonlinearity at communications wavelengths. Non-resonant nonlinearities have a fast response time (<1ps) but the nonlinear coefficient is low so long interaction lengths (>100m) of material and/or high pump powers (>>1pJ per pulse) are needed. On the other hand, resonant nonlinearities have a slow response time (>>1ps) but the nonlinear coefficient is high so short interaction lengths (<5mm) and low optical input powers (<1pJ) are sufficient to achieve appreciable nonlinear effects [78].

Both the device footprint and the total power consumption associated with various kinds of NLO switching elements have been studied extensively by R. Tucker et al [79] and K. Hinton et al [55, 80]. These researchers have concluded that photonic switching elements are unsuitable for complex tasks (such as clock recovery) but they are suitable for simple tasks (such as wavelength conversion). Furthermore, they have found that SOAs and Si nanowires are the most promising candidates to compete with electronics at high bit rates (≥100Gb.s[-1]) both in terms of device footprint and energy consumed per bit.

1.6   Objectives of PhD project

The principal aim of this PhD project was to investigate the carrier dynamics of several configurations of NLO devices to evaluate their viability for optical signal processing applications in next-generation WDM, OTDM or hybrid OTDM/WDM networks. It is vitally important to understand the carrier dynamics in these NLO components to support the design of all-optical switching elements in real communications systems.

Time-resolved, two-colour pump-probe spectroscopy was employed to measure the amplitude and phase dynamics in the device configurations following injection of pump pulses with a pulsewidth of ~3ps. These configurations involved active devices, passive devices, and/or a combination of both active and passive devices. The active regions in the components were based on InGaAsP/InP, AlInGaAs/InP or Si/SiO$_2$ material systems. The SOAs and EAMs had resonant nonlinearity whereas the Si waveguides had non-resonant nonlinearity.

In Chapter 2, the static and dynamic characteristics of different types of NLO devices are described. Also, the fundamental principles underlying signal processing functions such as wavelength conversion, demultiplexing, waveform sampling and format conversion are outlined.

Chapter 3 focuses on experimental measurements of the gain and phase dynamics of a single, long, highly nonlinear SOA that exhibited strong wavelength dependence. The active region in the SOA was based on the InGaAsP/InP material system. The remarkably fast gain and phase responses of the SOA under certain operation conditions are explained using a multi-section time domain model of the carrier dynamics.

Chapter 4 presents the carrier dynamics in the concatenated SOA-EAM-SOA (CSES) configuration. The active regions in the SOAs and EAM are based on the InGaAsP/InP material system. The dependence of the amplitude and phase response of the CSES configuration on the SOA current bias, EAM reverse bias and input signal wavelength is described. A simple impulse response model is developed to account for the main features in the amplitude and phase response of the CSES configuration.

In Chapter 5, the amplitude and phase dynamics of Si nanowires embedded in SU8 polymer waveguides are investigated. A phenomenological impulse response formalism is utilized to account for the carrier dynamics in the devices. Moreover, a discussion of the wavelength chirp dynamics in Si nanowires embedded in SU8 polymer waveguides and how this relates to an

experimental demonstration of two-copy wavelength conversion at 80Gb.s^{-1} by exploiting XPM in this type of device is given. However, the demonstration of two-copy wavelength conversion was carried out by Hua Ji and co-workers in DTU Fotonik and the author was not directly involved in those experiments.

Chapter 6 reports the absorption dynamics of a custom epitaxy design EAM which involved quantum well offsetting, using carbon as a p-dopant and valence band discontinuity minimization to reduce the sweepout time. The active region in this EAM was based on the AlInGaAs/InP material system. The absorption dynamics of this custom epitaxy design EAM are compared with those of a commercially available EAM which did not have these material modifications. Impulse response modelling is employed to extract the lifetimes associated with the various physical processes that contribute to the total response.

Finally, Chapter 7 consists of discussion and analysis of the principal findings of the experimental and computational work presented in the thesis.

Characteristics of NLO devices and their applications in optical signal processing

In this chapter, the characteristics of several kinds of NLO devices including SOAs, EAMs, Si nanowires, HNLF, PPLN and chalcogenide glass are discussed. State-of-the-art developments in optical signal processing functionalities such as wavelength conversion, format conversion and demultiplexing are reviewed. A summary of the material covered concludes the chapter.

2.1 Semiconductor optical amplifiers (SOAs)

2.1.1 Structure of SOAs

An SOA is a broadband, single-pass optoelectronic device that amplifies input optical signals when a current bias is applied to the device. To ensure that the SOA is a single-pass device, the reflectivity of the end facets is kept low ($\sim 10^{-4}$) using multiple antireflection coatings along with angled and window facet structures, so as to suppress cavity resonance effects [81]. Fig. 2.1.1 shows a simplified diagram of a double heterostructure SOA chip, where there are two interfaces between materials with different bandgaps (i.e. the interface between the intrinsic region and the n-type region, and the interface between the intrinsic region and the p-type region.
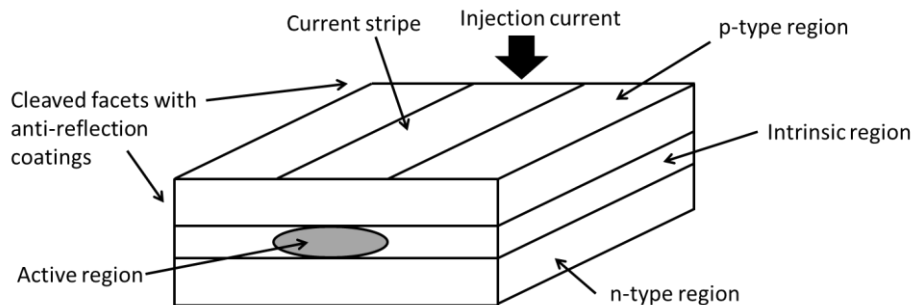
Fig. 2.1.1: Simplified diagram of a double heterostructure SOA chip.

A typical SOA consists of an active region incorporated into a waveguide which is completely surrounded by lower refractive index cladding [81]. The undoped active region is enclosed by p-type and n-type regions that supply the active region with electrons and holes when a current bias is applied to the device. The buried heterostructure of Fig 2.1.2 shows the interfaces between the active region and cladding regions. Typical choices for the direct bandgap III-V semiconductor compounds in SOAs that operate in the C-band are InGaAsP for the active region and doped InP for the p-type and n-type regions. An SOA has an active region cross-section area ~$0.1 \times 10^{-12} m^2$ (width ~1μm, height ~0.1μm) and length ~1mm.
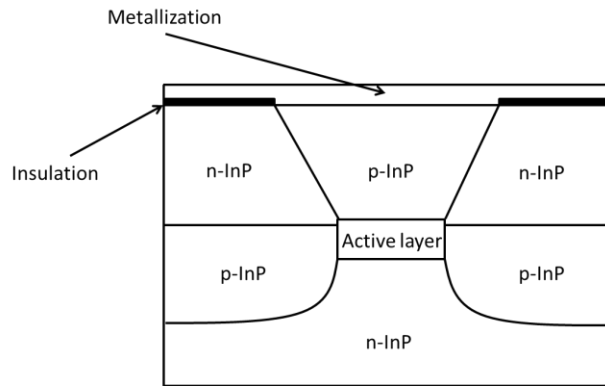
Fig. 2.1.2: Cross-section of buried heterostructure device.

The ratio of gain to applied current in an SOA can be enhanced by ensuring that charge carriers are confined to the active region rather than diffusing through the entire cross-section of the device. This can be achieved by exploiting the bandgap difference between the active region and the p-type and n-type doped regions to funnel charge carriers into the active region and by increasing the optical confinement factor i.e. the ratio of power in the active region to power in the total cross-section [81].

The width of the active region is relatively narrow (~0.5μm) so that it can only support a single transverse mode with two polarizations i.e. the transverse electric (TE) and transverse magnetic (TM) modes. For the TE mode, all components of the *electric field* of the optical signal are transverse to the direction of propagation. For the TM mode, all components of the *magnetic field* of the optical signal are transverse to the direction of propagation. Generally, the confinement factor is polarization-dependent so there are different values for the confinement factor for the TE and TM modes (Γ_{TE} and Γ_{TM} respectively). However, if polarization insensitive SOAs are required, several techniques can circumvent the difference between these two

14

confinement factors such as the use of square cross-section waveguides and tensile-strained layers in the active region. For square cross-section waveguides, the values of Γ_{TE} and Γ_{TE} can be equalized to achieve polarization insensitivity [82]. When tensile-strained materials are utilized to create polarization insensitive SOAs, the TM mode gain coefficient can be increased relative to the TE mode gain coefficient to compensate for the fact that $\Gamma_{TE} > \Gamma_{TE}$ [81, 83].

There are four main types of SOAs, based on the nature of the material in the active region: bulk, quantum well, quantum dash and quantum dot. The main difference between these structures lies in degree of confinement of the motion of electrons and holes within the material.

In a bulk SOA, the active region is a single slab of crystalline III-V material so carriers are free to move in all three dimensions (3D). This type of SOA is simple to fabricate and has the highest confinement factor compared to alternative structures. However, it has a relatively high transparency current and a relatively long response time.

For a multiple quantum well (MQW) SOA, the active region consists of multiple thin layers of crystalline III-V material. The layers are so thin that electrons and holes are effectively confined in a quasi-2D plane and this affects the density of states. An MQW SOA is advantageous as it generally has higher saturation output power, lower transparency current, higher differential gain and a faster response time compared to a bulk SOA [84]. However, an MQW SOA is more difficult to fabricate and more expensive than a bulk SOA.

For a quantum dash (QDash) SOA, the active region consists of arrays of wires or dashes with cross-section dimensions of 5 to 50nm which are self-assembled on a thin 2D film known as a wetting layer [85]. Electrons and holes are effectively confined within a quasi-1D region, which leads to quantization of the energy levels in the quantum dashes. With careful design of the waveguides, QDash SOAs can have higher saturation output power, lower transparency current, higher differential gain and a faster response time than both MQW and bulk SOAs [85].

For a quantum dot (QDot) SOA, the active region contains arrays of discrete nanoparticles where all sides of the particles have dimensions of 5 to 50nm which are self-assembled on a wetting layer [86-90]. Electrons and holes are effectively confined within a quasi-0D region and this leads to quantization of the energy levels in the quantum dots. However, there is wide variation in the size, composition, strain and/or shape of individual quantum dots in any real device, which gives rise to inhomogeneous broadening. Furthermore, room temperature conditions lead to homogeneous broadening of energy levels in the quantum dots. As a

consequence, the energy levels in real QDot SOAs are much broader than ideal QDot SOAs. With careful engineering of the waveguides, QDot SOAs can have higher saturation output power, lower transparency current, higher differential gain and a faster response time compared to both MQW and bulk SOAs [91, 92]. However, the cost and complexity associated with fabricating QDot and QDash SOAs is significantly greater than for MQW SOAs and bulk SOAs.

An idealized picture of the structure and energy levels in the conduction band each of these 4 types of material is given in Fig. 2.1.3. The band structure is considerably different in each case due to quantization of the energy levels. The conduction and valence bands split up into overlapping sub-bands which become narrower as the motion of the electrons and holes is restricted in more dimensions.
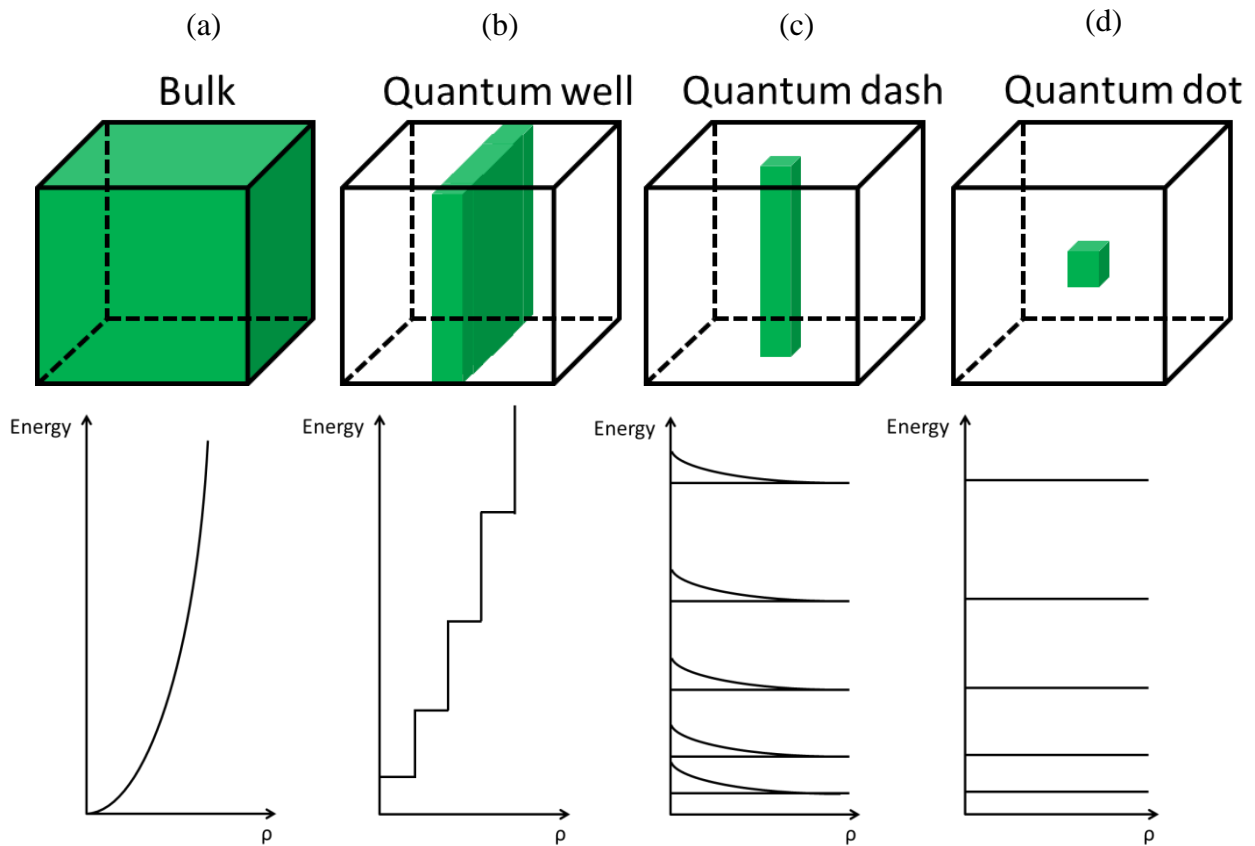
Fig. 2.1.3: Schematic view of the structure and energy band diagrams for (a) bulk, (b) quantum well, (c) quantum dash and (d) quantum dot materials.

2.1.2   Static SOA characteristics

The principle of operation in an SOA can be explained by examining the band structure of the material in the active region i.e. III-V semiconductor material with a direct bandgap. A rigorous description of the band structure in a semiconductor is a complex task but a good approximation is to assume that the bands have a parabolic shape, as shown in Fig. 2.1.4, where E refers to electron energy, k refers to the electron wavevector and E_g refers to the bandgap energy. There are several sub-bands in the valence band, and at room temperature both heavy holes and the light holes are present at the top of the valence band in III-V semiconductor compounds [93].
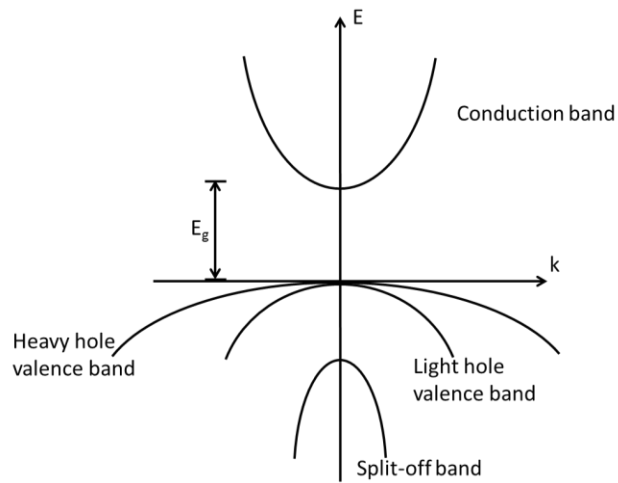
Fig. 2.1.4: Band structure diagram for a direct bandgap semiconductor with bandgap energy E_g.

When an electrical current is applied to an SOA, electrons are externally injected into the conduction band and holes are externally injected into the valence band. The SOA is designed so that population inversion occurs at a moderate current bias (>50mA) [94]. A population inversion occurs when more electrons are in a higher energy state than in a lower energy state. When a photon with energy greater than E_g enters the SOA while a population inversion exists in the device, it stimulates the recombination of an electron in the conduction band with a hole in the valence band, leading to the emission of another photon with identical frequency, phase, polarization and direction of propagation. This process is repeated many times along the length of the device i.e. the SOA amplifies the input optical signal. As mentioned in Section 2.1.1, one important consideration in the design of SOAs is the confinement factor Γ, defined by Eq. 2.1.1, where x and y refer to the cross-section dimensions and $\Psi(x,y)$ refers to the electric field.

$$\Gamma = \frac{\iint\limits_{active} |\Psi(x, y)|^2 \, dxdy}{\int\limits_{-\infty}^{\infty}\int\limits_{-\infty}^{\infty} |\Psi(x, y)|^2 \, dxdy} \qquad (2.1.1)$$

It is important to confine the input optical power to the active region as much as possible while simultaneously ensuring that the current density is sufficiently high to support a population inversion. Separate confinement heterostructure layers with an intermediate refractive index between the low index cladding and the high index active region can be incorporated into SOAs to maximize the confinement factor while maintaining a high carrier concentration [95].

The material gain of a semiconductor material g_m determines the gain per unit length experienced by an input optical signal. At wavelengths close to the gain peak, g_m can be described by Eq. 2.1.2, where a_m is the differential gain coefficient, N is the instantaneous carrier concentration, N_0 is the transparency carrier density and λ is signal wavelength.

$$g_m = a_m(N - N_0) \qquad (2.1.2)$$

As illustrated in Fig. 2.1.5, the material gain of an SOA is strongly wavelength dependent and there are 3 distinct wavelength operation regimes (see caption, where E_{photon} is photon energy).
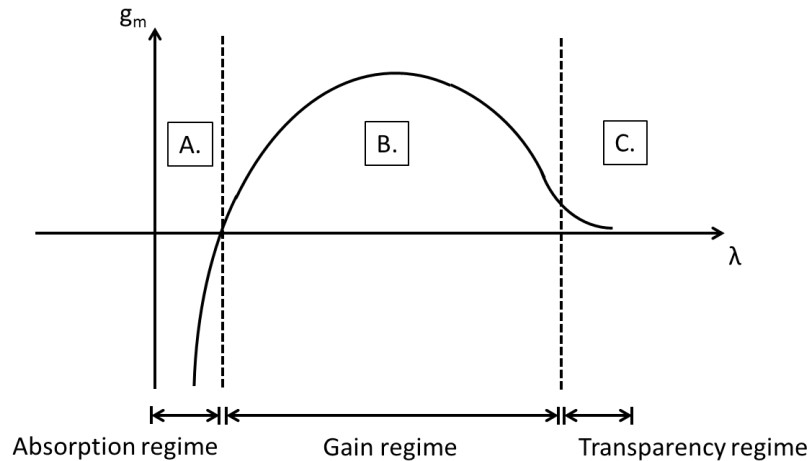
Fig. 2.1.5: Material gain spectrum in an SOA illustrating 3 wavelength operation regimes:

A. *$E_{photon} > E_{trans}$: Material gain is negative so input light is absorbed.*

B. *$E_{photon} < E_{trans} < E_g$: Material gain is positive so input light experiences net gain.*

C. *$E_{photon} < E_g$: Little interaction between input light and material.*

The modal gain g of an SOA takes the waveguide structure of the device into consideration, as only the light within the active region experiences appreciable gain and there are non-negligible scattering and absorption losses within any real waveguide. The modal gain is described by Eq. 2.1.3, where α_L refers to linear loss per unit length within the waveguide.

$$g = \Gamma a_m (N - N_0) - \alpha_L \qquad (2.1.3)$$

The modal gain can be used to calculate the power gain G (i.e. the ratio of output power to input power) of the SOA using Eq. 2.1.4, where L is the length of the active region.

$$G = \exp(gL) = \exp[\Gamma a_m (N - N_0)L - \alpha_L L] \qquad (2.1.4)$$

When an input optical signal experiences positive gain in an SOA, the carrier density falls due to stimulated emission. This drop in carrier density reduces the modal gain experienced by any other optical signal which subsequently passes through the device until the carrier density recovers to its original level. When the input signal power is low, the decrease in carrier density is low compared to the total population of carriers so the effect of gain saturation is negligible. However, when the input signal power is high, the decrease in carrier density represents a significant proportion of the total population of carriers so gain saturation cannot be neglected. The physics of gain saturation and carrier dynamics in SOAs will be discussed in Section 2.1.3.

2.1.3   Carrier dynamics in SOAs

As mentioned in Section 2.1.2, gain saturation is an important consideration in SOAs. When an optical pulse undergoes gain in an SOA, the carrier density drops and it takes a finite amount of time for the carrier density to recover to the undisturbed level. The carrier dynamics can be accurately modelled using the simple rate equation in Eq. 2.1.5, where I is the current bias, e is the charge of an electron, A is the active region cross-sectional area, τ_{CL} is the carrier lifetime, $P(t)$ is the optical signal power, h is Planck's constant and c is the speed of light in a vacuum [96]. Note that τ_{CL} is not strictly speaking a constant value as this parameter is dependent on carrier density.

$$\frac{dN(t)}{dt} = \frac{I}{eAL} - \frac{N(t)}{\tau_{CL}(N(t))} - \frac{\Gamma a_m P(t)(N(t) - N_0)}{A\left(\frac{hc}{\lambda}\right)} \tag{2.1.5}$$

The first term on the right hand side (RHS) of Eq. 2.1.5 relates to the increase in carrier density due to the current bias applied to the device, the second term relates to the reduction in carrier density due to non-radiative, spontaneous and Auger recombination processes, and the third term relates to the drop in carrier density when an input optical signal experiences gain in the SOA. The contribution of each of these effects are described in Eq. 2.1.6, where A_{nrad}, A_{rad} and A_{Auger} are the coefficients for non-radiative emission, radiative emission and Auger recombination respectively, and R_{tot} refers to the total rate of carrier recombination [97, 98].

$$\frac{N(t)}{\tau_{CL}(N(t))} = A_{nrad} N(t) + A_{rad} N^2(t) + A_{Auger} N^3(t) = R_{tot} \tag{2.1.6}$$

All of the principal recombination processes are illustrated schematically in Fig. 2.1.6 and an explanation of each process is given in the following paragraphs to explain their physical origin. Note that there are many different kinds of Auger recombination mechanisms and only one example of these mechanisms is displayed in Fig. 2.1.6(c).
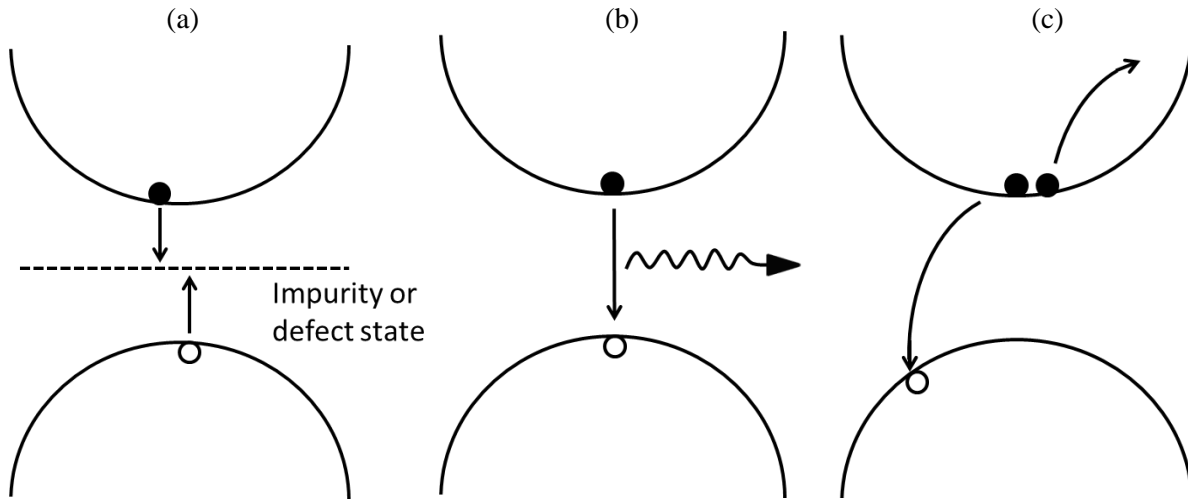
Fig. 2.1.6: (a) Surface or trap assisted non-radiative recombination, (b) spontaneous (radiative) recombination and (c) one example of an Auger recombination mechanism. The black dots denote electrons and the white dots denote holes.

Non-radiative recombination, also known as Shockley-Hall-Read recombination, is a process whereby carriers recombine without emitting photons [99]. An electron in the conduction band and a hole in the valence band recombine with the assistance of an intermediate energy state created by an impurity atom (i.e. a trap) or a defect in the crystal lattice. The impurity or defect state is able to absorb any difference in momentum between the electron and the hole. Energy is released in the form of a lattice vibration (i.e. a phonon), which heats up the material. Non-radiative recombination is directly proportional to the carrier density.

Radiative recombination is a two-body process whereby an electron recombines with a hole and a photon is emitted instantaneously during this transition [100]. Since both types of carrier must be present for radiative recombination to take place, this process has a square dependence on the carrier density.

Auger recombination is a three body interaction whereby an electron and a hole recombine in a band-to-band transition and the energy produced by this annihilation is given either to another electron or another hole [101]. The involvement of a third particle means that Auger recombination has a cubic dependence on the carrier density so Auger recombination is generally dominant at typical carrier concentrations for SOAs (approximately 10^{24}m^{-3}). Thus, for SOAs under typical operating conditions, Eq. 2.1.6 can be simplified to Eq. 2.1.7.

$$\frac{N(t)}{\tau_{CL}} \approx A_{Auger} N^3(t) \approx R_{tot} \qquad (2.1.7)$$

Eq. 2.1.7 can be used to estimate the static recombination time τ_{static} and the dynamic recovery time $\tau_{dynamic}$ for an SOA (see Eq. 2.1.8 and Eq. 2.1.9).

$$\tau_{static} = \frac{N}{R_{tot}} = \frac{1}{A_{Auger} N^2} \qquad (2.1.8)$$

$$\tau_{dynamic} = \frac{dN}{dR_{tot}} = \frac{1}{3 A_{Auger} N^2} \qquad (2.1.9)$$

The carrier density rate equation in Eq. 2.1.5 can explain the effect of gain saturation in an SOA as the input power (or the output power) increases. If a CW beam is incident upon an SOA,

this rate equation can be solved by setting $dN/dt = 0$, assuming that dynamic equilibrium is established in the SOA. The solution to this equation (in terms of modal gain g) is given by Eq. 2.1.10, where g_{unsat} is the unsaturated modal gain and P_{sat} is the saturation power.

$$g = \frac{\Gamma a_m \left(\dfrac{I\tau_{static}}{eAL} - N_0 \right)}{\left(1 + \dfrac{P\Gamma a_m \tau_{static}}{Ah\nu} \right)} = \frac{g_{unsat}}{1 + \dfrac{P}{P_{sat}}} \tag{2.1.10}$$

The optical signal propagation equation in the waveguide is given by Eq. 2.1.11, where z is distance along the length of the waveguide.

$$\frac{dP(z)}{dz} = gP(z) \tag{2.1.11}$$

Eq. 2.1.11 can be integrated from $z=0$ to $z=L$ with the boundary conditions $P(0)=P_{in}$ and $P(L)=P_{out}=GP_{in}$. The resulting implicit function defined by Eq. 2.1.12 describes the relationship between power gain G and output power P_{out}, where G_0 is the unsaturated gain of the SOA.

$$G = G_0 \exp\left(\frac{(1-G)}{G} \frac{P_{out}}{P_{sat}} \right) \tag{2.1.12}$$

This implicit expression for the dependence of power gain on the output power can be manipulated to calculate the saturation power P_{sat}.

A schematic diagram of a typical gain saturation curve is displayed in Fig. 2.1.7, where $P_{sat,out}$ is defined as the output power at the point where the power has been reduced to $0.5G_0$ (i.e. the gain has dropped by 3dB from the unsaturated gain level). $P_{sat,out}$ is related to the saturation power P_{sat} by Eq. 2.1.13.

$$P_{sat,out} = \frac{G_0 \ln 2}{G_0 - 2} P_{sat} \tag{2.1.13}$$
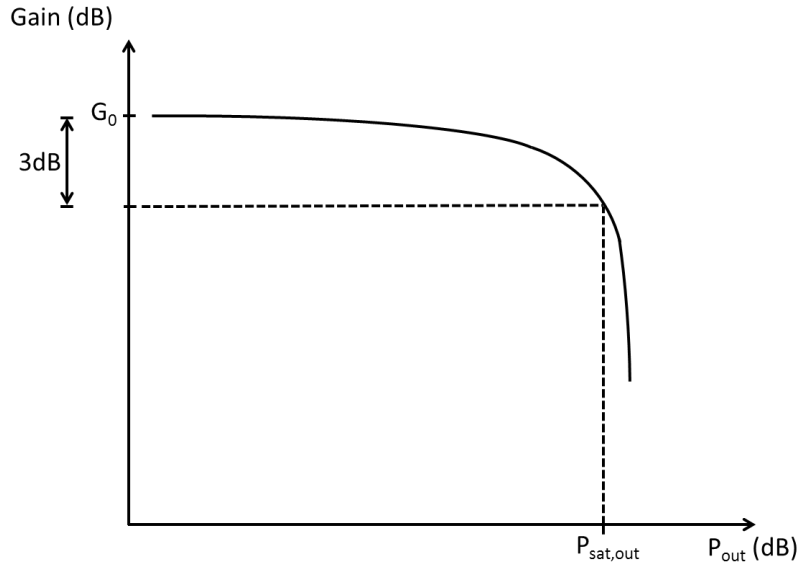
Fig. 2.1.7: Schematic diagram of gain saturation curve for an SOA, where G_0 refers to the unsaturated gain and P_{sat} refers to the saturated output power.

Another important consideration in an SOA is the existence of amplified spontaneous emission (ASE) in the device. This phenomenon can be understood by considering a photon that is emitted spontaneously due to radiative recombination without stimulus. This spontaneously emitted photon has random wavelength, phase and propagation direction. As it travels through the active region, this primary photon stimulates the emission of secondary photons at the same wavelength, leading to amplification of the primary seed photon. Depending on their initial direction of propagation, some of the secondary photons are guided along the length of the waveguide. The secondary photons accumulate at either end of the waveguide until they leave through one of the end facets and this phenomenon is known as amplified spontaneous emission. ASE photons represent noise in the optical signal output from an SOA. The ASE power depends on the carrier concentration and the ASE spectrum broadly corresponds with the gain spectrum. One technique to minimize ASE noise is to inject a high intensity optical signal or "holding beam" into the SOA, which acts to saturate the gain. This has the effect of reducing both the probability of spontaneous emission of primary photons and the carrier density available for amplifying these primary photons [102, 103].

If SOAs are employed as all-optical switching elements in future OTDM and hybrid OTDM/WDM systems, the temporal response of the SOA to an input signal must be as fast as possible. It was mentioned earlier in this section that when an input pump pulse experiences gain

in an SOA, the carrier density falls rapidly. For a subsequent pulse to receive the same amount of gain as the first pulse, the carrier density must recover to the initial, undisturbed carrier density. Otherwise, patterning effects will become apparent in the output signal and this is detrimental at high bit rates ($\geq$100Gb.s^{-1}) [96, 104].

   The normalized gain evolution of a typical bulk SOA following the arrival of a single pulse with pulse width of ~100fs and energy per pulse of ~100fJ is displayed in Fig. 2.1.8. The carrier density recovery consists of an initial ultrafast, intraband component followed by a slower, interband, band-filling process [81].
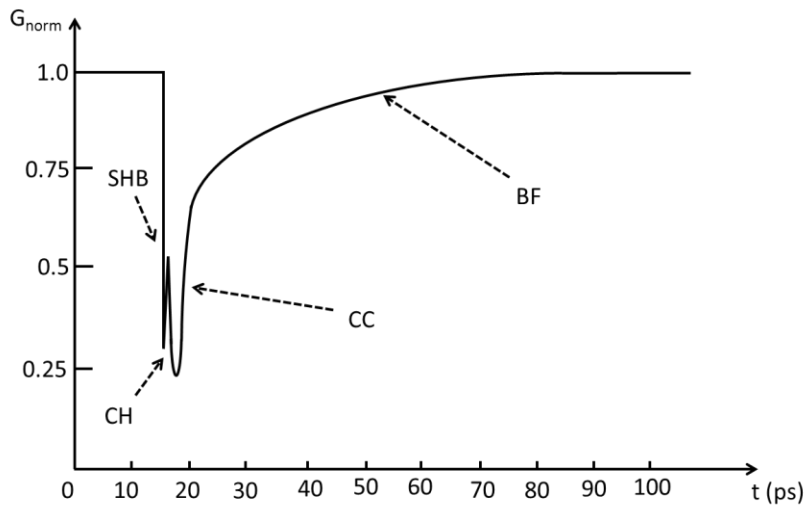
Fig. 2.1.8: Schematic diagram of gain evolution for a typical SOA, with the various processes in the gain evolution marked in the picture (SHB=spectral hole burning, CH=carrier heating, CC carrier cooling, BF=band-filling).

As shown in Fig. 2.1.8, there are four principal features in the gain evolution, namely spectral hole burning, carrier heating, carrier cooling and band-filling. In Fig. 2.1.9, a series of schematic diagrams illustrate the electron distribution in the conduction band of a bulk SOA before, during and after the arrival of a pump pulse (*E* refers to energy on the y-axis, and *ρ* refers to the density of states on the x-axis). Each of the processes labelled in Fig. 2.1.9 will be described in detail in the paragraphs below the figure.
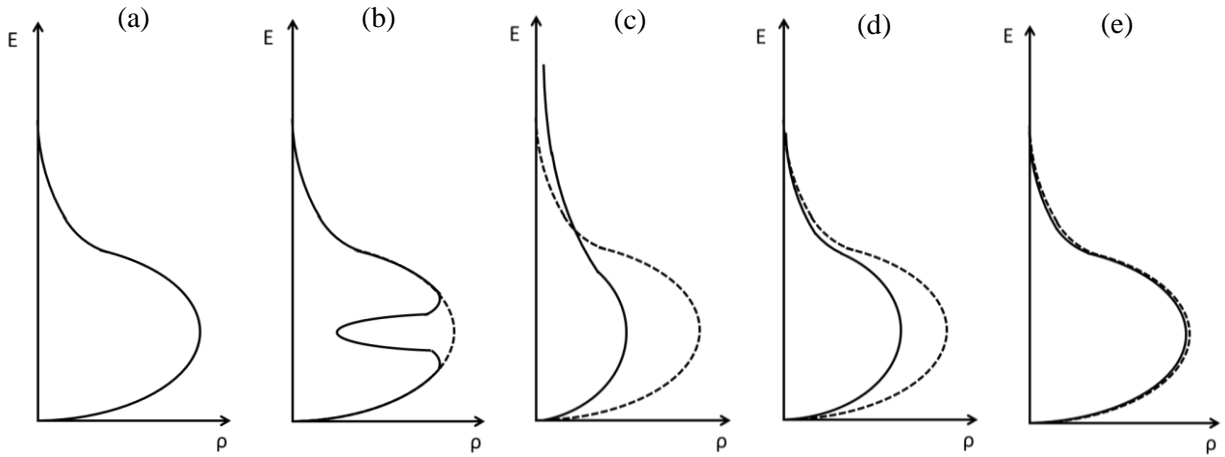
Fig. 2.1.9: Evolution of the electron distribution in the conduction band before and after the arrival of a pump pulse: (a) initial undisturbed distribution, (b) spectral hole burning, (c) carrier heating, (d) carrier cooling and (e) band-filling due to carrier injection.

Spectral hole burning: After the arrival of the pump pulse, the gain drops sharply as a result of spectral hole burning, whereby the pulse stimulates the recombination of carriers within a narrow spectral bandwidth compared to the total gain bandwidth [105]. Thus, carriers are preferentially depleted from a relatively small range of energies in the conduction and valence bands, and this leads to a "spectral hole" in the gain spectrum at a wavelength close to the pump wavelength. At high carrier densities, the spectral hole has a lifetime ~100fs, which is governed by the rate of carrier-carrier scattering [105].

Carrier heating: Following the creation of a spectral hole, the empty states within the spectral hole are rapidly filled by elastic collisions between carriers by means of Coulomb interactions within tens of femtoseconds [106, 107]. The Pauli Exclusion Principle means that carriers are forbidden to occupy identical states in the energy distribution. Carriers with high energies can fall into the empty states created by the spectral hole. Due to conservation of energy, the scattering partners receive the energy lost by the high energy carriers. After the scattering process is repeated many times, the net effect is the creation of a temporary Fermi-Dirac distribution at a higher effective temperature than the original, undisturbed distribution. The temperature of the transient Fermi-Dirac distribution is higher than the original distribution because the carriers removed by the pump pulses were below the mean temperature of the original distribution. The temporary Fermi-Dirac distribution has a lifetime of ~700fs [108].

25

Carrier cooling: After the formation of the temporary hot Fermi-Dirac distribution, the carriers with the highest energies in this distribution cool down by falling into empty states with lower energies via carrier-phonon scattering. The overall effect is for the hot carriers to transfer their kinetic energy to the crystal lattice, and the carrier distribution reverts to its original starting temperature, albeit with lower carrier density than before the arrival of the pump pulse. The process of carrier cooling is responsible for the majority of the ultrafast component in the gain recovery and it takes place on a timescale of ~1ps [109].

Band-filling: Finally, the depleted carrier distribution at the original temperature is replenished via band-filling due to the application of an external current bias to the SOA. It is important to remember that carrier injection occurs on a continuous basis. Before the arrival of the pump pulse, there is a dynamic equilibrium where the rate of carrier injection is balanced by the various recombination processes (non-radiative, spontaneous and Auger) so the gain remains at a constant level. However, after the arrival of the pump pulse and the subsequent depletion of carriers, the dynamic Auger recombination lifetime $\tau_{dynamic}$ changes due to the drop in carrier density as $\tau_{dynamic} \propto 1/N^2$ (see Eq. 2.1.9). At low carrier density, $\tau_{dynamic}$ is long, which means that in the initial stages of gain recovery, the carrier density increases rapidly because the rate of carrier injection far exceeds the rate of Auger recombination. However, as the carrier density goes up, this means that $\tau_{dynamic}$ becomes shorter so the rate of Auger recombination gradually increases as the carrier density increases. As a consequence of this changing rate of carrier recombination and a constant rate of carrier generation, the band-filling component of the gain evolution has a long exponential recovery tail with a typical lifetime of ~100ps. However, the recovery time at a given temperature can be decreased by increasing the current bias.

Input signal pulses to an SOA experience a phase shift as a result of the change in the refractive index of the material which necessarily accompanies the change in gain. The relationship between gain and phase is mathematically expressed using the Kramers-Kronig relations, which link the real and imaginary parts of the refractive index in any material [110]. The phase shift $\Delta\varphi(t)$ is given by Eq. 2.1.14, where L is the length of the active region, λ is the signal wavelength and $\Delta n(t)$ is the time-dependent refractive index change within the active region (defined in the frequency domain by Eq. 2.1.15).

$$\Delta\varphi(t) = \frac{2\pi L}{\lambda}\Delta n(t) \tag{2.1.14}$$

$$\Delta n(\omega) = \frac{c}{\pi}\int_{0}^{\infty}\frac{\Delta g(\omega')}{(\omega')^2 - \omega^2}d\omega' \tag{2.1.15}$$

In Eq. 2.1.14, ω' refers to angular frequency in the gain spectrum, ω refers to angular frequency in the refractive index spectrum and $\Delta g(\omega')$ refers to the change in net modal gain in the SOA gain spectrum at a given angular frequency ω'. As will be discussed in Section 2.1.4.6, when the SOA is placed inside an interferometric arrangement that exploits the XPM effect, a π phase shift is generally desirable (but not mandatory) for many types of signal processing operations [111]. The phase evolution of a typical bulk SOA following the arrival of a single pulse with pulse width ~100fs and energy per pulse of ~100fJ is displayed in Fig. 2.1.10.
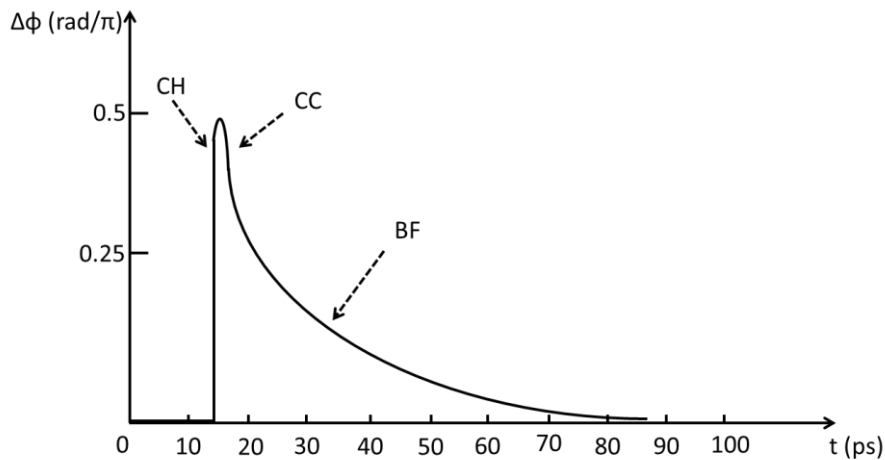
Fig. 2.1.10: Schematic diagram of phase evolution for a typical SOA.

As shown in Fig. 2.1.10, most of the processes which govern the shape of the gain evolution usually manifest themselves in the phase evolution. However, spectral hole burning is generally absent from the phase evolution when it is symmetrical around the centre frequency and when the probe wavelength is close to the pump wavelength [105]. Although carrier heating and carrier cooling effects are often visible in the phase evolution, their proportional contribution to the phase response is generally much lower than their contribution to the gain response.

The fact that the phase evolution of an SOA is dominated by the band-filling component can be explained by the fact that the ultrafast and the band-filling components have their own

separate values for the linewidth enhancement factor, otherwise known as the alpha factor α_{fac}. The precise definition of the alpha factor is the ratio of the derivative of the real and imaginary parts of the complex refractive index with respect to carrier density (see Eq. 2.1.16), where n_r is the real part of the refractive index and n_i is the imaginary part of the refractive index.

$$\alpha_{fac} = \left(\frac{dn_r}{dN}\right)\left(\frac{dn_i}{dN}\right)^{-1} \tag{2.1.16}$$

However, the alpha factor can be expressed in a more convenient formula to directly compare the experimentally measured gain and phase responses of an SOA [112]. For the band-filling nonlinearity, where there is a net increase in the carrier population, the alpha factor $\alpha_{fac,bf}$ is given by Eq. 2.1.17, where $n=n_r$. For the ultrafast nonlinearity, where there is no net change in the carrier population, changes in the gain and refractive index with respect to temperature T_K are employed to calculate the alpha factor $\alpha_{fac,uf}$ (see Eq. 2.1.18) [109].

$$\alpha_{fac,bf} = \frac{4\pi}{\lambda}\left(\frac{dn}{dN}\right)\left(\frac{dg}{dN}\right)^{-1} \tag{2.1.17}$$

$$\alpha_{fac,uf} = \frac{4\pi}{\lambda}\left(\frac{dn}{dT_K}\right)\left(\frac{dg}{dT_K}\right)^{-1} \tag{2.1.18}$$

Generally, $\alpha_{fac,uf} < \alpha_{facbf}$ because the band-filling nonlinearity involves increasing the total number of carriers present in the active region, whereas the ultrafast component merely involves redistribution of existing carriers within the active region [109].

The nonlinear properties of an SOA can be exploited in 3 main ways to allow the device to operate as an optical signal processing element, namely cross-gain modulation (XGM), cross-phase modulation (XPM) and FWM [94, 113].

XGM means that gain modulation of one optical signal affects the gain experienced by all other optical signals propagating in the SOA [94]. XGM can be advantageous as it is straightforward to implement for simple operations such as wavelength conversion and it allows high output powers to be achieved as it takes full advantage of the power gain in the SOA. However, XGM-based wavelength conversion leads to inversion of the data signal, the chirp of

the output signal is high, the noise figure is high, the extinction ratio of the output signal is low, and the switching capability is limited by the long full recovery time of an SOA due to nonlinear patterning effects [114, 115]. Nonlinear data patterning occurs at bit rates greater than the recovery rate, whereby the gain experienced by one pulse is not the same gain experienced by a successive pulse and this leads to variation in the modulation depth.

XPM means that the refractive index modulation induced by one optical beam affects the output phase of all other signals propagating in the SOA [94]. From a practical perspective, XPM is more complicated to implement compared to XGM, as it requires the use an interferometer to exploit the refractive index modulation. However, the switching capability of an XPM-based switch which uses push-pull interferometry has several advantages such as the fact that the polarity of the output signal can be controlled (i.e. data inversion can be eliminated), the output signal has low chirp and high extinction ratio, and the switching capability is not necessarily restricted by the long full recovery time of the SOA(s) [114, 116].

FWM is an intermodulation process whereby two or more input optical signals beat with each other in the SOA and modulate the carrier density and carrier distribution. This leads to the creation of gain and refractive index gratings in the SOA, which leads to the generation of signals at new optical frequencies [94, 117]. The main advantage of an FWM-based switch is that it allows higher speed operation compared to XGM-based and XPM-based switches. Furthermore, FWM is a coherent effect that preserves the phase of an input signal so FWM-based switches are transparent to signal format and therefore capable of performing signal processing operations on optical signals encoded using advanced modulation formats such as binary phase shift keying (BPSK) or quadrature phase shift keying (QPSK) [118-120]. The conversion efficiency in an FWM-based switch is generally quite low (typically less than -5dB) [121, 122], although R.P. Webb *et al* have recently demonstrated FWM conversion gain in an SOA for a frequency detuning of up to 400GHz [123].

2.1.4   *Enhancing the switching capability of SOAs*

Due to the long band-filling recovery time (~100ps) for a typical single SOA, it is necessary to employ various techniques to improve the switching capability of SOAs because they would otherwise be limited to switching at bit rates $\leq$10Gb.s^{-1}. For instance, the long recovery time of

the SOA can be circumvented by means of p-doping with Zn of the barriers in the MQW active region [124, 125], using a narrow bandpass filter (BPF) after the SOA [126, 127], or the application of a saturating CW holding beam [96, 128]. Moreover, SOAs with long recovery times can be placed inside push-pull interferometric configurations where XPM rather than XGM is exploited. Alternative options include the Turbo-Switch configuration [129] and the concatenated SOA-EAM configuration [130]. All of these techniques are discussed below.

2.1.4.1 Holding beams

The effective recovery time of an SOA can be enhanced by the use of an additional saturating CW or pulsed beam known as a "holding beam" at a different wavelength to the pump and probe signals input to the SOA [131]. The holding beam decreases the level to which the carrier density must recover after the arrival of a data signal pulse [132]. Although this technique leads to a dramatic reduction in the carrier recovery time, it reduces the extinction ratio and adds to the complexity of the configuration [124]. For wavelength conversion between a CW probe and a pulsed pump, if the CW probe has a high average power (>0dBm), it has a similar effect on the SOA as a holding beam [133-135].

2.1.4.2 Implanting p-type dopants into active region

It was found by L. Zhang *et al* that the recovery time can be reduced by introducing p-type dopants in the active region of an MQW SOA [124, 125]. When there was no p-type doping in the MQW section, the 1/e recovery time was 38ps. By contrast, it was found that when the barriers between quantum wells were doped with p-type dopants such as Zn, the 1/e recovery time was as low as 11ps. This increase in the recovery rate was attributed to the improvement in the differential material gain in the MQW section by L. Zhang *et al* [125].

2.1.4.3 Narrow bandpass filtering

M.L. Nielsen *et al* and Y. Liu *et al* have demonstrated signal processing functions such as demultiplexing and wavelength conversion at bit rates up to 640Gb.s^{-1} using an SOA

concatenated with a narrow BPF (see Fig. 2.1.11(a)) [126, 127]. The operating principle of this configuration is based on the fact that the BPF selects the blue-shifted sideband of the modulated CW probe (see Fig. 2.1.11(b)) [127].
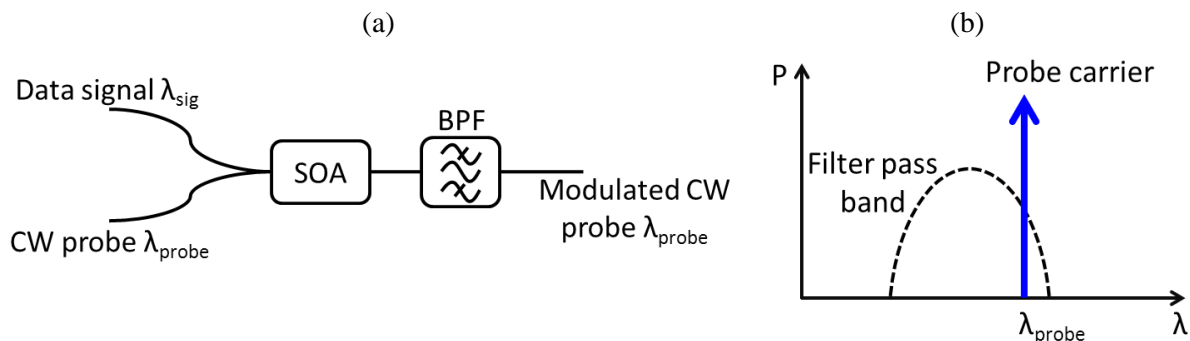
Fig. 2.1.11: (a) SOA + narrow BPF switching configuration, (b) schematic diagram showing the location of the BPF passband relative to the CW probe.

The gain dynamics of the SOA are slow due to the long band-filling tail in the recovery, but the chirp dynamics (due to modulation of the refractive index by the pump) in the SOA are fast. The leading edge of the modulated probe is red-shifted whereas the trailing edge is blue-shifted. Thus, the leading edge of the modulated probe moves the signal outside the passband of the BPF, so the transmittance of the configuration falls sharply. Subsequently, the trailing edge of the modulated probe moves the signal back into the passband of the BPF, so the transmittance of the configuration rises rapidly. The net effect is that the detuned BPF is capable of extracting the fast chirp dynamics in the SOA. The response time of this system is ultimately governed by the ultrafast carrier heating in the SOA [126]. This type of switch offers benefits such as simple construction and high speed operation ($\geq$100Gb.s^{-1}). However, the output signal suffers from a low extinction ratio and it is difficult to monolithically integrate the system onto a single chip.

2.1.4.4 Turbo-Switch configuration

The Turbo-Switch is a configuration which was proposed by R. Giller *et al* in 2006 that improves the switching capability of SOAs without exploiting interference effects and without degrading the optical-signal-to-noise-ratio (OSNR) [129]. The Turbo-Switch is a relatively simple and stable configuration, and it inherently diminishes the patterning effects which become apparent when high speed serial data signals are input to an SOA. A Turbo-Switch essentially

consists of two similar or identical SOAs in series which are separated by a broad band pass filter (BPF) as illustrated schematically in Fig. 2.1.12.
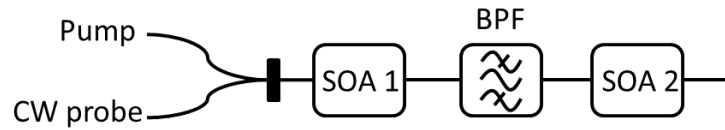
Fig. 2.1.12: Conventional Turbo-Switch configuration (SOA1+BPF+SOA2).

The operation principle of the Turbo-Switch can be summarized as follows. A CW probe beam and pump pulses are input to SOA1, where XGM between pump and probe takes place. Schematic diagrams of the CW probe input to SOA1, the gain dynamics of SOA1, and the probe output from SOA1 are displayed in Fig. 2.1.13.
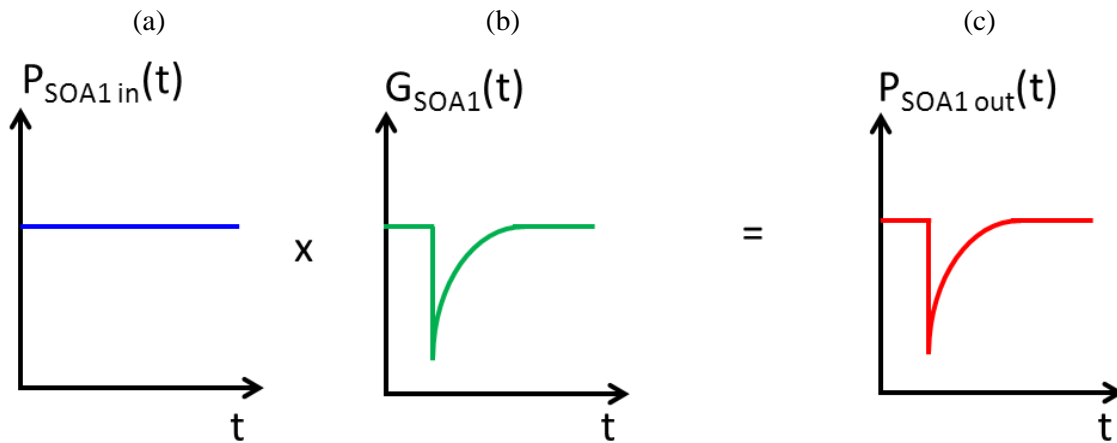
Fig. 2.1.13: (a) CW probe input to SOA1, (b) gain dynamics of SOA1 in response to the pump pulse and (c) modulated CW probe output from SOA1.

In Fig. 2.1.13(a), it is apparent that the CW probe power is constant when it enters SOA1. If the CW probe power is moderate (~0dBm), it has the same effect as a holding beam and this reduces the interband recovery time. The gain evolution of SOA1 in response to a pump pulse is illustrated in Fig. 2.1.13(b) and this is imprinted on the CW probe due to XGM between pump and CW probe, leading to the modulated CW probe output from SOA1. To prevent XGM between pump and probe taking place in SOA2, the BPF is tuned so that it prevents the amplified pump pulses leaving SOA1 from reaching SOA2. However, the BPF allows transmission of the full spectrum of the modulated CW probe to SOA2. In Fig. 2.1.14, schematic diagrams of the

signals input to SOA2, the gain response of SOA2 due to the effect of the modulated CW probe and the probe output from SOA2 are displayed.
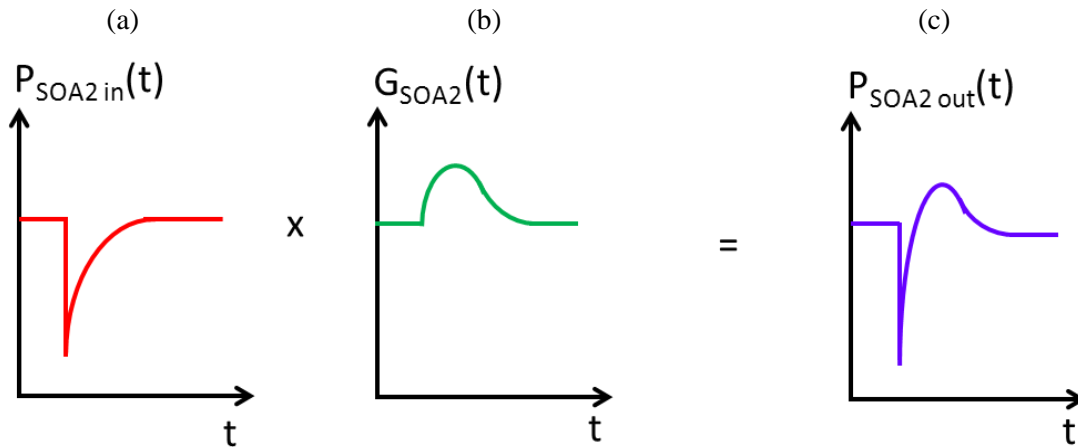
Fig. 2.1.14: (a) Modulated CW probe input to SOA2, (b) gain dynamics of SOA2 in response to the modulated CW signal and (c) the signal output from SOA2.

As shown by Fig. 2.1.14(b), self-gain modulation (SGM) or self-interaction of the modulated CW probe occurs in SOA2, which means that the gain rises when the instantaneous probe power is low and the gain falls when the instantaneous probe power is high. The net effect of the carrier dynamics in SOA2 is negation of most of the slow interband tail in the gain and phase recovery profiles. Moreover, there is an overshoot in the gain recovery, an effect that can act to reduce patterning effects [129].

2.2.4.5 Concatenation of an SOA with an EAM

E. Zhou *et al* have suggested that another means of counteracting the slow tail in the gain response of a single SOA is to concatenate an EAM with the SOA, which can take the form of either co-propagation or counter-propagation configurations [130, 136]. An SOA and an EAM have opposing modulation characteristics and this can be exploited by using the EAM response to cancel out the slow recovery tail in the gain response of an SOA. However, the sweepout time for photogenerated carriers in the EAM should be carefully engineered to match the band-filling gain recovery time in the SOA [130]. Furthermore, the performance of the counter-propagation SOA-EAM configuration is better than the co-propagation SOA-EAM configuration, but the counter-propagation configuration is more complicated to implement.

2.1.4.6 Push-pull interferometers

Interferometers are frequently deployed in optical communications for applications such as electro-optic modulation, comb generation and detection of signals with advanced modulation formats such as DPSK [137-140]. They are especially useful in optical signal processing because SOAs can be placed inside push-pull interferometric configurations using a differential switching scheme to improve their performance because the switching window of an interferometer can be designed to be less than the full carrier recovery lifetime [141]. In principle, the main types of interferometers that can be employed for the purpose of cancelling out the long band-filling recovery tail of an SOA include the symmetric Mach-Zehnder interferometer (SMZI), the asymmetric Mach-Zehnder interferometer (AMZI), the TOAD (terahertz optical asymmetric demultiplexer) loop and the ultrafast nonlinear interferometer (UNI) [141]. A brief description of each of these types of interferometers is given below.

Symmetric Mach-Zehnder interferometer (SMZI)

The SMZI relies on push-pull operation, otherwise known as differential phase modulation to achieve ultrafast, low-power (<100fJ per pulse) switching. To create an SMZI, two SOAs are placed inside a Mach-Zehnder interferometer, one in each arm (see Fig. 2.1.15(a)) [142]. The operation principle underlying the SMZI is illustrated in Fig. 2.1.15(b). At the input 50:50 coupler, an input data signal is split into two components, one for each arm of the interferometer. There is a nonlinear phase change in each SOA due to the refractive index modulation induced by each pulse but there is a time delay between the maximum phase shift for each SOA. The two split signal components recombine and interfere at the 50:50 output coupler, and the long recovery tail in the two phase responses cancel each other out to create a short, rectangular-like switching window that is ultimately determined by the pulsewidth of the signal pulses [142].
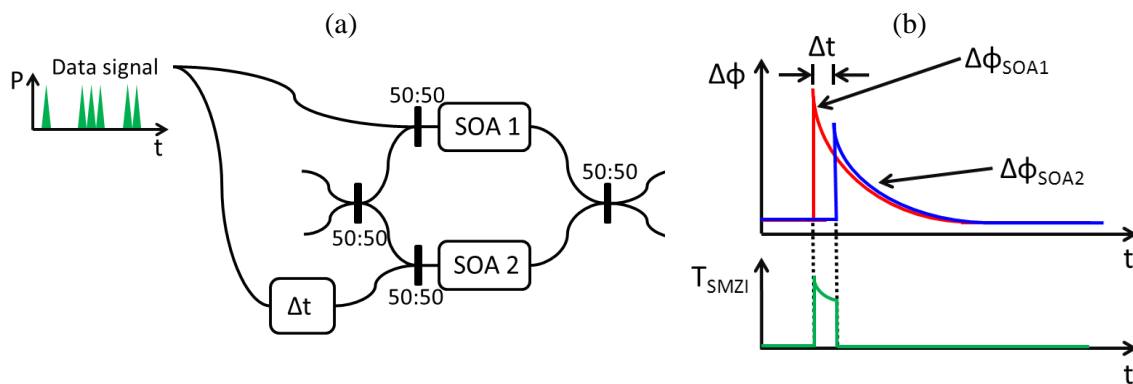
Fig. 2.1.15: (a) Push-pull SMZI switch and (b) the operation principle of the switch.

Although switching is based on a refractive index change induced by a carrier density change in the SOAs, the push-pull mechanism partially negates the slow carrier recovery time in each SOA [143]. However, the carrier density cannot not fully recover between consecutive pulses at bit rates >10Gb.s^{-1} so data patterning still poses a problem for this switching configuration. The SMZI configuration is advantageous as it can be integrated onto a single chip and it is capable of performing optical signal processing functions at bit rates ≥168Gb.s^{-1} in RZ-OOK format [144].

Asymmetric Mach-Zehnder interferometer (AMZI)

The AMZI or delay interferometer (DI), configuration relies on the same general operation principles as the SMZI configuration but the SOA is not placed inside the interferometer (see Fig. 2.1.16). Instead, a separate AMZI is placed after a single SOA, where the modulated signal from the SOA is split at a 50:50 input coupler and one arm goes through a phase shifting element while the other arm goes through a delay line within the AMZI. The signals in each arm recombine at the 50:50 output coupler and the long carrier recovery time of the single SOA can be effectively eliminated by the AMZI when the phase shifting element is suitably biased.
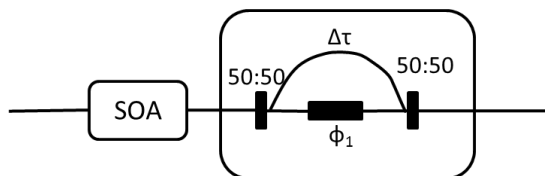
Fig. 2.1.16: Schematic diagram of SOA-AMZI switch (φ$_1$=phase shifting element, Δτ=delay line).

35

The AMZI can be constructed from discrete components (cascaded polarization controllers, a calcite crystal and polarizer) to create a cross-polarization delay interferometer [145], or it can be integrated on a silica-on-silicon or III-V semiconductor platform [146-148]. The SOA-AMZI configuration offers benefits such as ease of integration, polarization insensitivity, and the ability to operate at high speed ($\geq$100Gb.s^{-1}) [146].

Terahertz optical asymmetric demultiplexer (TOAD) interferometer

The terahertz optical asymmetric demultiplexer (TOAD) loop interferometer consists of a loop mirror containing an SOA offset by a length Δx from the loop centre (see Fig 2.1.17) [149]. The offset, the pulsewidth and the length of the SOA active region collectively determine the minimum achievable width of the switching window for the TOAD loop.
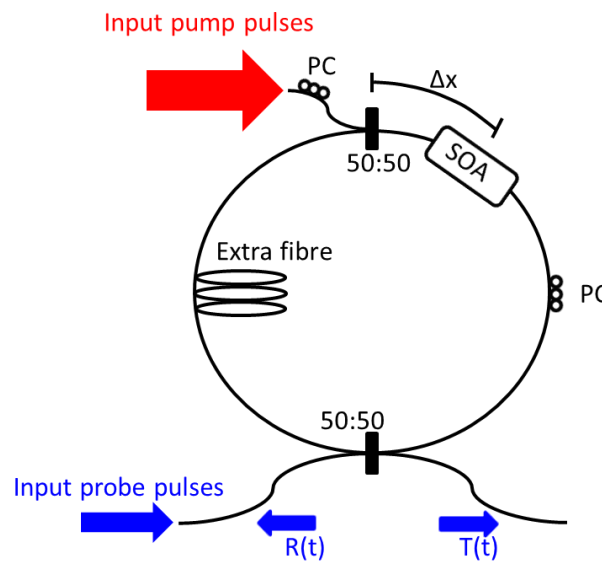
Fig. 2.1.17: TOAD loop schematic diagram.

When a probe pulse is incident upon the TOAD loop, it is split into two counter-propagating (clockwise and counter-clockwise) pulses at the 50:50 base coupler. In the absence of an input pump pulse, the polarization of the TOAD is biased so that the clockwise and counter-clockwise probe pulses return to the base coupler at the same time, so there is full reflection of the initial input probe pulse. When a pump pulse is incident upon the SOA, the gain and phase of the SOA are modulated. This means that the clockwise and counter-clockwise probe pulses return to the

base coupler at different times and this leads to a proportion of the initial input probe pulse being transmitted while the remainder of the power is reflected. Due to the counter-propagation geometry, the switching capability of the TOAD is limited to bit rates ≤50Gb.s^{-1} by the length of the SOA [150-152]. However, the properties of the TOAD can be exploited for real-time monitoring of the gain and phase response of an NLO device by simultaneously measuring the time-dependent reflection coefficient $R(t)$ and the transmission coefficient $T(t)$ for the loop, where t refers to time [109, 153].

Ultrafast nonlinear interferometer (UNI)

The ultrafast nonlinear interferometer (UNI) is a balanced, single arm interferometer that consists of a length of polarization maintaining fibre (PMF) followed by an SOA and a second length of PMF (see Fig. 2.1.18) [154]. The first segment of PMF splits an incoming signal pulse into two orthogonal polarizations (referred to as the leading signal pulse and the trailing signal pulse respectively) that are coupled into one facet of the SOA. A counter-propagating control pulse is coupled into the other facet of the SOA. The control pulse temporally overlaps the delayed signal pulse and induces gain and phase nonlinearities in the SOA. After travelling through the SOA, the two signal pulses are recombined in the second length of PMF and they interfere in a polarizer.
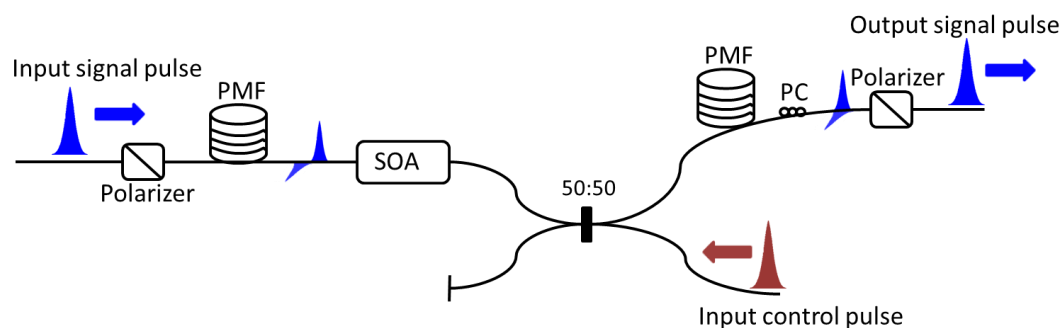
Fig. 2.1.18: Illustration of the operation of the UNI switch configuration.

Advantages of the UNI configuration include its low switching energy requirements, potential for integration, no external stabilization is required and it is capable of operating at bit rates ≥100Gb.s^{-1} [71, 150, 155].

2.2   Electro-absorption modulators

2.2.1   Structure of EAMs

An EAM is an optoelectronic device that is primarily employed in fibre optic communications for external modulation of CW laser beams at data rates <100Gb.s^{-1} [156, 157] but it can also be used as a photonic microwave mixer or a dual-functional modulator/detector [158]. An EAM has a similar structure to an SOA i.e. it generally consists of p-i-n semiconductor layers, with the intrinsic region having a higher refractive index than the surrounding p-type and n-type doped sections.   However, by contrast with an SOA where a current bias is applied to the device, a reverse voltage bias is applied to an EAM. A typical EAM has active region cross-section area ~0.1×10^{-12}m^2 and length ~100μm. EAMs are widely deployed as external modulators because they can operate at high data rates, no zero biasing voltage is required, only a low driving voltage is necessary (typically ≤5V), they can be integrated with lasers, and they have low or even negative chirp [158, 159]. One important disadvantage associated with EAMs is their limited power handling capability, which is a problem that is not shared by electro-optic modulators (EOMs) containing LiNbO$_3$ as the active element [160].

Apart from the ubiquitous use of EAMs as external modulators, it is possible to exploit the saturable absorption characteristics of this type of device to realize optical signal processing functionalities using the cross-absorption modulation (XAM) effect. The XAM effect in EAMs is advantageous as it avoids the signal inversion associated with the XGM effect in SOAs. However, as the EAM absorbs light and does not provide gain to an input signal, it must be pumped by a strong optical beam to achieve a strong modulation contrast ratio [157].

2.2.2   Static EAM characteristics

The optical absorption coefficient in the active medium of an EAM changes in the presence of an electric field [158]. There are two distinct types of electro-absorption effects, namely the Franz-Keldysh Effect (FKE) and the Quantum Confined Stark Effect (QCSE) [158]. The former mainly applies to bulk EAMs whereas the latter applies to MQW EAMs. Both FKE and QCSE are strongly wavelength-dependent effects [158].

The energy band diagrams in Fig. 2.2.1 illustrate the principle of FKE in a bulk EAM. In the absence of an applied electric field (see Fig. 2.2.1(a)), the energy of a single photon (in the infrared region) cannot provide sufficient energy to promote an electron from the conduction band to the valence band at point P_1. However, when an electric field is applied to the EAM (see Fig. 2.2.1(b)), the energy bands are tilted and an electron in the valence band can make the transition to the conduction band using a mechanism known as photo-assisted interband tunnelling [158], where the photon energy is equal to the energy between the valence band at point P_1 and the conduction band at point P_2. In the following diagrams, $\hbar$ is the reduced Planck's constant and ω is the angular frequency of the incoming photon.
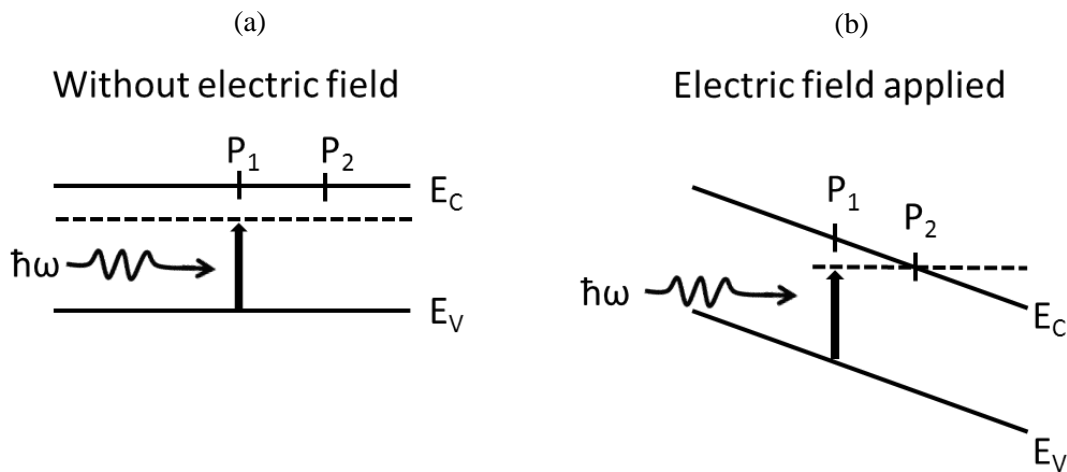
Fig. 2.2.1: FKE in an EAM, where E_C and E_V refer to the energy level of the conduction band and valence band respectively. (a) Energy band diagram in the absence of an applied electric field and (b) energy band diagram in the presence of an applied electric field.

A schematic diagram of the absorption spectrum for a bulk EAM as a function of applied reverse bias is shown in Fig. 2.2.2. In the absence of an applied reverse bias, there is a sharp drop in absorption at the bandgap wavelength λ_{bg}. When a reverse bias is applied to the EAM, the energy bands are tilted and the evanescent tails of the electron and hole wavefunctions can tunnel into the bandgap. Thus, absorption below the bandgap energy becomes possible and this leads to a red-shifted absorption spectrum (see Fig. 2.2.2).
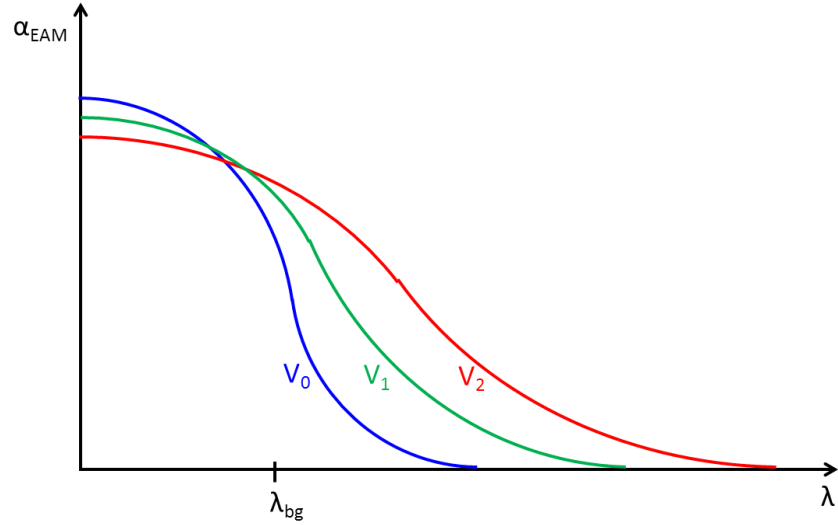
Fig. 2.2.2: Absorption spectrum for a bulk EAM with no applied reverse bias (blue line) and non-zero applied reverse bias (green line and red line). Note that $V_0=0V$ and $|V_2|>|V_1|$.

Fig. 2.2.3 illustrates the principle of QCSE in an MQW EAM. The electrons and holes in a quantum well in an MQW EAM are highly confined and the energy levels are quantized to form sub-bands, i.e. defined discrete energy levels [158]. The electrons and holes confined in the quantum wells are bound as excitons, although the binding energy of these excitons is much greater than for excitons in bulk semiconductor.
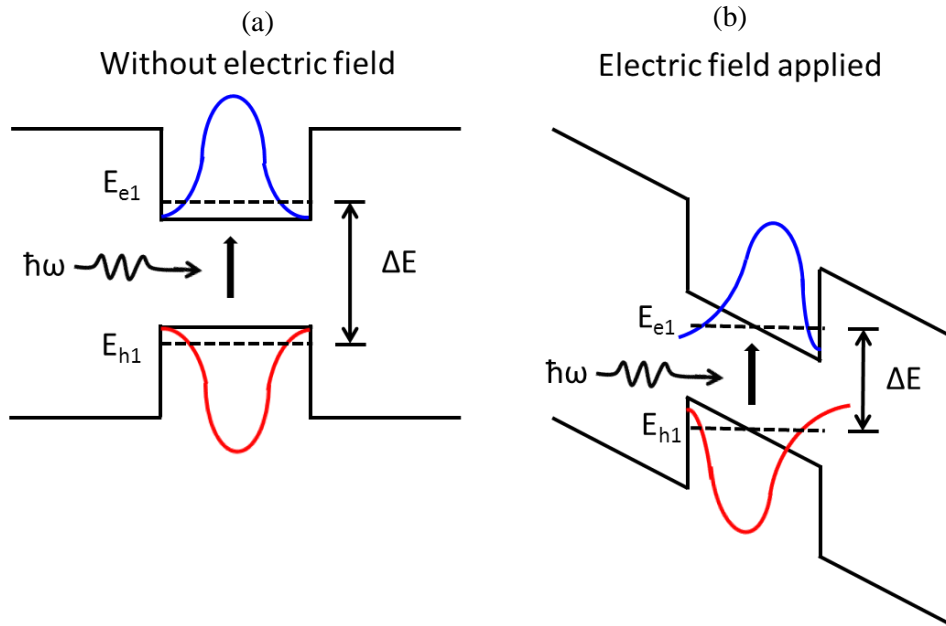
Fig. 2.2.3: Diagram illustrating QCSE in an EAM, where E_{e1} and E_{h1} refer to the first electron and hole energy levels respectively, and ΔE refers to the separation between E_{e1} and E_{h1}.

In the absorption spectrum for an MQW EAM, the locations of step edges are located at intersubband energy gaps denoted by E_{cv} (see Eq. 2.2.1, where E_g is the bandgap energy, E_e is the electron energy level in the conduction band and E_h is the hole energy in the valence band).

$$E_{cv} = E_g + E_e + E_h \qquad (2.2.1)$$

As the reverse bias increases, the degree of confinement of carriers in each quantum well is reduced, the electron energy level E_e and hole energy level E_h of the bound states in each quantum well decrease due to tilted energy bands, and the exciton peaks become broader. All of these changes lead the absorption spectrum becoming increasingly red-shifted as the reverse voltage bias increases [158]. Additionally, the electron-hole overlap decreases as the reverse bias increases and this lowers the exciton peaks in the absorption spectrum [158]. A schematic diagram of the absorption spectrum for an MQW EAM is shown in Fig. 2.2.4.
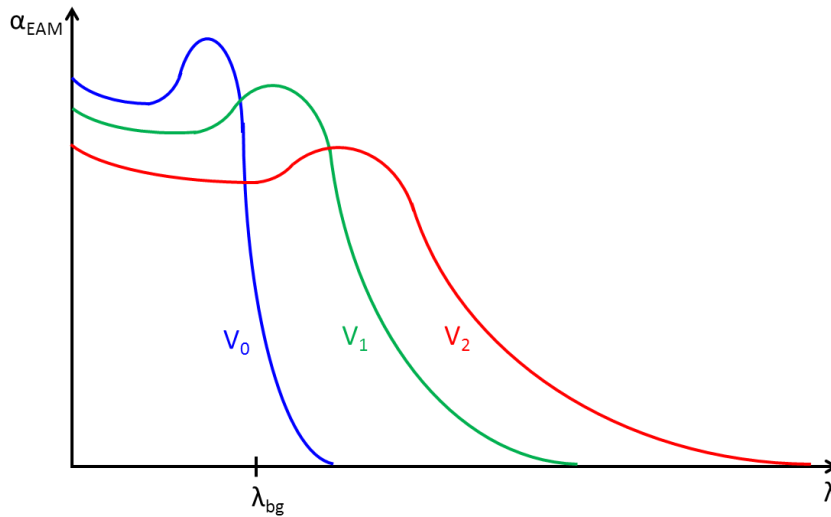
Fig. 2.2.4: Absorption spectrum for an MQW EAM with no applied reverse bias (blue line) and nonzero applied reverse bias (green line and red line). Note that $V_0=0V$ and $|V_2|>|V_1|$.

As shown in Fig. 2.2.4, when there is no applied reverse bias, there is a clearly defined exciton absorption peak and a sharp band-edge at the bandgap wavelength λ_{bg}. When there is a nonzero reverse bias applied to the EAM, the height of the exciton peak decreases and becomes red-shifted, while the entire absorption spectrum becomes red-shifted.

2.2.3   Carrier dynamics in EAMs

The absorption coefficient in an EAM is a function of electric field, carrier density, carrier temperature and photon density [161]. The carrier density dynamics are governed by Eq. 2.2.2 and Eq. 2.2.3 respectively, where N_e is the electron density, J_e is the electron flux, v_g is the photon group velocity, α_m is the modal absorption coefficient, S is the photon density, β_{tpa} is the two photon absorption (TPA) coefficient, R_e is the electron recombination rate, N_h is the hole density, J_h is the hole flux and R_h is the hole recombination rate [161].

$$\frac{\partial N_e}{\partial t} + \frac{\partial J_e}{\partial x} = v_g \alpha_m S + v_g \beta_{tpa} S^2 - R_e \qquad (2.2.2)$$

$$\frac{\partial N_h}{\partial t} + \frac{\partial J_h}{\partial x} = v_g \alpha_m S + v_g \beta_{tpa} S^2 - R_h \qquad (2.2.3)$$

As shown in Eq. 2.2.4 and Eq. 2.2.5, the electron and hole fluxes are themselves functions of carrier density, where x is distance, $v_{e,dr}$ is electron drift velocity, D_e is electron diffusion coefficient, $v_{e,dr}$ is hole drift velocity and D_h is hole diffusion coefficient [161].

$$J_e = N_e v_{e,dr} - D_e \frac{\partial N_e}{\partial x} \qquad (2.2.4)$$

$$J_h = N_e v_{h,dr} - D_h \frac{\partial N_h}{\partial x} \qquad (2.2.5)$$

The electron and hole drift velocities are dependent both on the electric field and on the mobility of each type of carrier. The carrier temperature influences the absorption dynamics because the temperature affects the carrier mobilities and the carrier sweepout rate [161, 162].

For a bulk EAM, electrons and holes are generated uniformly across the absorbing intrinsic region by incoming photons, as shown in Fig. 2.2.5(a). Electrons drift towards the n-type contact and holes drift towards the p-type contact under the influence of the applied electric field and the built-in potential. The carriers accumulate at the heterojunctions until they are swept out from the intrinsic region. For an MQW EAM, there are two additional transport processes, namely carrier escape and carrier recapture by quantum wells (see Fig. 2.2.5(b)).
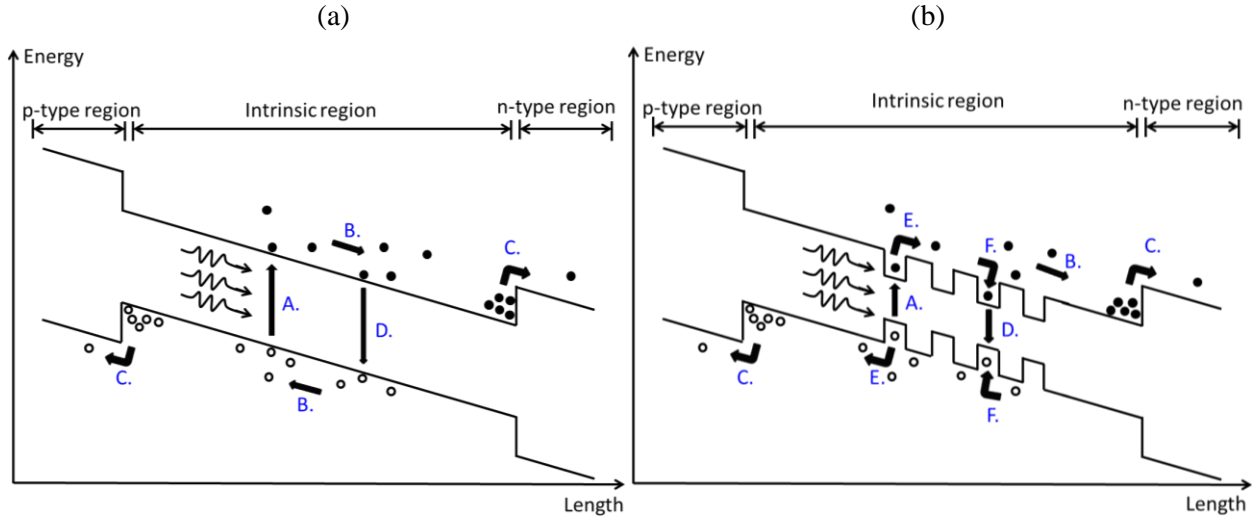
Fig. 2.2.5: Transport processes in (a) a bulk EAM and (b) an MQW EAM. The processes are as follows: (A) Carrier excitation, (B) drift-diffusion transport, (C) carrier sweepout from intrinsic region, (D) spontaneous recombination. For the MQW EAM, there are two additional transport processes: (E) carrier escape from quantum wells, (F) recapture of carriers into quantum wells.

The absorption dynamics are dominated by the influence of the effective electric field within the intrinsic region [161]. While the photo-generated carriers remain in the intrinsic region, they screen the applied electric field and this leads to a blue-shift of the absorption spectrum. The absorption cannot recover to the steady-state level until all carriers have been swept out completely into the contacts. The carriers leave the intrinsic region via thermionic emission and Fowler-Nordheim tunnelling, as illustrated in Fig. 2.2.6.
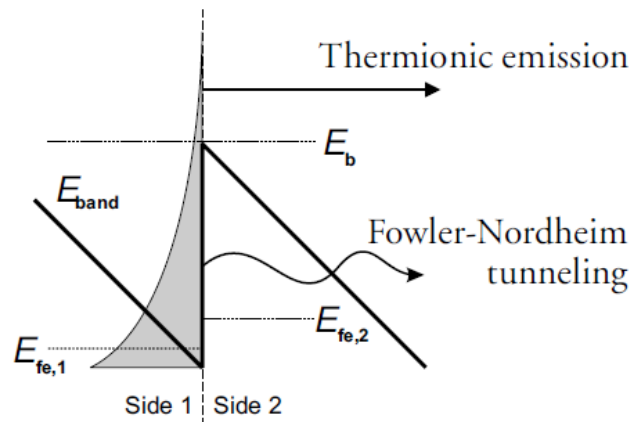
Fig. 2.2.6: Thermionic emission and Fowler-Nordheim tunnelling at an energy barrier.

43

The sweepout rates via thermionic emission and Fowler-Nordheim tunnelling are limited by the effective mass of the carrier and the height of the energy barrier at the valence band discontinuity. Since the valence band typically has a greater discontinuity than the conduction band and holes have a larger effective mass than electrons, holes are usually swept out at a slower rate compared to electrons [163].

The transport of carriers out of the quantum wells and through the heterojunctions is dominated by thermionic emission [161, 162]. The electron current density $J_{e,th}$ due to thermionic emission is given by Eq. 2.2.6, where e is the charge of an electron, k_B is the Boltzmann constant, T is temperature, $\hbar$ is the reduced Planck constant, $m_{e,1}$ is the electron mass on Side 1 (see Fig. 2.2.6), $m_{e,2}$ is the electron mass on Side 2, $E_{fe,i}$ are the Fermi energy levels on either side of the barrier and $E_{b,e}$ is the barrier energy for electrons.

$$J_{e,th} = -\frac{e(k_B T)^2}{2\pi^2 \hbar^3} \left(\frac{2}{m_{e,1}^{-1} + m_{e,2}^{-1}} \right) \left[\exp\left(-\frac{E_{b,e} - E_{fe,1}}{k_B T} \right) - \exp\left(-\frac{E_{b,e} - E_{fe,2}}{k_B T} \right) \right] \qquad (2.2.6)$$

The current density for holes due to thermionic emission can be found using a similar expression.

Fig. 2.2.7 shows the transmission evolution for a bulk EAM following the arrival of a ~100fs pump pulse and energy ~1pJ. There are four principal features in the transmission evolution, namely spectral hole burning, carrier heating, carrier cooling and carrier sweepout.
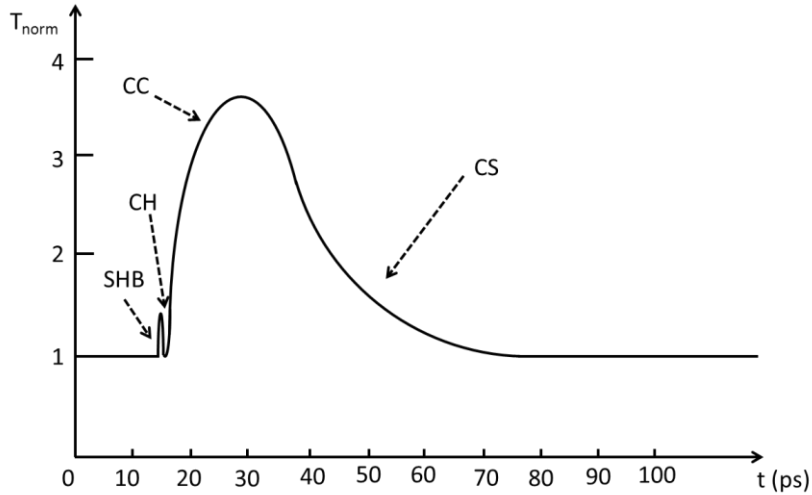
Fig. 2.2.7: Transmission evolution for a typical EAM following excitation by a single ~1pJ pump pulse (pulsewidth ~100fs) (SHB=spectral hole burning, CH=carrier heating, CC=carrier cooling, CS=carrier sweepout).

Spectral hole burning: The transmission increases rapidly as the pump pulse generates a large number of carriers within a narrow range of energies, leading to the creation of a spectral hole. The spectral hole is filled due to thermalization by carrier-carrier scattering within ~100fs [161].

Carrier heating: Carrier-carrier scattering leads to spreading out of the carrier distribution generated by the formation of a spectral hole. The thermal distribution of the carriers has a greater temperature than the surrounding crystal lattice. This carrier distribution at an elevated temperature has a lifetime ~500fs [161].

Carrier cooling: Following the creation of a hot carrier distribution, the carriers cool to the lattice temperature via carrier-phonon scattering within a lifetime ~1ps [164].

Carrier sweepout: The final stage in the transmission response depends on the removal of the photogenerated carriers from the absorption region [161]. The carriers pile up at the heterojunctions until they are swept out via thermionic emission and Fowler-Nordheim tunnelling.

To visualize the carrier dynamics within an EAM, a series of diagrams illustrate the electron distribution in the conduction band of a bulk EAM before, during and after the arrival of a pump pulse in Fig. 2.2.8. The solid lines indicate the instantaneous carrier distribution and the dotted line denotes the equilibrium carrier distribution.
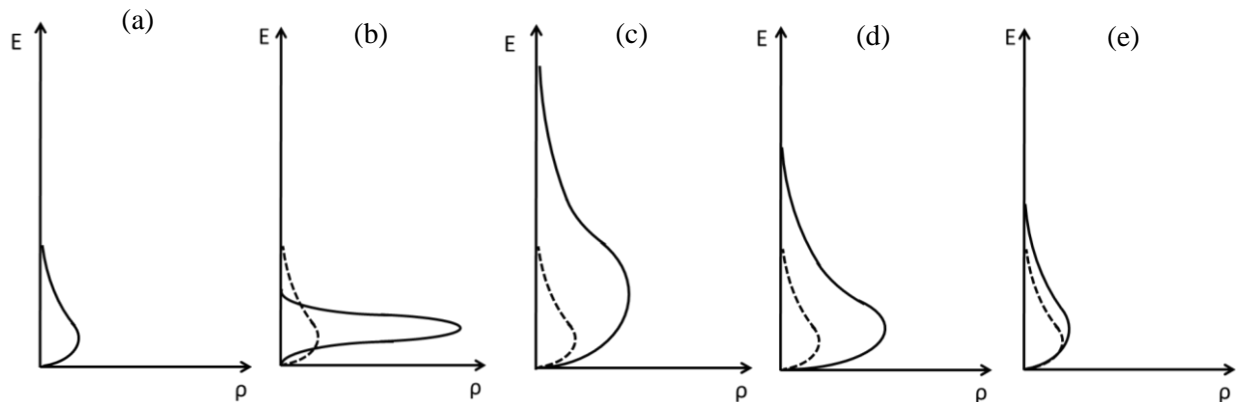
Fig. 2.2.8: Evolution of the electron distribution in the conduction band before and after the arrival of a pump pulse. (a) Initial undisturbed distribution, (b) spectral hole burning, (c) carrier heating, (d) carrier cooling and (e) carrier sweepout from the intrinsic region.

Optical pulses launched into an EAM experience a phase shift associated with the absorption change due to the relationship between the real and imaginary parts of the refractive index in any medium governed by the Kramers-Kronig relations [110]. However, the magnitude of the phase shift is typically quite small ($\Delta\varphi_{max}\sim0.1\pi$ rad). Fig. 2.2.9 shows the phase evolution for a typical bulk EAM (corresponding to the transmission evolution illustrated in Fig. 2.2.4).
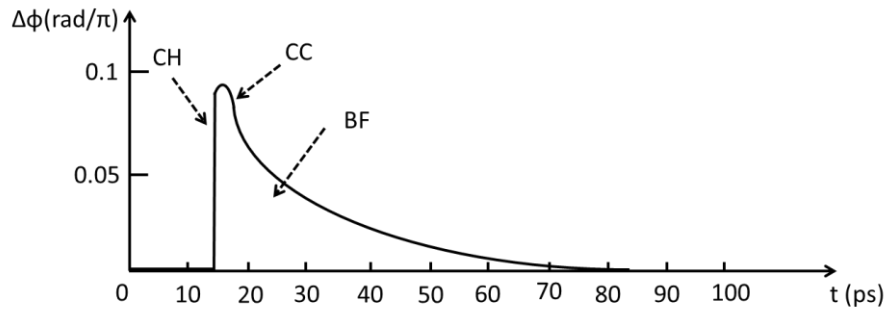
Fig. 2.2.9: Schematic diagram of phase evolution for a typical EAM following excitation by a single ~1pJ pump pulse (pulsewidth ~100fs).

2.2.4   Enhancing the switching capability of EAMs

The switching capability of any EAM is ultimately limited by the relatively long time taken for photogenerated carriers to be swept out from the intrinsic region into the contacts and, in the case of an MQW EAM, by the time taken for carriers to escape from quantum wells. Thus, it is important to minimize the sweepout time and quantum well escape time to enable high speed signal processing with EAMs. The application of a reverse bias to an EAM leads to a decrease in the sweepout time but ideally, the reverse bias should be as low as possible (<5V) because a high reverse bias leads to high transmission loss [165] and strong patterning effects due to large fluctuations in the local temperature within the EAM [166]. It is desirable to incorporate design features in the EAM which reduce the sweepout time and/or quantum well escape time without requiring the application of a high reverse bias (≥5V).

2.2.4.1   Reduction in barrier height at heterojunctions

It has been shown that it is possible to increase the sweepout rate in an EAM by reducing the height of the barriers at the interface between the intrinsic region and the contacts by introducing

gallium into the barrier composition [167]. N. El Dahdah *et al* investigated the carrier dynamics in InGaAs-InGaAsP MQW EAMs and they found that when the valence barrier height was 105meV, the shortest 1/e recovery time achievable was 15ps at a reverse bias of 3V. However, when the valence barrier height was reduced to 33meV, it was possible to attain a 1/e recovery time of 7ps at a reverse bias of 2V [167].

2.2.4.2 *Reduction in barrier width and height of quantum wells*

It was demonstrated by A.M. Fox *et al* that the use of low or thin barriers between individual quantum wells in an MQW EAM can dramatically reduce the time taken for carriers to escape from the quantum wells from ~100ps (for high, thick barriers) to below ~10ps (for low, thin barriers) without adversely affecting the electroabsorption performance i.e. the degree of exciton broadening is minimal [168].

2.3 Silicon (Si) waveguides

2.3.1 Structure of Si waveguides

A silicon wire waveguide, otherwise known as a Si nanowire, is a single mode channel waveguide formed on top of a silicon dioxide (SiO_2) layer resting on a silicon substrate. The waveguide is surrounded by cladding material with a lower refractive index than silicon e.g. SiO_2, silicon oxynitride (SiON), or a polymer such as SU8 or PSQ-LH. This type of platform is known as silicon-on-insulator (SOI) [169, 170]. One notable feature of Si waveguides is the strong confinement of light due to the high index contrast between the Si core ($n_{Si} \approx 3.5$) and the cladding (e.g. $n_{SiO2} \approx 1.5$). Refractive index contrast Δ is defined by Eq. 2.3.1, where n_1 is the refractive index of the core and n_2 is the refractive index of the cladding.

$$\Delta = \frac{n_1^2 - n_2^2}{2n_1^2}$$
(2.3.1)

For example, a Si nanowire with SiO_2 cladding has an index contrast of 0.4. By comparison, the index contrast in standard SMF is 0.06. Fig. 2.3.1(a) shows a cross-section through a Si nanowire where h denotes the core height and w denotes the core width, while the diagram in Fig. 2.3.1(b) illustrates the 3D structure of a spot-size converter at the end of a Si nanowire [171].
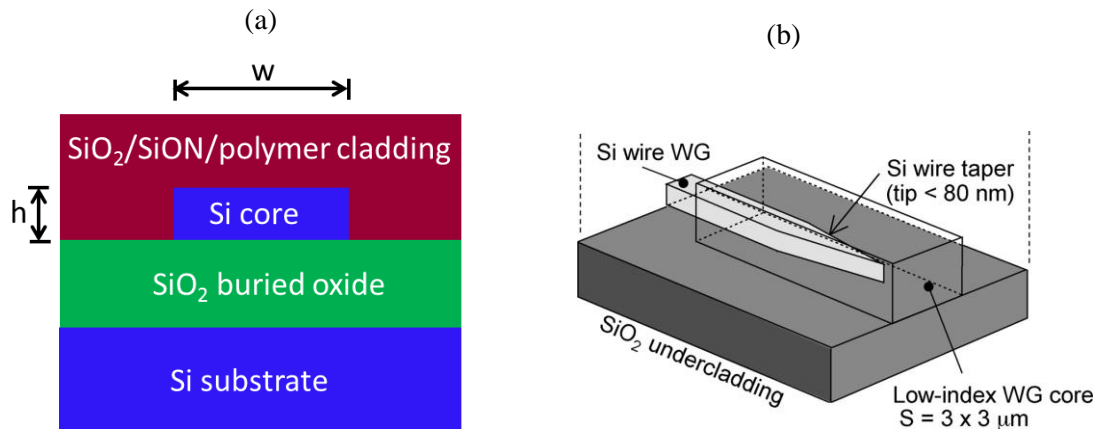
Fig. 2.3.1: (a) Schematic cross-section through an SOI waveguide and (b) spot size converter realized using tapered sections at the ends of the waveguide.

The strong optical confinement in Si means that the cross-section area can be reduced to submicron dimensions (100 to 300nm for the core height, 300 to 450nm for the core width and 5mm for the waveguide length). The ultrasmall geometry of Si nanowires is advantageous for optical signal processing because NLO effects that become apparent at high light intensities can be achieved at comparatively low input pulse energies (~10pJ per pulse).

One critically important aspect of a Si nanowire is the coupling efficiency between the waveguide and external optical components such as optical fibres. The effective mode area of a Si nanowire is typically ~1μm^2 whereas the effective mode area of standard SMF is ~100μm^2. This difference in mode field size means that if direct coupling between the Si nanowire and SMF were attempted, coupling losses up to 20dB per facet could be expected [171]. To circumvent this problem, one solution is to create tapered sections at both ends of the Si nanowire, where the taper width is typically 40 to 80nm. When light transits through the tapered sections, it gradually leaks out into the surrounding low refractive index cladding material. This allows the effective area to expand to ~10μm^2, which can reduce the coupling loss between the device and standard SMF to approximately 3dB per connection. When tapered optical fibres are employed to couple light into the Si nanowire, the coupling loss can be reduced further.

Another key factor in a Si nanowire is propagation loss within the waveguide. There are several contributions to propagation loss in these devices including linear loss mechanisms such as scattering from the sidewalls and impurities in the crystal lattice and nonlinear loss mechanisms such as two photon absorption (TPA) and free carrier absorption (FCA). Both of the nonlinear loss mechanisms will be discussed in more depth in the Section 2.3.2, so only linear loss will be discussed in this section. The principal origin of scattering losses in a Si nanowire is sidewall roughness. If the average magnitude of sidewall roughness is greater than ±10nm, the propagation loss can reach values as high as 60dB.cm^{-1}. However, if the average magnitude of the sidewall roughness is maintained to within ±2nm, the propagation loss can be as low as 3dB.cm^{-1} [171]. Although this value for propagation loss is far greater than the propagation loss for optical fibre (approx. 0.2dB.km^{-1}), it is sufficiently low to create viable passive and active photonic components on an SOI chip [172].

One more crucial factor that should be taken into account when considering a Si nanowire is its dispersion properties. Due to the sub-micron cross-section dimensions of a Si nanowire, the material dispersion is dominated by waveguide dispersion. In fact, dispersion engineering is

possible, whereby the dispersion relations are determined by the geometry of the Si nanowire. This ability to manage the dispersion relations permits precise control over the interaction between co-propagating signals in the device. The reason for this can be explained by examining the walk-off length L_w, which is a parameter that governs the distance over which co-propagating pump and probe pulses pass through each other's envelope. L_w is defined in Eq. 2.3.2, where T_{p0} is the half-width of the pump pulse, and β_{p1} and β_{s1} are the first order dispersion coefficients at the pump and probe wavelengths respectively [173]. The parameters β_{p1} and β_{s1} can also be referred to as the reciprocal group velocities at the pump and probe wavelengths.

$$L_w(\lambda) = \frac{T_{p0}}{\left| \beta_{p1}(\lambda) - \beta_{s1}(\lambda) \right|}$$

(2.3.2)

To increase the interaction between the pump and probe signals by maximizing the walk-off length, it is necessary to minimize the absolute difference between the reciprocal group velocities and this can be achieved by careful selection of the width and/or height of the Si nanowire.

A wide range of passive and active Si photonic devices have been reported in the literature, including Raman amplifiers, Raman lasers, modulators, light emitting devices (LEDs) employing Ge/GeSn/Si technology, photodetectors using Ge-on-Si technology, AWGs, microresonators and optical filters [172, 174, 175]. All of these developments suggest that Si photonics can be exploited to build complex photonic circuits containing a variety of components that are integrated onto a single chip e.g. low-cost miniature transceivers [176]. Moreover, silicon photonics could be employed in future microprocessors in multicore computing systems for on-chip interconnects and chip-to-chip electrical interfaces [177, 178].

Moreover, silicon-based nanophotonic devices are important candidates for optical signal processing applications because Si waveguides offer large optical nonlinearity, compactness, low power consumption, and the potential for integration with microelectronic or nanoelectronic circuits [179]. A variety of NLO phenomena have been observed in Si waveguides including SRS, SPM, XPM and FWM [180]. All of these effects can be exploited to create switching elements that require relatively low optical input powers and can be integrated with electronics using well-established CMOS processing techniques [180]. In Section 2.3.2, the carrier dynamics in Si nanowires will be explored.

2.3.2   Carrier dynamics in Si waveguides

When a light pulse is input to a Si waveguide, the intensity *I(t,z)* is attenuated due to several processes including linear loss, TPA and FCA [179]. TPA can occur in silicon as photons at telecommunication wavelengths have energy (E_{photon}=0.8eV at 1550nm) greater than half the indirect bandgap for silicon ($E_{g,indirect}$=1.1eV). As a direct consequence of TPA, free carriers are generated and these free carriers can absorb more photons until they recombine, primarily via surface recombination. The intensity is governed by Eq. 2.3.3, where *I(t,z)* is the intensity of the incident light, *z* is distance from the input facet, α_{lin} is the linear loss coefficient, β_{tpa} is the TPA coefficient, σ_{fca} is the FCA cross-section and *N(t,z)* is the free carrier density [179].

$$\frac{dI(t,z)}{dz} = -\alpha_{lin} I(t,z) - \beta_{tpa} I^2(t,z) - \sigma_{fca} N(t,z) I(t,z) \qquad (2.3.3)$$

The value for α_{lin} can vary from 3 to 60dB.cm^{-1} depending on the surface roughness of the device, as sidewall scattering is the main source of linear loss. Typical values for β_{tpa} in the literature range from 0.5x10^{-9} to 0.9x10^{-9}m.W^{-1} while σ_{fca} is 1.45x10^{-21}(λ/1.55x10^{-6})^2 m^2 [179, 181]. The TPA coefficient β_{tpa} is related to the imaginary part of the third-order susceptibility tensor $\chi_{Im}^{(3)}$, as shown in Eq. 2.3.4, where *c* is the speed of light, λ is the signal wavelength, n_0 is the linear refractive index and ε_0 is the permittivity of free space.

$$\beta_{tpa} = \frac{3\pi\chi_{Im}^{(3)}}{c\varepsilon_0 \lambda n_0^2} \qquad (2.3.4)$$

The free carrier density as a function of time is described by Eq. 2.3.5, where *h* is the Planck constant, *v* is the photon frequency and τ_{fc} is the free carrier lifetime [179].

$$\frac{dN(t,z)}{dt} = \frac{\beta_{tpa}}{2hv} I^2(t,z) - \frac{N(t,z)}{\tau_{fc}} \qquad (2.3.5)$$

Diffusion of the free carriers away from the area where the optical mode is confined and the free carrier lifetime is determined by carrier recombination at the interfaces between the waveguide and the substrate or cladding [179]. For Si waveguides with submicron cross-section dimensions, τ_{fc} can vary from 200ps [182, 183] to 25ns [169], although it is typically ~1ns for Si nanowires with SiO$_2$ cladding [179, 180, 184].

Fig. 2.3.2 illustrates the transmission evolution of a Si nanowire following the input of a ~100pJ pulse with a pulsewidth of ~100fs, which has been normalized relative to the steady-state transmission prior to the arrival of the pulse.
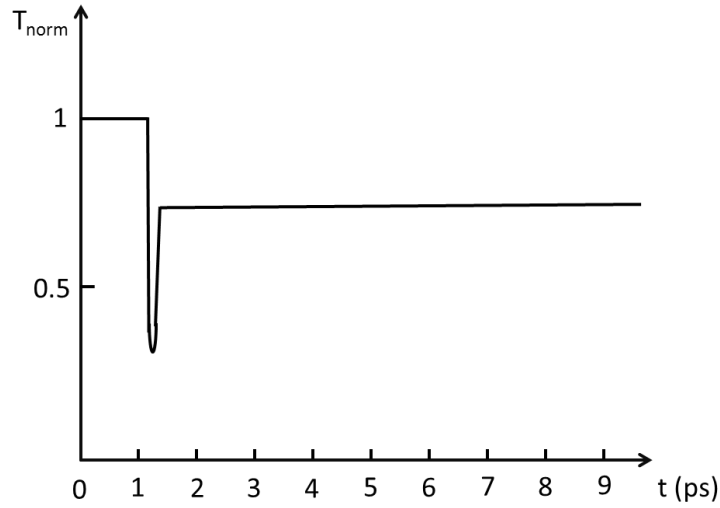
Fig. 2.3.2: Schematic diagram of transmission evolution for a Si nanowire.

As indicated by Fig. 2.3.2, the transmission instantaneously drops when the pulse arrives due to TPA. Following this ultrafast process, there is a long-lived (~1ns) FCA recovery tail.

Furthermore, optical pulses experience a change in refractive index due to the Kerr effect and the presence of free carriers, given by Eq. 2.3.6 and Eq. 2.3.7 respectively, Δn_{Kerr} is the Kerr-induced change in refractive index, Δn_{fcpe} is the change in refractive index due to the free carrier plasma effect (FCPE) and n_2 is the nonlinear refractive index [179, 185].

$$\Delta n_{Kerr}(t,z) = n_2 I(t,z) \qquad (2.3.6)$$

$$\Delta n_{fcpe}(t,z) = -[8.8 \times 10^{-22} N(t,z) + 8.5 \times 10^{-18} N^{0.8}(t,z)] \qquad (2.3.7)$$

Eq. 2.3.8 shows how n_2 is related to the real part of the third-order susceptibility tensor $\chi_{Re}^{(3)}$.

$$n_2 = \frac{3\chi_{Re}^{(3)}}{4c\varepsilon_0 n_0^2} \tag{2.3.8}$$

The changes in the refractive index due to the Kerr effect and the FCPE affect the instantaneous phase of optical pulses passing through the device and the total magnitude of this phase change $\Delta\varphi(t)$ is given by Eq. 2.3.9, where L_{int} is the length of the waveguide over which the pulse experiences the refractive index changes and λ is the signal wavelength of the incident light.

$$\Delta\varphi(t, z) = \frac{2\pi L_{int}}{\lambda}[\Delta n_{Kerr}(t, z) + \Delta n_{fcpe}(t, z)] \tag{2.3.9}$$

Fig. 2.3.3 shows the phase evolution of a Si nanowire following the input of a ~100pJ pulse with a pulsewidth of ~100fs.
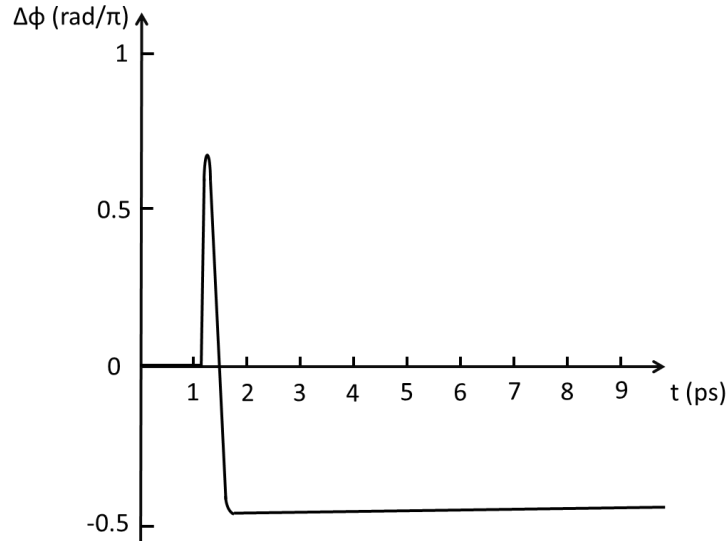
Fig. 2.3.3: Schematic diagram of phase evolution for a typical Si nanowire.

As demonstrated in Fig. 2.3.3, the phase evolution is determined by similar phenomena to those that manifest themselves in the corresponding transmission evolution. Initially, within the duration of the pulsewidth, there is a positive ultrafast response due to the Kerr effect. Following the ultrafast transient response, there is a negative and long-lived phase response from the FCPE due to the presence of free carriers in the device.

2.3.3   Enhancing the switching capability of Si waveguides

It is desirable to mitigate the phenomenon of FCA in Si waveguides due to the relatively long free carrier lifetime (~1ns), which can limit their switching capability [186]. Techniques that minimize the impact of FCA are explored in the following paragraphs.

2.3.3.1   Reduction of waveguide dimensions

For bulk silicon, the free carrier lifetime is typically several microseconds [180]. The free carrier lifetime is limited by the time taken for carriers to diffuse away from the effective mode area to the sidewalls and for surface recombination to take place. The lifetime can be reduced by minimizing the cross-section area of the Si waveguide to reduce the diffusion time and maximize the surface-area-to-volume ratio [187]. Thus, Si waveguides with cross-section dimensions <1μm (i.e. Si nanowires) have a shorter free carrier lifetime compared to rib waveguides with cross-section dimensions >1μm [169]. However, the width and height of the Si nanowires cannot be reduced below 200nm as this would lead to light leaking out from the waveguides [188].

2.3.3.2   Integration of waveguide into p-i-n diode

One extremely effective technique that reduces FCA in Si nanowires is removal of the free carriers by integrating a p-i-n diode structure across the waveguide [180, 189]. When a reverse bias is applied to the device, the free carriers generated by TPA are quickly swept out of the waveguide under the influence of the electric field. A.C. Turner-Foster *et al* achieved a reduction in the free carrier lifetime from 3ns to 12.2ps using the structure illustrated in Fig. 2.3.4, [180]. However, the inclusion of a p-i-n diode structure increases the complexity of device fabrication.
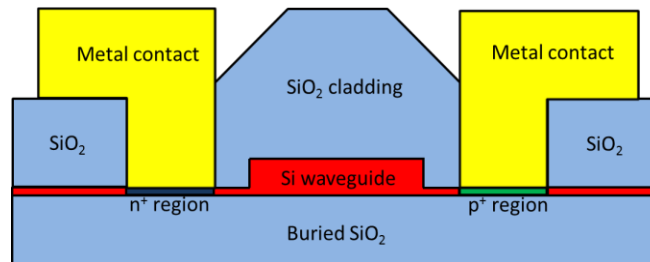
Fig. 2.3.4:Cross-section through Si nanowire with p-i-n diode integrated across waveguide [180].

2.3.3.3   Porous silicon

The NLO properties of nanoporous silicon waveguides have been studied by P. Apiratikul *et al* [190]. This material is promising for optical switching because the large internal surface area of porous silicon dramatically increases the rate of surface recombination compared to standard crystalline silicon, without affecting the size of the ultrafast Kerr effect response. By employing nanoporous silicon rather than crystalline silicon in the waveguide, a reduction in the free carrier lifetime from 1.1ns to 200ps was attained by P. Apiratikul *et al* [190].

2.3.3.4   Amorphous hydrogenated silicon

The replacement of pure crystalline silicon (c-Si) by amorphous hydrogenated silicon (a-Si:H) has been studied in recent years [191, 192]. Compared to c-Si, this type of material has a wider bandgap and a shorter carrier lifetime due to the terminated dangling bonds in a-Si:H. The fact that the bandgap energy in a-Si:H (1.7eV) is higher than for c-Si (1.1eV) means that there is reduced TPA in a-Si:H so less free carriers are generated. Y. Shoji *et al* have demonstrated a Kerr effect phase response time <100fs in an a-Si:H waveguide with only a minor amount of FCA, even at an energy per pump pulse of 10pJ [191]. Unfortunately, a serious disadvantage is the instability and degradation of a-Si:H following long-term exposure to high intensity light [192] due to the Staebler-Wronski effect.

2.3.3.5   Ion implantation

It has been shown that ion implantation by certain chemical elements (e.g. helium or oxygen ions) can significantly reduce the free carrier lifetime by creating ion-induced defect states to act as recombination centres within the waveguide rather than relying on surface recombination alone [193]. M. Waldow *et al* reported a free carrier lifetime of 15ps in a silicon microresonator that had been implanted by oxygen ions [194]. However, this remarkably short lifetime comes at the expense of a substantial increase in the propagation loss (up to 70dB.cm^{-1}).

2.3.3.6 *Silicon organic hybrid (SOH) technology*

One means of avoiding the problem of free carrier generation is using silicon organic hybrid (SOH) technology [176]. This technology takes advantage of the strong optical confinement in silicon while a polymer cladding provides the nonlinear functionality. Suitable nonlinear polymers for the cladding material include polypyrrole, polythiophene (PT) and polydiacetyline (PDA) molecules [195]. These compounds have large delocalized electron systems with exceptionally high $\chi^{(3)}$ coefficients and low TPA coefficients as they have bandgap energies (1.8eV) greater than twice the energy of photons at communications wavelengths (0.8eV). Exploitation of the nonlinear properties of these polymer materials can be accomplished by simply coating a strip Si waveguide with the polymer but a more efficient method is to employ a slot Si waveguide configuration (see Fig. 2.3.5).
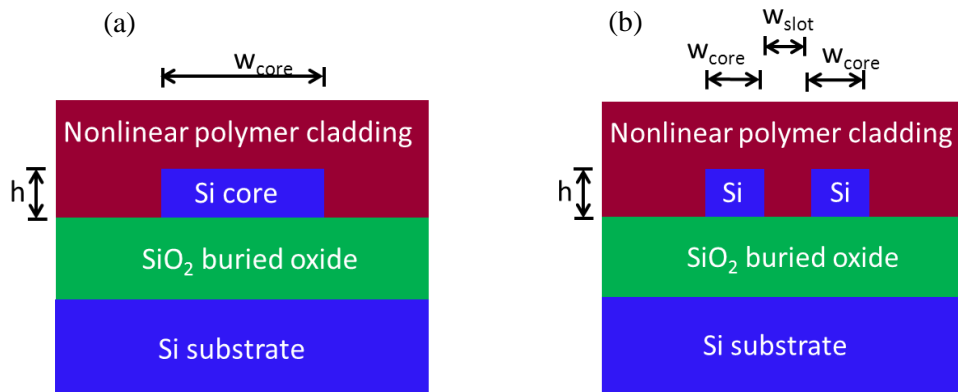
Fig. 2.3.5: Cross-section through (a) strip waveguide and (b) slot waveguide.

As shown in Fig. 2.3.5(a), the strip waveguide is similar to a standard Si nanowire, with the exception that the cladding layer is a nonlinear polymer which makes a small contribution to the total nonlinearity of the device. However, for the slot waveguide illustrated in Fig. 2.3.5(b), the electric field of the optical signal is almost completely confined to the slot, i.e. the space between the two silicon "rails". There is negligible TPA and therefore almost no generation of free carriers within the silicon rails. As a consequence, the switching capability of the device is not hindered by the recombination time of free carriers in silicon. C. Koos *et al* have demonstrated demultiplexing from 170.8Gb.s^{-1} to 42.7Gb.s^{-1} using slot waveguides [196] and J. Leuthold *et al* have fabricated an SOH electro-optic modulator with a bandwidth of 100Gb.s^{-1} [176].

2.4   *Highly nonlinear fibre (HNLF)*

One promising means of realizing optical signal processors is to exploit the third order nonlinearity in optical fibres [197, 198]. Fibre nonlinearities have an almost instantaneous ultrafast response, leading to an ultra-broad wavelength conversion band and high speed operation [197]. However, to create practical devices, it is necessary to enhance the nonlinearity of the fibre and to manage dispersion in the fibre. The nonlinearity in optical fibre manufactured using silica can be increased by doping the fibre with germanium dioxide (GeO_2) to create HNLF, which leads to a nonlinear coefficient $\gamma=20.4W^{-1}km^{-1}$ for this type of fibre [199]. Alternatively, HNLF made from lead-based ($PbSiO_3$), chalcogenide-based (e.g. Ag_2Se_3) or bismuth-oxide-based (Bi_2O_3) glass can be employed, all of which have much higher nonlinear coefficients compared to silica-based fibre. For example, lead silicate fibre has a nonlinear coefficient up to $\gamma=640W^{-1}km^{-1}$ [200], bismuth oxide fibre has $\gamma=1360W^{-1}km^{-1}$ [201] and chalcogenide fibre has $\gamma=1200W^{-1}km^{-1}$ (although this can be increased to $\gamma=2270W^{-1}km^{-1}$ if the fibre is tapered) [202].

Although there has been a great deal of progress in the field of optical signal processing using HNLF, there are several fundamental problems with using HNLF in real systems including the large device footprint and the need for optical amplification (i.e. gain blocks) after the fibres (to ensure cascadability of devices) [80]. Furthermore, the long length of HNLF (which can range from 1m [203] to 1km [197]) means that it cannot be integrated with other photonic components on a single semiconductor chip, unlike SOAs, EAMs and Si nanowires.

2.5 *Periodically poled lithium niobate (PPLN)*

Periodically poled lithium niobate (PPLN) is an engineered, quasi phase matched material that can be used to realize signal processing functions such as wavelength conversion, second harmonic generation and demultiplexing [204, 205]. PPLN consists of a length of $LiNbO_3$ where the orientation of the crystal is periodically inverted or "poled" (see Fig. 2.5.1). $LiNbO_3$ is a ferroelectric material i.e. each unit cell has a net electric dipole moment. An intense electric field applied to the crystal can invert the structure of a unit cell and thereby invert the direction of the electric dipole moment. In PPLN, the inverted portions of the crystal generate photons that are π radians out of phase with the generated photon that would have been created at that point in the crystal if it was not poled. By selecting the right periodicity for flipping the orientation of the crystal, newly generated photons will interfere constructively with previously generated photons. Thus, the number of generated photons grows as light travels through PPLN, resulting in high conversion efficiency (i.e. the ratio of generated photons to input photons).
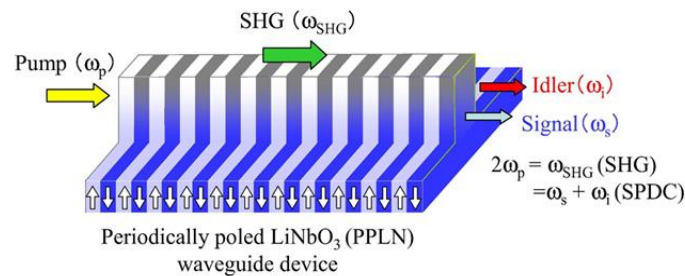
Fig. 2.5.1: PPLN device in ridge waveguide structure used in second harmonic generation (SHG).

A typical PPLN waveguide has cross-section area $\sim 50 \times 10^{-12} m^2$ and length $\sim$5cm [206]. PPLN waveguides are potential candidates as all-optical switching elements due to their ultrafast response, high conversion efficiency and compactness [206]. However, a PPLN waveguide attenuates an input signal so it is necessary to place gain blocks after the devices to ensure cascadability. Also, it is difficult to monolithically integrate PPLN with other photonic components on a III-V semiconductor or silicon platform, although hybrid integration using silica-based planar lightwave circuits (PLCs) is possible [207].

2.6   *Chalcogenide waveguides*

The Kerr effect in chalcogenide waveguides containing materials such as As_2S_3 and As_2Se_3 can be utilized for optical signal processing functions such as regeneration, wavelength conversion and demultiplexing at data rates up to 640Gb.s^{-1} via XPM or FWM [208, 209]. Chalcogenide waveguides are typically fashioned into either planar rib waveguides or photonic crystal fibres that have cross-section area ~$1x10^{-12}m^2$ and length ranging from 5cm [209] to 1m [210].
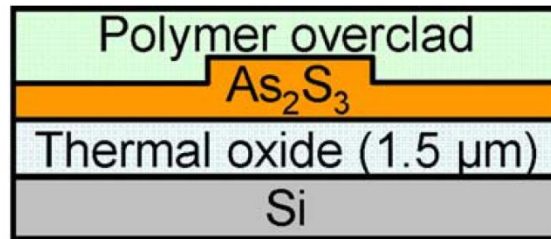
Fig. 2.6.1: Chalcogenide waveguide structure consisting of As$_2$S$_3$ deposited on silica (SiO$_2$)

Chalcogenide devices have several advantages such as their low power consumption, their strong optical confinement and their near-instantaneous Kerr effect response time that is not associated with significant generation of free carriers. However, they are difficult to integrate with photonic components made from different materials, they require high optical input powers and they suffer from problems related to mechanical stability and photosensitivity [211].

2.7   Optical signal processing functionalities

A brief description of several kinds of optical signal processing functionalities which are expected to play a role in next-generation WDM, OTDM and hybrid OTDM/WDM optical networks is provided in this section.

2.7.1   Wavelength conversion

Wavelength conversion is a process whereby a data signal imprinted on an optical carrier at wavelength λ_1 is translated to another optical carrier at wavelength λ_2 at the line rate of the data signal. By allowing wavelength channels to be assigned on a link-to-link basis, a connection can be made from one point to another point in the network with limited blocking probability as long as any wavelength channel is available on intermediate links [212]. Without wavelength conversion technology, there is a "wavelength continuity" restraint, which means that the same wavelength channel must be used from source to destination and this limits the efficiency and flexibility of the network [213]. Wavelength conversion adds flexibility and efficiency to future dynamically allocated WDM optical networks by simplifying network management and reducing latency [214-216]. The diagram of wavelength conversion in Fig. 2.7.1 serves to illustrate the main concept behind this functionality.
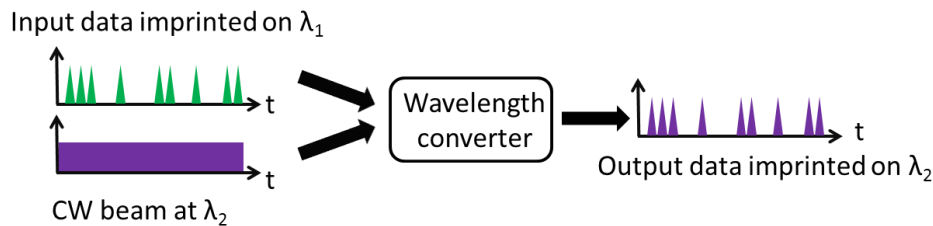
Fig. 2.7.1: Schematic diagram showing the principle of wavelength conversion.

Desirable features of a wavelength converter would be a broad tuning wavelength range for routing and switching [217], bit rate transparency [218, 219], and modulation format transparency [219, 220]. A summary of wavelength conversion experiments using various NLO devices reported in the literature to date is given in Table 2.6.1.

Date	Device configuration	SM	Format	Bit rate	Ref.
2011	Si nanowire (SU8 cladding)	FWM	RZ-OOK	640Gb.s^{-1}	[221]
2011	Si nanowire (SU8 cladding)	FWM	RZ-DPSK	320Gb.s^{-1}	[220]
2009	PPLN	SHG/DFG	RZ-QPSK	320Gb.s^{-1}	[222]
2009	Chalcogenide WG (As$_2$S$_3$)	FWM	RZ-OOK	160Gb.s^{-1}	[223]
2008	HNLF	XPM	RZ-OOK	640Gb.s^{-1}	[224]
2006	SOA + narrow BPF	XGM/XPM	RZ-OOK	320Gb.s^{-1}	[225]
2006	Turbo-Switch	XGM	RZ-OOK	170Gb.s^{-1}	[41]
2005	EAM + AMZI	XAM	RZ-OOK	100Gb.s^{-1}	[226]
2000	SOA + AMZI	XGM	RZ-OOK	100Gb.s^{-1}	[146]

Table 2.7.1: Experimental demonstrations of wavelength conversion using NLO devices (SM=switching mechanism, DPSK=differential phase shift keying, QPSK=quadrature phase shift keying, WG=waveguide).

It can be seen from Table 2.7.1 that wavelength conversion has been demonstrated in many types of NLO devices at high data rates ($\geq$100Gb.s^{-1}) and in a variety of modulation formats. Thus, wavelength conversion based on NLO components has excellent potential for implementation in next-generation optical networks.

2.7.2   Demultiplexing

Demultiplexing is an operation whereby data transmitted on multiple wavelength or time slot channels at the line rate on a long haul fibre optic link is separated out into individual channels at the base rate. In the case of a WDM network, demultiplexing can be implemented using an array of BPFs or an AWG. However, in the case of an OTDM network, demultiplexing generally requires a clock signal at the base data rate to successfully extract the individual time slot channels. A simplified diagram of an OTDM demultiplexer is illustrated in Fig. 2.7.2 and state-of-the-art developments in OTDM demultiplexing are listed in Table 2.7.2.
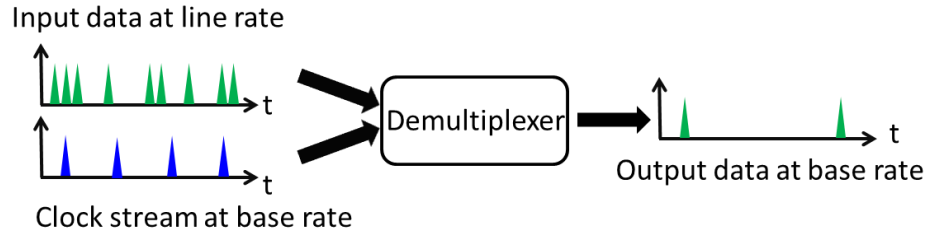
Fig. 2.7.2: OTDM demultiplexing schematic diagram.

Date	Device configuration	SM	Format	Bit rate	Ref.
2010	Si nanowire (SU8 cladding)	FWM	DPSK	1.28Tb.s^{-1}	[227]
2010	Si nanowire (SU8 cladding)	FWM	RZ-OOK	1.28Tb.s^{-1}	[228]
2010	PPLN	SFG	RZ-OOK	320Gb.s^{-1}	[229]
2009	Chalcogenide WG (As$_2$S$_3$)	FWM	RZ-OOK	640Gb.s^{-1}	[230]
2009	HNLF	XPM	RZ-OOK	1.28Tb.s^{-1}	[39]
2007	SOA + narrow BPF	XGM/XPM	RZ-OOK	640Gb.s^{-1}	[231]
2002	EAM	XAM	RZ-OOK	80Gb.s^{-1}	[232]
2000	SOAs in SMZI	XPM	RZ-OOK	168Gb.s^{-1}	[144]

Table 2.7.2: Experimental demonstrations of demultiplexing using NLO devices.

2.7.3   Format conversion

Format conversion involves translating a data signal from one modulation format to a different modulation format. This could become extremely important in future WDM, OTDM and hybrid OTDM/WDM optical networks, as advanced modulation formats are frequently employed in core networks and they must be converted to simpler modulation formats in metro and access networks, and vice versa. Furthermore, RZ is the preferred format for OTDM due to its tolerance of fibre nonlinearities, whereas NRZ is the preferred modulation format for WDM owing to its high spectral efficiency and timing jitter tolerance [233], so techniques to convert RZ signals to NRZ signals and vice versa will be critically important in hybrid OTDM/WDM networks. A simplified diagram of the process of conversion from the NRZ-OOK format to the RZ-OOK format is provided in Fig. 2.7.3.
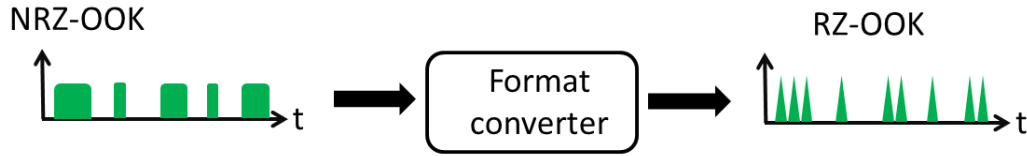
Fig. 2.7.3: Diagram illustrating the principle of NRZ-OOK to RZ-OOK format conversion.

A great deal of progress has been reported in the literature on format conversion between NRZ-OOK to RZ-OOK and between advanced modulation formats and simpler modulation formats. For instance, I. Kang *et al* successfully demonstrated format conversion from RZ-OOK to RZ-QPSK using SOAs embedded in an SMZI at a bit rate of 173Gb.s^{-1} in 2009 [234]. G.W. Lu *et al* managed to achieve format conversion from RZ-QPSK to RZ-DPSK using HNLF at a bit rate of 320Gb.s^{-1} in 2009 [235]. H.C.H. Mulvad *et al* converted a DPSK OTDM serial data signal at a line rate of 640Gb.s^{-1} to a DWDM parallel data signal on a 25GHz grid using a Si nanowire [236]. A representative sample of developments in the field of format conversion is provided in Table 2.7.3. A single-headed arrow implies that only one-way format conversion has been demonstrated, whereas a double-headed arrow signifies that two-way format conversion has been demonstrated.

Date	Device configuration	SM	FC	Bit rate	Ref.
2011	Si nanowire	FWM	OTDM-DPSK → DWDM	640Gb.s^{-1}	[236]
2011	SOA + DI	FWM	RZ-OOK ↔ NRZ-OOK	40Gb.s^{-1}	[237]
2010	SOA in SMZI	XPM	RZ-OOK → RZ-AMI	40Gb.s^{-1}	[238]
2009	HNLF	FWM	RZ-QPSK → RZ-DPSK	320Gb.s^{-1}	[235]
2009	SOAs in SMZI	XPM	RZ-OOK → RZ-QPSK	173Gb.s^{-1}	[234]
2007	SOA + narrow BPF	XGM/XPM	NRZ-OOK → RZ-OOK	40Gb.s^{-1}	[233]
2007	Turbo-Switch	XGM	NRZ-OOK → RZ-OOK	40Gb.s^{-1}	[239]

Table 2.7.3: Experimental demonstrations of format conversion using NLO devices (FC=format conversion, AMI=alternate mark inversion)

2.7.4   Signal monitoring

To monitor the quality of an OTDM data signal at the full line rate, an image of the signal can be obtained by employing an optical sampling technique to extract samples from the data stream. This is achieved by sending the OTDM data signal along with a sampling pulse train at a repetition rate of several hundred MHz (i.e. the sampling frequency) into an NLO device. The sampling pulses temporally scan through the data signal and this allows a picture of the data signal to be built up by detecting the output from the gate using a low-bandwidth photodetector and low-speed electronics [240]. A simple sampling gate is shown in Fig. 2.7.4 and a selection of waveform sampling experiments reported in the literature is provided in Table 2.7.4.
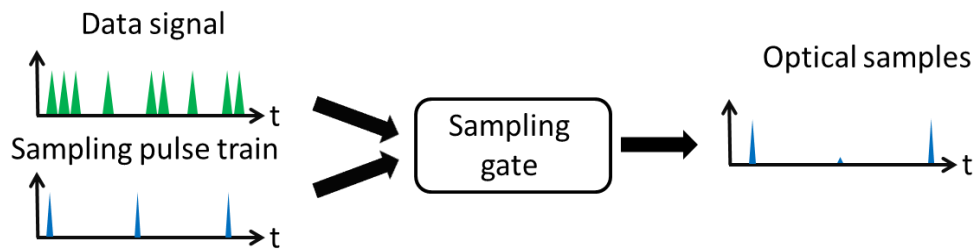
Fig. 2.7.4: Diagram illustrating an all-optical sampling system.

Date	Device configuration	SM	Format	Bit rate	Ref.
2010	Si nanowire	FWM	RZ-OOK	$1.28Tb.s^{-1}$	[241]
2010	Chalcogenide WG (As_2S_3)	FWM	RZ-OOK	$640Gb.s^{-1}$	[242]
2009	HNLF	FWM	RZ-OOK	$320Gb.s^{-1}$	[243]
2008	EAM	XAM	RZ-OOK	$40Gb.s^{-1}$	[244]
2004	PPLN	SFG	RZ-OOK	$640Gb.s^{-1}$	[245]
2001	SOA in SMZI	XPM	RZ-OOK	$320Gb.s^{-1}$	[246]

Table 2.7.4: Experimental demonstrations of optical sampling using NLO devices.

2.6.5   Packet header processing

Optical packet switching is a technique that is likely to play a key role in next-generation optical communications networks [216, 247, 248]. There are two main ways in which packet switched networks can be implemented, namely the hybrid electrooptical method and the all-optical

method. In the hybrid electrooptical approach, the optical packet header is processed in the electronic domain while the packet payload stays in the optical domain [247], whereas in the all-optical approach, both the packet header processing and the packet payload remain in the optical domain at all times. Packet header processing is illustrated in Fig. 2.7.5, where the 1x2 packet header processor decides whether the input data signal should be routed to Port 1 or Port 2.
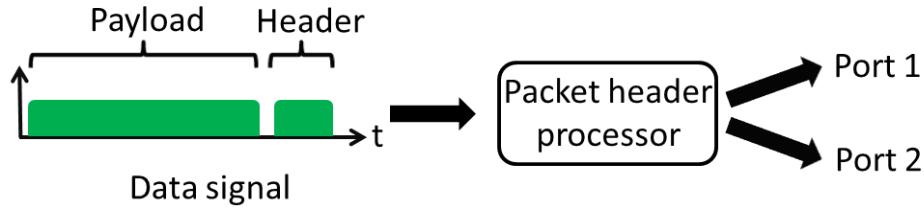
Fig. 2.7.5: Diagram illustrating packet header processing.

Reported experiments on all-optical packet header processors are shown in Table 2.6.5.

Date	Device configuration	SM	Format	Bit rate	Ref.
2008	SOAs in MZI	XGM/XPM	RZ-OOK	160Gb.s^{-1}	[249]
2007	SOA	FWM/XPolM	RZ-OOK	10Gb.s^{-1}	[250]
2006	SOAs in UNI	XGM/XPM	RZ-OOK	40Gb.s^{-1}	[251]
2004	SOA in TOAD loop	XGM/XPM	RZ-OOK	10Gb.s^{-1}	[74]

Table 2.7.5: Experimental demonstrations of packet header processing using NLO devices (XPolM=cross-polarization modulation).

As shown in Table 2.7.5, until 2008, the data rate at which all-optical packet header processing has been demonstrated experimentally was limited to ≤40Gb.s^{-1}, which suggested that it might prove difficult to apply this technique in real systems. However, since 2008, demonstrations of all-optical packet switching at bit rates of 160Gb.s^{-1} using SOAs in interferometric arrangements have been reported [252, 253]. However, R. Tucker *et al* suggest that it may prove difficult for all-optical packet header processing to achieve savings in energy consumption over electronic or hybrid electrooptical packet header processing, as it is a relatively complex operation [79].

2.7.6   2R and 3R regeneration

As an optical signal travels through an optical fibre, it experiences attenuation and dispersion effects. In OTDM or hybrid OTDM/WDM networks, these effects lead to a reduction in the energy per pulse, timing jitter and pulse broadening of the pulses. For long haul links in these networks, mitigation of these deleterious effects would be necessary to obtain a sufficiently high OSNR at the receiver. This can be achieved by employing 2R or 3R regenerators. A 3R regenerator provides re-amplification, re-shaping and re-timing of pulses to counteract against attenuation, pulse distortion and timing jitter respectively. For a 2R regenerator, the re-timing functionality is absent. In general, a 3R regenerator requires clock recovery so it tends to be more complex than a 2R regenerator. A summary of the state-of-the-art in 2R and 3R regeneration reported in the literature is given in Table 2.7.6.

Date	Device configuration	Format	Regenerator type	Bit rate	Ref.
2012	PPLN	RZ-OOK	2R	640Gb.s^{-1}	[254]
2007	SOA-EAM	NRZ-OOK	2R	10Gb.s^{-1}	[255]
2007	Si nanowire	RZ-OOK	2R	10Gb.s^{-1}	[256]
2004	HNLF	RZ-OOK	2R	320Gb.s^{-1}	[257]
2003	EAM	RZ-OOK	3R	80Gb.s^{-1}	[166]
2001	SOAs in SMZI	RZ-OOK	3R	84Gb.s^{-1}	[258]

Table 2.7.6: Experimental demonstrations of 2R and 3R regeneration using NLO devices.

2R and 3R regeneration has been demonstrated in a range of NLO devices up to data rates of 640Gb.s^{-1}. The modest bit rate at which regeneration has been performed in devices such as Si nanowires and EAMs indicates that this functionality may not be suitable for next-generation optical networks without a substantial increase in the speed of regeneration in these NLO elements. Moreover, the emergence of forward error correction (FEC) techniques employed at the receivers in core networks means that 2R and 3R regeneration of data signals may be redundant in future optical networks [259].

2.6.7 Logic gates

To realize complex signal processing operations in the optical domain, logic gates are required to implement Boolean algebraic functions such as AND, OR, NOT and XOR operations [141]. A representative sample of logic gates implemented using NLO devices reported in the literature appear in Table. 2.7.7.

Date	Device configuration	SM	Format	Gate type	Bit rate	Ref.
2011	Si nanowire	FWM	RZ-DPSK	XOR	$40Gb.s^{-1}$	[260]
2009	HNLF	FWM	RZ-DPSK	XOR	$40Gb.s^{-1}$	[261]
2008	PPLN	FWM	RZ-DPSK	XOR	$40Gb.s^{-1}$,	[262]
2006	Turbo-Switch	XGM	RZ-OOK	XOR	$85Gb.s^{-1}$	[263]
2006	SOA	XGM/ FWM	RZ-OOK	XNOR, AND, NOR, NOT	$10Gb.s^{-1}$	[264]
2005	SOAs in SMZI	XGM/ XPM	RZ-OOK	AND, OR, XOR	$10Gb.s^{-1}$	[265]
2004	SOA	FWM	RZ-DPSK	XOR	$20Gb.s^{-1}$	[266]

Table 2.7.7: Selection of experimental demonstrations of logic gates using NLO devices.

It is apparent from Table 2.7.7 that practically any kind of logic gate can be implemented in the optical domain using NLO devices, at least in principle. However, the switching capability of many types of logic gates such as NOT and NOR gates has been limited to $\leq 40Gb.s^{-1}$, which indicates that it may not be feasible to implement these kinds of logic gates in real systems.

2.8   *Summary*

The main aim of this chapter was to introduce the basic properties of NLO devices and to review the state-of-the-art in optical signal processing. The structure and possible switching mechanisms of several types of NLO devices such as SOAs, EAMs, Si nanowires, PPLN, HNLF and chalcogenide waveguides were outlined. A literature review of optical signal processing functionalities in systems-level experiments including wavelength conversion, format conversion and demultiplexing realized using NLO components was presented. Although many of these functionalities have been demonstrated at high bit rates ($\geq 100 \text{Gb.s}^{-1}$), further work on improving the response time of these components is necessary to enable further increases in their switching capability. In the remaining chapters of this thesis, experimental data and computational modelling related to the temporal response of switching configurations that incorporate SOAs, Si nanowires and/or EAMs will be presented. The advantages and disadvantages of each individual switching configuration will be analysed and their potential applications will be discussed.

Long, highly nonlinear and strongly wavelength-dependent SOA

This chapter presents the gain and phase dynamics of a long, highly nonlinear SOA which displayed strong wavelength dependence. When a high current bias (≥400mA) was applied to the SOA, the full gain recovery time was as low as 9ps and the corresponding phase response had a prominent ultrafast component at particular pump and probe wavelengths, although the full phase recovery time remained relatively long (~60ps). A multi-section time domain model of the carrier dynamics in the SOA verified that the long length and high power gain of the SOA were critical factors governing the behaviour of the device. A summary of the experimental and computational data is given and potential applications of this type of SOA are discussed. Parts of the research detailed in this chapter are based on the following publications:

[1] "Fast gain recovery rates with strong wavelength dependence in a non-linear SOA," <u>Ciaran S. Cleary</u>, Mark J. Power, Simon Schneider, Roderick P. Webb, Robert J. Manning, *Optics Express*, vol. 18, pp. 25726-25737 (2010)

[2] "Wavelength dependent fast gain recovery in a non-linear SOA," <u>Ciaran S. Cleary</u>, Mark J. Power, Simon Schneider, Roderick P. Webb, Robert J. Manning, *Proc. Photonics Ireland (Dublin, Ireland)*, paper A68 (2011)

3.1   *Background*

It has been firmly established in the literature that the carrier recovery time of an SOA is strongly dependent on optical input power, signal polarization, current bias and active region dimensions [96, 153, 267-271]. However, the relationship between the recovery time for SOAs and the optical signal wavelength is less clear-cut [272]. A study by R. Giller *et al* involving two-colour pulsed pump and probe signals did not detect any dependence of the SOA recovery time on the probe wavelength [153] whereas investigations by T. Takeyama *et al* and W. Mathlouthi *et al* involving single-colour pulsed pump and probe signals found that there was

significant variation in the SOA recovery time as a function of wavelength [272, 273]. Furthermore, it has been reported that that for XGM between a pump and CW probe signal in a long SOA (>1mm active region length), the gain and phase responses of the SOA have a definite dependence on the wavelength of input optical signals [272, 274]. In particular, when the probe is a saturating CW beam (which partially acts as a holding beam), it has been confirmed from both experiments and computational modelling that the gain recovery time reaches a minimum when the CW probe wavelength is located close to the peak in the small signal gain spectrum [268, 275]. However, for the experiments reported by X. Li *et al*, even when the CW probe wavelength was optimized, the 10/90 gain recovery time (the time taken for the gain to change from 10% to 90% of full recovery) remained long (>250ps) owing to the low operating drive currents (≤120mA) and the relatively high pulsewidth of the input pump pulses (65ps) [275].

Further striking evidence for the dependence of the response time of an SOA on the wavelength of input optical signals was observed by a Yi An, a PhD student based in Tyndall National Institute in 2008. It was found that when a saturating CW beam was input to a highly nonlinear MQW SOA manufactured by CIP Photonics with length of approximately 2mm and a gain peak of 1560nm, the gain recovery time was faster when the pump was blue-shifted relative to the CW beam compared to when the pump was red-shifted relative to the CW beam. At a fixed CW beam wavelength of 1554.5nm and a modulation depth of 30%, the full gain recovery time was 25ps when the pump wavelength was 1539.9nm, whereas the full gain recovery time was 60ps when the pump wavelength was 1564.0nm (see Fig. 3.1.1).
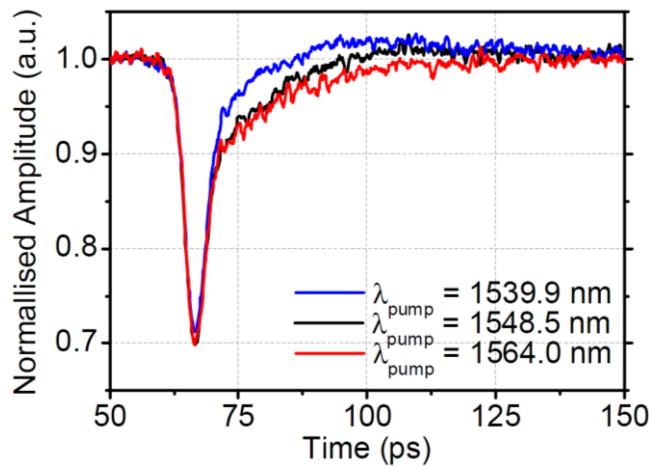
Fig. 3.1.1: Gain dynamics in highly nonlinear SOA at a current bias of 500mA, with a CW beam wavelength of 1554.5nm and the pump wavelength varied from 1539.9nm to 1564.0nm [276].

Simon Schneider, an undergraduate student from Karlsruhe Institute of Technology, pursued this research work further during the course an MSc internship project in Tyndall National Institute in 2010 [277]. One aspect of this project involved measuring the gain and phase dynamics of a highly nonlinear MQW SOA embedded in a packaged SMZI manufactured by CIP Photonics (serial no. 3415) that was designed to act as a 2R regenerator. Both SOAs in the SMZI had a small signal gain peak of 1560nm and the total length of each waveguide was estimated to be 3.5mm based on the ripple spacing in the gain spectra (although the active region effective length in each SOA was closer to 2mm).

Dynamic characterization of SOA1 in SMZI 3415 was carried out using a time-resolved pump-probe spectroscopy test-bed incorporating an optical sampling oscilloscope (OSO) with ~1ps resolution, as shown in Fig. 3.1.2. Regarding the depiction of SMZI 3415 in this figure, the dotted line around the whole system signifies that the components were set inside a single package fabricated using hybrid integration techniques.
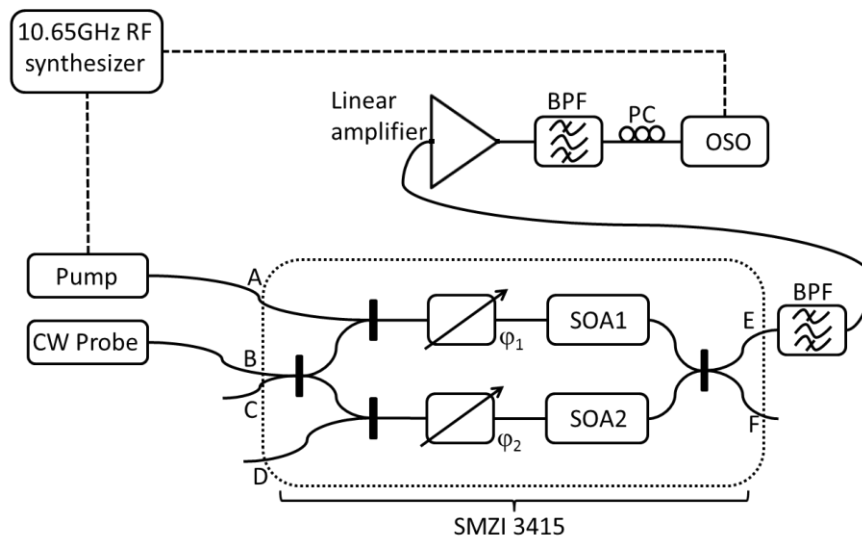
Fig. 3.1.2: Experimental test-bed for measuring the gain and phase response of SOA1 inside SMZI 3415. Solid lines represent optical links and dashed lines represent electrical links, and the linear amplifier was an SOA operated in the linear regime. (PC=polarization controller, φ_1=phase shifting element in upper arm, φ_2=phase shifting element in lower arm).

The 1545nm pump was a 2.5ps pulse clock stream generated by an actively mode-locked tunable laser at a repetition rate of 10.65GHz. The average pump power was 3.4dBm before entering SMZI 3415. The CW probe wavelength was varied from 1550nm to 1600nm in steps of 10nm. The average CW probe powers were 6.70dBm, 6.47dBm and 4.00dBm for the 1550nm, 1570nm

and 1600nm probe beams respectively. A current bias of 500mA was applied to SOA1. Although it was intended that only the gain and phase dynamics of SOA1 would be measured, it was necessary to apply a low current bias to SOA2 (<160mA) and to apply a voltage bias to the phase shifters in each arm of the interferometer to achieve a good extinction ratio (approximately 25dB) for the output signal from the interferometer.

The gain and phase dynamics of SOA1 measured using pump-probe spectroscopy are displayed in Fig. 3.1.3 and it is apparent from this figure that the shape of both the gain evolution and the phase evolution of SOA1 were profoundly affected by the choice of CW probe wavelength. Moreover, unlike previously reported experiments on the wavelength dependence of the temporal response of SOAs, the rate of recovery for SOA1 in SMZI 3415 was extraordinarily fast at one particular probe wavelength.
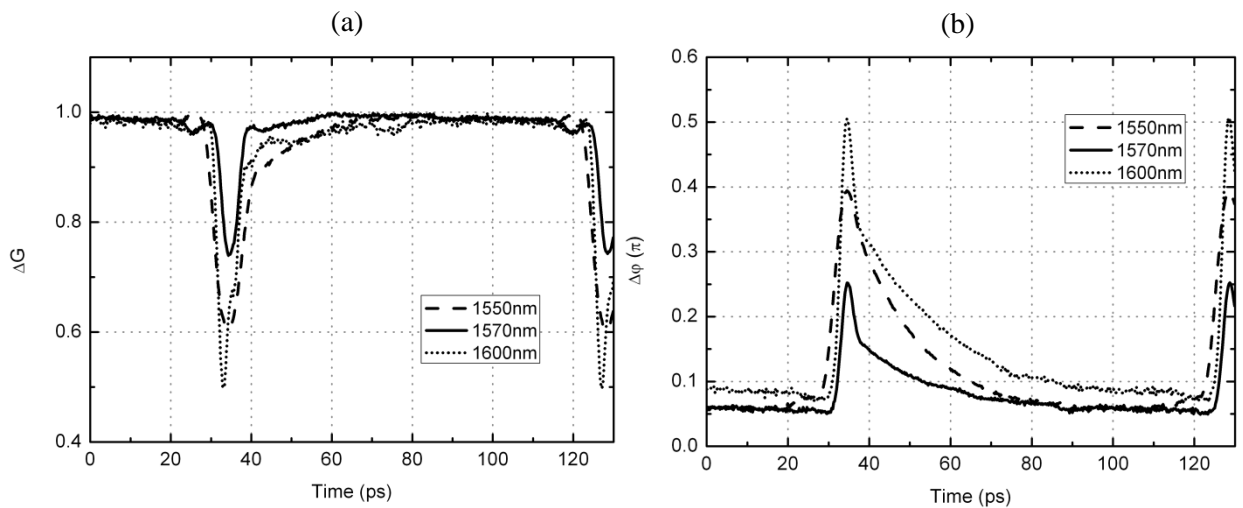
Fig. 3.1.3: (a) Normalized gain and (b) phase response for a single SOA placed inside a push-pull Mach-Zehnder interferometer [277].

In Fig. 3.1.3(a), the full gain recovery time was 75ps for the 1550nm CW probe, 23ps for the 1570nm CW probe and 45ps for the 1600nm CW probe. When the CW probe was set to 1570nm, the gain response was dominated by an ultrafast component, there was almost no trace of a slow band-filling component, and the 10/90 gain recovery time was 3ps.

However, in Fig. 3.1.3(b), there was a slow recovery tail in the corresponding phase response for the 1570nm CW probe, although the 1/e recovery lifetime of the phase response for the 1570nm CW probe (i.e. 8ps) was less than the 1/e recovery time of the phase response for the

1550nm CW probe (i.e. 15ps). Also, the ultrafast contribution to the total phase response was more pronounced for the 1570nm CW probe compared to the 1550nm CW probe.

Based on the encouraging data obtained from this preliminary research into the carrier dynamics of highly nonlinear SOAs carried out by Yi An and Simon Schneider, a more comprehensive investigation of the wavelength dependence of XGM in long, highly nonlinear MQW SOAs was undertaken by the author in collaboration with Mark Power from Tyndall National Institute. The behaviour of single SOAs was investigated rather than SOAs embedded in an interferometer so as to reduce coupling losses and to exclude the possibility of any additional wavelength dependence associated with the interferometric configuration. The primary goal of this study was to characterize this kind of SOA under a wide range of different pump and probe wavelength conditions with a view to assessing the practicability of employing the SOA in all-optical switching applications under optimum device operation conditions.

3.2 Experimental details

Two long, highly nonlinear, buried heterostructure SOAs manufactured by CIP Photonics were chosen for the investigation into the correlation between the carrier recovery time and input signal wavelength. The material composition of these SOAs consisted of GaInAsP in the active region and InP in the p-type and n-type regions. Both SOAs were highly nonlinear owing to their high confinement factors (0.18) and the long length of their active regions (2.2mm). The principal difference between these SOAs was that the gain spectra were shifted relative to one another. The first SOA (serial no. 03429) had a gain peak at a longer wavelength than the second SOA (serial no. 03735). The devices were selected to determine whether or not the separation between the input optical signals and the small signal gain peak had a decisive impact on the carrier dynamics in SOAs.

Static characterization of the SOAs was performed to ascertain the coupling losses, gain spectra and gain saturation curves. This information was important for understanding the dynamical behaviour of both SOAs. To measure the coupling loss of input and output ports of each SOA, CW laser light was launched into the unbiased SOA and the resultant photocurrent was measured as a function of input optical power. Based on the assumption that all of the input light was absorbed in the active region, it was possible to determine the coupling loss of each port using the slope of this graph. For SOA 03429, the coupling losses were 1.4dB for the input facet and 0.8 dB for output facet. For SOA 03735, the coupling losses were 1.4dB for the input facet and 1.9dB for the output facet.

The small signal gain spectra for both SOAs were measured to pinpoint the exact position of the gain peak. The gain spectra were obtained by injecting a low power signal (-35dBm average power) from a CW tunable laser into the device and measuring the output power as a function of wavelength (see Fig. 3.2.1). SOA 03429 had a gain peak at 1565nm and a 3dB gain bandwidth of 38nm, whereas SOA 03735 had a gain peak at 1505nm and a 3dB gain bandwidth of 32nm. The undulations in the curves near the gain peak can be attributed to gain ripple, a phenomenon caused by interference between adjacent longitudinal modes.
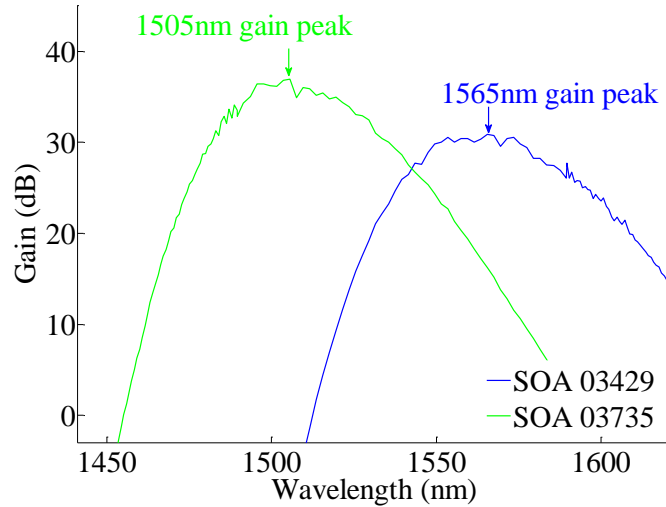
Fig. 3.2.1: Small signal chip gain spectra for SOA 03429 (blue) and SOA 03735 (green) at a current bias of 500mA.

Following acquisition of the small signal gain spectra, the gain saturation curves for the SOAs were obtained by launching CW laser light into the device at a fixed wavelength and measuring the output power as a function of input power. The power gain can be calculated from the ratio of output power to input power. The wavelength of the CW light input to SOA 03429 was 1565nm and the wavelength of the light input to SOA 03735 was 1510nm. The 3dB saturated output powers for SOA 03429 and SOA 03735 at a current bias of 500mA respectively were determined as 15dBm and 16dBm respectively (see Fig. 3.2.2).
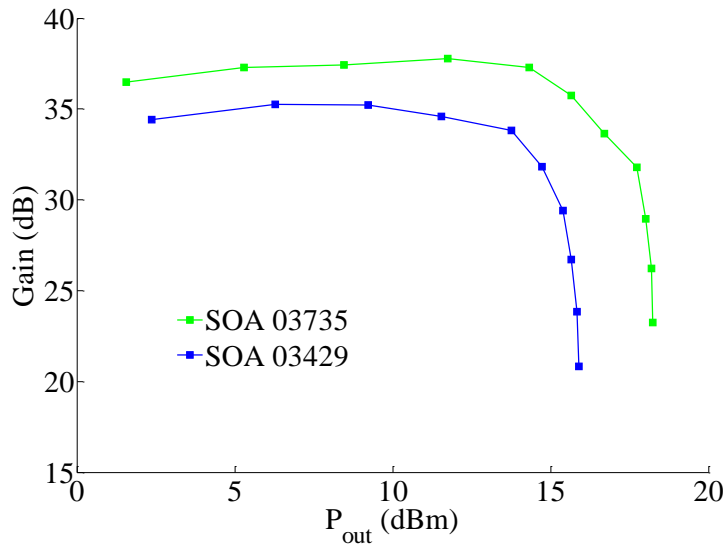
Fig. 3.2.2: Chip gain saturation curves for SOA 03429 at a wavelength of 1565nm and SOA 03735 at a wavelength of 1510nm, at a current bias of 500mA in both cases.

Thus, the static characteristics of SOA 03429 were highly similar to those of SOA 03735, with the exception that the gain spectra of the two devices were shifted with respect to one another.

Subsequent to the static device measurements, dynamic characterization of the two SOAs was initiated using pump-probe spectroscopy. The pump was a 2.5ps pulse clock stream from an actively mode-locked tunable laser, whose repetition rate was reduced from 10.65GHz to 665MHz using a LiNbO$_3$ optical modulator. This pump pulse stream was combined with a CW probe beam at a 50:50 coupler before both signals were launched into the SOA under test. The signal from the SOA under test was sent through a BPF to remove the pump signal and ASE noise. The resultant signal at the probe wavelength was amplified using an EDFA and the filtered output from the EDFA passed into a 10:90 coupler, where 90% of the signal entered into an OSO and 10% of the signal entered into an optical spectrum analyser (OSA). The experimental test-bed for these measurements on the gain and phase dynamics of the SOAs is illustrated in Fig. 3.2.3. The AMZI with a fixed time delay of 94ps (corresponding to a 1 bit delay at a repetition rate of 10.65GHz) shown in this diagram was not present in the setup during gain evolution measurements but it was present in the system when the phase evolution was measured.
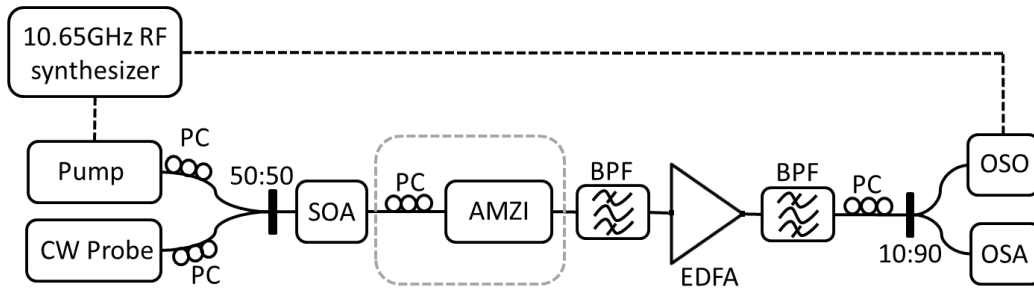
Fig. 3.2.3: Schematic of the test-bed for measuring the gain and phase dynamics of an SOA. The dashed line surrounding the AMZI signifies that this component was only present for determining the phase response of the SOA.

The wavelengths of the pump and CW probe signals were varied within the ranges $1535 \leq \lambda_{pump} \leq 1570$nm and $1535 \leq \lambda_{probe} \leq 1580$nm respectively. The pump and CW probe wavelengths were restricted by the wavelength operating ranges of various components in the setup including EDFAs, BPFs and the mode-locked pump laser. The CW probe power was maintained at -3.5dBm, the average pump power varied from -27dBm to -7dBm (i.e. the pump pulse energy varied from 3 to 130fJ) and the SOA current bias varied from 100 to 500mA.

The gain evolution of the SOA could be measured directly by the OSO. However, to deduce the phase evolution of the SOA, it was necessary to utilize both the gain evolution and the signal output from the AMZI. The AMZI has one input port and two output ports, but only the input port and one of the output ports was required for these experiments. As illustrated in Fig. 3.2.4 which shows a schematic of the packaged AMZI device, the input fibre is connected to a 50:50 1x2 coupler (denoted C_1) and one output from C_1 passes through a fixed time delay in Arm 1 while the other output from C_1 passes through a phase-shifting element in Arm 2 (the constant phase shift imparted by this element to an optical signal can be controlled by applying an external voltage bias). After that, the two paths of the interferometer are recombined at a 50:50 2x2 coupler (denoted C_2) and the outputs from C_2 represent the two AMZI output ports.
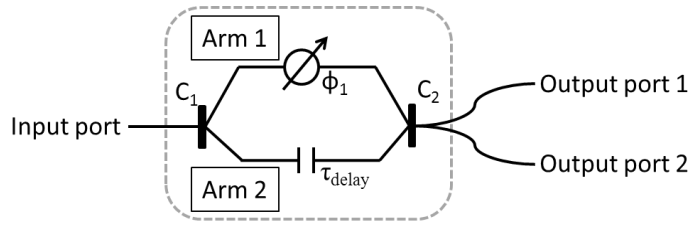
Fig. 3.2.4: Diagram of the integrated AMZI device employed to measure the phase response of the SOA under test. In one arm of the interferometer, there is a phase-shifter denoted by φ_1 and in the other arm of the interferometer there is a fixed optical time delay denoted by τ_{delay}.

The electric field $E_{output,1}$ of the optical signal for the first dark pulse output from the AMZI from the constructive interference port (output port 1) is given by Eq. 3.2.1 [278].

$$E_{output,1} = E_{arm,1} + E_{arm,2} = g_0 E_0 e^{i\varphi_0} + g(t)E_0 e^{i\varphi(t)} = g_0 E_0 e^{i\varphi_0}\left(1 + \frac{g(t)e^{i\Delta\varphi(t)}}{g_0}\right) \quad (3.2.1)$$

In Eq. 3.2.1, g_0 is the signal electric field gain of the undisturbed SOA, E_0 is the input electric field to the SOA, φ_0 is the phase of the optical signal in the undisturbed SOA, $\varphi(t)$ is the time-dependent phase of the optical signal in the excited SOA at time t after the arrival of the pump pulse and $\Delta\varphi(t)$ is the phase change in the excited SOA (i.e. the difference between $\varphi(t)$ and φ_0). The origin of Eq. 3.2.1 is visually explained in Fig. 3.2.5, where the shaded blue region indicates the location of the first dark pulse in the signal output from output port 1 in the AMZI.
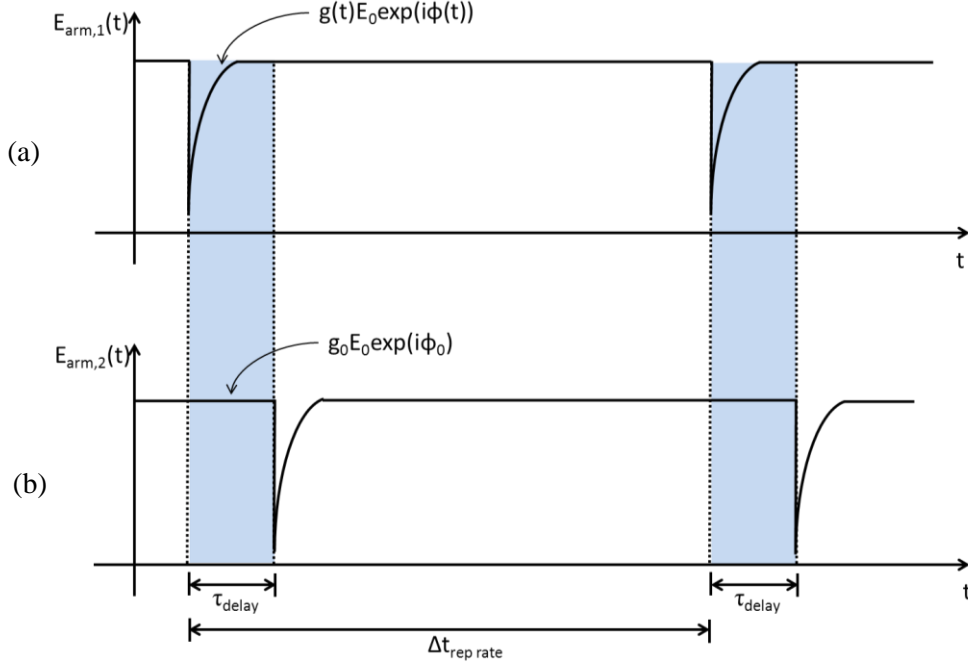
Fig. 3.2.5: Diagram showing the evolution of the electric field of the probe signal components in each arm of the interferometer.

Note that in Fig. 3.2.5, $\Delta t_{rep\ rate}$ represents the period of the pump pulse train (1.5ns in this case) and τ_{delay} is the fixed time delay in one arm of the AMZI (94ps in this case). The power P_{det} detected by the OSO is proportional to the modulus squared of the electric field (see Eq. 3.2.2).

$$P_{\det} \propto E_{output,1}{}^{*} E_{output,1} = G_0 |E_0|^2 \left(1 + \frac{G(t)}{G_0} + 2\sqrt{\frac{G(t)}{G_0}} \cos(\Delta \varphi(t)) \right) \tag{3.2.2}$$

In Eq. 3.2.2, G_0 represents the steady-state power gain level and $G(t)$ is the time-dependent power gain of the SOA following excitation by a pump pulse. A voltage bias was applied to the phase-shifting element and it was adjusted such that the steady-state (or fully recovered) power level was maximized. We define T_{norm} as the ratio of the time-dependent output power from the AMZI normalized relative to the steady-state power level (see Eq. 3.2.3). The factor of 1/4 in the equation ensures that $T_{norm}=1$ when $G(t)=G_0$ and $\Delta\varphi(t)=0$.

$$T_{norm} = \frac{1}{4} \left(1 + \frac{G(t)}{G_0} + 2\sqrt{\frac{G(t)}{G_0}} \cos(\Delta \varphi(t)) \right) \tag{3.2.3}$$

This equation can be rearranged to produce an expression for the phase change (see Eq. 3.2.4).

$$\Delta\varphi(t) = \cos^{-1}\left[\frac{4T_{norm} - \dfrac{G(t)}{G_0} - 1}{2\sqrt{\dfrac{G(t)}{G_0}}}\right]$$

(3.2.4)

A schematic diagram of the gain evolution of the SOA and the output signal from output port 1 from the AMZI is presented in Fig. 3.2.6 to provide a conceptual idea of the method of calculating the phase evolution of the SOA.
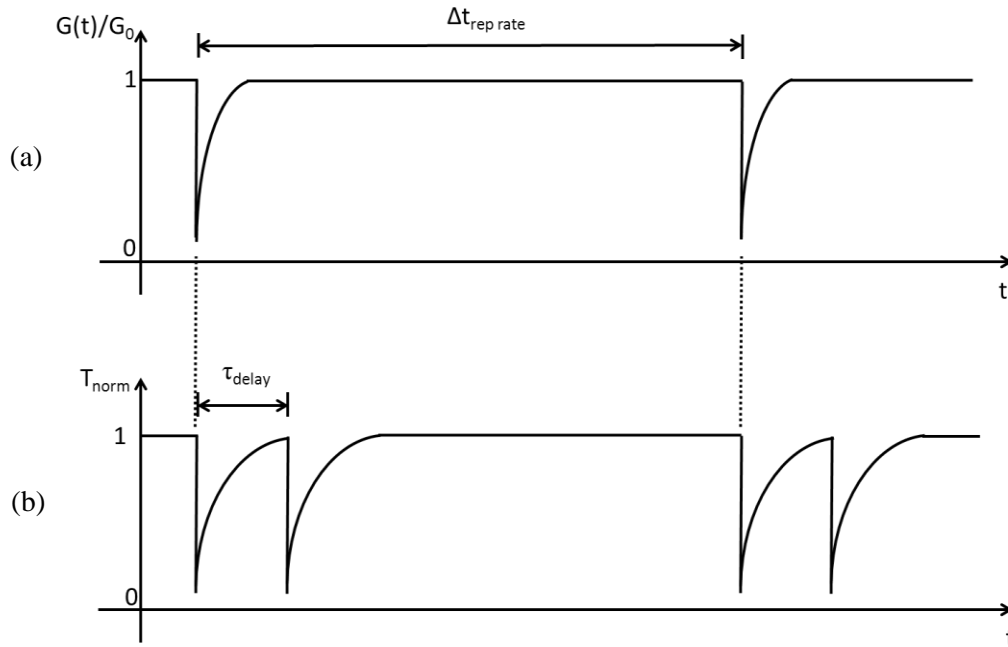
Fig. 3.2.6: (a) The normalized gain evolution of the SOA and (b) the normalized signal output from the AMZI after adjustment of the applied voltage bias to the phase-shifting element.

It can be seen in Fig. 3.2.6 that for every drop in the gain evolution in response to the arrival of a pump pulse, there were two transient features in the signal output from the AMZI (separated by an interval equal to τ_{delay}). It was necessary to align the onset of the gain response with the onset of the first feature in the signal output from the AMZI before employing Eq. 3.2.4 to compute the phase evolution of the SOA.

3.3   Experimental gain and phase data for SOA 03429

3.3.1   General trends in gain and phase evolutions

Fig. 3.3.1 shows the gain recovery profiles for SOA 03429 when the CW probe was fixed at 1550nm while the pump was varied from 1535 to 1570nm. For all of the following measurements, the current bias applied to SOA 03429 was 500mA unless otherwise stated.
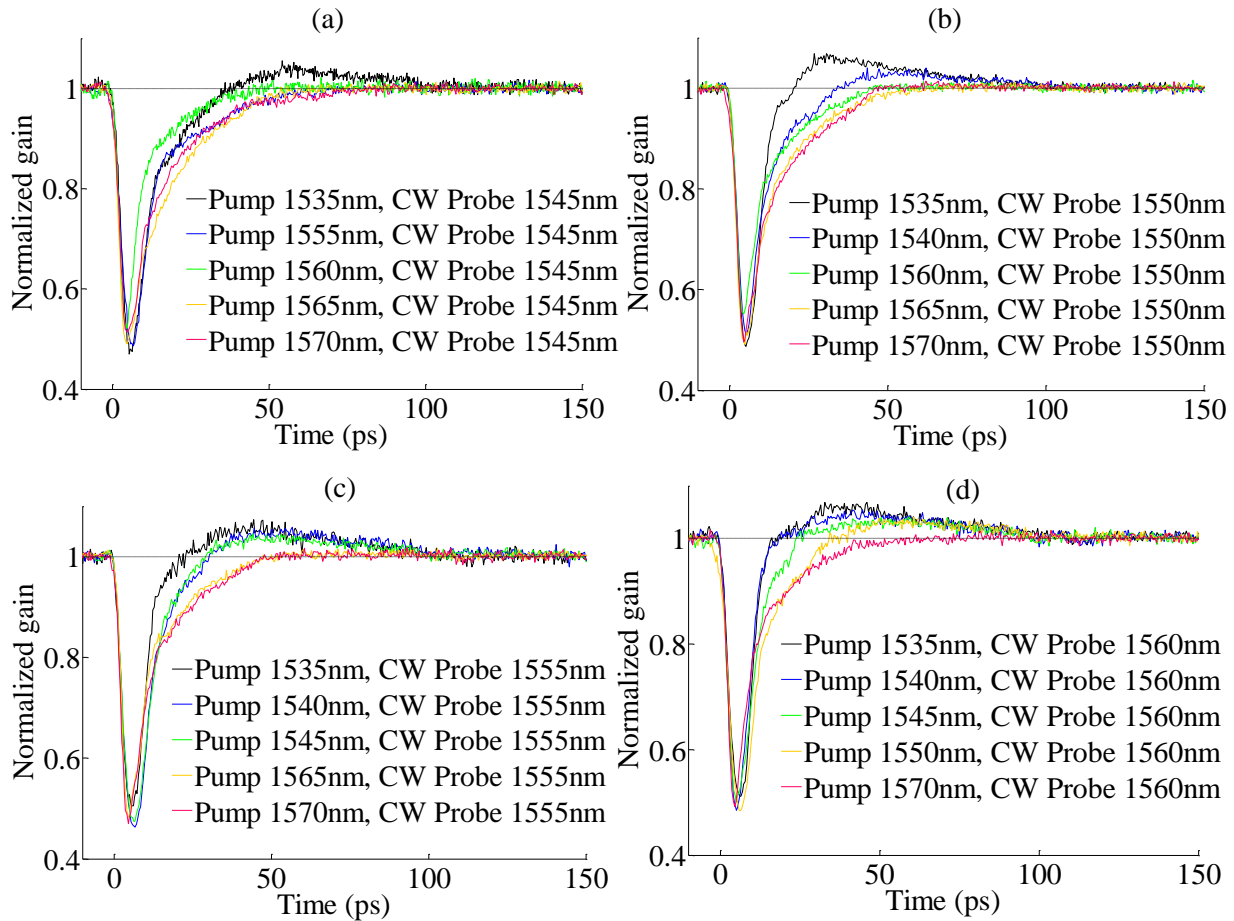
Fig. 3.3.1: Gain evolution for SOA 03429 at a current bias of 500mA with pump wavelength varied while the CW probe was fixed at (a) 1545nm, (b) 1550nm, (c) 1555nm and (d) 1560nm.

A consistent pattern emerges in Fig. 3.3.1, whereby the gain recovery time was significantly lower when pump wavelength was blue-shifted with respect to the CW probe wavelength, compared to when the pump wavelength was red-shifted with respect to the CW probe wavelength. Moreover, there was a prolonged (~80ps) overshoot of low magnitude when the pump was blue-shifted relative to the CW probe but this feature was absent when the pump was

red-shifted relative to the CW probe. Furthermore, the gain recovery time became progressively faster as the CW probe wavelength approached the gain peak wavelength (1565nm).

The phase evolutions for SOA 03429 corresponding to the gain responses shown on the previous page are illustrated in Fig. 3.3.2. Note that some of the phase responses display sudden discontinuities because the calculation of the phase evolution was extremely sensitive to noise when the phase change was close to zero, which is consistent with the fact that the phase was calculated using the inverse cosine function.
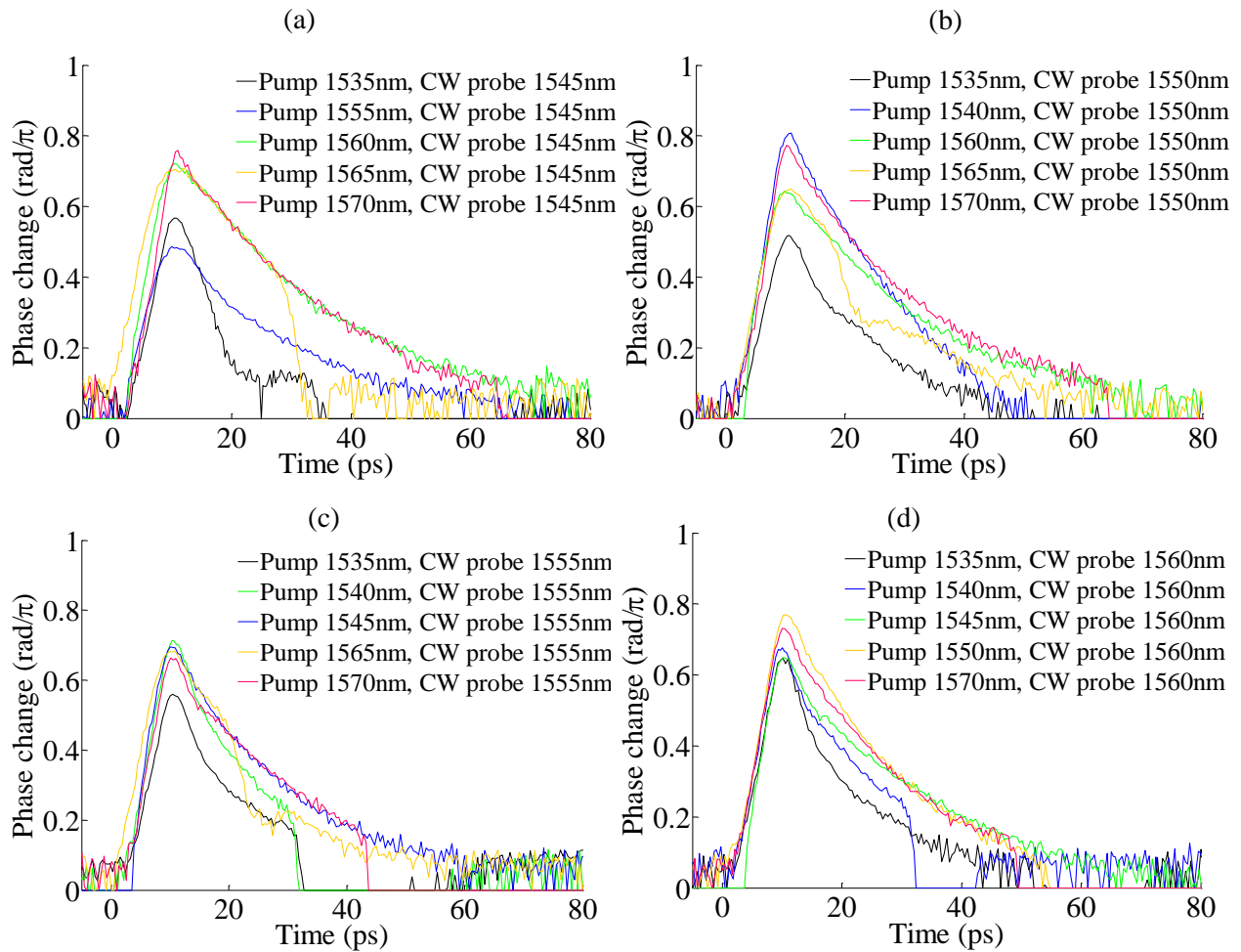
Fig. 3.3.2: Phase evolution for SOA 03429 at a current bias of 500mA with pump wavelength varied and the CW probe fixed at (a) 1545nm, (b) 1550nm, (c) 1555nm and (d) 1560nm.

As illustrated in Fig. 3.3.2, the phase evolutions were invariably longer than the corresponding gain evolutions, as the long band-filling recovery tail in the phase response was always present. However, it can be seen that the contribution of the ultrafast component in the phase response

generally became more pronounced when the gain responses were optimized e.g. the phase evolution for the 1535nm pump and 1560nm CW probe in Fig. 3.3.2(d).

As well as measuring the gain and phase response of SOA 03429 when the wavelengths of the pump and CW probe signals were tuned, the gain response of the SOA was measured at different modulation depths by varying the pump power (see Fig. 3.3.3).
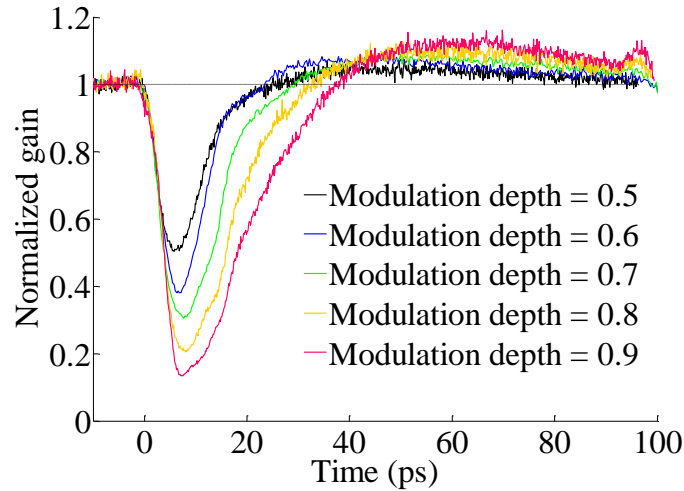
Fig. 3.3.3: Gain evolution for SOA 03429 at a fixed current bias of 500mA for various modulation depths, with 1535nm pump and 1565nm CW probe signals.

It can be deduced from Fig. 3.3.3 that the full gain recovery time increased from 15.6ps to 30.0ps as the modulation depth increased from 0.5 to 0.9. However, the gain response always had a protracted overshoot of low magnitude at all modulation depths.

Furthermore, the influence of the current bias applied to the SOA on the gain response was investigated while all remaining parameters were fixed. The gain response of SOA 03429 under different drive currents is displayed in Fig. 3.3.4. It can be observed in this figure that the choice of current bias applied to SOA 03429 was a crucial factor in the gain response time. When the current bias was low to moderate ($\leq$300mA), there was a long gain recovery tail (followed by a tiny overshoot when the current was between 200-300mA). When the current bias was high (>300mA), the gain response was dominated by an ultrafast component followed by a long overshoot of relatively low magnitude. The noticeable peak in the overshoot at t=25ps was due to a ghost pulse that leaked through the $LiNbO_3$ modulator which served to reduce the repetition rate of the pump pulse train from 10.65GHz to 665MHz.
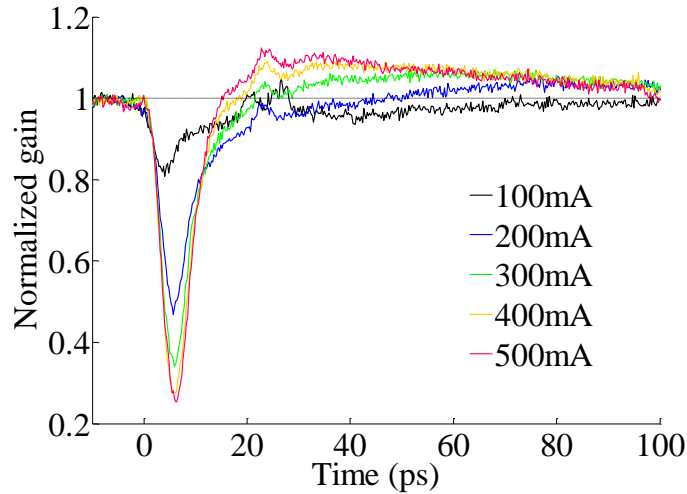
Fig. 3.3.4: Gain evolution for SOA 03429 at various drive currents, with 1535nm pump and 1565nm CW probe signals.

3.3.2   SOA recovery time dependence on probe – gain peak separation

To quantify the dependence of the carrier dynamics on the choice of probe wavelength, the 10/90 recovery times of the gain and phase evolutions were determined and plotted as a function of probe – gain peak wavelength separation (see Fig. 3.3.5).
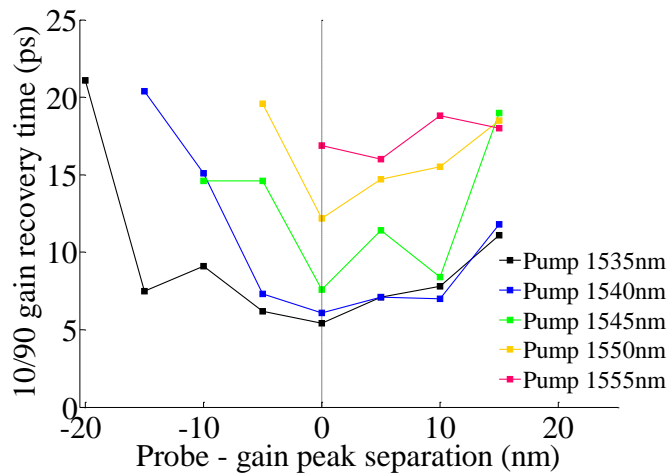
Fig. 3.3.5: 10/90 gain recovery time as a function of probe – gain peak wavelength separation for SOA 03429 at a current bias of 500mA, where the pump wavelength was constant for each individual curve.

As shown in Fig. 3.3.5, when the pump wavelength was 1545nm, 1550nm or 1560nm, the data was inconclusive. However, when the pump wavelength was either 1535nm or 1540nm and the

CW probe wavelength was adjacent to the small signal gain peak, the 10/90 gain recovery time was reduced compared to when the CW probe was distant from the gain peak. This trend is consistent with the experimental and computational modelling work reported by X. Li *et al* [275]. However, one major difference between these two sets of results is that the 10/90 gain recovery times presented in this thesis were as low as 6ps, whereas the 10/90 gain recovery times reported by X. Li *et al* were >250ps [275].

3.3.3   SOA recovery time dependence on pump – probe separation

To characterize the relationship between the recovery time and the separation (or detuning) between the pump and probe wavelengths, the 10/90 gain recovery times were plotted as a function of pump – probe wavelength separation, as illustrated in Fig. 3.3.6.
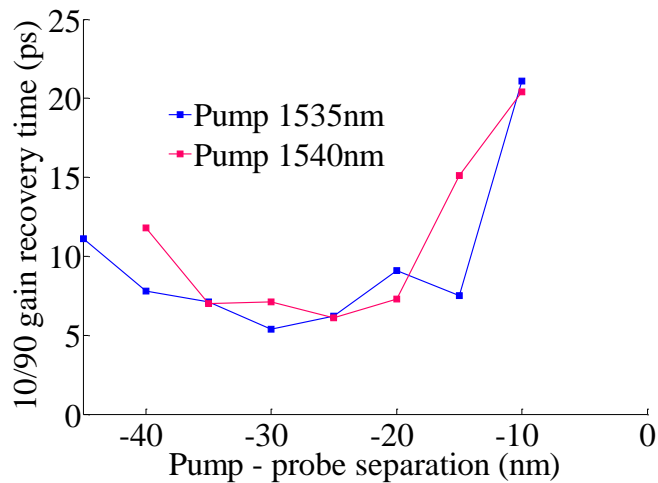
Fig. 3.3.6: 10/90 gain recovery time as a function of pump – probe wavelength separation for SOA
03429 at a current bias of 500mA, with the pump fixed in each individual curve.

For each curve in Fig. 3.3.6, the pump wavelength stayed constant and the probe wavelength was varied. There was an approximately parabolic shape to the two curves. The best recovery times were attained when the pump – probe wavelength separation was within 20 to 30 nm.

In Fig. 3.3.7, the 10/90 gain recovery times and the corresponding 1/e phase recovery times are plotted as a function of pump – probe separation, with the probe wavelength fixed in each individual curve.
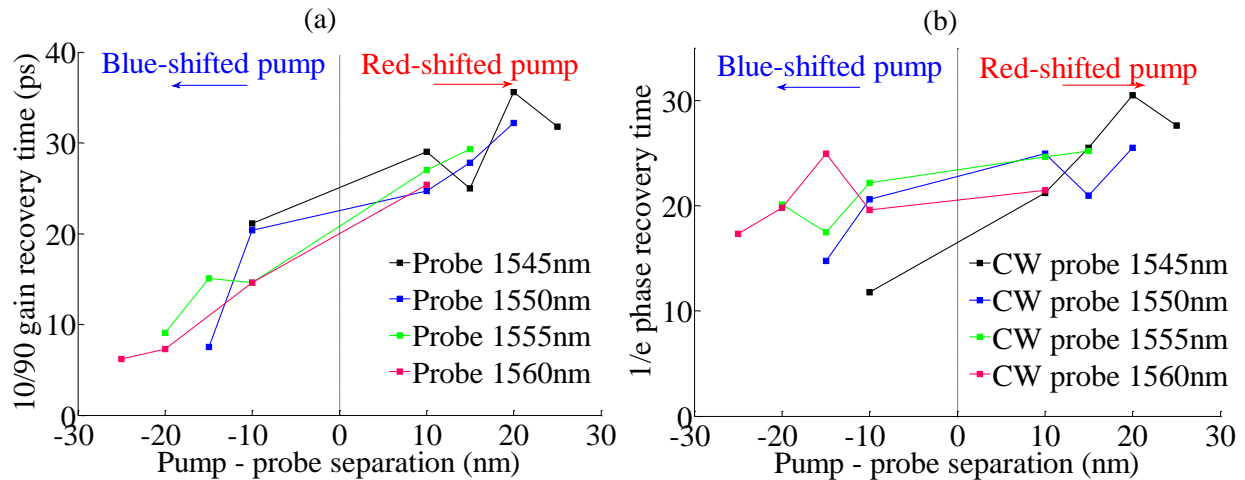
Fig. 3.3.7: (a) 10/90 gain recovery time and (b) 1/e phase recovery time for SOA 03429 at a current bias of 500mA as a function of pump – probe separation, with the probe wavelength fixed in each curve.

The graphs in Fig. 3.3.7 demonstrate that there was a steady rise in both the 10/90 gain recovery times and the 1/e phase recovery times as the pump wavelength increased. The shortest 10/90 recovery times were obtained when the pump wavelength was blue-shifted relative to the probe.

3.3.4   Optimum gain and phase responses

It was clear that the carrier dynamics in SOA 03429 were strongly dependent on the choice of both the pump and CW probe wavelengths. It was found that once certain criteria were satisfied, the gain response consisted almost exclusively of an ultrafast component (full gain recovery time as low as 9ps), followed by a small band-filling component in the form of an extended overshoot of low magnitude. The minimum full gain recovery time was remarkably fast compared to typical full recovery times ≥60ps for the fastest SOAs reported in the literature [102, 269, 279]. The corresponding phase response had a distinct ultrafast component followed by a slow recovery tail (full phase recovery time was as low as 60ps). The requirements for attaining this fast gain response included a high current bias (≥400mA), the pump wavelength had to be blue-shifted relative to the probe wavelength, the probe wavelength had to be close to the small signal gain peak (1565nm), and the pump-probe separation wavelength had to be maintained within 20 to 30nm. Several gain and phase responses for SOA 03429 under optimal operation conditions are displayed in Fig. 3.3.8.
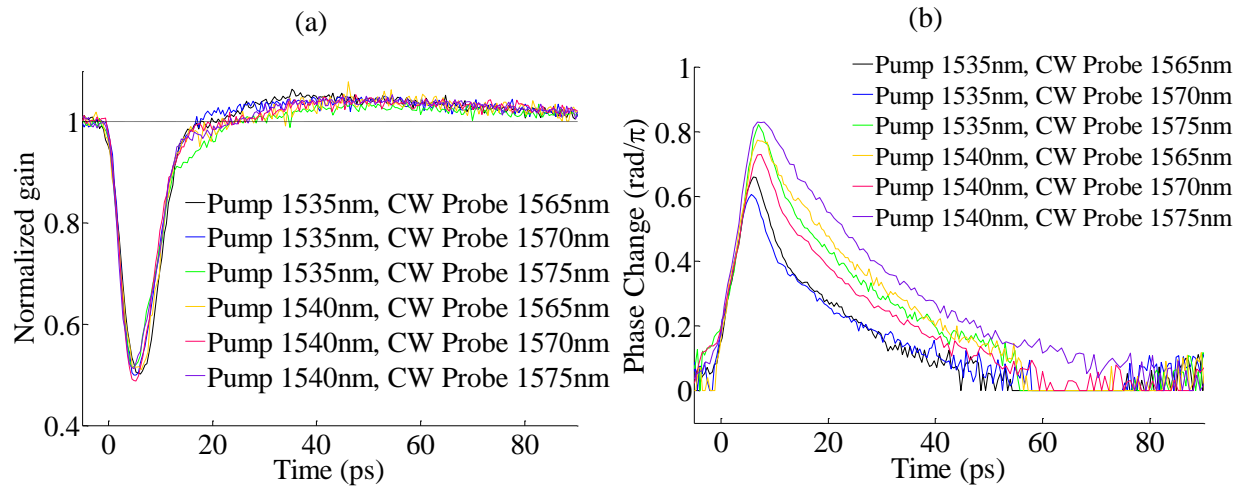
Fig. 3.3.8: Graphs of (a) gain and (b) phase as a function of time for the optimum pump – probe separation for SOA 03429 at a current bias of 500mA.

As evidenced by Fig. 3.3.8, it was possible to achieve a near-total ultrafast gain response and a phase response with a prominent ultrafast component for a range of pump and probe wavelengths. The phase response was longer than the gain response as the phase evolution was primarily governed by carrier depletion whereas the gain evolution was influenced by both carrier depletion and ultrafast effects such as spectral hole burning and carrier heating [112].

3.4   Experimental amplitude and phase data for SOA 03735

With respect to SOA 03735, the gain response of this device at a current bias of 500mA did not reveal the same degree of wavelength dependence as that shown by SOA 03429. Several gain evolutions for SOA 03735 are shown in Fig. 3.4.1, where the CW probe wavelength was fixed and the pump was varied from the blue to the red of the CW probe. The average CW probe power was -3.5dBm and the average pump power was -17dBm (i.e. the energy per pump pulse was 30fJ) at the input port of the SOA.
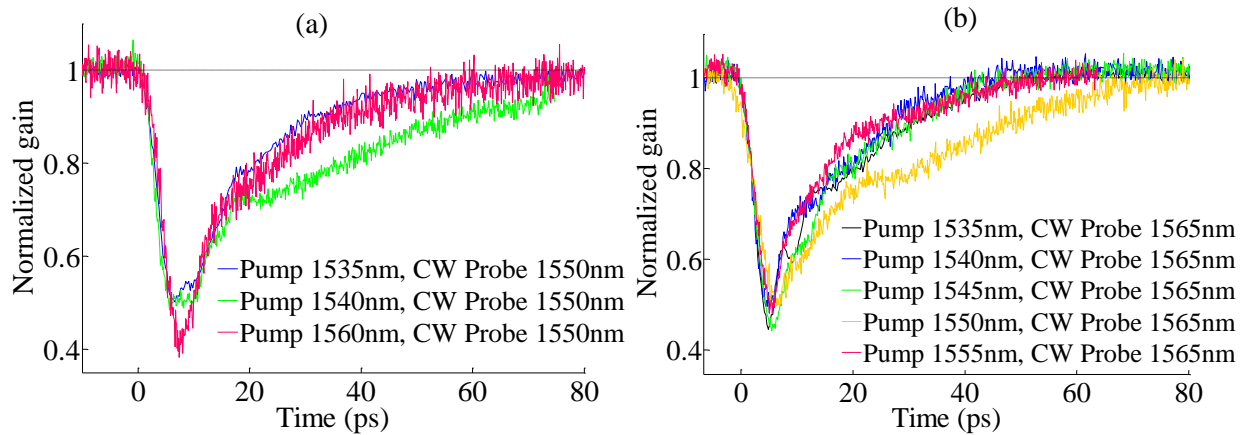
Fig. 3.4.1: Gain evolution of SOA 03735 for a fixed CW probe wavelength of (a) 1550nm and (b) 1565nm, while the pump wavelength was varied.

As illustrated in Fig. 3.4.1, although there was a slight dependence on the input signal wavelengths, there was no marked drop in the gain response time and no appreciable overshoot when the pump wavelength was blue-shifted relative to the CW probe wavelength. The CW probe was always far away from the small signal gain peak for SOA 03735 (1505nm) and this was the reason that the gain response time of this device remained long (>60ps) for these measurements, as will be explained in Section 3.6.

3.5 *Theory and modelling*

Subsequent to the experimental investigation of the carrier dynamics in SOA 03429 and SOA 03735 under different operation conditions, the behaviour of SOA 03429 was analysed in detail. At this point, it is worth re-stating that in the case of SOA 03429, a predominant ultrafast gain response followed by a prolonged overshoot of low magnitude in a long, highly nonlinear SOA was observed when the following conditions were fulfilled:

- High current bias (≥400mA)
- CW probe wavelength close to small signal gain peak wavelength (1565nm)
- Pump wavelength was blue-shifted with respect to CW probe wavelength
- Pump-probe separation wavelength was maintained within 20 to 30nm.

As a starting point for an explanation of the carrier dynamics in SOA 03429, it is important to bear in mind that a moderate power (-3.5dBm) CW probe beam was launched into the SOA for all of the time-resolved measurements, which induced gain saturation within the device. To illustrate the impact of the moderate power CW probe upon the gain spectrum, the small signal gain spectra for the SOA both with and without the CW probe are shown in Fig. 3.5.1.
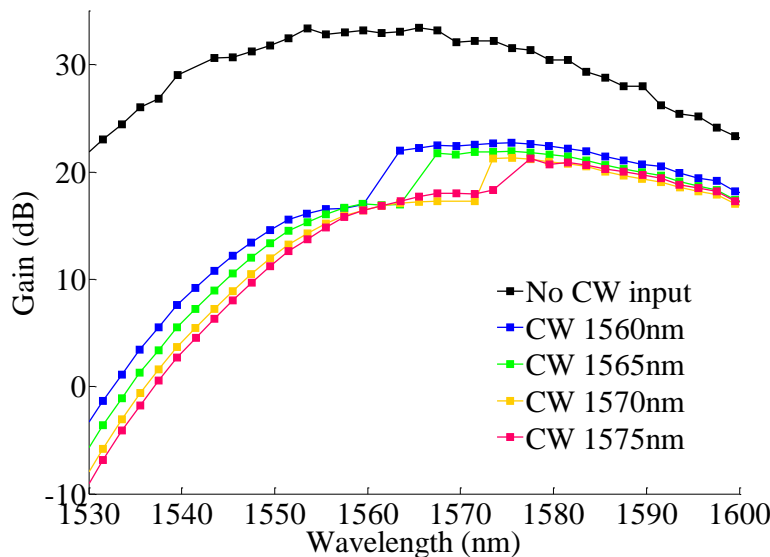
Fig. 3.5.1: Power gain spectra for SOA 03429 with a moderate power (-3.5dBm) CW input beam and with no CW input beam at wavelengths close to the small signal gain peak (1565nm).

It can be seen in Fig. 3.5.1 that the CW probe beam significantly suppressed the whole gain spectrum when the CW probe was located close to the small signal gain peak (1565nm). Furthermore, the degree of suppression of the gain spectrum was stronger at wavelengths to the blue of the CW probe compared to the amount of gain suppression at wavelengths to the red of the CW probe. In fact, the transparency point of the SOA was approximately 1535nm in the presence of a saturating CW probe beam.

A schematic diagram of the density of states in the conduction and valence bands near the input facet and the output facet of the device is given in Fig. 3.5.2 to provide an insight into the effect of the saturating CW probe beam on the carrier density along the length of the SOA.
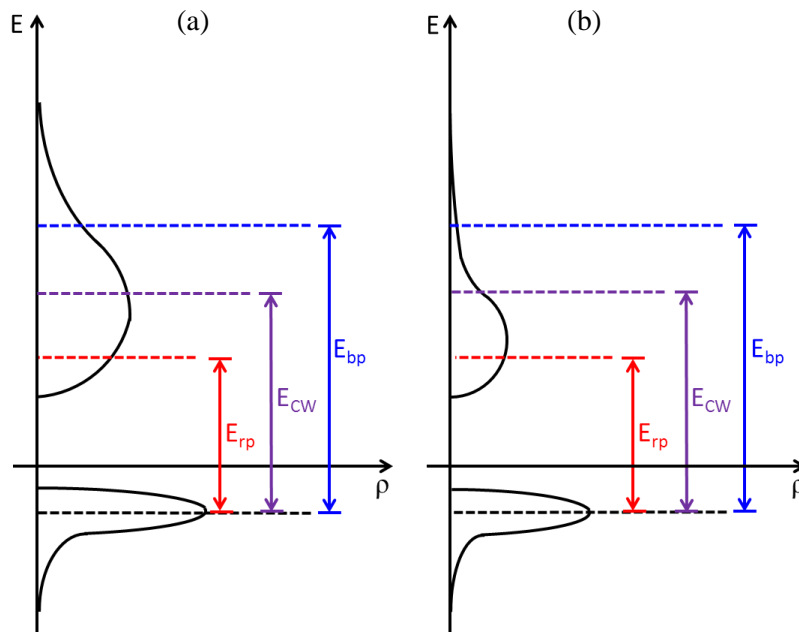
Fig. 3.5.2: Schematic diagram showing the density of states (a) near the input facet and (b) near the output facet of the SOA (E_{rp}=photon energy for red-shifted pump, E_{CW}=photon energy for CW probe, E_{bp}=photon energy for blue-shifted pump).

As shown in Fig. 3.5.2(a), near the input facet of the SOA, the carrier density is sufficiently high to provide gain to the red-shifted pump, the blue-shifted pump and the CW probe signals. As shown in Fig. 3.5.2(b), the saturating CW probe has depleted the carriers to such an extent that it induces transparency at the CW probe wavelength near the output facet of the SOA. As a consequence, the carrier density would not be sufficient to provide net gain to the blue-shifted pump signal, although it would still be able to provide net gain to the red-shifted pump signal.

It was surmised that when the pump was blue-shifted relative to the CW probe, the gain experienced by the pump became negative at some point along the length of the active region and this led to attenuation of the pump after this point. In the section where the pump experienced positive gain, XGM took place between the pump and the CW probe. In the section where the pump experienced absorption, SGM of the modulated CW probe signal took place and this compensated for the slow band-filling tail in the response of the SOA. This theory would explain why the behaviour of SOA 03429 under optimum operational circumstances resembled the response of the conventional Turbo-Switch configuration [129] (see Fig. 3.5.3).
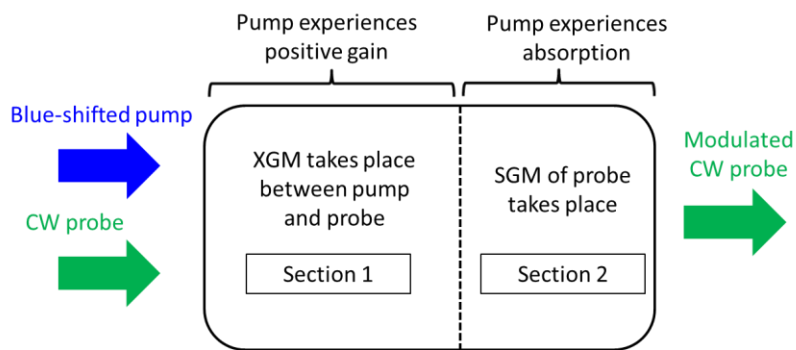
Fig. 3.5.3: Diagram of SOA 03429 showing the hypothesized manner in which the device acted similarly to the Turbo-Switch when the pump was to the blue of the CW probe (and the CW probe was close to the small signal gain peak).

By contrast, when the pump was red-shifted relative to the CW probe, the gain experienced positive gain throughout the active region. Therefore, XGM took place throughout the SOA and the slow tail in the response of the SOA was not eliminated (see Fig. 3.5.4).
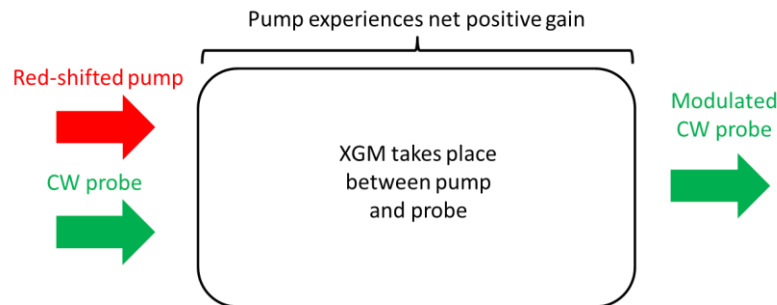
Fig. 3.5.4: Diagram of SOA 03429 showing the hypothesized behaviour of the device when the pump was to the red of the CW probe.

This theory explains why it was necessary for the CW probe wavelength to be adjacent to the small signal gain peak to achieve fast gain and phase responses. When the CW probe wavelength was situated close to the gain peak wavelength, the gain spectrum was suppressed to the greatest possible extent. This meant that the blue-shifted pump experienced absorption over a large proportion (≥50%) of the active region and there was sufficient SGM of the probe to negate the slow tail in the gain and phase responses. When the CW probe moved away from the small signal gain peak, the degree of suppression of the gain spectrum was reduced and the blue-shifted pump experienced absorption over a smaller proportion (<<50%) of the active region.

Moreover, the theory can account for the observation that the gain and phase responses became faster as the pump became increasingly blue-shifted. When the pump wavelength decreased, the proportion of the length of the active region over which the pump experienced absorption increased, leading to a greater amount of SGM of the probe.

Finally, this theory provides a rationale for the high current bias (≥400mA) needed to obtain a predominantly ultrafast gain response. When a high current bias was supplied to the SOA, the input signals experienced high power gain near the input facet. This led to dramatic depletion of carriers further on along the length of the device and ensured that absorption of the pump could take place over a large proportion (≥50%) of the active region.

This explanation of the behaviour of the device was verified by computational modelling conducted by Dr Rod Webb in Tyndall National Institute. The SOA model employed by Dr Rod Webb was a multi-section time-domain rate equation model of the carrier dynamics [123], similar to the model described by G. Talli *et al* [133] but with some extra features. Firstly, the material gain was modelled using the approach outlined by J. Leuthold *et al* [280]. Secondly, the length dependence of both gain and ASE spectra was included in the model. Thirdly, changes in carrier temperature were included in the model to take carrier heating into consideration.

The active region was divided up into k sections ($k=50$ for these simulations) along its total length L_{total}. Rate equations for the carrier density and carrier temperature were solved and a polynomial approximation to the gain spectrum was evaluated for each section and time step based on the power and wavelength of the pump, CW probe and ASE signals entering and exiting every individual section, as illustrated in Fig. 3.5.5. Both forward-propagating and backward-propagating ASE signals were included in the model, where the ASE spectral density was available indirectly for all positions and times in the SOA but the spectrum was represented

by a small number of parameters instead of a large number of spectral samples, so as to minimize the computational complexity [98, 133]. However, under the circumstances, ASE had only a limited impact upon the carrier dynamics because the saturating CW probe power suppressed the gain spectrum and, by extension, the ASE spectrum within the SOA.
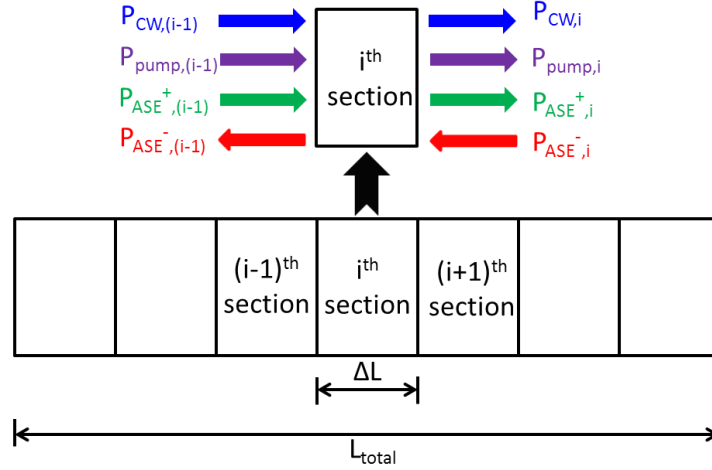
Fig. 3.5.5: Active region divided into equally long sections of length ΔL for the simulating the carrier dynamics in the SOA (The length of each section ΔL is given by ΔL=L$_{total}$/k).

The propagation of the pump, CW probe, forward-propagating ASE and backward-propagating ASE signals through the active region were modelled using Eq. 3.5.1, where P_{sig} refers to the optical power of the signal in question, λ_{sig} is the signal wavelength, N is the total instantaneous carrier density, t is time, v_g is the group velocity of the signal, Γ is the optical confinement factor, $g_m(\lambda_{sig},N)$ is the material gain and α_L is the waveguide loss per unit length [123].

$$\frac{\partial P_{sig}}{\partial z} + \frac{\partial P_{sig}}{v_g \partial t} = (\Gamma g_m(\lambda_{sig},N) - \alpha_L)P_{sig} \qquad (3.5.1)$$

The material gain $g_m(\lambda_{sig},N)$ was modelled using the approach proposed by J. Leuthold *et al*, as described by Eq. 3.5.2, where λ_z is the bandgap wavelength, $g_p(N)$ is the peak gain and $\lambda_p(N)$ is the wavelength at the peak in the gain spectrum. It was assumed that λ_z was constant and this assumption enabled calculation of the gain and ASE spectra along the length of the device [123].

$$g_m(\lambda_{sig}, N) = g_p(N) \left[3\left(\frac{\lambda_z - \lambda_{sig}}{\lambda_z - \lambda_p(N)}\right)^2 - 2\left(\frac{\lambda_z - \lambda_{sig}}{\lambda_z - \lambda_p(N)}\right)^3 \right] \qquad (3.5.2)$$

The peak gain $g_p(N)$ and the wavelength at the peak in the gain spectrum $\lambda_p(N)$ were modelled using Eq. 3.5.3 and Eq. 3.5.4 respectively, where a_0 is the differential gain coefficient, $N_{eff}(N)$ is the effective carrier density (used to account for carrier heating effects), N_0 is the transparency carrier density, and λ_{p0}, b_0 and b_1 are parameters adjusted to fit the measured gain spectrum.

$$g_p(N) = a_0(N_{eff}(N) - N_0) \qquad (3.5.3)$$

$$\lambda_p(N) = \lambda_{p0} - b_0(N_{eff}(N) - N_0) - b_1(N_{eff}(N) - N_0)^2 \qquad (3.5.4)$$

The rate equation for modelling the carrier density in each section of the active region is given by Eq. 3.5.5, where $N_i(t)$ is the instantaneous carrier density in the ith section, I is the current bias, A is the cross-sectional area, R_{tot} is the total recombination rate, e is charge of an electron, h is Planck's constant, c is the speed of light in a vacuum, A is the cross-sectional area of the active region, P_1 is the pump power, P_2 is the CW probe power, λ_1 is the pump wavelength, λ_2 is the CW probe wavelength, $W_{ASE,i}^+(t)$ is the forward-propagating ASE power spectral density in the ith section and $W_{ASE,i}^-(t)$ is the backward-propagating ASE power density in the ith section [133].

$$\frac{\partial N_i(t)}{\partial t} = \frac{I}{eAL_{total}} - R_{tot}(N_i) - g_m(\lambda_1, N_i)\frac{\Gamma P_1 \lambda_1}{Ahc} - g_m(\lambda_2, N_i)\frac{\Gamma P_2 \lambda_2}{Ahc} - \int g_m(\lambda', N_i)[W_{ASE,i}^+ + W_{ASE,i}^-]\frac{\lambda'}{Ahc}d\lambda' \qquad (3.5.5)$$

Using band modelling, it has been found that the effect of carrier heating in the centre of the gain region can be modelled to a good approximation using an effective carrier density $N_{eff}(N)$, which can be evaluated using Eq. 3.5.6, where T is the instantaneous temperature of the conduction band carriers and T_0 is the steady-state carrier temperature.

$$N_{eff}(N) = N - \frac{\partial N_{eff}}{\partial T}(T - T_0) \qquad (3.5.6)$$

The carrier temperature was modelled using Eq. 3.5.7, which assumes that the change in temperature is proportional to the number of carriers removed by stimulated emission and that the temperature decays exponentially, where is ε_T is a constant and τ_{ch} is the carrier cooling lifetime (~1ps). The $\sqrt{N}$ term was included as an approximation to band modelling data.

$$\frac{\partial T}{\partial t} = \frac{\varepsilon_T \Gamma g_m P \lambda}{\sqrt{N} A h c} - \frac{(T - T_0)}{\tau_{ch}} \tag{3.5.7}$$

Simulations on the carrier dynamics within the SOA were performed at a CW probe wavelength at 1550nm and the pump wavelength was either blue-shifted (1535nm) or red-shifted (1565nm) relative to the CW probe. The CW probe power was -3.5dBm and the pump pulse energies were 17fJ and 0.7fJ for the blue-shifted and red-shifted pump signals respectively at the input of the device. The pump pulse energies were chosen to ensure that the modelled and experimentally measured gain evolutions had the same modulation depth (i.e. 50%).

Fig 3.5.6 shows the modelled carrier density variation along the SOA active region length both with and without the saturating CW probe, together with the approximate transparency carrier density level for a blue-shifted pump and a red-shifted pump. In this context, transparency refers to the point where there is zero power gain (i.e. modal gain) in the SOA.
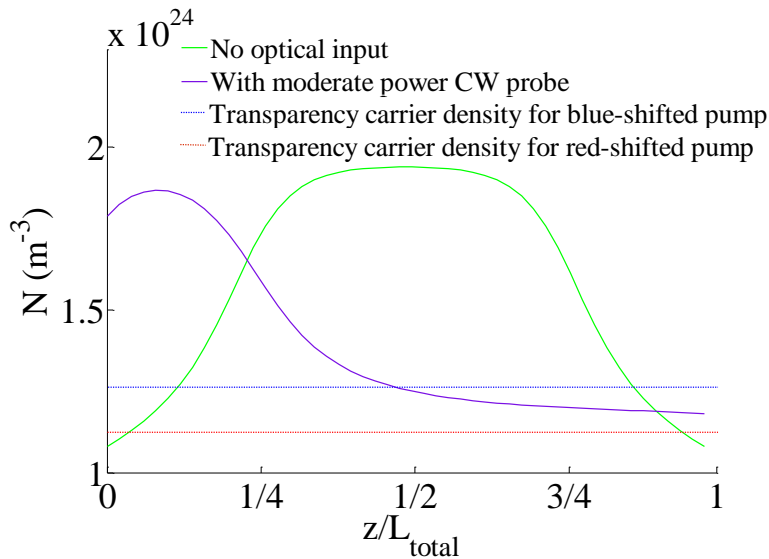
Fig. 3.5.6: Carrier density as a function of length within the active region, where L_{total} =2.2mm.

It can be inferred from Fig. 3.5.6 that when there was no optical input, the forward and backward travelling ASE were at their maximum levels at both ends of the active region, which led to symmetrical reductions in the carrier density. When the moderate power CW probe was input to the device, the forward travelling power was enhanced and the carrier density beyond the first quarter of the SOA progressively decreased until transparency at the probe wavelength was induced at the output facet. The backward travelling ASE was also reduced but still created a small dip in the carrier density close to the input facet. It can be seen in Fig. 3.5.6 that the carrier density dipped below the approximate transparency carrier density for the blue-shifted pump beyond the midpoint of the active region. However, the carrier density always remained above the approximate transparency carrier density for the red-shifted pump.

The calculated modal gain spectra at various points in the active region when the CW probe was launched into the SOA are plotted in Fig. 3.5.7. The wavelengths of the saturating CW probe and both the blue-shifted and red-shifted pumps are marked by vertical dashed lines, while the transparency level (zero gain) is marked by a horizontal dashed line.
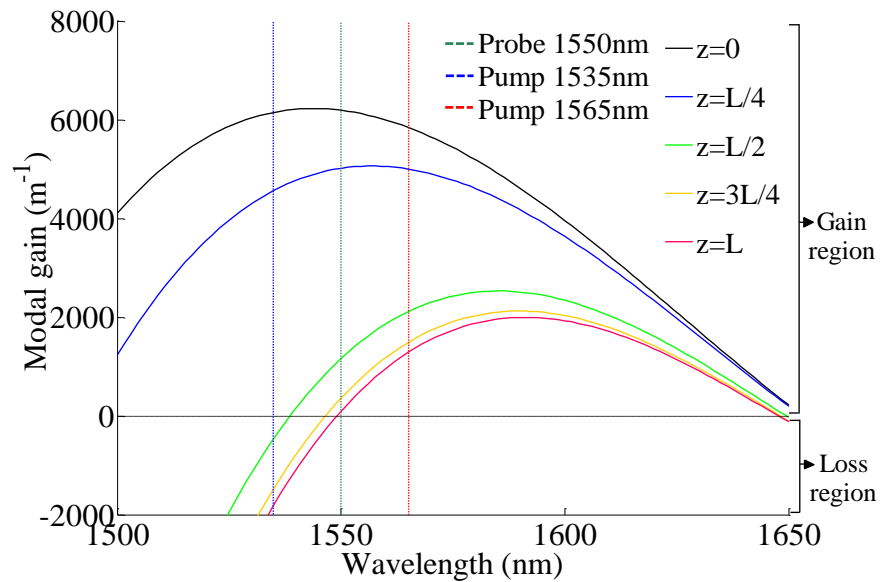
Fig. 3.5.7: Steady-state gain spectra at various points along the length of the active region (z=0 denotes the input facet and z=L denotes the output facet).

It can be discerned from Fig. 3.5.7 that the peak gain decreased and the wavelength of the peak in the gain spectrum became increasingly red-shifted as a function of distance in the active region. Both pump wavelengths (1535nm and 1565nm) and the 1550nm CW probe wavelength

experienced positive gain at the input facet (*z*=0). The gain experienced by the CW probe decreased until transparency at this wavelength was reached at the output facet (*z=L*). The red-shifted pump always experienced positive gain throughout the length of the active region, although the gain decreased as a function of length. However, for the blue-shifted pump signal, it initially experienced positive gain but subsequently it experienced negative gain (i.e. loss) beyond the midpoint of the active region (*z=L/2*). [41, 129].

The modelled evolutions of the total signal power at various points along the length of the active region for the blue-shifted (1535nm) pump and the red-shifted pump (1565nm) are displayed in Fig. 3.5.8. The scales on the x-axis and y-axis in both graphs are identical to facilitate direct comparison between the two graphs. The pump power can be distinguished from the probe power by the fact that the pump signal is manifested as a sharp upward spike whereas the probe signal is manifested as a constant steady-state power level (before the arrival of the pump pulse) followed by a rapid drop in power (immediately after the arrival of the pump pulse) and a subsequent slow recovery tail.
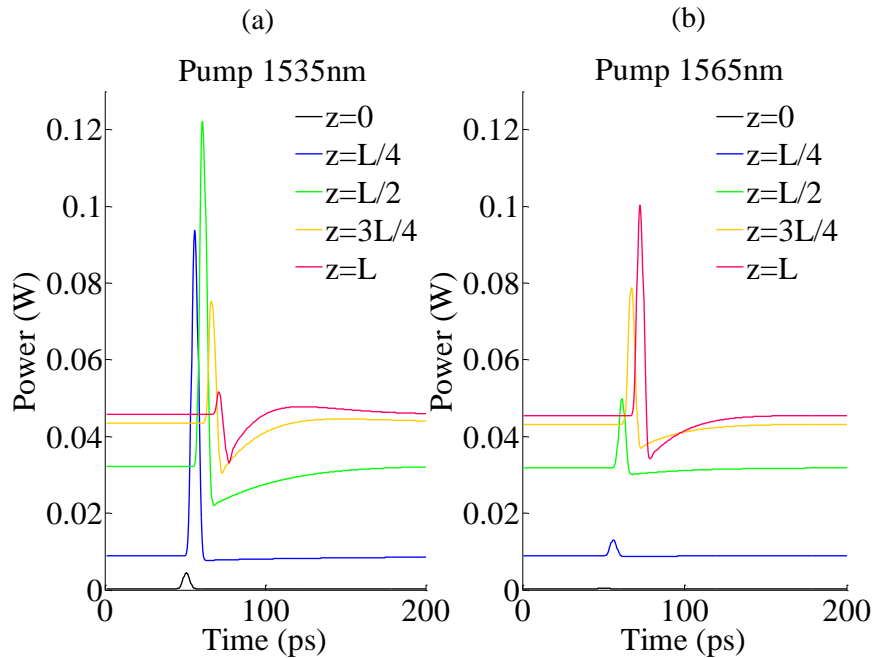
Fig. 3.5.8: Total (pump and CW probe) power evolution at various points along the length of the active region for (a) blue-shifted pump and (b) red-shifted pump relative to the CW probe.

For the blue-shifted (1535nm) pump in Fig. 3.5.8, the pump power was low at *z*=0. The pump power increased up until *z=L/2*, after which it began to decrease to the extent that the

pump signal had almost disappeared when it reached $z=L$. The steady-state probe power level was low at $z=0$ and gradually increased as the signal advanced through the active region. At $z=L/2$, a long recovery tail with duration ~100ps was visible in the probe power evolution. However, beyond the midpoint of the active region, the recovery tail in the probe power evolution became progressively shorter. At $z=L$, the duration of the recovery tail was ~25ps and an overshoot was visible in the probe power evolution.

For the red-shifted (1565nm) pump in Fig. 3.5.8, the pump power continued to grow as the signal advanced through the active region. For the probe power evolution, a long recovery tail with duration ~100ps was visible at $z=L/2$ and it remained almost as long as this at $z=L$.

The modelled evolutions of the carrier density at various stages along the length of the active region for the blue-shifted pump (1535nm) and the red-shifted (1565nm) pump are displayed in Fig. 3.5.9. The scales on the x-axis and y-axis in both graphs are identical to facilitate direct comparison between the two graphs.
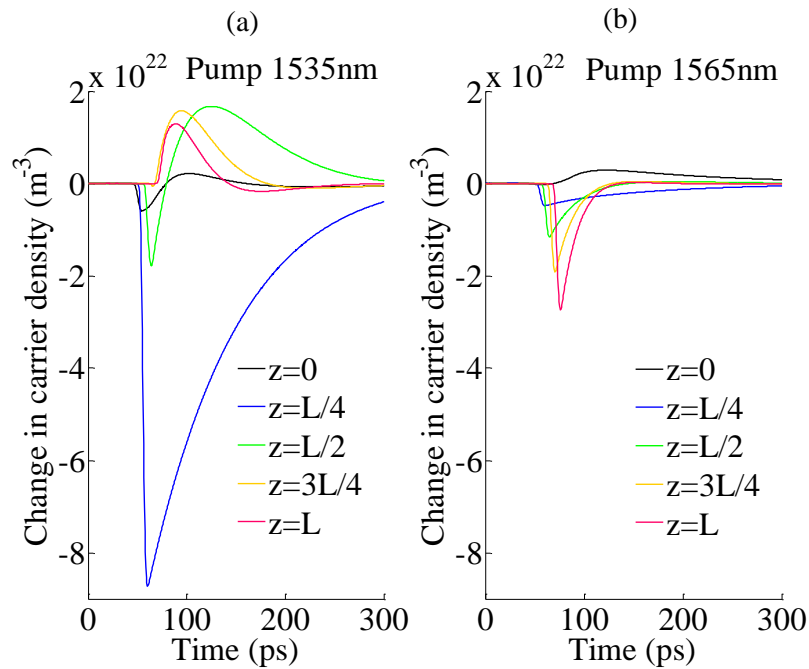
Fig. 3.5.9: Change in carrier density at various points along the length of the active region for (a) blue-shifted pump and (b) red-shifted pump relative to the CW probe.

For the blue-shifted (1535nm) pump in Fig. 3.5.9, the carrier density falls sharply and it takes a long time to fully recover (~300ps) at $z=L/4$, indicating that XGM between the pump and probe took place in the first half of the active region, where the pump experienced gain. However,

beyond the midpoint of the SOA, where the pump began to undergo absorption, the change in carrier density reversed from negative to positive values, indicating that SGM of the probe took place in the second half of the active region. The degree of SGM of the probe was strong enough to effectively eliminate the slow recovery tail in the gain response of the SOA.

However, for the red-shifted (1565nm) pump in Fig. 3.5.9, the change in carrier density was practically always negative, except at *z=0* where the influence of backwards-propagating ASE was dominant. This suggests that the red-shifted pump always experienced gain so XGM between the pump and probe took place along the full length of the active region. Although SGM of the probe did occur to some extent, it was too limited to have a significant impact on the slow recovery tail in the gain response of the SOA.

Finally, the experimental and modelled gain evolutions with a fixed CW probe wavelength of 1550nm and pump wavelengths of 1535nm and 1565nm are shown in Fig. 3.5.10.
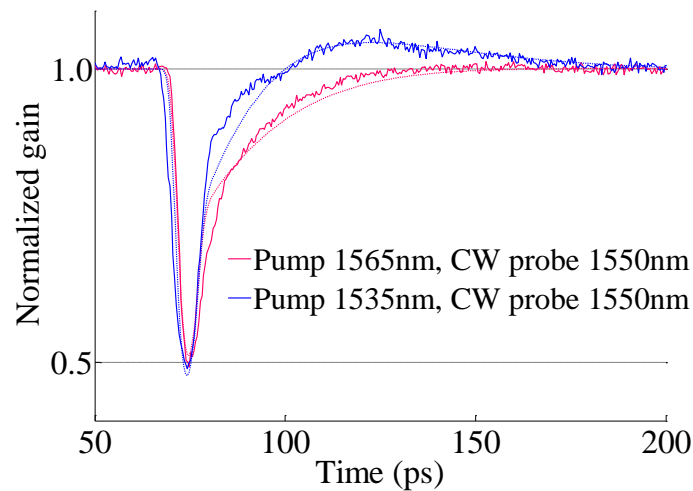
Fig. 3.5.10: Experimental (solid line) and modelled (dotted line) gain evolution for SOA 03429, where the CW probe wavelength was 1550nm.

In Fig. 3.5.10, it is discernible that there was excellent agreement between the measured and modelled gain evolution for SOA at these pump and CW probe wavelengths. Minor discrepancies between the measured and modelled data may be attributable to polarization dependence in the SOA that was not accounted for in the model.

3.6   Summary

The carrier dynamics of two long, highly nonlinear MQW SOAs were investigated using a pump-probe spectroscopy test-bed incorporating pulsed pump and CW probe signals. For SOA 03429 (with a small signal gain peak of 1565nm), the gain recovery rate was strongly dependent and the phase recovery rate was weakly dependent on the wavelength of input optical signals. There was a marked contrast between the gain evolution for a pump that was blue-shifted relative to the CW probe and a pump that was red-shifted relative to the CW probe:

- When the CW probe was close to the small signal gain peak, the pump was to the blue of the CW probe, the pump – probe separation was set to 20 to 30nm and a high current bias (≥400mA) was applied to the SOA, gain recovery profiles consisting almost entirely of an ultrafast component accompanied by a prolonged overshoot of low magnitude were observed. A full gain recovery time as low as 9ps was attainable under optimized conditions. Although the phase recovery rate was slower than the gain recovery rate, it followed a similar trend to the gain recovery rate as a function of pump – probe separation.
- When the pump was red-shifted relative to the CW probe, the gain and phase recovery lifetimes were longer, the ultrafast contribution to the recovery was negligible and there was no gain overshoot.

Computational modelling of the carrier dynamics in SOA 03429 was consistent with the theory that the behaviour of this SOA was reminiscent of the Turbo-Switch configuration when the pump was blue-shifted relative to the CW probe, where the pump was essentially filtered out beyond the middle of the active region. In the first half of the active region where the blue-shifted pump experienced gain, XGM between pump and probe occurred. In the second half of the active region where the blue-shifted pump was attenuated, SGM of the probe took place and this neutralized the slow band-filling tail in the gain and phase response of the probe signal coming from the first half of the active region.

In relation to SOA 03735 (with a small signal gain peak of 1505nm), even though it had a similar active region length and confinement factor to SOA 03429, it did not exhibit an

exceptionally fast gain response because the available pump and probe wavelengths were not in the optimum wavelength operation regime. The observation that the gain evolution of SOA 03735 did not change substantially as the pump wavelength varied from the red of the CW probe to the blue of the CW probe can be ascribed to the fact that the CW probe was far away from the small signal gain peak for the device. For this reason, the gain spectrum of SOA 03735 was never adequately suppressed to ensure absorption of the pump in the active region. To observe amplitude recovery with a substantial ultrafast component, it would be necessary to have the CW probe wavelength located close to the gain peak of 1505nm and for the pump wavelength to be to the blue of this CW probe wavelength. However, it was impossible to achieve these operation conditions due to the wavelength ranges of the tunable laser sources, the OSO and the filters available in the lab.

In terms of potential applications of the research outlined in this chapter, devices similar to SOA 03429 could be exploited in optical signal processing applications, as there are several advantages to using this kind of device, including the fact that only a single nonlinear device is needed and it can supply high power gain (~30dB in the small signal regime) to an input data signal. However, there are limitations associated with employing this type of device, such as restrictions on the choice of wavelength and the requirement for a high current bias ($\geq$400mA). With this in mind, this type of SOA could be deployed to realize optical signal processing functions such as demultiplexing, format conversion or packet header processing, where the wavelengths of the input optical signals are fixed at their optimum values for that particular SOA. If devices similar to SOA 03429 were inserted into a push-pull interferometric arrangement, the interferometric response time may be slower than the gain recovery times measured here as the total phase recovery time remained long (~60ps) for all measurements.

Concatenated SOA-EAM-SOA (CSES) configuration

In this chapter, the amplitude and phase dynamics of a concatenated SOA-EAM-SOA configuration are presented. A near-total ultrafast amplitude response (full amplitude recovery time as low as 10ps) was observed under optimum operation conditions whereas the phase response was considerably longer. The behaviour of the system could be manipulated by careful choice of input signal wavelength, SOA drive currents and EAM reverse bias voltage. Experimental data and impulse response modelling indicated that the slow tail in the gain response of the first SOA could be eliminated by a combination of XAM between pump and probe in the EAM, and SGM of the probe in the second SOA. An overview of the experiments and modelling is given and potential applications of this switching configuration are discussed in the summary to this chapter. Aspects of the research contained in this chapter are based on the following publications:

[1] "High speed cross-amplitude modulation in concatenated SOA-EAM-SOA," Ciaran S. Cleary, Robert J. Manning, *Optics Express*, vol. 20, pp. 14338-14349 (2012)

[2] "Amplitude and phase dynamics of concatenated SOA-EAM-SOA configuration," Ciaran S. Cleary, Robert J. Manning, *Proc. ECOC (Amsterdam, Netherlands)*, paper P2.04 (2012)

4.1   *Background*

As outlined in Chapter 2, the Turbo-Switch configuration has proven to be a promising candidate for realizing optical signal processing due to the ability of the second SOA (SOA2) to cancel out the slow recovery tail in the gain and phase response of the first SOA (SOA1). However, one fundamental problem associated with the Turbo-Switch is that it is exceedingly difficult to

monolithically integrate the entire system onto a single chip owing to the structure of the tunable BPF, which is an interference filter consisting of multiple thin-film layers of dielectric materials (e.g. TiO_2, SiO_2, Al_2O_3, etc.) deposited on a glass substrate [281, 282]. The problem is compounded by the fact that the steepness of the wavelength pass band in the BPF increases as the number of layers increases, so many layers (>10) are required to achieve narrow bandwidth and sharp roll-off [281]. To successfully integrate an optical switch that operates on the same basic principles as the conventional Turbo-Switch, it is essential to substitute the tunable BPF with an alternative component that blocks the pump while transmitting the full spectrum of the modulated CW probe from SOA1 to SOA2 and is compatible with standard III-V and/or silicon semiconductor device fabrication techniques.

One possible solution to this problem would be to employ an EAM as an absorptive filter between SOA1 and SOA2 to create a concatenated SOA-EAM-SOA (CSES) configuration. A schematic diagram of this modified version of the Turbo-Switch is provided in Fig. 4.1.1.
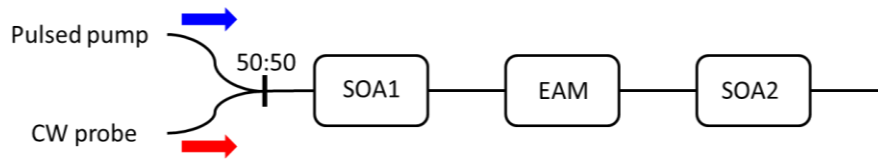
Fig. 4.1.1: Schematic diagram of CSES configuration

When an EAM is employed in the CSES configuration to remove the pump signal while transmitting the modulated CW probe output from SOA1, the pump must be blue-shifted relative to the probe to ensure that there is stronger absorption of the pump compared to the absorption of the probe in the EAM (i.e. to maximize the difference in absorption $\Delta\alpha_{pp}$), as shown in Fig. 4.1.2.
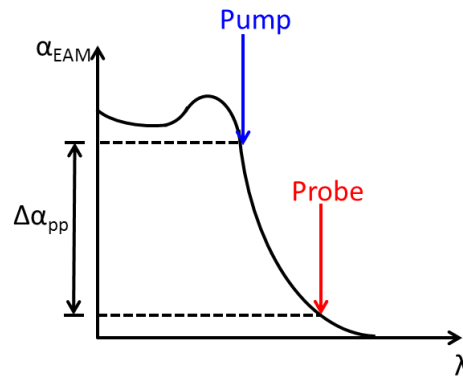
Fig. 4.1.2: Schematic diagram showing the location of the pump and probe wavelengths in the EAM absorption spectrum when the EAM is incorporated into the CSES configuration.

However, one major difference between an EAM and a BPF is that both pump and probe signals are affected by carrier dynamics in an EAM whereas this issue does not arise in a BPF. It was mentioned in Chapter 2 that when a pump pulse is incident upon an EAM, the pump photons are absorbed and generate electron-hole pairs in the intrinsic region. These photo-generated carriers give rise to space-charge screening of the applied electric field and this leads to a drop in absorption due to QCSE and FKE. Thus, any co-propagating probe beam experiences an increase in transmission and this effect is known as XAM.

Furthermore, due to the shallow slope of the absorption spectrum, it is inevitable that there will be a certain amount of absorption of the modulated CW probe output from SOA1 which leads to self-amplitude modulation (SAM) of the probe in the EAM. This effect can be explained by the fact that in the steady-state scenario, dynamic equilibrium is reached in the EAM whereby there is constant rate of carrier generation by the CW probe photons and these carriers are swept out at the same rate from the intrinsic region. When a dark pulse in the modulated CW probe beam output from SOA1 arrives at the EAM, this leads to a drop in carrier generation in the EAM. As a consequence, the effective applied reverse bias increases and the transmission falls due to QCSE and FKE. Additionally, absorption of the CW probe by the EAM leads to reduced SGM of the probe in SOA2.

The effect of XGM between a pump pulse and a CW probe beam in an SOA, and XAM between a pump pulse and a CW probe beam in an EAM are both schematically illustrated in Fig. 4.1.3 to assist in the interpretation of the carrier dynamics of the entire CSES configuration.
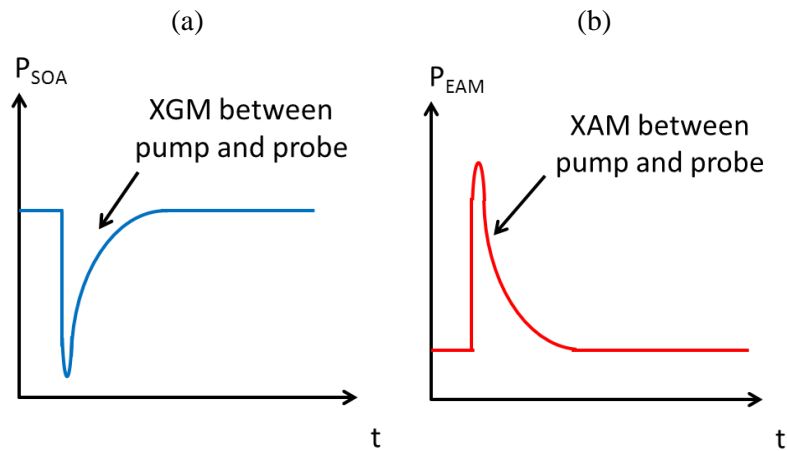
Fig. 4.1.3: (a) XGM between a pump pulse and a CW probe in an SOA and (b) XAM between a pump pulse and a CW probe in an EAM.

The amplitude dynamics of the modulated CW probe as it progresses through the CSES configuration are given in Fig. 4.1.4 to explain the general trends in the experimental data that will be presented later on in this chapter.
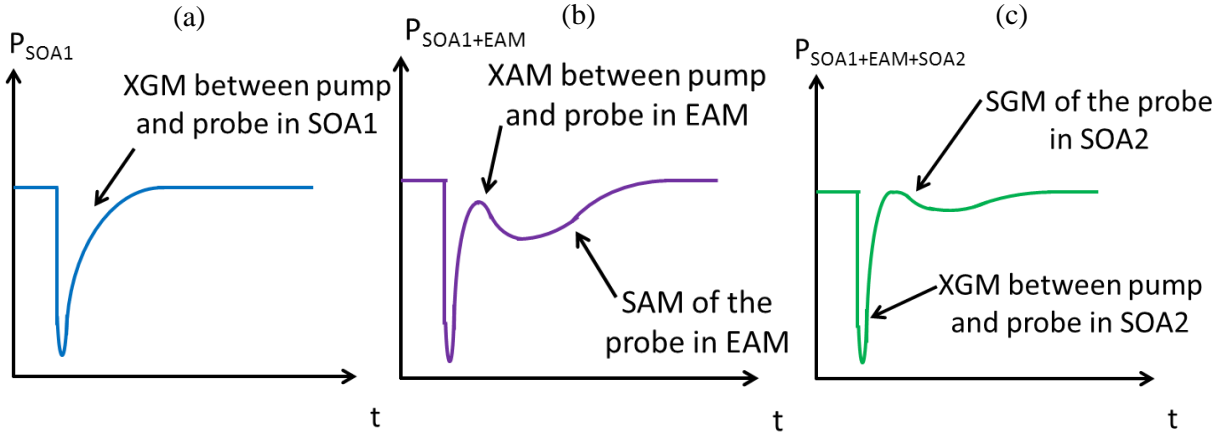
Fig. 4.1.4: Evolution of the probe as it progresses through the CSES configuration. (a) XGM between a pump pulse and CW probe in SOA1, (b) XAM between pump and probe, and SAM of the probe in the EAM, and (c) XGM between pump and probe, and SGM of the probe in SOA2.

It can be seen in Fig. 4.1.4 that XAM between pump and probe in the EAM reduces the response time whereas SAM of the probe in the EAM increases the total response time of both the SOA1+EAM system and SOA1+EAM+SOA2 system (i.e. the entire CSES configuration). Thus, in the context of the CSES configuration, it is desirable to keep absorption of the modulated CW probe in the EAM to an absolute minimum so the probe wavelength should be red-shifted as much as possible and the EAM bias should be minimized.

It was apparent from the outset of this investigation that the CSES configuration would have a major drawback in the form of strong wavelength dependence owing to the nature of the EAM absorption spectrum. Despite this shortcoming, which could limit its potential for certain optical signal processing functions such as wavelength conversion, it is anticipated that the ease of integration of the entire CSES configuration should be a sufficiently strong motivation to employ the configuration for functionalities such as demultiplexing and format conversion.

Previously published research by E. Zhou *et al* involved a single SOA concatenated with an EAM, whereby the opposing absorption response due to XAM between pump and probe in the EAM was exploited to nullify the slow tail in the SOA gain response [130, 136]. Also, research on both single and multiple SOA-EAM pairs for the purpose of 2R regeneration was carried out

by F. Ohman *et al* and T. Vivero *et al*, where the step-like power transfer function of the SOA was exploited to regenerate high intensity bits and the step-like power transfer function of the EAM was utilized to regenerate low intensity bits in an input optical signal [283-285]. However, the studies on SOA-EAM pairs for 2R regeneration did not include time-resolved measurements on XGM, XPM or XAM effects between multiple input optical signals in the SOA-EAM pairs.

In this chapter, the carrier dynamics in the CSES configuration are presented and discussed. The configuration consisted of discrete components rather than components integrated on a single chip. This approach was chosen as it facilitated measurement of the amplitude and phase response of individual components in the CSES as well as the amplitude and phase response of the entire CSES configuration. However, it should be relatively straightforward to monolithically integrate the CSES configuration in the future, as integration of SOAs with EAMs has already been demonstrated for research on mode-locked ring lasers [286], up-down frequency conversion for radio-on-fibre systems [287], modulators for advanced photonic integrated circuits (PICs) [288], modulators for FTTH access networks [289, 290] and 2R regenerators [283-285]. The work described in this chapter is distinct from existing publications in the literature because the intended primary function of the EAM was to act as a low pass filter between SOA1 and SOA2.

4.2   Experimental details

Two commercially available InGaAsP/InP double heterostructure SOAs manufactured by Kamelian Photonics with almost identical properties (with serial numbers 021222 and 021223) were selected to act as the SOAs in the CSES configuration. These SOAs were chosen because they did not display exceptionally fast carrier dynamics on their own. It was decided that SOA 021223 would act as "SOA1" and SOA 021222 would act as "SOA2" when they were incorporated into the CSES configuration.

Both SOAs had a length of 1mm and a confinement factor of 0.4. For SOA 021223, the insertion losses were determined as 2.0dB and 2.3dB for the input and output facets respectively. For SOA 021222, the insertion losses were determined as 3.0dB and 3.9dB for the input and output facets respectively. The small signal chip gain spectra of both SOAs were measured by injecting low power light (-35dBm average power) and measuring the output power over a broad range of wavelengths (see Fig. 4.2.1). The gain ripple in the spectra can be ascribed to residual reflections from the end facets in each SOA.
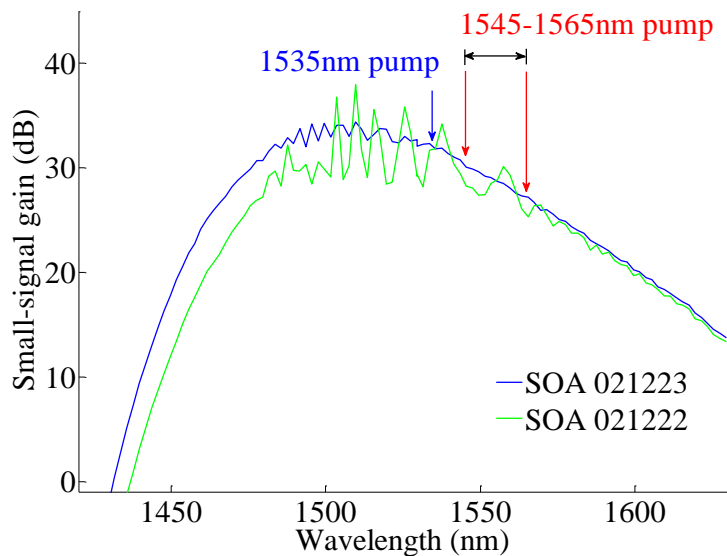
Fig. 4.2.1: Small signal chip gain spectra for SOA 021223 and SOA 021222 (400mA current bias).

The location of the shortest available pump wavelength from the mode-locked laser (1535nm) and the range of possible CW probe wavelengths (1545-1565nm) are marked in Fig. 4.2.1 to help interpret the carrier dynamics of the CSES configuration that will be presented later on in this chapter. It can be deduced from Fig. 4.2.1 that the small signal gain peak was located at 1505nm

for SOA 021223 and at 1510nm for SOA 021222. The 3dB gain bandwidth was approximately 60nm for both SOAs at a current bias of 400mA. The gain saturation curves for both SOAs measured at 1510nm are shown in Fig. 4.2.2.
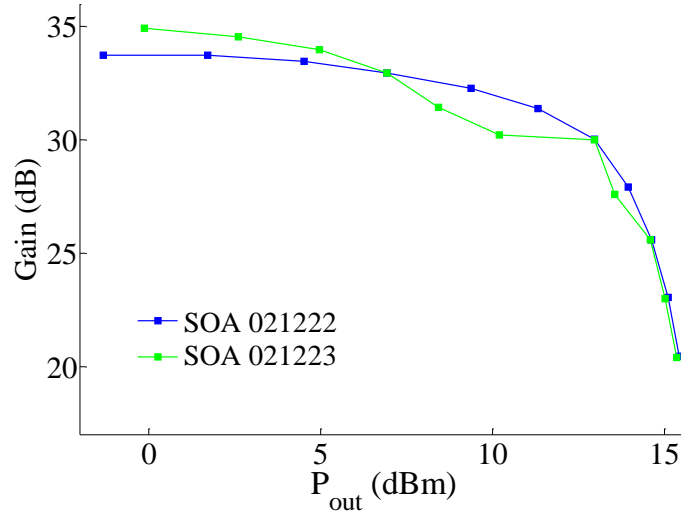
Fig. 4.2.2: Gain saturation curves for (a) SOA 021223 and (b) SOA 021222 at a current bias of 400mA.

It can be inferred from Fig. 4.2.2 that the saturated output power was 12dBm for SOA 021223 and 8dBm for SOA 021222 at a current bias of 400mA. The parameters for SOA 021223 and SOA 021222 are summarized in Table 4.2.1.

	SOA 021223	SOA 021222
Confinement factor	0.4	0.4
Effective length	1.0mm	1.0mm
Input coupling loss	2.0dB	3.0dB
Output coupling loss	2.3dB	3.9dB
3dB bandwidth at 400mA	62nm	60nm (approx.)
Small signal gain peak wavelength	1505nm	1510nm
Small-signal peak gain (current bias 400mA)	34dB	30dB (approx.)
Saturated output power (current bias 400mA)	12dBm	8dBm

Table 4.2.1: Static characteristics of both SOAs employed in the CSES configuration.

Following the static characterization of the SOAs, the static properties of an InGaAsP/InP double heterostructure MQW EAM manufactured by CIP Photonics (serial number 05045) were

measured, with the intention of inserting this EAM into the CSES configuration. The measured input and output coupling losses were 3.1dB and 2.9dB respectively for EAM 05045. The absorption spectra of the EAM with the applied reverse bias voltage varied between 0 to 5V were measured when the CW input power was -10dBm (see Fig. 4.2.3).
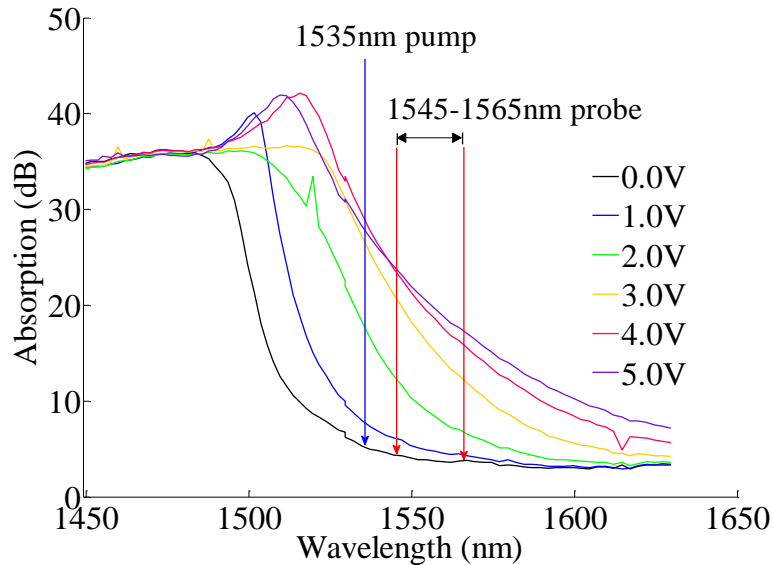
Fig. 4.2.3: Absorption spectra for EAM 05045 with CW input power of -10dBm and the reverse bias voltage varied from 0 to 5V.

Fig. 4.2.3 shows that even though the band edge of the EAM was situated at 1500nm, it was possible to achieve strong absorption of the pump (the shortest pump wavelength available was 1535nm) at a reverse bias ≥2.0V. However, there was also non-negligible absorption of the CW probe at a reverse bias ≥2.0V within the range of wavelengths that could be measured by the time-resolved spectroscopy test-bed. It is believed that the peaks in absorption close to the band edge at reverse bias values of 4.0V and 5.0V were not due to excitonic effects. Instead, we ascribe this feature to the possibility that some stray light from the input fibre did not couple into the waveguide and this stray light destructively interfered with the attenuated light output from the waveguide, leading to a wavelength dependent peak in absorption.

Following static characterization of the SOAs and the EAM, the amplitude and phase dynamics of the entire CSES configuration, as well as those of the individual discrete components comprising the CSES, were measured using the test-bed illustrated schematically in Fig. 4.2.4, where "SOA1" refers to SOA 021223, "EAM" refers to EAM 05045 and "SOA2" refers to SOA 021222. When measurements on individual components in the CSES were carried

out, all other components in the section between the first 50:50 coupler and the first BPF were removed. Pump pulses and a CW probe beam were combined using a 2x1 50:50 coupler before being sent to the device(s) under test (DUT). The 1535nm pump consisted of a 3ps pulse train whose repetition rate was reduced from 10.65GHz to 665MHz using a LiNbO$_3$ modulator. The CW probe wavelength was varied between 1545nm and 1565nm. The mean CW probe power was fixed at -4.3dBm and the energy per pump pulse was fixed at 90fJ at the input of SOA1.

The amplitude evolution was normalized relative to the steady-state amplitude level when no pump pulse was incident on the DUT. The AMZI in Fig. 4.2.4 was not present when amplitude measurements were recorded but it was necessary to insert the AMZI into the test-bed to ascertain the phase evolution. As outlined in Chapter 3, the phase evolution of the DUT was calculated using both the amplitude response and the output waveform from the AMZI [291]. However, unlike the AMZI mentioned in Chapter 3, the AMZI employed in the experiments on the CSES configuration had a time delay of 400ps.
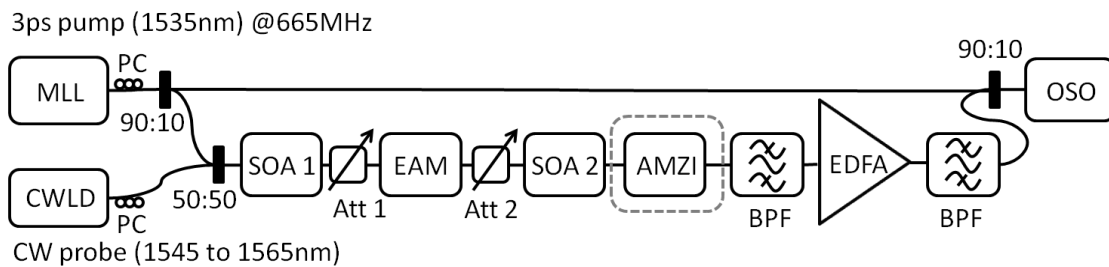
Fig. 4.2.4: Time-resolved spectroscopy test-bed for measuring the amplitude evolution of the CSES and its constituent components (MLL=mode-locked laser, CWLD=CW laser diode, Att=variable optical attenuator,).

The experimentally-measured amplitude and phase dynamics of the SOAs and EAM that constituted the CSES, as well as the dynamics of the complete CSES system, are described in the following section. The overarching term "amplitude dynamics" was chosen to denote the intensity response of the CSES configuration to encompass both the gain dynamics in the SOAs and the absorption dynamics in the EAM.

4.3   Experimental amplitude and phase data

4.3.1   Carrier dynamics in SOA1, SOA1+EAM and SOA1+EAM+SOA2

Preliminary experiments on SOA1+EAM in series

Before a full, rigorous study into the behaviour of the entire CSES was commenced, preliminary measurements on the amplitude dynamics of SOA1+EAM in series were carried out to gain an initial insight into the behaviour of this system. A representative sample of these preliminary measurements is displayed in Fig. 4.3.1.
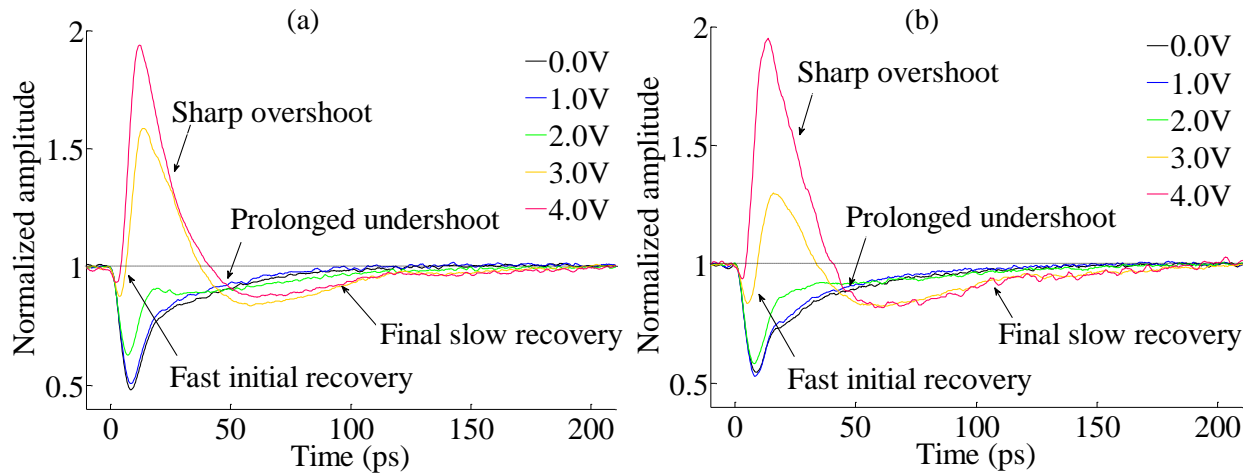
Fig. 4.3.1: Normalized amplitude of SOA1+EAM in series with drive current of 400mA (SOA1) and reverse bias voltage varied from 0 to 4V (EAM). The pump was located at 1535nm, the energy per pump pulse was 20fJ, the average CW input power was -3.3dBm, and the CW was at (a) 1550nm and (b) 1560nm.

It can be seen in Fig. 4.3.1 that when no reverse bias was applied to the EAM, the system had an amplitude evolution typical for the gain recovery of a single SOA i.e. an initial ultrafast component followed by a slow band-filling recovery tail. When the reverse bias on the EAM increased above 1.0V, there were several changes in the amplitude response of the system but the total amplitude recovery remained long (~150ps). When the EAM reverse bias was 2.0V, there was some degree of compensation for the slow tail in the gain response of SOA1. When the EAM reverse bias was ≥3.0V, the amplitude response consisted of a fast initial ultrafast component, followed by a sharp overshoot, a prolonged undershoot below the steady-state level and final slow recovery. XAM between pump and probe in the EAM was responsible for the

overshoot, and SAM of the modulated CW probe inside the EAM was responsible for the undershoot in the amplitude response of the SOA1+EAM configuration.

To prove that SAM of the probe was taking place in the EAM, the amplitude dynamics of the SOA1+BPF+EAM system were measured. The purpose of the BPF was to prevent transmission of the pump to the EAM and thereby to remove the effect of XAM between pump and probe in the EAM. A selection of the amplitude evolutions obtained from these measurements is shown in Fig. 4.3.2 and it can be discerned in these graphs that SAM of the modulated CW probe was taking place within the EAM when a non-zero reverse bias was applied to the EAM.
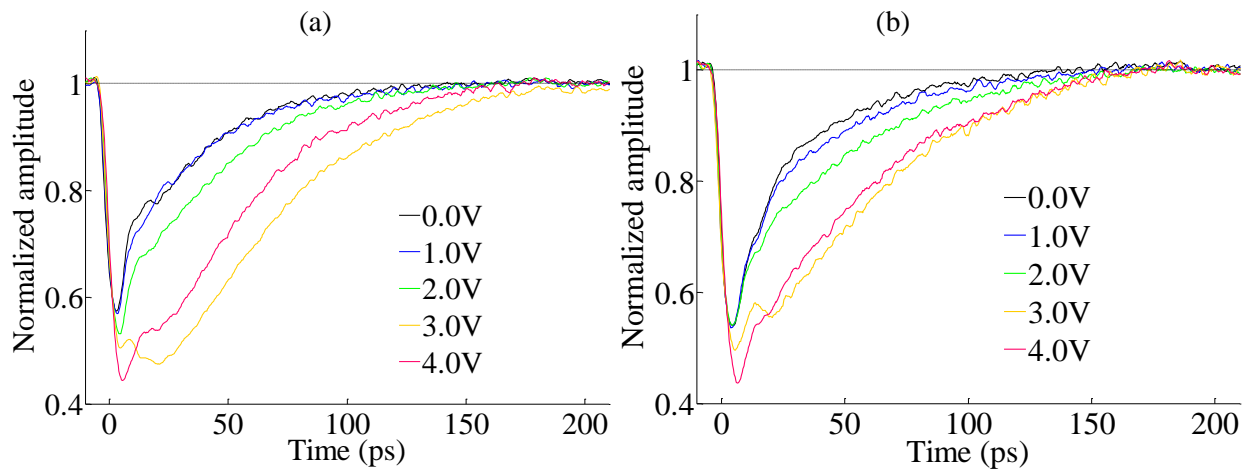
Fig. 4.3.2: Normalized amplitude of SOA1+BPF+EAM in series with drive current of 400mA (SOA1) and reverse bias voltage varied from 0 to 4V (EAM). The pump was at 1535nm, the energy per pump pulse was 20fJ, the average CW input power was -3.3dBm, and the CW was at (a) 1550nm and (b) 1560nm.

Following these preliminary measurements, a systematic study of the behaviour of the CSES and its individual constituent components was undertaken.

SOA1

The normalized gain (or amplitude) and phase evolutions of SOA1 are displayed in Fig. 4.3.3. The subsidiary double peaks that appeared at intervals of 94ps were due to 10.65GHz components in the pump signal that were not completely suppressed by the LiNbO$_3$ modulator. In Fig. 4.3.3(a), the gain recovery time was dependent on the current bias and the 1/e gain recovery time varied from 38 to 74ps. Fig. 4.3.3(b) shows that the phase recovery time was dependent on the current bias and the 1/e phase recovery time varied from 38 to 66ps.
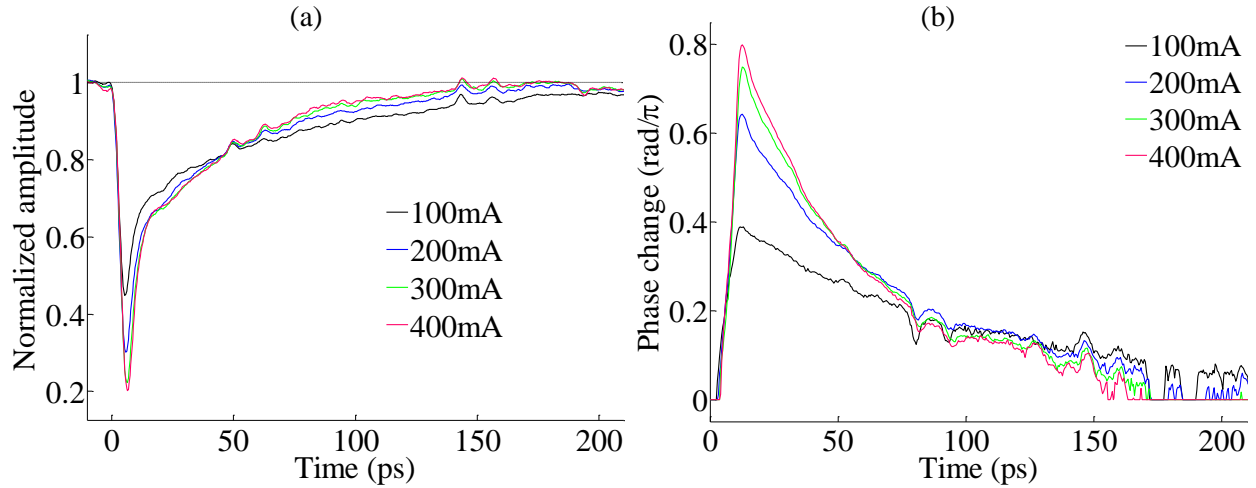
Fig. 4.3.3: (a) Normalized gain and (b) phase evolution for SOA1 with 1565nm probe and with current bias varied from 100 to 400mA.

<u>*EAM*</u>

First of all, the amplitude evolution of the EAM was measured using a moderate probe input power (2.3dBm) and a selection of these results are displayed in Fig. 4.3.4. The phase evolution of the EAM could not be accurately determined as the total phase shift was so low (<0.1π rad) that it was difficult to distinguish the phase evolution from random noise [226].
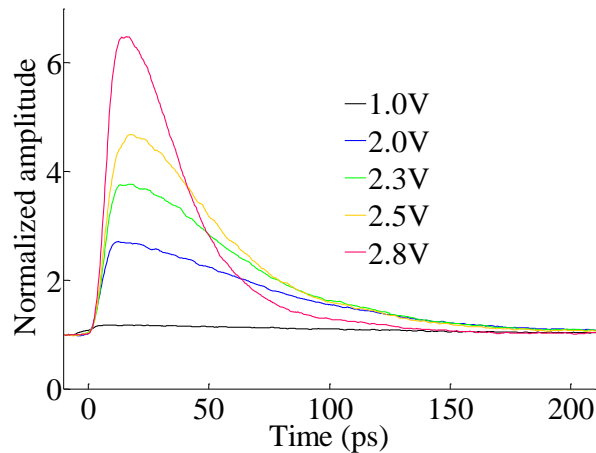
Fig. 4.3.4: Normalized amplitude evolution for EAM with reverse bias varied from 1 to 2.8V, with 1565nm probe, average probe input power of 2.3dBm and energy per pump pulse of 0.8pJ.

Then, the amplitude evolution of the EAM under operating conditions similar to those when it was part of the CSES configuration was measured (see Fig. 4.3.5). For these measurements, the CW probe input power to the EAM was set to 9.5dBm because in the context of the CSES

112

configuration, the output power from SOA1 at the probe wavelength was within the range 8.0 to 11.8dBm when the current bias was varied from 100mA to 400mA.
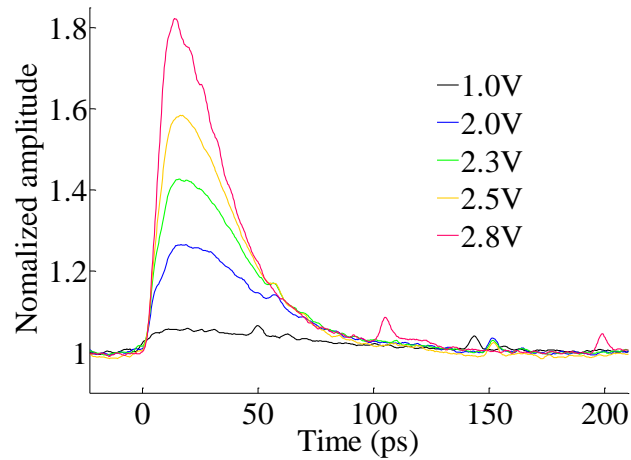
Fig. 4.3.5: Normalized amplitude evolution for EAM with reverse bias varied from 1 to 2.8V, with 1565nm probe, average probe input power of 9.5dBm and energy per pump pulse of 0.6pJ.

By comparing Fig. 4.3.4 and Fig. 4.3.5, it is clear that the maximum change in transmission was reduced and the amplitude recovery time decreased when the CW probe input power increased.

SOA1+EAM

Both the amplitude and phase evolutions of the SOA1+EAM system were measured under various operating conditions and a selection of this data can be found in Fig. 4.3.6 and Fig. 4.3.7.
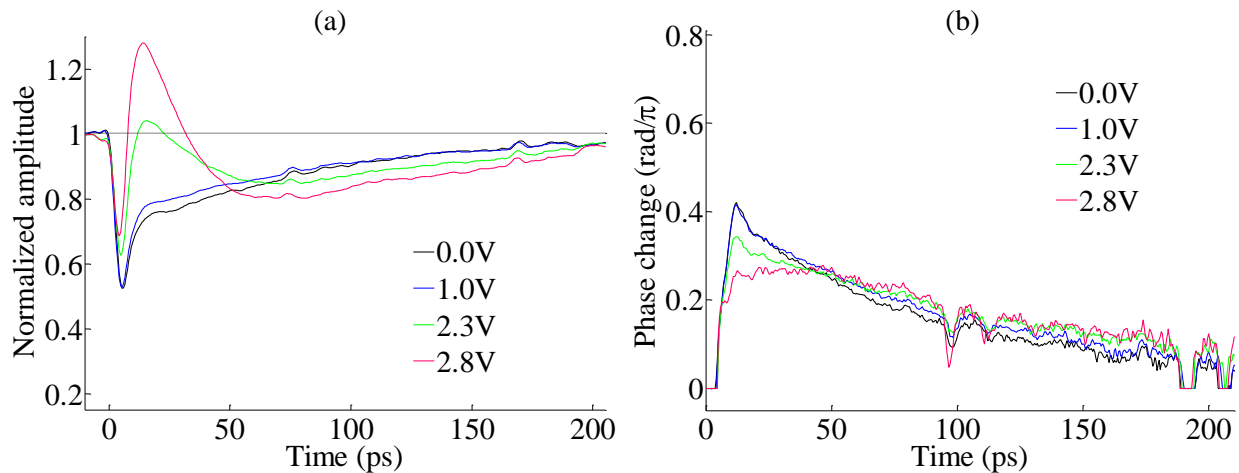
Fig. 4.3.6: (a) Normalized amplitude and (b) phase change for SOA1+EAM with 1565nm probe, drive current of 100mA (SOA1) and reverse bias voltage varied from 0 to 2.8V (EAM).

113
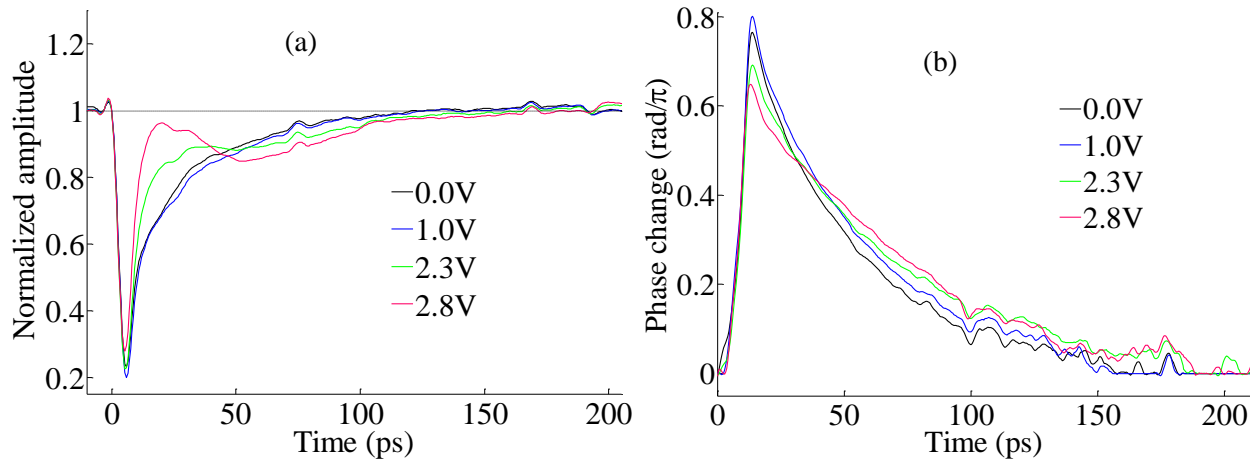
Fig. 4.3.7: (a) Normalized amplitude and (b) phase change for SOA1+EAM with 1565nm probe,

drive current of 400mA (SOA1) and reverse bias voltage varied from 0 to 2.8V (EAM).

Fig. 4.3.6(a) and Fig. 4.3.7(a) show that the amplitude response time of the SOA1+EAM combination decreased as the EAM reverse bias increased to 2.3V. This was due to partial compensation for the slow tail in the gain recovery of SOA1 via XAM between pump and probe in the EAM. However, as the bias increased above 2.3V, following the initial fast recovery, there was a prolonged undershoot ($\geq$50ps) due to SAM of the probe in the EAM, because absorption of the probe in the EAM increased as the reverse bias increased. The undershoot was greater when the current bias on SOA1 was 100mA compared to the undershoot when the current bias on SOA1 was 400mA. This can be explained by the fact that when a higher drive current was applied to SOA1, the average probe power input to the EAM was higher and this led to a reduction in the total change in transmission within the EAM.

In Fig. 4.3.6(b) and Fig. 4.3.7(b), the total phase shift of the SOA1+EAM combination decreased as the EAM bias increased, because the phase change associated with the increase in transmission of the EAM (due to XAM between pump and probe) opposed the phase change associated with the drop in transmission of SOA1. The total phase recovery time increased as the EAM reverse bias increased. This can be ascribed to the long-lived phase change associated with SAM of the modulated probe in the EAM.

Entire CSES configuration (SOA1+EAM+SOA2)

Finally, the amplitude and phase evolutions of the CSES configuration (SOA1+EAM+SOA2) were measured under various operation conditions. In Fig. 4.3.8, the CSES amplitude evolutions

where the current bias on SOA2 was either 100mA or 400mA (while the current bias on SOA1 was fixed at 100mA) are displayed. The scales on the x-axis and y-axis on both graphs in the figure are identical to enable direct comparison between them.
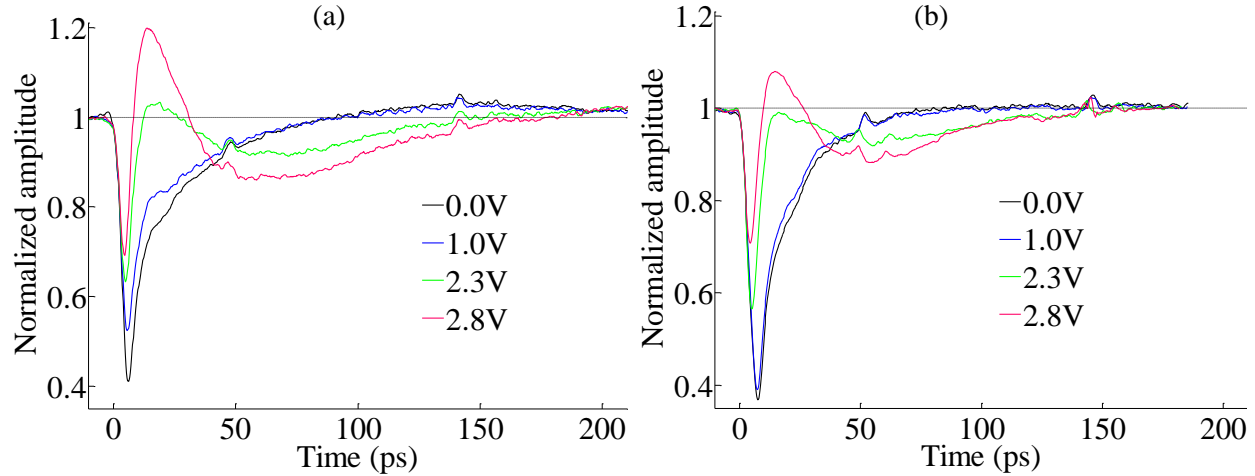
Fig. 4.3.8: Normalized amplitude for CSES configuration with SOA1 current bias of 100mA, EAM reverse bias varied from 0 to 2.8V and SOA2 current bias of (a) 100mA and (b) 400mA.

It can be perceived in Fig. 4.3.8 that an increase in the current bias on SOA2 led to a reduction in the magnitude of both the overshoot and undershoot in the amplitude response of the system. When the 2.3V (red line) curves in Fig. 4.3.8(a) and Fig. 4.3.8(b) are compared, it can be seen that there was greater compensation for the slow tail in the gain response of SOA1.

Both the amplitude and phase evolutions of the CSES configuration when the current bias was 400mA for SOA1 and 100mA for SOA2 are displayed in Fig. 4.3.9.
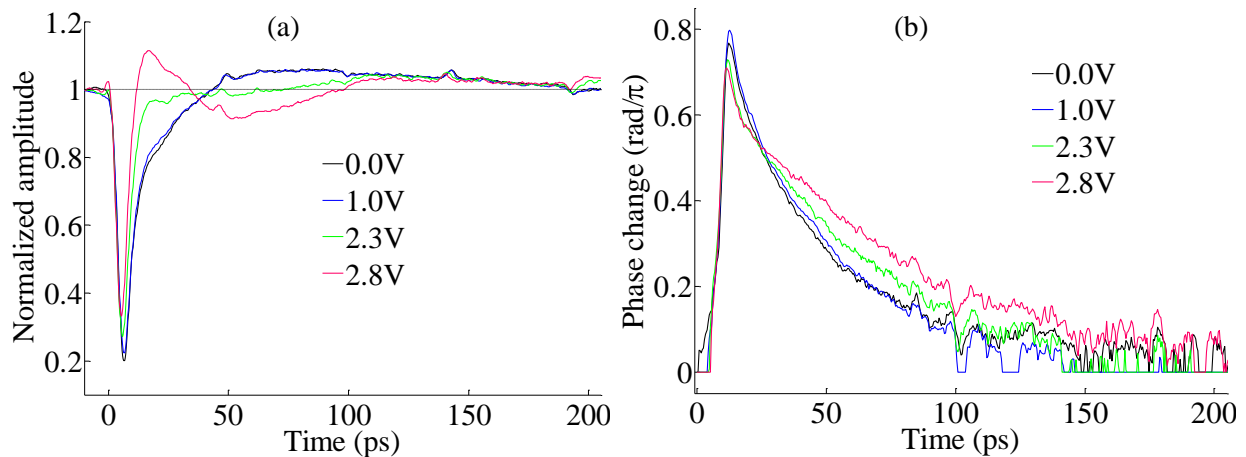
Fig. 4.3.9: (a) Normalized amplitude and (b) phase evolution for CSES configuration with current bias of 400mA (SOA1) and 100mA (SOA2) and EAM reverse bias varied from 0 to 2.8V.

In Fig. 4.3.9(a), the amplitude response time of the CSES decreased as the EAM bias increased from 0 to 2.3V. When the EAM reverse bias increased above 2.3V, there was a prolonged undershoot in the amplitude response due to SAM of the probe in the EAM. In Fig. 4.3.9(b), the total phase shift decreased and the phase recovery time increased as the EAM reverse bias increased, due to SAM of the probe in the EAM and SGM of the probe in SOA2.

Both the amplitude and phase evolutions of the CSES configuration when the current bias was 400mA for SOA1 and 400mA for SOA2 are displayed in Fig. 4.3.10. Fig. 4.3.10(a) shows that the amplitude response time of the CSES decreased as the EAM bias increased from 0 to 2.3V. In fact, a near-ideal amplitude response was obtained at an EAM reverse bias of 2.3V, with a 1/e recovery time of 2.6ps (full recovery time of 10ps) and negligible overshoot. When the EAM bias increased above 2.3V, there was a prolonged undershoot in the amplitude response, which was caused by SAM of the probe in the EAM. In relation to the phase responses in Fig. 4.3.10(b), it was apparent that the total phase shift decreased and the phase recovery time increased as the EAM bias increased, similar to the trend in Fig. 4.3.9(b).
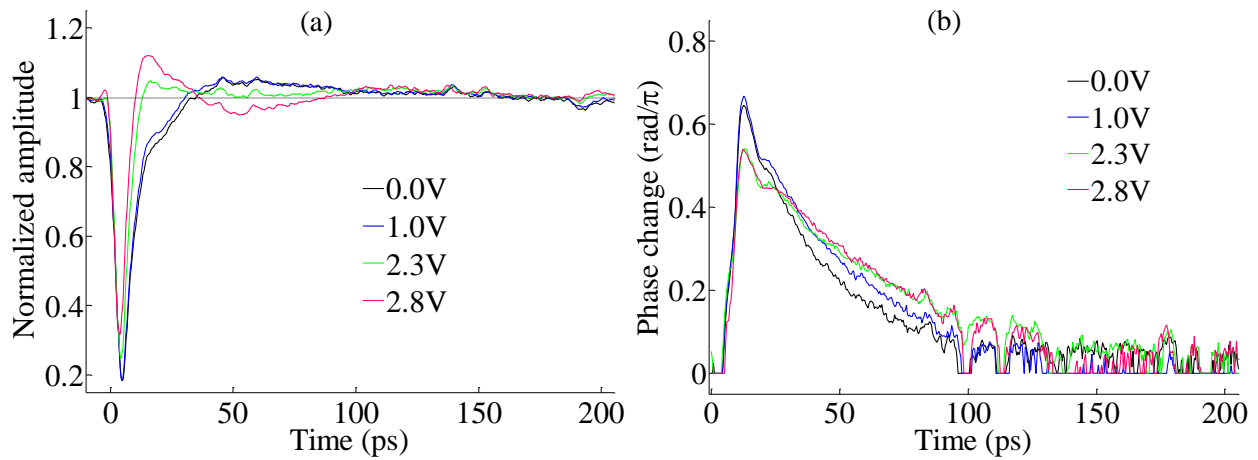
Fig. 4.3.10: (a) Normalized amplitude and (b) phase evolution for CSES configuration with current bias of 400mA (SOA1) and 400mA (SOA2) and EAM reverse bias varied from 0 to 2.8V.

In fact, it was possible to achieve a similarly impressive amplitude response as long as the SOA current bias was moderate ($\geq$300mA for SOA1, $\geq$200mA for SOA2) and the EAM reverse bias was within the range $2.1 \leq V_{EAM} \leq 2.5V$. For instance, Fig. 4.3.11 demonstrates that when there was a current bias of 300mA on SOA1 and 200mA on SOA2 and a reverse bias of 2.2V on the EAM, the amplitude response was dominated by an ultrafast component. However, the full phase response remained comparatively long (~150ps).
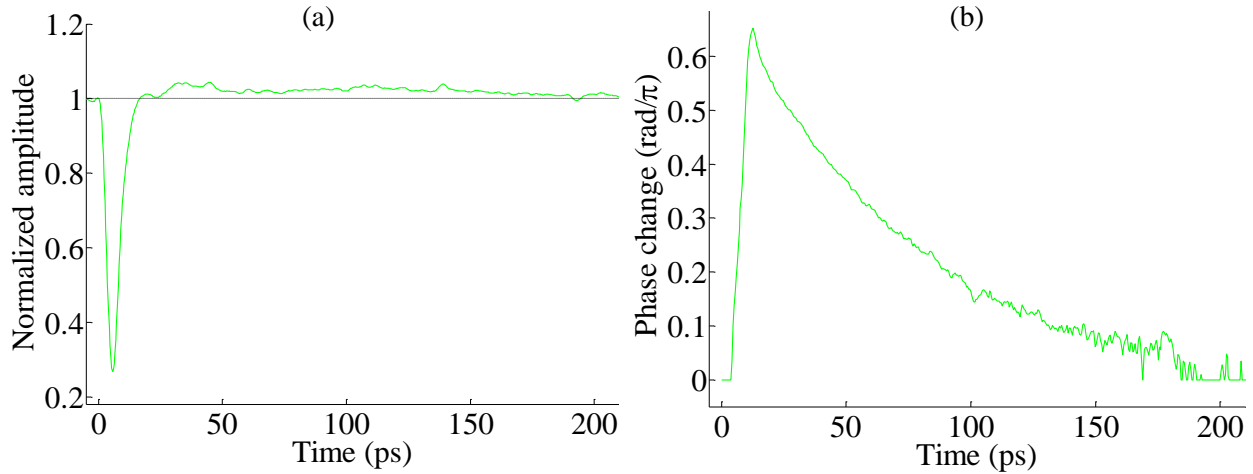
Fig. 4.3.11: (a) Normalized amplitude and (b) phase evolution for CSES configuration with current bias of 300mA (SOA1), 200mA (SOA2) and EAM reverse bias of 2.2V.

4.3.2   Evolution of the probe signal as it propagated through the CSES

Fig. 4.3.12 illustrates the amplitude and phase dynamics after each component in the CSES, where the current bias on both SOAs was 400mA and the EAM reverse bias was 0.0V.
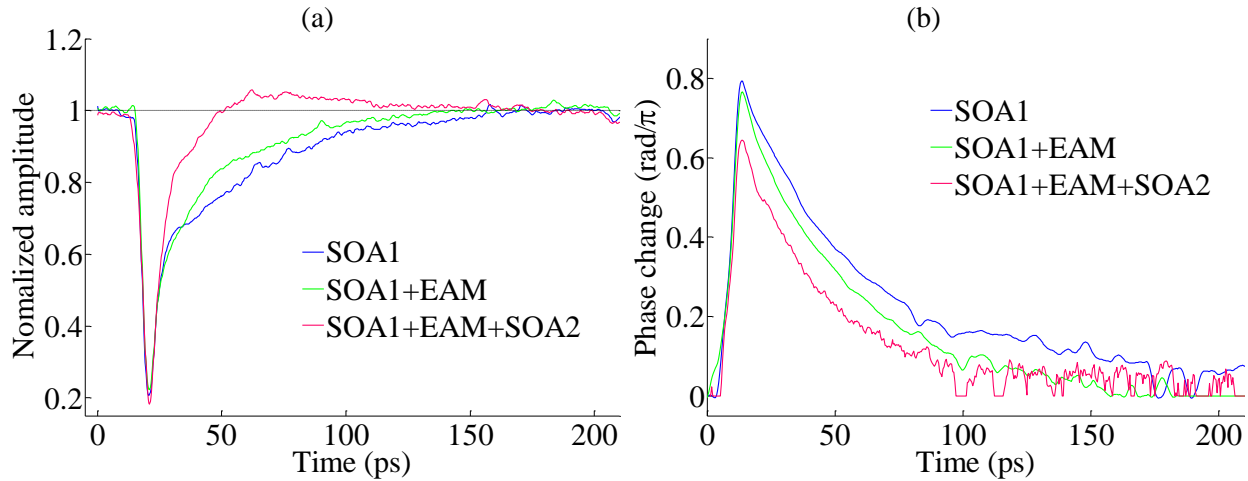
Fig. 4.3.12: (a) Normalized amplitude and (b) phase evolution for 1565nm probe, where the SOA bias currents were 400mA (SOA1), 400mA (SOA2) and the EAM reverse bias was 0.0V.

In Fig. 4.3.12(a), there was practically no XAM between pump and probe or SAM of the probe in the EAM. However, SGM of the probe in SOA2 partially compensated for the slow tail in the gain response of SOA1. Fig. 4.3.12(b) shows there was a slight decrease in the total phase shift and the phase recovery time due to SGM of the probe in SOA2.

117

Fig. 4.3.13 illustrates the amplitude and phase dynamics after each component in the CSES configuration, where the current bias on both SOAs was 400mA and EAM bias was 2.3V.
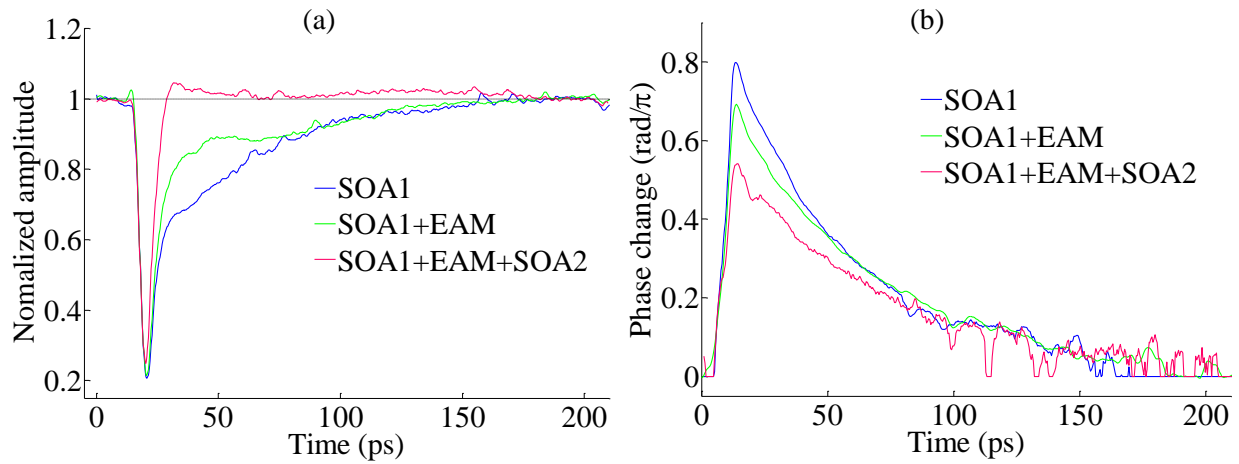
Fig. 4.3.13: (a) Normalized amplitude and (b) phase evolution for 1565nm probe, where the SOA bias currents were 400mA (SOA1), 400mA (SOA2) and the EAM reverse bias was 2.3V.

Fig. 4.3.13(a) demonstrates that the combination of XAM between pump and probe in the EAM and SGM of the probe in SOA2 nullified the slow tail in the gain response of SOA1. Fig. 4.3.13(b) shows that the total phase recovery time remained long but there was a fall in the total phase shift due to XAM between pump and probe in the EAM and SGM of the probe in SOA2.

Fig. 4.3.14 illustrates the amplitude and phase dynamics after each component in the CSES configuration, where the current bias on both SOAs was 400mA and EAM bias was 2.8V.
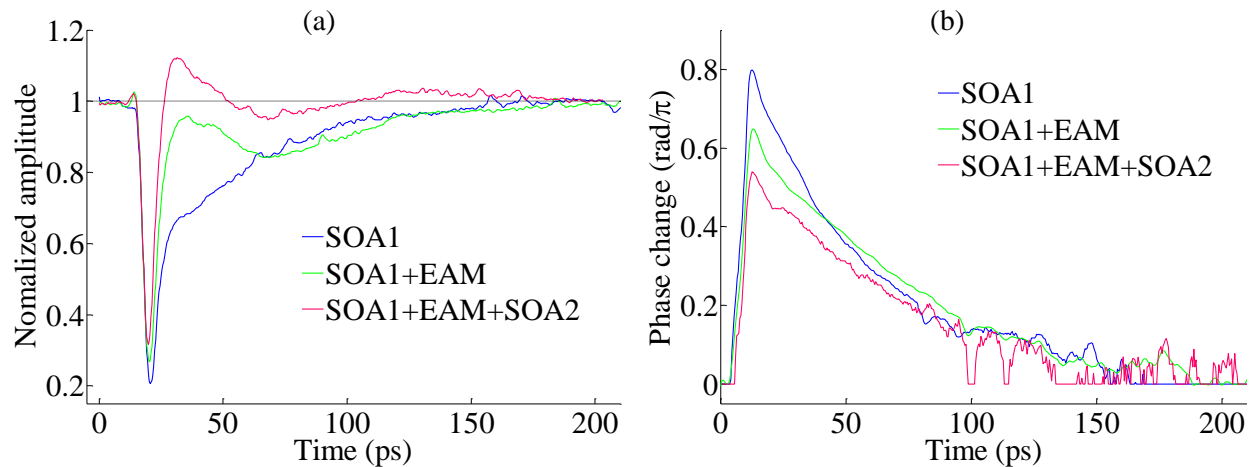
Fig. 4.3.14: (a) Normalized amplitude and (b) phase evolution for 1565nm probe, where the SOA bias currents were 400mA (SOA1), 400mA (SOA2) and the EAM reverse bias was 2.8V.

118

Fig. 4.3.14(a) shows that when the EAM reverse bias was >2.5V, XAM between pump and probe and SAM of the probe in the EAM led to both an overshoot and undershoot in the amplitude response output from both the EAM and SOA2. Fig. 4.3.14(b) shows that the total phase shift decreased as the probe signal progressed through the CSES because the dominant phase changes in the EAM and SOA2 both opposed the phase change in SOA1.

4.3.3   Carrier dynamics in SOA2 when it was incorporated into the CSES

To illustrate the response of SOA2 while it was incorporated into the CSES configuration, a low power (-20dBm) CW signal at 1545nm was input to SOA2, along with the 1535nm pump and the 1565nm modulated CW probe from the SOA1+EAM system. Only the CW signal at 1545nm was transmitted to the OSO and a representative selection of this data is shown in Fig. 4.3.15.
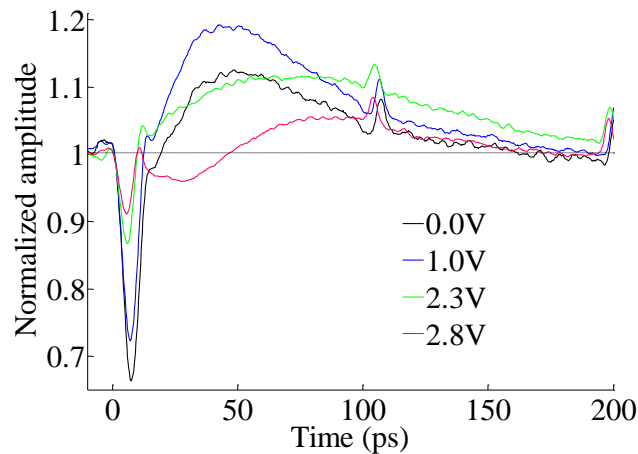
Fig. 4.3.15: Transmission evolution for SOA2 within the CSES, with drive currents of 300mA (SOA1), 300mA (SOA2) and EAM bias varied from 0 to 2.8V.

As shown in Fig. 4.3.15, for all values of EAM reverse bias, SGM of the probe took place in SOA2 but the overall shape of this overshoot changed as the EAM bias was tuned. When the EAM bias was ≤1.0V, the drop in transmission near t=0 implies that a significant amount of XGM between pump and probe took place in SOA2. When the EAM bias was 2.3V, the degree of XGM between pump and probe in SOA2 was relatively low, while there was sufficient SGM of the probe to compensate for the slow tail in the gain response of SOA1. When the EAM bias

increased above 2.3V, there was less XGM between pump and probe in SOA2, but there was also less SGM of the probe in SOA2 due to high attenuation of the probe power by the EAM.

4.3.4   Trends in 10/90 amplitude recovery times for the CSES configuration

To quantify the general trends in the response time of the CSES configuration at various values for the current bias applied to the SOAs and reverse bias voltage applied to the EAM, the 10/90 (10% to 90%) amplitude recovery times for the CSES are plotted as a function of EAM voltage bias at different SOA drive currents are displayed in Fig. 4.3.16. Identical scales are employed in Fig. 4.3.16 to facilitate direct comparison between the two graphs. The lines between points are meant to act as a guide to the eye (i.e. they are not fitted curves).
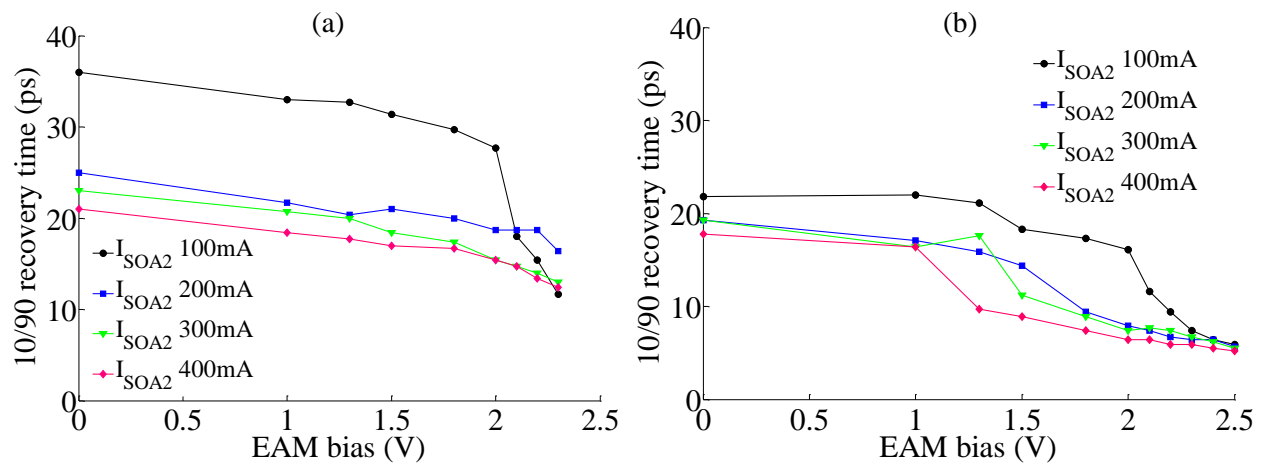
Fig. 4.3.16: 10/90 amplitude recovery times for the CSES as a function of EAM voltage bias with a current bias of (a) 200mA and (b) 400mA on SOA1 (I_{SOA2} refers to the current bias on SOA2).

In Fig. 4.3.16(a), the CSES amplitude recovery time decreased both when the SOA2 current bias increased and when the EAM reverse bias increased. Similar trends can be seen in Fig. 4.3.16(b) but the recovery times are all shorter relative to those in Fig. 4.3.16(a) due to the greater current bias applied to SOA1. The 10/90 recovery times for the CSES when the EAM reverse bias increased beyond 2.3V for Fig. 4.3.16(a) and 2.5V for Fig. 4.3.16(b) are not shown in the graphs. When the EAM bias was greater than these values, although the initial amplitude response was very fast (<10ps), the undershoot in the response following the overshoot resulted in the amplitude dropping below the threshold of 90% full recovery.

4.3.5   Dependence of the CSES amplitude response on signal wavelength

To illustrate the dependence of the temporal response of the CSES configuration on the choice of signal wavelength, the amplitude evolutions for the CSES while the probe wavelength was varied are displayed in Fig. 4.3.17. This figure demonstrates that the CSES amplitude recovery rate improved as the CW wavelength increased. At shorter CW wavelengths, the EAM absorbed more probe power so there was reduced SGM of the probe in SOA2. At longer CW wavelengths, the EAM absorbed less probe power, leading to increased SGM in SOA2.
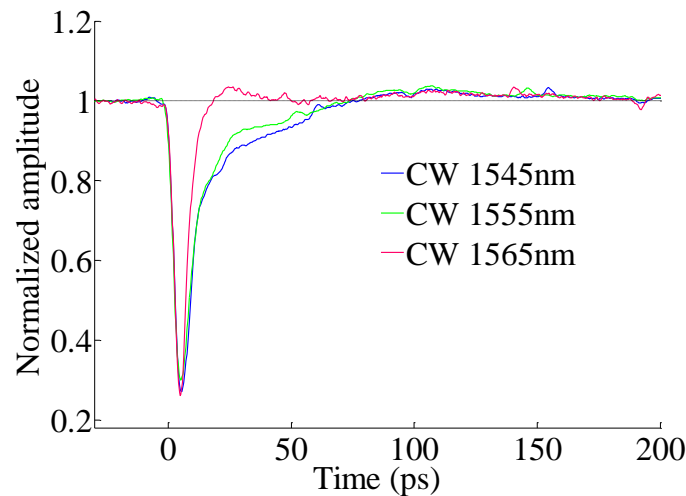
Fig. 4.3.17: Normalized amplitude evolution of the CSES for several different CW wavelengths, with SOA bias currents of 400mA (SOA1), 300mA (SOA2) and a reverse bias of 2.3V applied to the EAM.

4.3.6   Dependence of the CSES amplitude response on signal power

To highlight the dependence of the temporal response of the CSES configuration on signal power, the CSES amplitude evolution for several values of attenuation on Att1 and Att2 are displayed in Fig. 4.3.18. As illustrated in the diagram of the time-resolved spectroscopy test-bed in Fig. 4.2.4, Att1 was a variable attenuator situated between SOA1 and the EAM, and Att2 was a variable attenuator situated between the EAM and SOA2.
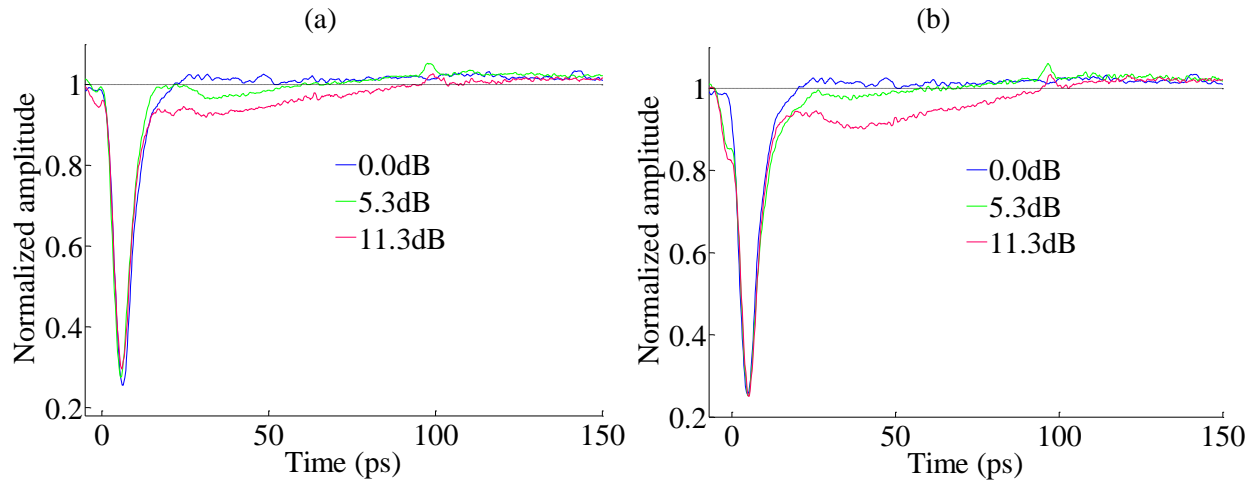
Fig. 4.3.18: Normalized CSES amplitude evolution with (a) various values of attenuation on Att1 and (b) various values of attenuation on Att2, with a 1565nm probe, SOA bias currents of 400mA (SOA1), 300mA (SOA2) and an EAM bias of 2.2V.

Fig. 4.3.18(a) demonstrates that when the attenuation on Att1 increased, this meant that the power of the pump and probe signals input to the EAM decreased so the CSES amplitude recovery time increased. This can be explained by the fact that there was a reduction in the amount of XAM between pump and probe in the EAM and reduced SGM of the probe in SOA2, leading to less compensation for the slow tail in the gain recovery of SOA1. Similarly, Fig. 4.3.18(b) shows that when the input power of the pump and probe signals into SOA2 decreased, the CSES amplitude recovery time increased due to a reduction in SGM of the probe in SOA2.

4.3.7   Comparison between the CSES and the conventional Turbo-Switch

To enable a direct comparison between the CSES configuration and the conventional Turbo-Switch configuration (while using identical SOAs), the EAM was replaced by a BPF with a 3dB bandwidth of 4.0nm and the amplitude and phase dynamics of this SOA1+BPF+SOA2 combination were measured. The amplitude and phase dynamics for this Turbo-Switch at a current bias of 400mA on SOA1 with various values for current bias on SOA2 are displayed in Fig. 4.3.19. The pump wavelength was 1535nm and the CW probe wavelength was 1565nm.
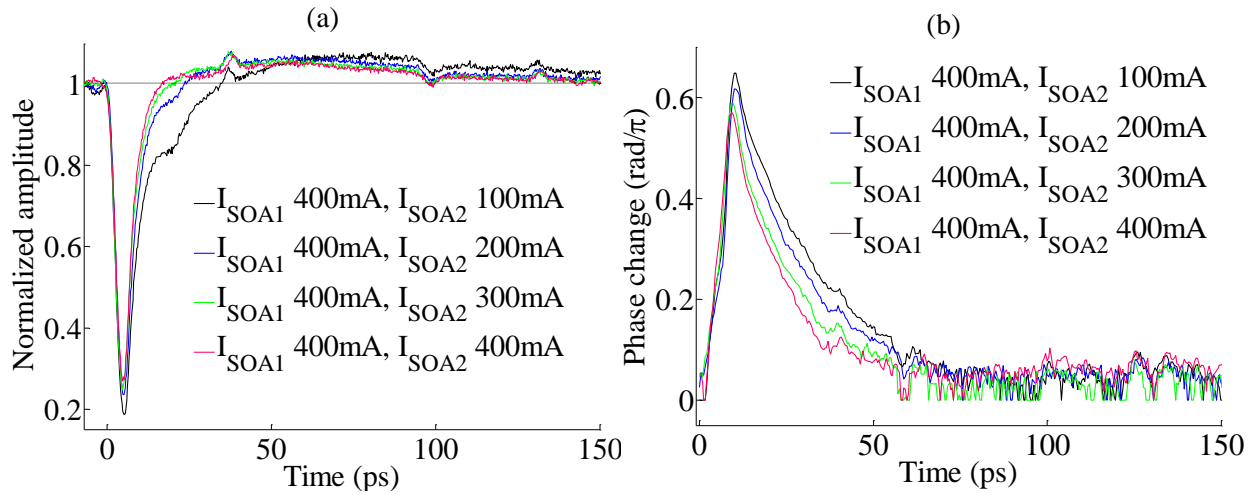
Fig. 4.3.19: (a) Amplitude and (b) phase evolution of Turbo-Switch configuration when the current bias applied to SOA1 was 400mA and the current bias applied to SOA2 was varied.

As shown in Fig. 4.3.19, both the amplitude and phase recovery times in the Turbo-Switch decreased as the current bias applied to SOA2 increased, owing to enhanced SGM of the probe in SOA2 as the current bias increased.

To highlight the contrast between the slow recovery rate of SOA1 and the fast recovery rate of the Turbo-Switch., the amplitude and phase dynamics of the probe signal at the output ports from both SOA1 and SOA2 are illustrated in Fig. 4.3.20.
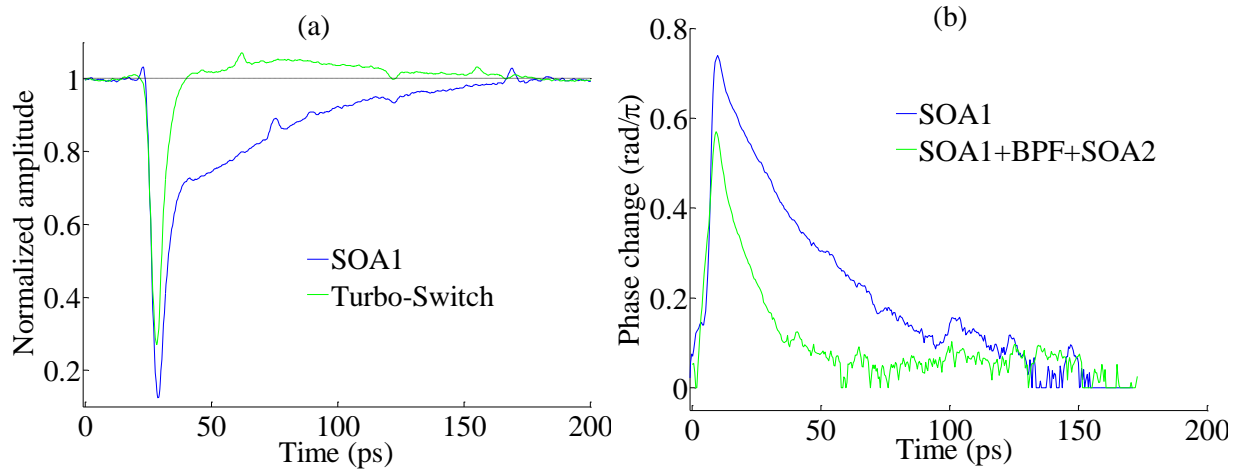
Fig. 4.3.20: (a) Amplitude and (b) phase evolution of SOA1 at a current bias of 400mA and the entire Turbo-Switch configuration at a current bias of 400mA for both SOAs.

It is immediately apparent from Fig. 4.3.20 that the Turbo-Switch configuration led to a dramatic reduction in both the gain and phase response time in the probe signal output from SOA1. The

full gain recovery time for SOA1 at 400mA was 160ps whereas the full amplitude recovery time for the Turbo-Switch was 11ps. Similarly, the full phase recovery time for SOA1 was ~150ps whereas the full phase recovery time for the Turbo-Switch was ~50ps.

Finally, a low power (-20dBm) CW signal at 1545nm was input to SOA2 and the amplitude dynamics of this signal were measured to observe the carrier dynamics in SOA2 while it was within the Turbo-Switch configuration (see Fig. 4.3.21).
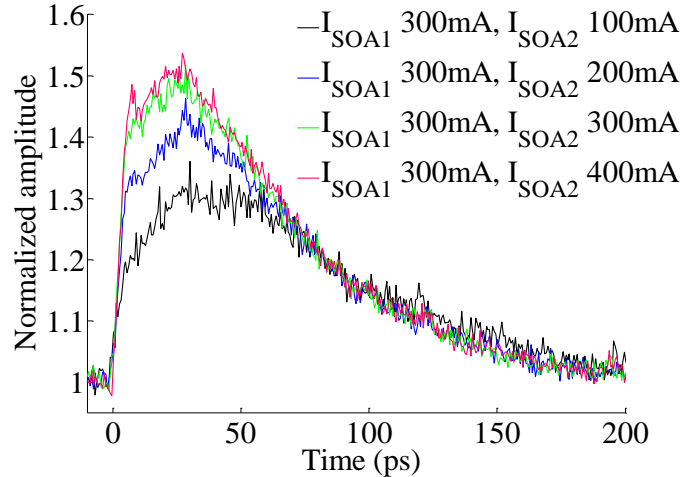
Fig. 4.3.21: Amplitude evolution of SOA2 while part of the Turbo-Switch configuration.

Fig. 4.3.21 shows that the carrier density with SOA2 increased in response to the arrival of the dark pulse in the modulated CW probe signal, demonstrating that there was a significant amount of SGM of the probe (with negligible XGM between pump and probe) in SOA2. This led to efficient compensation for the slow tail in the gain and phase response from SOA1, which accounts for the high speed response of the entire Turbo-Switch configuration [129].

It is instructive to compare the response of SOA2 in the Turbo-Switch configuration in Fig. 4.3.21 with the response of SOA2 in the CSES configuration in Fig. 4.3.15 under the same SOA current bias conditions (300mA applied to each SOA). The magnitude of the SGM component in SOA2 in the CSES configuration was consistently lower than the magnitude of the SGM response in SOA2 in the Turbo-Switch configuration, due to the strong degree of attenuation of the probe power by the EAM in the CSES configuration. This led to less efficient compensation for the slow tail in the amplitude and phase response in the CSES configuration. This problem may be alleviated in an integrated version of the CSES configuration, where the coupling loss between the SOAs and EAM could be significantly reduced.

4.4 Theory and modelling

A simple impulse response model was developed to explain the observed behaviour of the amplitude and phase dynamics of the CSES configuration. This phenomenological approach allowed the strength and lifetimes of various components in the response of the system to be extracted without requiring the use of detailed carrier dynamics equations [105, 292]. Firstly, the gain and phase coefficient impulse response, $g_{coeff,x}(t)$ and $\varphi_{coeff,x}(t)$, of each SOA were modelled using Eq. 4.4.1 and Eq. 4.4.2, where the subscript x refers to either SOA1 or SOA2.

$$g_{coeff,x}(t) = a_{bf,x} \exp\left(\frac{-t}{\tau_{bf,x}}\right) + a_{ch,x} \exp\left(\frac{-t}{\tau_{ch,x}}\right) \tag{4.4.1}$$

$$\varphi_{coeff,x}(t) = \left(\frac{1}{2\pi}\right)\left[\alpha_{bf,x}a_{bf,x} \exp\left(\frac{-t}{\tau_{bf,x}}\right) + \alpha_{ch,x}a_{ch,x} \exp\left(\frac{-t}{\tau_{ch,x}}\right)\right] \tag{4.4.2}$$

In Eq. 4.4.1 and Eq. 4.4.2, t refers to time, the subscripts "bf" and "ch" refer to the carrier recovery processes of band-filling and carrier-heating, $\tau_{bf,x}$ and $\tau_{ch,x}$ refer to the time constants of these recovery processes and the coefficients $a_{bf,x}$ and $a_{ch,x}$ represent the relative significance of the band-filling and carrier heating processes [293]. Likewise, the alpha factors $\alpha_{bf,x}$ and $\alpha_{ch,x}$ are linewidth enhancement factors for band-filling and carrier heating respectively. The fitted time constants for band-filling and carrier heating were $38 \leq \tau_{bf} \leq 65$ps and 1ps respectively for both SOA1 and SOA2 (the band-filling time constants varied with current bias). To reproduce the gain and phase evolutions for each SOA, $g_{coeff,x}(t)$ and $\varphi_{coeff,x}(t)$ were convolved with a modelled sech^2 pump pulse, $y_{pump}(t)$ (see Eq. 4.4.3, Eq. 4.4.4 and Eq. 4.4.5).

$$y_{pump}(t) = A_{pump} \sec h^2\left(\frac{1.7627(t-t_{pump,0})}{\tau_{pump}}\right) \tag{4.4.3}$$

$$g_{conv,x}(t) = y_{pump}(t) * g_{coeff,x}(t) \tag{4.4.4}$$

$$\varphi_{conv,x}(t) = y_{pump}(t) * \varphi_{coeff,x}(t) \tag{4.4.5}$$

In Eq. 4.4.3, A_{pump} determines the magnitude of the modelled pump pulse, $t_{pump,0}$ determines the position in time of the pump pulse relative to the start of the gain coefficient impulse response and τ_{pump} refers to the full width at half maximum (FWHM) of the pump pulse (i.e. 3ps). The convolved gain, $g_{conv,x}(t)$, was converted into a modelled power gain response (Eq. 4.4.6).

$$G_{conv,x}(t) = \exp(g_{conv,x}(t)) \tag{4.4.6}$$

$G_{conv,x}(t)$ was multiplied by a normalized CW input (i.e. unity) to calculate the modelled power gain evolution. The parameters contained in $y_{pump}(t)$, $g_{coeff}(t)$ and $\varphi_{coeff,x}(t)$ were selected to obtain a good fit between the modelled and measured data for both the normalized power gain and phase responses of SOA1 and SOA2. In Fig. 4.4.1, the experimental power gain and phase evolutions of SOA1 are compared with the corresponding modelled evolutions. For the experimentally measured curves, a current bias of 400mA was applied to SOA1 and the average CW power and the pump pulse energy input to the SOA were -4.3dBm and 90fJ respectively.
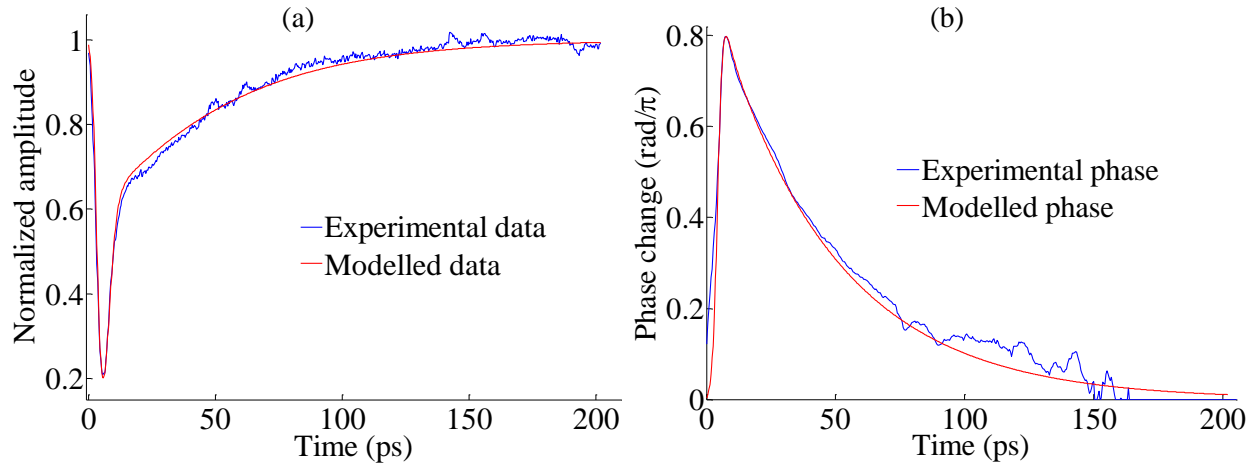
Fig. 4.4.1: Experimentally measured (blue) and modelled (red) data for (a) the normalized gain response and (b) the phase response of SOA1 with a current bias of 400mA.

The various parameters used to fit the gain and phase responses of SOA1 at a current bias of 400mA are given in Table 4.4.1.

$a_{bf,SOA1}$	$\tau_{bf,SOA1}$ (ps)	$a_{ch,SOA1}$	$\tau_{ch,SOA1}$ (ps)	$\alpha_{bf,SOA1}$	$\alpha_{ch,SOA1}$
1.7	38	13.5	1	10.7	0.8

Table 4.4.1: Parameters used to fit the gain and phase responses of SOA1.

After fitting the power gain and phase response of each individual SOA, the output from the SOA1+EAM system was modelled. When an optical pulse is incident on an MQW EAM, electron-hole pairs are generated in the quantum wells. The photo-generated carriers escape from the quantum wells and drift towards the n-type and p-type contacts under the influence of the electric field. The carriers accumulate at the heterojunctions until they are swept out into the contacts. Both carrier escape from the wells and carrier sweepout at the heterojunctions occurs via thermionic emission and tunnelling [161, 162]. The accumulated carriers create a space-charge field which screens the effective electric field within the active region, leading to a blue-shift in the absorption spectrum which persists until the carriers are swept out into the contacts [158].

To model the behaviour of the EAM without using detailed rate equations, it was assumed that the main contribution to the absorption dynamics was from carrier-induced electric field screening [130, 294, 295]. The field screening is proportional to the population of photo-generated carriers in the intrinsic region. Thus, the change in effective applied voltage $\Delta V_{coeff,EAM}(t)$ is proportional to the change in carrier density $\Delta N_{EAM}(t)$ (see Eq. 4.4.7).

$$\Delta V_{coeff,EAM}(t) \propto \Delta N_{EAM}(t) \tag{4.4.7}$$

The impulse response of the EAM voltage change $\Delta V_{coeff,EAM}(t)$ was modelled using Eq. 4.4.8.

$$\Delta V_{coeff,EAM}(t) = -a_v \exp\left(\frac{-t}{\tau_{V,rec}}\right)\left(1 - \exp\left(\frac{-t}{\tau_{V,rise}}\right)\right) \tag{4.4.8}$$

In Eq. 4.4.8, a_v determines the maximum total change in effective reverse bias voltage from the steady-state value, $\tau_{V,rise}$ is the rise time constant, and $\tau_{V,rec}$ is the recovery time constant. The rise time may reflect the fact that it takes a finite amount of time for electrons and holes to escape from the quantum wells and screen the electric field [296]. The recovery time constant reflects the time taken for carriers to be swept out into the contacts. For the fitting procedure, the rise time constant was varied within the range $6 \leq \tau_{V,rise} \leq 12 ps$ and the recovery time constant was

varied within the range $23 \leq \tau_{V,rec} \leq 40$ps (these time constants varied with the applied reverse bias). The fitting parameters used to model the carrier dynamics in the EAM are given in Table 4.4.2.

V_{EAM} (V)	$\tau_{V,rise}$ (ps)	$\tau_{V,rec}$ (ps)	a_V (V)
1.0	6	40	0.7
2.0	8	30	1.5
2.3	9	26	1.9
2.5	11	25	2.3
2.8	12	23	2.7

Table 4.4.2: Parameters used to fit the absorption and phase dynamics in EAM.

The modelled pump pulse, $y_{pump}(t)$, and the modelled probe output from SOA1, $G_{conv,SOA1}(t)$, were both convolved with $\Delta V_{coeff,EAM}(t)$ to account for XAM between pump and probe and SAM of the probe in the EAM respectively (see Eq. 4.4.9 and Eq. 4.4.10).

$$\Delta V_{conv,pump,EAM}(t) = y_{pump}(t) * \Delta V_{coeff,EAM}(t) \tag{4.4.9}$$

$$\Delta V_{conv,probe,EAM}(t) = G_{conv,SOA1}(t) * \Delta V_{coeff,EAM}(t) \tag{4.4.10}$$

These convolutions were summed using a weighting factor $W_{ampl,EAM}$ (which varied from 0.005 to 0.020) to account for the smaller probe absorption compared to pump absorption in the EAM.

$$\Delta V_{sum,EAM}(t) = \Delta V_{conv,pump,EAM}(t) + W_{ampl,EAM} \Delta V_{conv,probe,EAM}(t) \tag{4.4.11}$$

This weighted sum was added to the steady-state reverse bias $V_{initial}$ to calculate the temporal evolution of the effective reverse bias, $V_{EAM}(t)$.

$$V_{EAM}(t) = V_{initial} + \Delta V_{sum,EAM}(t) \tag{4.4.12}$$

In turn, $V_{EAM}(t)$ was used to calculate the EAM transmission evolution $T_{EAM}(t)$ by utilizing a static voltage-dependent transmission function derived from experimental data measured for an input CW signal at a wavelength of 1565nm and input power 9.5dBm (see Fig. 4.4.2).
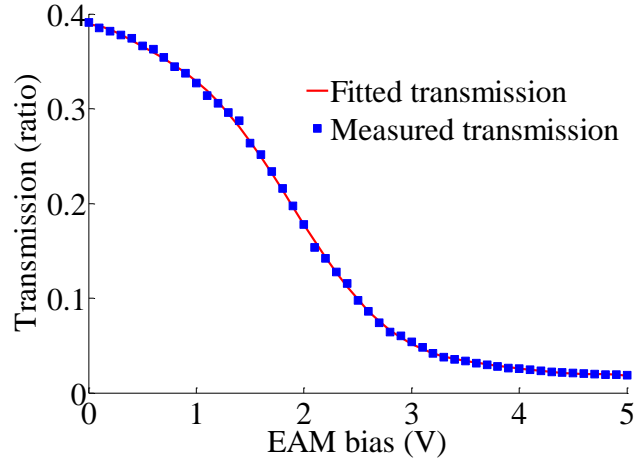
Fig. 4.4.2: EAM transmission as a function of reverse bias at a signal wavelength of 1565nm with measured data (blue dots) and 9th order polynomial fitted curve (red line).

To illustrate the effectiveness of the fitting procedure applied to the carrier dynamics within the EAM, the measured and modelled evolutions for the transmission change in the EAM after the arrival of a pump pulse while a saturating (9.5dBm) CW probe beam is incident on the device at two values for the applied reverse bias are shown in Fig. 4.4.3.
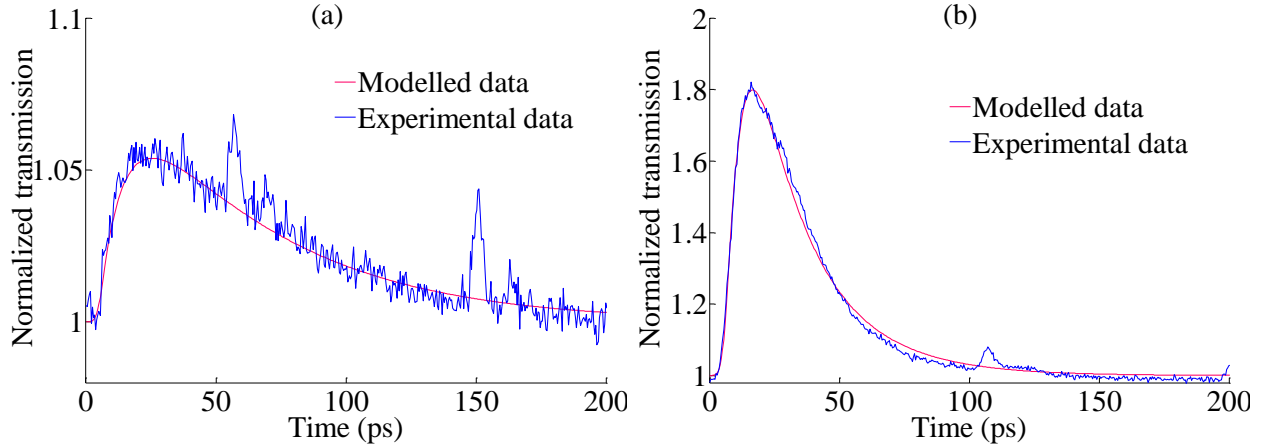
Fig. 4.4.3: Transmission evolution in the EAM at a reverse bias of (a) 1.0V and (b) 2.8V.

In relation to modelling the phase response of the EAM, the phase change was assumed to be directly proportional to the change in effective applied voltage (see Eq. 4.4.13).

$$\varphi_{coeff,EAM}(t) \propto \Delta V_{coeff,EAM}(t) \tag{4.4.13}$$

On the basis of Eq. 4.4.13, the phase change in the EAM $\varphi_{EAM}(t)$ was estimated by multiplying $\Delta V_{sum,EAM}(t)$ by a coupling coefficient, $W_{phase,EAM}$ (approximately 0.7), which is analogous to the alpha factor linking the gain and phase responses in an SOA (see Eq. 4.4.14).

$$\varphi_{EAM}(t) = W_{phase,EAM} \Delta V_{sum,EAM}(t) \qquad (4.4.14)$$

The amplitude evolution of the SOA1+EAM system was calculated by multiplying the input signal at the probe wavelength by the transmission of the EAM (see Eq. 4.4.15).

$$G_{SOA1+EAM}(t) = G_{conv,SOA1}(t)T_{EAM}(t) \qquad (4.4.15)$$

Similarly, the phase evolution for the SOA1+EAM system was calculated by summing the phase change in the SOA and the phase change in the EAM (see Eq. 4.4.16).

$$\varphi_{SOA1+EAM}(t) = \varphi_{SOA,1}(t) + \varphi_{EAM}(t) \qquad (4.4.16)$$

Fig. 4.4.4 shows the modelled EAM input, transmission and output, together with the experimentally measured output from SOA1+EAM at the probe wavelength for an SOA bias current of 400mA at two different EAM reverse bias voltages. The corresponding phase responses of SOA1+EAM are shown in Fig. 4.4.5.
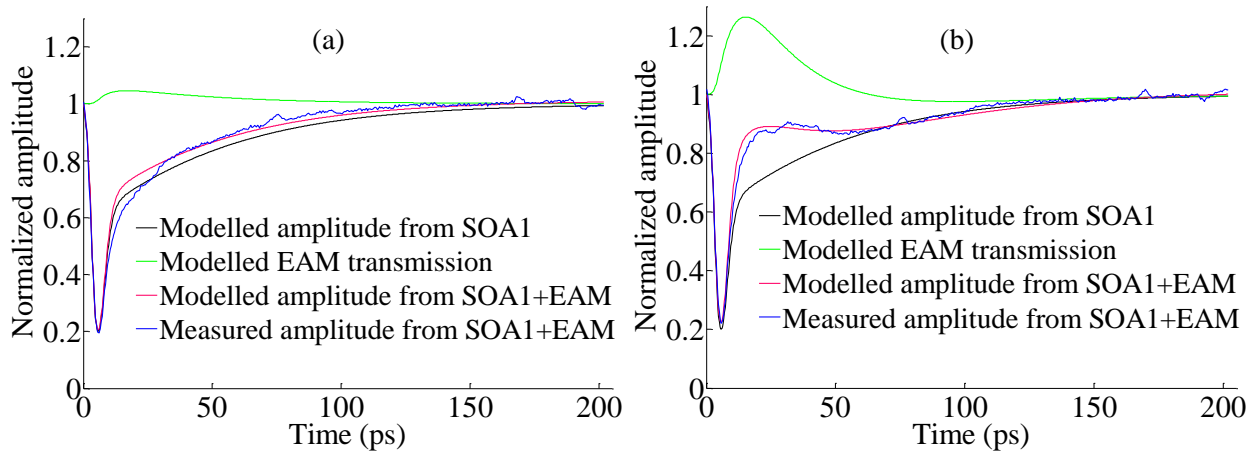
Fig. 4.4.4: Modelled and measured amplitude response of SOA1+EAM with current bias of 400mA applied to SOA1 with (a) 1.0V and (b) 2.5V across EAM.
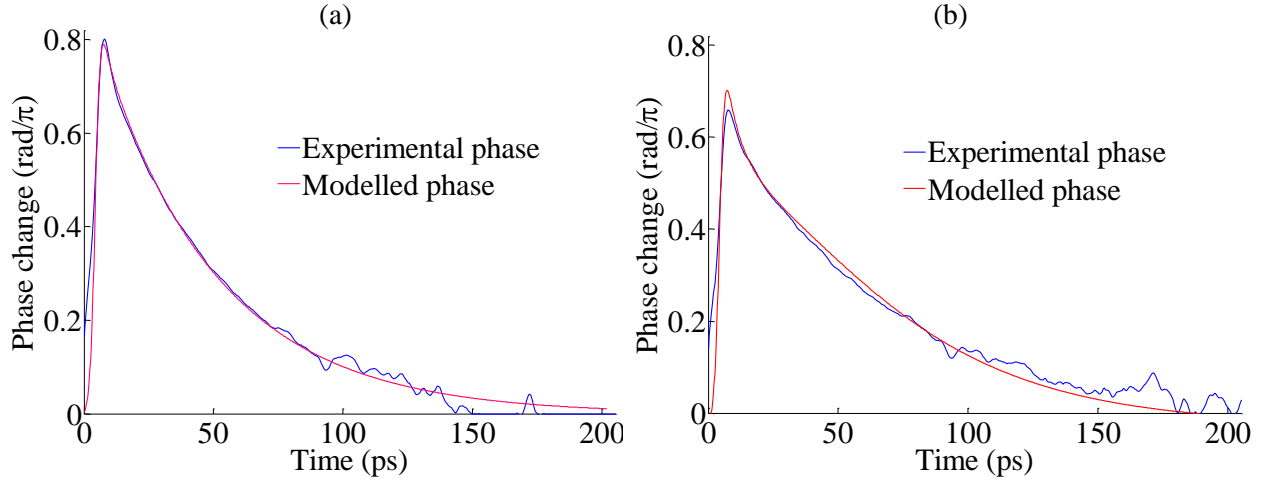
Fig. 4.4.5: Modelled and measured phase response of SOA1+EAM with current bias of 400mA applied to SOA1 with (a) 1.0V and (b) 2.5V across EAM.

Fig. 4.4.4 and Fig. 4.4.5 show that it was possible to attain a reasonably good fit between the measured and modelled evolutions of both the amplitude and phase in the SOA1+EAM system.

Following this procedure, $y_{pump}(t)$ and $G_{SOA1+EAM}(t)$, were both convolved with $g_{coeff,SOA2}(t)$ and $\varphi_{coeff,SOA2}(t)$ to account for both XGM between pump and probe, and SGM of the probe in SOA2 (see Eq. 4.4.17, Eq. 4.4.18, Eq. 4.4.19 and Eq. 4.4.20).

$$g_{conv,pump,SOA2}(t) = y_{pump}(t) * g_{coeff,SOA2}(t) \tag{4.4.17}$$

$$g_{conv,probe,SOA2}(t) = G_{SOA1+EAM}(t) * g_{coeff,SOA2}(t) \tag{4.4.18}$$

$$\varphi_{conv,pump,SOA2}(t) = y_{pump}(t) * \varphi_{coeff,SOA2}(t) \tag{4.4.19}$$

$$\varphi_{conv,probe,SOA2}(t) = G_{SOA1+EAM}(t) * \varphi_{coeff,SOA2}(t) \tag{4.4.20}$$

These convolutions were added together using weighting factors ($W_{ampl,SOA2,pump}$ and $W_{ampl,SOA2,probe}$ for the amplitude, and $W_{phase,SOA2,pump}$ and $W_{phase,SOA2,probe}$ for the phase) to account for the fact that the probe input power was greater than the pump input power into SOA2 (see Eq. 4.4.21 and Eq. 4.4.22). These weighting factors are given in Table 4.4.3.

$$g_{SOA2}(t) = W_{ampl,pump,SOA2} g_{conv,pump,SOA2}(t) + W_{ampl,probe,SOA2} g_{conv,probe,SOA2}(t) \tag{4.4.21}$$

$$\varphi_{SOA2}(t) = W_{phase,pump,SOA2} \varphi_{conv,pump,SOA2}(t) + W_{phase,probe,SOA2} \varphi_{phase,probe,SOA2}(t) \tag{4.4.22}$$

$W_{fac,g1, SOA2}$	$W_{fac,g2, SOA2}$	$W_{fac,ph1, SOA2}$	$W_{fac,ph2, SOA2}$
0.04	0.01	0.01	0.02

Table 4.4.3: Weighting factors utilized to account for the fact that the probe power was greater than the pump power input to SOA2.

The weighted sum of these convolutions was used to calculate the power gain and this was multiplied by the probe input to SOA2 to produce the modelled amplitude evolution $G_{CSES,total}(t)$ (see Eq. 4.4.23). Likewise, the modelled phase evolution (see Eq. 4.4.23) for the CSES configuration was calculated by summing the phase change for the SOA1+EAM system and the phase change in SOA2 (see Eq. 4.4.24).

$$G_{CSES,total}(t) = G_{SOA1+EAM}(t)\exp(g_{SOA2}(t)) \tag{4.4.23}$$

$$\varphi_{CSES,total}(t) = \varphi_{SOA1+EAM}(t) + \varphi_{SOA2}(t) \tag{4.4.24}$$

In Fig. 4.4.6, the modelled SOA2 input, transmission evolution and output, in addition to the measured output from the CSES configuration at the probe wavelength are displayed.
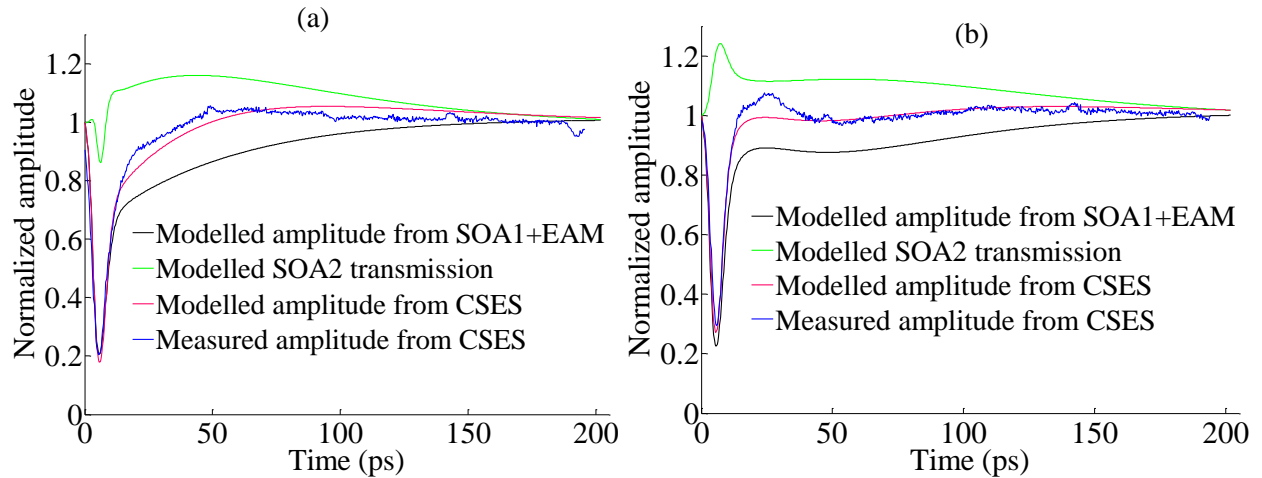
Fig. 4.4.6: Modelled and measured amplitude response of entire CSES with current bias of 400mA on SOA1 and current bias of 300mA, with (a) 1.0 and (b) 2.5V across EAM.

The corresponding phase responses of the CSES configuration at the same EAM bias voltages are shown in Fig. 4.4.7.
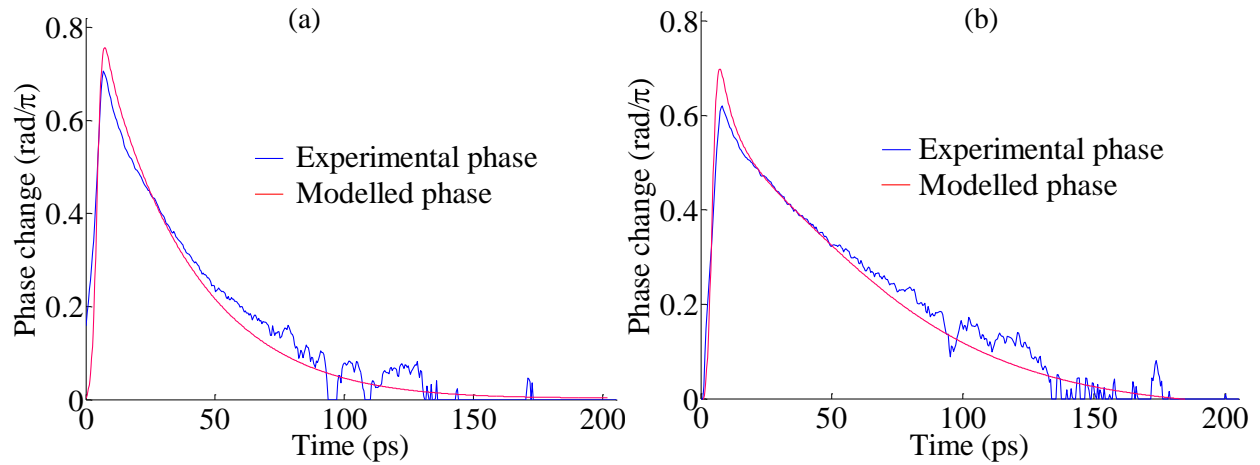
Fig. 4.4.7: Modelled and measured amplitude response of CSES configuration with current bias of 400mA applied to SOA1 with (a) 1.0V and (b) 2.5V across EAM.

In Fig. 4.4.6(a), it can be seen that when the EAM bias was low ($\leq$1.0V), the transmission of SOA2 contained contributions from both XGM between the pump and probe and SGM of the probe in SOA2. In the modelled transmission of SOA2, XGM manifests itself as a drop in transmission near t=0 while SGM manifests itself as a rise in transmission. In Fig. 4.4.6(b), where the EAM bias was higher (>1.0V), the pump was absorbed by the EAM and there was negligible XGM between pump and probe in SOA2. For that reason, the transmission of SOA2 primarily consisted of a component due to SGM of the probe. In Fig. 4.4.7, it can be seen that there was qualitative agreement between the measured and modelled phase response for the CSES. The reasonably good agreement between the modelled and measured data for the amplitude and phase evolutions shows that the impulse response model could account for the principal features in the carrier dynamics of the CSES configuration.

4.5   *Wavelength conversion using the CSES*

To illustrate one potential application of the CSES configuration, the system was employed in a proof-of-principle demonstration of wavelength conversion of an RZ-OOK 2^7-1 pseudo-random bit sequence (PRBS) signal at a bit rate of 10.65Gb.s^{-1}. As the CSES phase response was slower than the amplitude response, the phase was the limiting factor in this experiment. A schematic diagram of the wavelength conversion test-bed is displayed in Fig. 4.5.1.
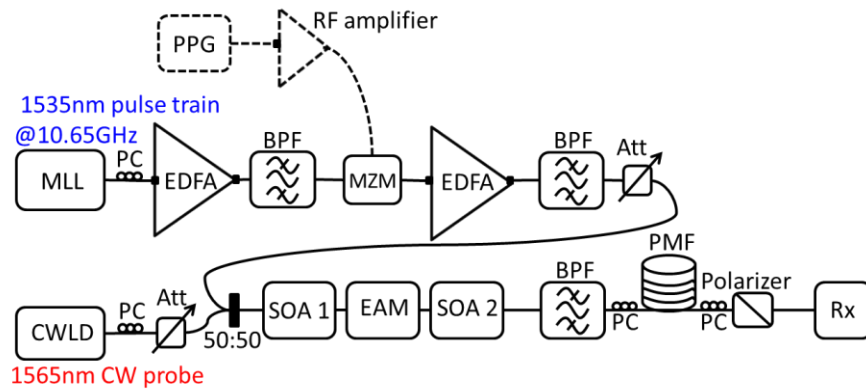
Fig. 4.5.1: Experimental system used to carry out wavelength conversion with the CSES configuration (PPG = pulse pattern generator, Rx = receiver).

As shown in Fig. 4.5.1, a tunable mode-locked laser was used to generate 3ps pulses at 1535nm with a repetition rate of 10.65GHz and the pulse train was amplified using an EDFA before being sent into a LiNbO$_3$ MZM. A 2^7-1 PRBS generated by a pulse pattern generator (PPG) was imprinted onto the pulse train and the resulting RZ-OOK data signal was amplified by an additional EDFA before being combined at a 50:50 coupler with a CW probe beam at 1565nm. Both the original data signal at 1535nm and the CW probe were launched into the CSES, where the CW probe was modulated by the data signal. The original RZ-OOK data signal at 1535nm was filtered out at the output from the CSES, leaving only the modulated CW probe beam which can be viewed as an inverted wavelength-converted (WC) signal at 1565nm.

This inverted data signal was transposed into a non-inverted (i.e. RZ-OOK) data signal by employing an interferometric arrangement based on the delayed interference signal converter (DISC) topology [145, 146]. The interferometer was constructed using two PCs, a segment of polarization maintaining fibre (PMF) wrapped around a piezoelectric cylinder and a polarizer

[41], and the operation principle of the interferometer is as follows. The modulated CW probe entered the segment of PMF, where it was split into two orthogonally polarized components ("fast" and "slow" components) that travelled along the two axes of the PMF. The first PC (at the input to the PMF) was adjusted to ensure that the incoming probe signal was at 45º to the principal axes of the PMF. The "fast" and "slow" components experienced a differential time delay of 5ps while they progressed through the PMF and this led to polarization rotation between the two components when they interfered at the polarizer situated after the second PC (at the output from the PMF) [297]. The interference between the "fast" and "slow" components resulted in suppression of the optical carrier so the output signal from the polarizer was a non-inverted RZ-OOK signal at 1565nm [41].

Finally, the WC RZ-OOK data signal at 1565nm was input to a receiver (Rx) to measure the bit error rate (BER). The structure of the receiver is displayed in Fig. 4.5.2.
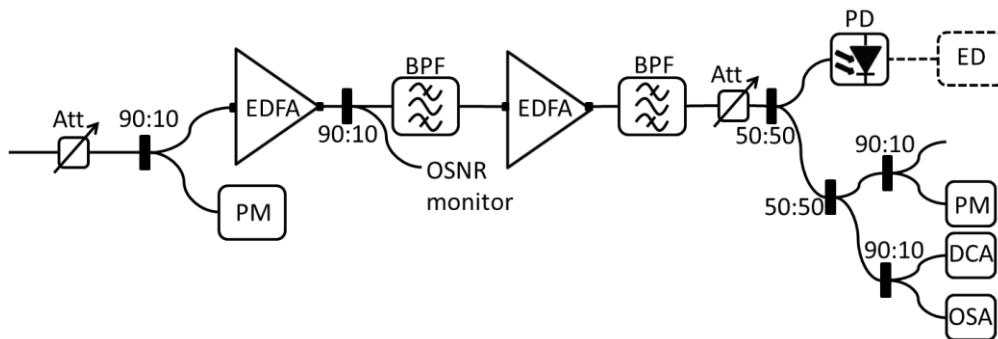
Fig. 4.5.2: Schematic diagram of receiver used for BER measurements (PD=high speed photodiode, ED=error detector, PM=power monitor, DCA=digital communications analyser).

The BER was measured as a function of received power for both the back-to-back (B2B or BtB) signal (at 1535nm) and the WC signal (at 1565nm), and the data is displayed in Fig. 4.5.3. The CW probe power input to the CSES was -3dBm, the energy per pump pulse was 80fJ, the current bias applied to each SOA was 300mA and the reverse bias applied to the EAM was 2.3V. The sensitivity was -36.5dBm for the WC signal, representing a power penalty of 1.5dB compared to the sensitivity for the BtB signal.
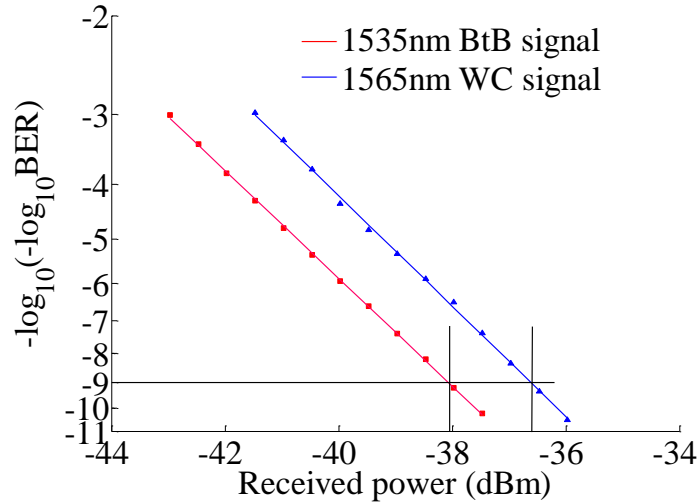
Fig. 4.5.3: Graph of BER vs received power for 1535nm BtB (red dots and fitted line) and WC 1565nm signal (blue dots and fitted line), showing sensitivity of -36.5dBm and a power penalty of 1.5dB.

The inverted signal output from the CSES configuration, as well as the RZ data signal output from the CSES+DISC configuration under the operating conditions outlined in the last paragraph were measured using the OSO. Typical data from these time resolved measurements is displayed in Fig. 4.5.4 and Fig. 4.5.5.
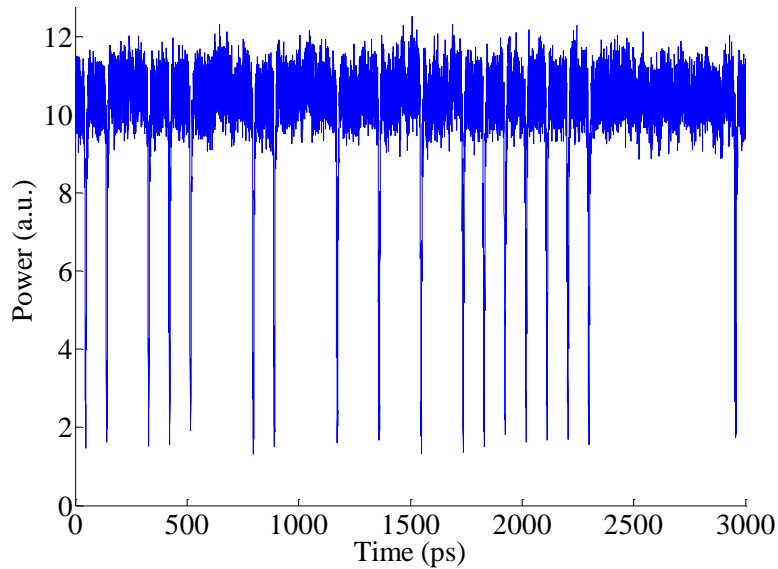
Fig. 4.5.4: WC inverted signal at 1565nm from the CSES configuration.
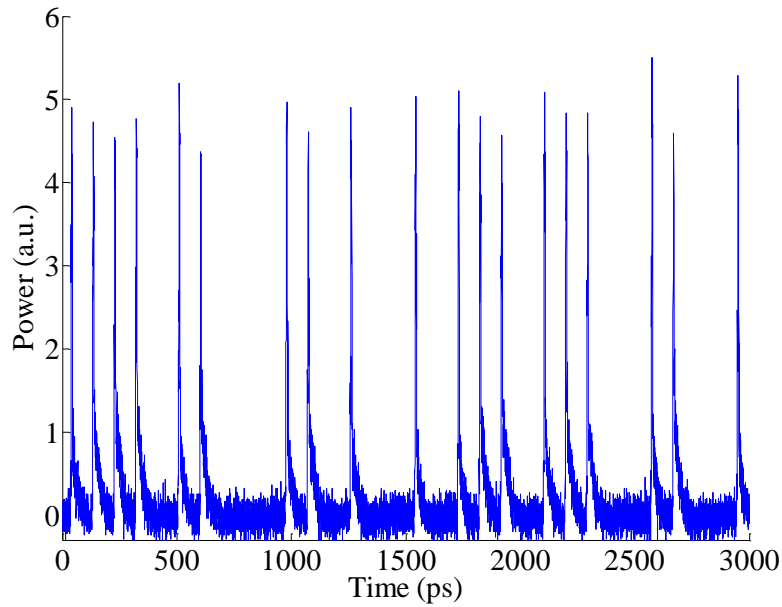
Fig. 4.5.5: WC RZ-OOK signal at 1565nm from the CSES+DISC configuration.

In Fig. 4.5.5, that there was only a small amount of patterning in the inverted output from the CSES configuration. However, as shown in Fig. 4.5.5, there was a slightly greater amount of patterning in the RZ output from the CSES+DISC configuration, which can be ascribed to the fact that the output from the DISC interferometer depends on both the amplitude and phase of the input signal, and the phase response of the CSES configuration was longer than the corresponding amplitude response.

4.6   Summary

The CSES configuration showed full amplitude recovery times as low as 10ps at a modulation depth of 70% under certain operating conditions. The CSES phase response time was consistently much slower than the amplitude response. The carrier dynamics in the CSES were strongly influenced by the choice of signal wavelength, SOA current bias and EAM voltage bias.

Full amplitude recovery within 10ps (1/e recovery time of 2.6ps), consisting predominantly of an ultrafast component without an overshoot was attainable using the CSES configuration when the pump was at the shortest wavelength that could be produced by the mode-locked laser (1535nm), the CW probe was at the longest wavelength that could be detected by the optical sampling oscilloscope (1565nm), the current bias on the SOAs was moderate ($\geq$300mA for SOA1, $\geq$200mA for SOA2) and the EAM bias was within the range $2.1 \leq V_{EAM} \leq 2.5V$. However, the full phase recovery time for the CSES configuration was always ~150ps.

By comparison, for the conventional Turbo-Switch, a high current bias (400mA) had to be applied to both SOA1 and SOA2 to completely neutralize the slow tail in the gain recovery of SOA1. However, the full phase response of the Turbo-Switch (~50ps) was faster than the full phase response of the CSES configuration operating under optimum operation conditions (~150ps). Apart from the speed of the phase response, another disadvantage associated with the CSES configuration was that fine control over the EAM reverse bias was required to optimize the amplitude response whereas this problem does not arise with the Turbo-Switch.

Good qualitative agreement was obtained between the experimental amplitude and phase responses of the CSES configuration and the corresponding responses calculated using an impulse response model. The modelling indicated that the high speed amplitude response of the CSES when the EAM bias was within the range $2.1 \leq V_{EAM} \leq 2.5V$ resulted from a combination of XAM between pump and probe in the EAM and SGM of the probe in SOA2. However, when the EAM reverse bias increased to >2.5V, the amplitude and phase response times increased due to enhanced SAM of the probe in the EAM.

A monolithically integrated version of the CSES operated under optimum operating conditions could be employed as a compact switching device in high speed ($\geq$100Gb.s^{-1}) WDM, OTDM, or hybrid OTDM/WDM networks, as its amplitude recovery time is limited only by ultrafast recovery processes in the SOAs, pump pulse width and modulation depth. It has been

demonstrated that it is possible to integrate SOAs and EAMs on a single chip in the literature [298-301]. To reduce the deleterious effects of SAM of the probe in the EAM, it would be preferable to employ an EAM with a band edge closer to the pump signal. This can be achieved by tailoring the structure of the quantum wells in the active region [302, 303].

Due to the nature of the EAM absorption spectrum, the temporal response of the CSES configuration is inherently dependent on the wavelength of input optical signals. Thus, similarly to the case with the long, highly nonlinear SOA described in Chapter 3, wavelength conversion over a broad range of signal wavelengths would not be feasible using the CSES. However, the CSES configuration could be employed for functions such as demultiplexing, format conversion or packet header processing, where the wavelengths of the input optical signals are fixed at their optimum operation values for the CSES configuration.

Aside from applications in high speed all-optical signal processing, the timescales of the data presented in this chapter indicate that QAM signal generation at 10Gbaud may be possible using the CSES configuration [304]. This means that the CSES configuration could improve upon experiments reported by B. Schrenk et al, where generation of advanced modulation formats has been demonstrated at modest bit rates (1Gb.s^{-1}) using an integrated SOA-REAM chip. For these experiments, the reflective EAM (i.e. REAM) serves as an intensity modulator and the SOA (which operates in the saturation regime) serves as a phase modulator [305]. Also, a full wave cycle can be achieved using the CSES at high values for the EAM bias (>2.5V) and this feature could be exploited to generate ultra wideband signals for radio-over-fibre applications, similarly to the way in which the SOA-EAM configuration and the conventional Turbo-Switch have both been utilized for this purpose in experiments reported in the literature [306-308].

Silicon nanowires embedded in SU8 polymer waveguides

This chapter presents the amplitude and phase dynamics of silicon nanowires (with lengths varying from 3.6 to 14.9mm) embedded in an SU8 polymer waveguide, measured using pump-probe spectroscopy. A phenomenological impulse response model used to fit the experimental data of the carrier dynamics within the silicon nanowires indicated that the free carrier lifetime was between 7.5 to 16.2ns and the TPA coefficient and Kerr coefficient were $3x10^{-12}m.W^{-1}$ and $4x10^{-18}m^2.W^{-1}$ respectively. A summary of the experimental and computational data is provided and suitable applications of these silicon nanowires are discussed. Parts of the research described in this chapter are based on the following publications:

[1] "Dynamic characterization and impulse response modelling of amplitude and phase response of silicon nanowires," <u>Ciaran S. Cleary</u>, Hua Ji, James M. Dailey, Roderick P. Webb, Robert J. Manning, Michael Galili, Palle Jeppesen, Minhao Pu, Kresten Yvind, Leif K. Oxenlowe, IEEE Photonics Journal, vol. 5, pp. 4500111 (2013)

[2] "Two-copy wavelength conversion of an 80Gbit/s serial data signal using cross-phase modulation and detailed Pump-Probe Characterization," H. Ji, <u>C.S. Cleary</u>, J.M. Dailey, J. Wang, H. Hu, R.P. Webb, R.J. Manning, M. Galili, P. Jeppesen, M. Pu, K. Yvind, L.K. Oxenlowe, *Proc. European Conference on Optical Communication (Amsterdam, Netherlands)*, paper We.2.E.3 (2012)

[3] "Dynamic characterization of silicon nanowires using a terahertz optical asymmetric demultiplexer-based pump-probe scheme," H. Ji, <u>C.S. Cleary</u>, J.M. Dailey, R.P. Webb, R.J. Manning, M. Galili, P. Jeppesen, M. Pu, K. Yvind, L.K. Oxenlowe, *Proc. IEEE Photonics Conference (Burlingame, USA)*, paper WQ6 (2012)

5.1 Background

As discussed in Chapter 2 that Si waveguides with submicron cross-section dimensions show tremendous potential for use as optical switches in high speed OTDM communication systems

due to their low linear material loss, high third-order nonlinear coefficient, wide bandwidth and compact size [180]. The high linear refractive index of silicon at telecommunication wavelengths ($n_{Si} \approx 3.5$ at 1550nm) [309] leads to high modal confinement in Si waveguides with sub-micron dimensions manufactured using SOI technology [310]. Furthermore, SOI waveguides can be fabricated using mature CMOS technology, opening up the possibility of monolithic integration of multifunctional electronic and photonic components on a single low-cost chip [76, 311]. The fact that Si waveguides can be fabricated using technology similar to the well-established, cost-effective techniques developed for high volume manufacture of integrated electronic circuits is a significant advantage over alternative NLO materials such as III-V compounds, HNLF and PPLN, all of which are far more expensive and more difficult to integrate.

By contrast with the active device configurations involving III-V compounds described in Chapter 3 and Chapter 4, Si waveguides are generally operated as passive devices i.e. they do not require an applied current bias to function. This feature can be advantageous as it means that Si waveguides do not consume power when there are no input data signals. Unfortunately, it also means that Si waveguides generally do not provide net gain to input data signals (unless Raman amplification is exploited [312]) and the minimum input power for nonlinear effects to become apparent in Si nanowires (>10pJ per pulse) is considerably greater than the corresponding minimum input power required for active devices such as SOAs (<1pJ).

Third order ultrafast effects such as FWM [313], cross-amplitude modulation [77, 179], XPM [314], SPM [170] and SRS [315] in Si waveguides have been studied in depth [310]. The exploitation of these nonlinear effects in Si waveguides has enabled the demonstration of a variety of optical signal processing operations including OTDM demultiplexing, waveform sampling, wavelength conversion, and 2R signal regeneration [241, 256, 316, 317].

However, the efficiencies of nonlinear processes in silicon such as FWM, XPM, SPM and SRS are limited by the nonlinear loss mechanisms of TPA and TPA-induced FCA [180, 196]. Electromagnetic radiation at telecommunication wavelengths has a photon energy (E_{photon}=0.8eV at 1550nm) greater than half the indirect bandgap for silicon ($E_{g,indirect}$=1.08eV) and this stimulates TPA at high pump intensities ($>1 \times 10^{13}$W.m^{-2}). There are two distinct TPA mechanisms, namely degenerate TPA and non-degenerate TPA. Degenerate TPA refers to the simultaneous absorption of two photons with exactly the same wavelength (e.g. two pump photons, both with energy E_p) via a phonon-assisted process i.e. a phonon is absorbed or emitted

to ensure conservation of momentum in the interaction. Non-degenerate TPA refers to the simultaneous absorption of two photons with different wavelengths (e.g. one pump photon with energy E_p and one probe photon with energy E_s) via a phonon-assisted process. The band structure of silicon is shown in Fig. 5.1.1, which illustrates the direct bandgap ($E_{g,direct}$=3.4eV) and the indirect bangap ($E_{g,indirect}$=1.08eV) .
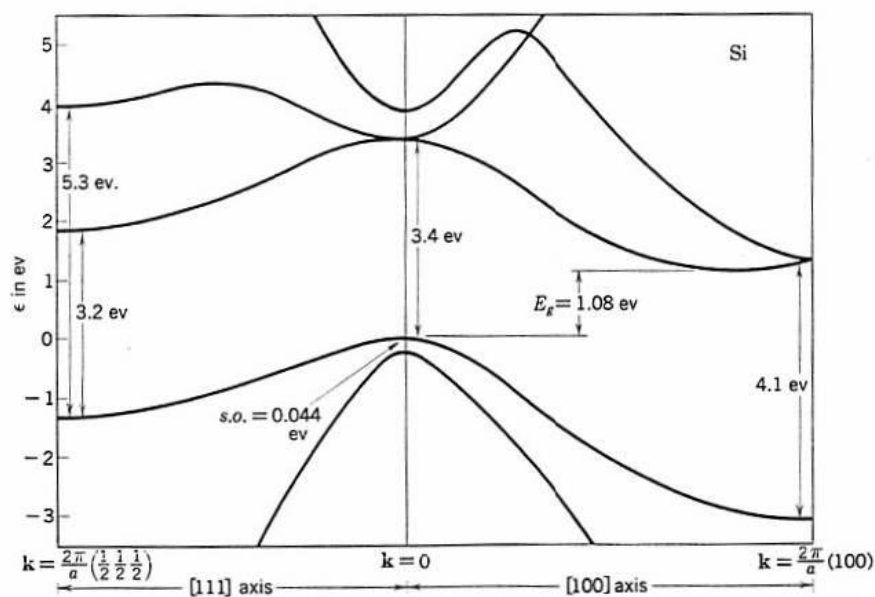
Fig. 5.1.1: Band structure for silicon.

A simplified diagram of degenerate TPA and non-degenerate TPA in silicon are illustrated in Fig. 5.1.2 to explain the difference between these two mechanisms.
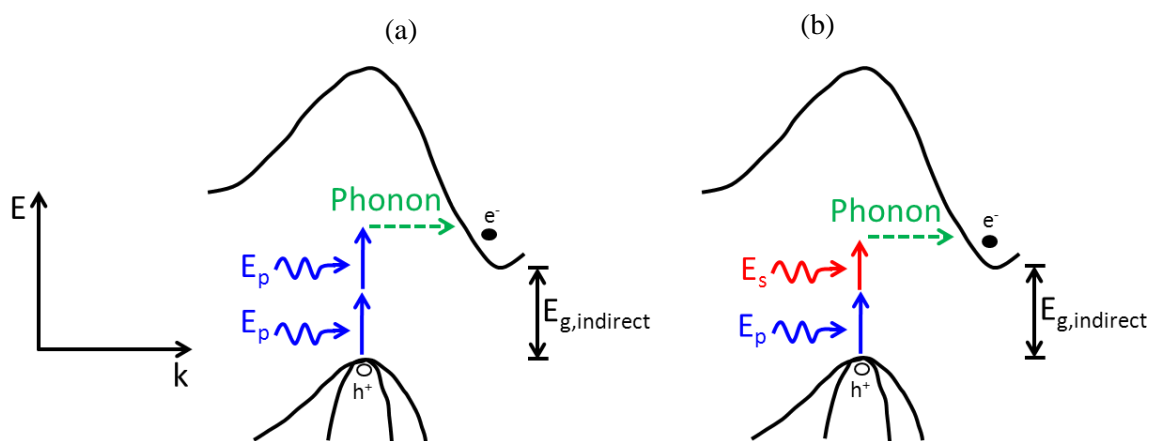
Fig. 5.1.2: Schematic illustration of (a) degenerate TPA of two pump photons and (b) non-degenerate TPA of one pump photon and one probe photon (E_p=pump photon energy, E_s=probe photon energy, $E_{g,indirect}$=indirect bandgap energy for silicon).

As a consequence of TPA, free carriers are generated in the material and these carriers can absorb more photons until they recombine, primarily via surface recombination [179]. In general, the relatively long FCA lifetime limits the switching capability of Si waveguides. For bulk silicon, the free carrier lifetime is several microseconds, but for Si waveguides with submicron cross-section dimensions, the free carrier lifetime can be much lower (several nanoseconds [179]) due to an enhanced surface recombination rate. As outlined in Chapter 2, the free carrier lifetime can be further reduced by material modifications such as helium ion implantation [318], using porous silicon [190] or polysilicon [319], or incorporation of a p-i-n diode structure across the waveguide [180]. Alternatively, TPA in silicon can be circumvented using silicon-organic-hybrid (SOH) technology, where the electric field is confined to a slot waveguide filled with highly nonlinear organic material with a lower TPA coefficient than silicon [176].

Time-resolved pump-probe spectroscopy can be employed to determine the lifetime constants associated with effects such as TPA and FCA. To date, amplitude dynamics in Si waveguides with SiO_2 cladding have been extensively reported in the literature by research groups such as A. Liu *et al*, R. Dekker *et al*, and A.C. Turner-Foster *et al* [77, 179, 180, 193, 320]. Generally, the free carrier lifetime in Si waveguides (without the use of material modifications such as helium implantation, the incorporation of a p-i-n diode or SOH technology) has been estimated to lie within the range 0.5 to 25ns [169, 179, 314, 321, 322]. Both the amplitude and phase dynamics of Si nanowires with SiO_2 cladding have been studied by S. Suda *et al* [182, 183] who estimated a free carrier lifetime of 200ps. They attributed this remarkably short free carrier lifetime to the high degree of sidewall roughness in their devices (illustrated by the fact that the propagation loss was 20dB.cm^{-1}), which led to an enhanced rate of surface recombination. Furthermore, T. Vallaitis *et al* measured the carrier dynamics of SOH waveguides with both strip and slot geometries, and estimated a free carrier lifetime of 1.2ns for the strip waveguides [323].

At first glance, these time-resolved measurements would appear to suggest that the switching capability of un-modified Si waveguides might be limited to bit rates <10Gb.s^{-1}. However, a research group based in the Danish Technical University (DTU Fotonik) have demonstrated a broad range of functionalities using the effect of FWM in Si nanowires embedded in SU8 polymer such as demultiplexing, waveform sampling, serial-to-parallel (OTDM to WDM) format

conversion, and wavelength conversion at extremely high bit rates (up to 1.28Tb.s^{-1}) [63, 227, 228, 324, 325]. These demonstrations were remarkable considering the fact that there were no complicated design features associated with the fabrication of these Si waveguides.

Although the research group in DTU Fotonik had conducted a wide range of systems-level experiments using these Si nanowires embedded in SU8 polymer, they did not have the facilities to accurately measure the temporal response of each device. For that reason, a collaborative project was initiated between the author's research group and DTU Fotonik to investigate the carrier dynamics in the Si nanowires. The original intention was to determine whether or not the generated free carriers affected the FWM efficiency and to find out if the SU8 polymer cladding had any impact upon the carrier dynamics of the devices.

This chapter presents measurements of the amplitude and phase dynamics of these Si nanowires embedded in SU8 polymer using a pump-probe spectroscopy test-bed incorporating a terahertz optical asymmetric demultiplexer (TOAD) interferometric loop. The time-resolved measurements were conducted by the author in collaboration with Hua Ji, a postdoctoral researcher from DTU Fotonik. An impulse response model was employed to extract values for the TPA coefficient β_{tpa}, the Kerr coefficient n_2, the TPA figure of merit (FOM) and the free carrier lifetime τ_{fc}. Furthermore, analysis of the phase change evolution indicated that the wavelength chirp of the probe signal due to XPM between pump and probe had the same order of magnitude on both the red-shifted and blue-shifted sides of the probe wavelength. This served as the basis for realizing two-copy wavelength conversion at a bit rate of 80Gb.s^{-1} between an RZ-OOK pulsed data signal and a CW probe beam by simultaneously extracting the red-shifted and blue-shifted sidebands in the optical spectrum of the modulated CW probe signal output from the Si nanowire. However, the demonstration of two-copy wavelength conversion was conducted by Hua Ji and co-workers in DTU Fotonik, and the author of this thesis was not directly involved in this experimental demonstration. Finally, a summary of the experimental and modelling work on Si nanowires embedded in SU8 polymer concludes the chapter.

5.2   *Experimental details*

The Si nanowires had cross-section dimensions of 450nm x 240nm and total lengths of 3.6mm, 4.9mm or 14.9mm, which included tapered sections at both ends of the nanowires that were 0.3mm long each. The Si nanowires were embedded within a 3.4μm x 3.4μm polymer (SU8-2005) waveguide to decrease the fibre-to-chip coupling loss through better mode-matching with the tapered access fibres [316, 317]. SU8 polymer was chosen as the cladding material as it is more convenient to handle and easier to fabricate compared to SiO_2 while still allowing a low coupling loss to be achieved [326]. However, one drawback associated with SU8 is that it has a lower damage threshold power than SiO_2. The nanowires were operated as passive devices so there was no applied forward current bias or voltage reverse bias. Total insertion losses for the nanowires varied from 5 to 8dB and the propagation loss was determined as 4.5dB.cm^{-1}. A schematic diagram of the device is shown in Fig. 5.2.1, along with scanning electron microscope (SEM) images of a real device.
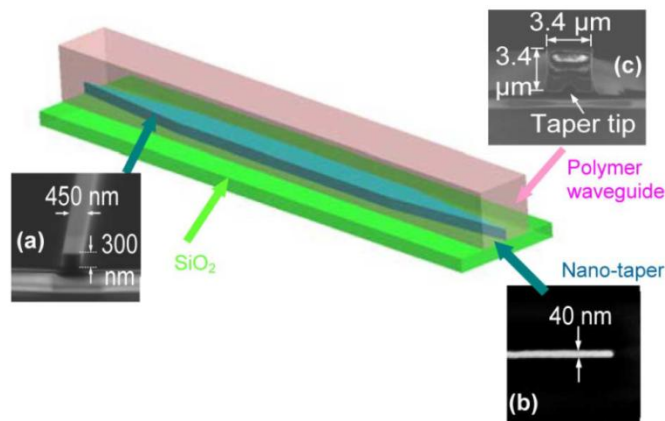
Fig. 5.2.1: Schematic representation of a Si nanowire embedded in SU8 polymer waveguide, along with SEM images of a real device.

An illustration of the TOAD loop test-bed used to measure the carrier dynamics of the Si nanowires is displayed in Fig. 5.2.2. This time-resolved spectroscopy system is a stable, relatively inexpensive configuration which allows real-time evaluation of both the amplitude and phase evolution of any NLO device. For all of these experiments, the 3.5ps pump and 2.5ps probe pulses were clock streams emitted by actively mode-locked lasers, whose repetition rates were reduced from 10.65GHz to 665MHz using $LiNbO_3$ MZMs. The pump and probe

wavelengths were fixed at 1555nm and 1540nm respectively. The pump and probe powers at the Si nanowire input were within the ranges 9dBm$\leq P_{pump}\leq$17dBm and -31dBm$\leq P_{probe}\leq$-27dBm respectively. These pump and probe powers translate into energy per pulse of 12pJ$\leq E_{pump}\leq$75pJ and 1fJ$\leq E_{probe}\leq$3fJ respectively. The polarizations of both the pump and probe pulses were adjusted so that they were aligned with the TE mode of the Si nanowire. A small frequency shift Δf was applied to the radio frequency (RF) drive to the probe laser to allow each probe pulse to scan temporally through the amplitude and phase evolution the Si nanowire in response to a pump pulse.

Fig. 5.2.2: TOAD loop system for measuring amplitude and phase dynamics of a Si nanowire placed inside the interferometric loop (Si wg = silicon waveguide/nanowire).

The operational principle of this test-bed is described in detail by R. Giller [153, 327] and Alan Riordan [328] but it is summarized here. The reflected and transmitted signals from the TOAD loop measured by the "R" and "T" photodiodes (normalized relative to their steady-state levels before the arrival of a pump pulse) can be used to reconstruct both the amplitude and phase responses of the Si nanowire devices with ~1ps temporal resolution. Due to the fact that this measurement system produces the cosine of the phase change, the *absolute value* of the phase response can be measured but the *sign* of the phase excursion cannot be determined directly by the system.

As shown in Fig. 5.2.3, the pulsed probe beam was input to the 50:50 base coupler of the TOAD loop, where the probe pulses were divided into two counter-propagating components, one of which entered the Si nanowire before the other component (the anti-clockwise travelling component arrived at the nanowire first).
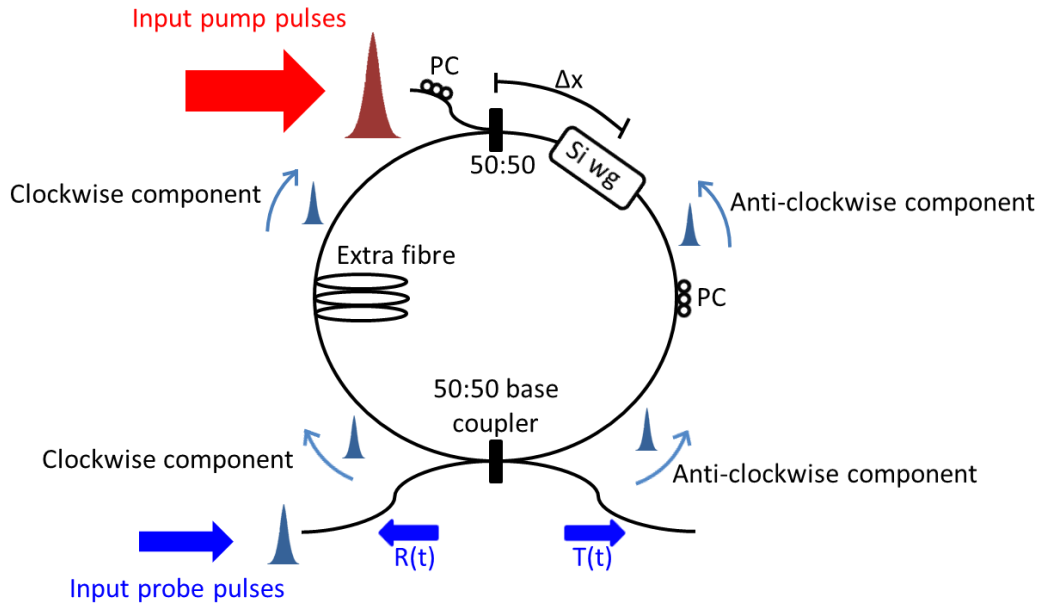
Fig. 5.2.3: Schematic diagram of TOAD loop test-bed.

The polarization of the incoming probe signal was adjusted with a PC before injection into the TOAD loop so that it was aligned with the principal axis of the Si nanowire. The polarization of the TOAD loop was biased for full reflection of the probe in the absence of a pump pulse by suitably adjusting a PC inside the loop. A pump pulse incident on the Si nanowire and timed to arrive after the anti-clockwise component but before the clockwise probe component, resulted in amplitude and phase modulation in the clockwise probe component. Although the carrier density in the Si nanowire did not fully recover before the arrival of the next pump pulse, there were net amplitude and phase differences between the two probe components recombining at the 50:50 base coupler. The constantly changing delay between the pump and probe pulses led to time dependent reflection $R(t)$ and transmission $T(t)$ coefficients for the TOAD loop that were detected on photodiodes and observed in real time on a low-bandwidth (100kHz) electronic oscilloscope triggered at the frequency Δf. The pump and ASE signals leaving the TOAD loop from the 50:50 base coupler were filtered out using broad BPFs, to ensure that only the probe

signal entered the "R", "T" and "PP" photodiodes. The normalized amplitude $G_{norm}(t)$ and phase change $\Delta\varphi(t)$ evolutions of the Si nanowire were derived directly from the R and T coefficients, and the coupling ratio of the TOAD's base coupler $d^2{:}k^2$ using Eq. 5.2.1 and Eq. 5.2.2, where $d^2{\approx}k^2{\approx}0.5$ and θ_0 was an offset term which compensated for the polarizing nature of the device.

$$G_{norm}(t) = \frac{R(t) + T(t) - d^2}{k^2} \qquad (5.2.1)$$

$$\Delta\varphi(t) = \cos^{-1}\left[\frac{R(t) - T(t) + (d^2 - k^2)(d^2 - k^2 G_{norm}(t))}{4d^2 k^2 \cos\theta_0 \sqrt{G_{norm}(t)}}\right] \qquad (5.2.2)$$

The normalized amplitude $G_{norm}(t)$ calculated from Eq. 5.2.1 was compared with the amplitude modulation of the probe traversing the optically excited Si nanowire measured directly after the device by the "PP" photodiode as illustrated in Fig. 5.2.2. This ensured the precision of the amplitude calculations and, by extension, the accuracy of the phase change calculations.

5.3   Experimental amplitude and phase data

5.3.1   Carrier dynamics in Si nanowires with different lengths

The amplitude and phase response dynamics of the 3.6mm long Si nanowire measured using the TOAD loop pump-probe spectroscopy test-bed are shown in Fig. 5.3.1. The amplitude curves shown in Fig. 5.3.1(a) were determined using the power measured by the "PP" photodiode, normalized relative to the power level immediately before the arrival of the pump pulse. The phase evolutions shown in Fig. 5.3.1(b) were calculated using the reflection and transmission coefficients measured by the "R" and "T" photodiodes shown in Fig. 5.2.2.
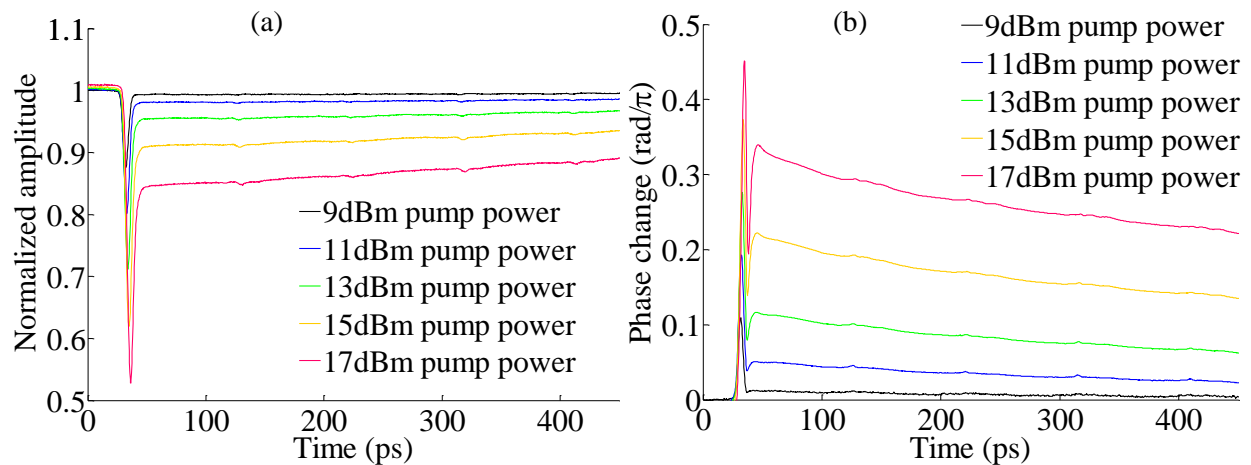
Fig. 5.3.1 (a) Amplitude and (b) phase dynamics of 3.6mm long Si nanowire, with probe input power of -27dBm and pump input power varied from 9dBm to 17dBm at the input to the chip.

In Fig. 5.3.1(a), the amplitude response consisted of an initial ultrafast component followed by a long-lived recovery tail, which were due to TPA and FCA respectively. In Fig. 5.3.1(b), the associated phase response consisted of an initial ultrafast component succeeded by a long-lived component, which were due to the Kerr effect and FCPE respectively. The TPA and Kerr components had sub-picosecond recovery times, whereas the FCA and FCPE components had a recovery time of several nanoseconds. The phase shift due to TPA was positive whereas the phase shift due to FCPE was negative [77, 329, 330], although this is not immediately apparent from Fig. 5.3.1(b) as the TOAD loop test-bed only measured the absolute value of the phase. However, at high pump powers (>11dBm), there was a sharp dip in phase following the TPA component and this marks the point where the phase flipped from positive to negative values.

To confirm that the phase shifts attributed to the Kerr effect and FCPE had the expected opposite signs, a 1555nm pump pulse train at a repetition rate of 665MHz and a 1540nm CW probe were combined at a 50:50 coupler and both signals were input to the 3.6mm long Si nanowire. At the input to the Si nanowire, the average pump power was 15dBm and the average CW probe power was 5.5dBm. A BPF was used to block the pump while transmitting the modulated CW probe after the Si nanowire. The modulated CW probe from the Si nanowire was sent into an AMZI with a 1 bit delay at 10.65GHz (i.e. 94ps) and the signal from one of the output ports of the AMZI was sent into the OSO. The reverse bias applied to the phase shifting element in the AMZI was adjusted such that the steady-state transmission was situated at the midpoint between maximum and minimum transmission, as shown in Fig. 5.3.2. It can be inferred from this figure that the sign of the phase shift associated with the Kerr effect was opposite to the phase shift associated with FCPE. However, this graph does not give the absolute sign of the phase change.
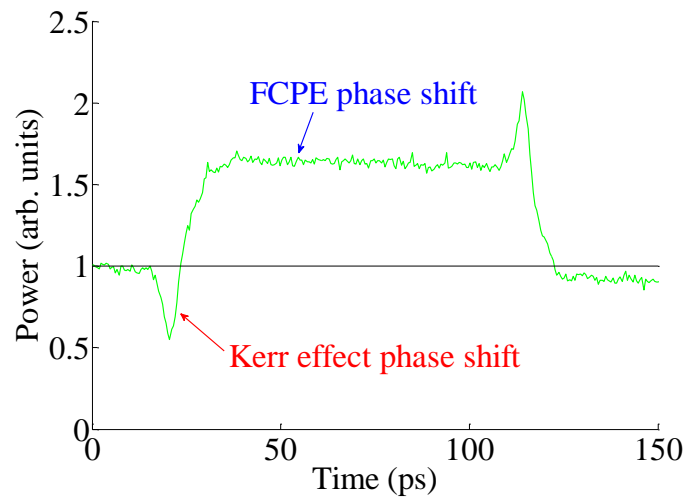
Fig. 5.3.2: Signal output from the AMZI placed after the 3.6mm long Si nanowire with CW probe input power of 5.5dBm and pump power of 15dBm.

Furthermore, the amplitude and phase responses for the 4.9mm long Si nanowire and the 14.9mm long Si nanowire are displayed in Fig. 5.3.3 and Fig. 5.3.4 respectively. The carrier dynamics in the 4.9mm long and 14.9mm long nanowires were quite similar to those for the 3.6mm long Si nanowire. The relatively low modulation depth for the amplitude response in the 4.9mm long Si nanowire may have been due to higher coupling losses in this waveguide compared to the other waveguides. However, Fig. 5.3.4 shows that there was a greater modulation depth and a larger total phase shift in the 14.9mm long Si nanowire compared to the 3.6mm long Si nanowire, which was due to the longer interaction length in the former.
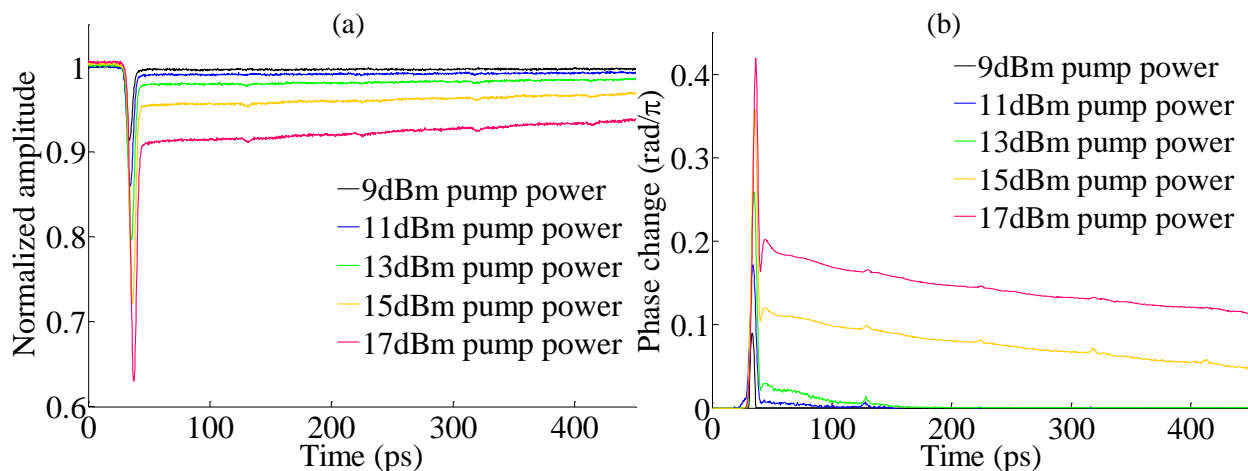
Fig. 5.3.3: (a) Amplitude and (b) phase dynamics of 4.9mm long Si nanowire, with probe input power of -27dBm and pump input power varied from 9dBm to 17dBm at the input to the chip.
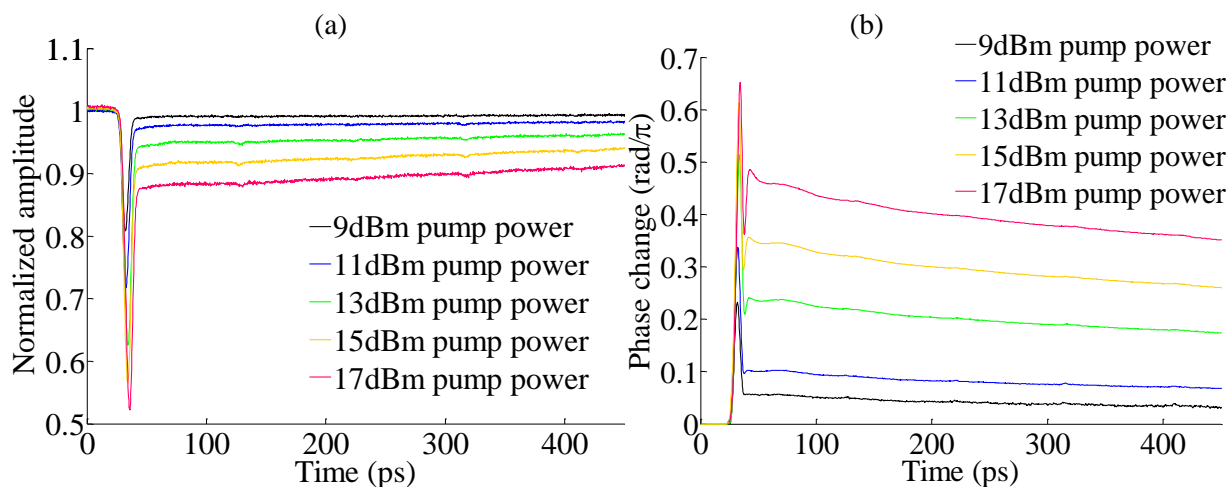
Fig. 5.3.4: (a) Amplitude and (b) phase dynamics of 14.9mm long Si nanowire, with probe input power of -27dBm and pump input power varied from 9dBm to 17dBm at the input to the chip.

5.3.2   *Time delay between minimum amplitude and maximum phase shift*

It is important to note that the individual curves in Fig. 5.3.1, Fig. 5.3.3 and Fig. 5.3.4 have been aligned so that the rising edge of each curve started at the same point in time, so as to facilitate direct comparison of the magnitude of each response. However, in reality, the point of maximum phase change and minimum amplitude in each curve shifted in time as a function of pump power, as demonstrated in the un-aligned data shown in Fig. 5.3.5.
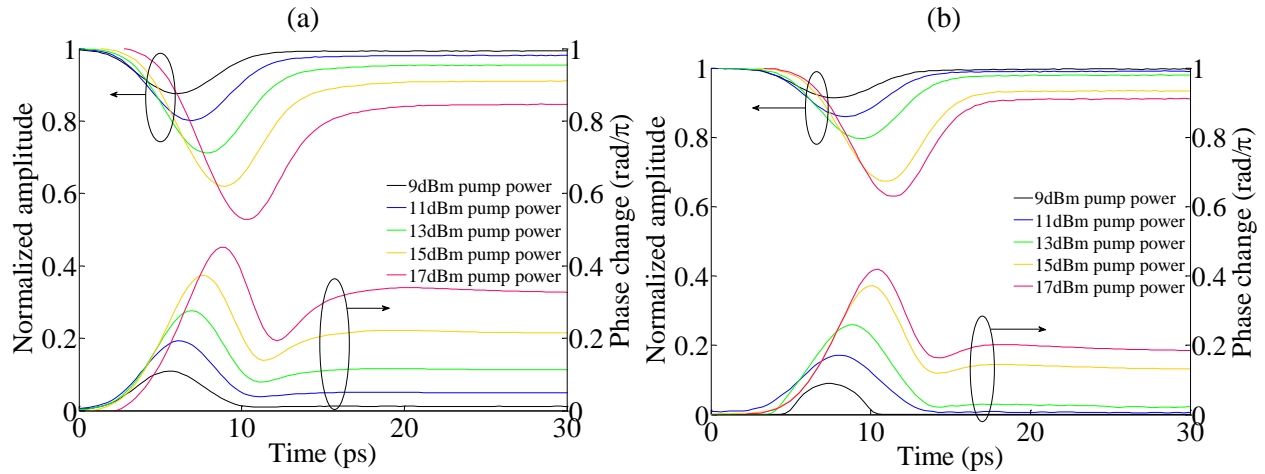
Fig. 5.3.5: Amplitude and phase dynamics without alignment of the responses at the rising edge of each response of (a) 3.6mm long Si nanowire and (b) 4.9mm long Si nanowire.

It is evident from Fig. 5.3.5 that the points of minimum amplitude and maximum phase change shifted in time as a function of pump power. The exact origin of this phenomenon is uncertain but it may be due to heating effects (i.e. phonon generation) by both TPA and FCA [77, 179, 331], as the rapid generation of carriers in the Si nanowires at high input powers (>11dBm) may have created a "phonon bottleneck" that had a relaxation time of several picoseconds [332]. Alternatively, this phenomenon may be due to pulse broadening associated with TPA [333].

Moreover, Fig. 5.3.5 indicates that there was a relative delay between the point of minimum amplitude (i.e. maximum amplitude change) and the point of maximum phase change at a given pump power. This apparent relative delay can be ascribed to asymmetry in the phase response of the Si nanowire due to the fact that free carriers generated by the leading edge of the pump pulse subsequently led to FCA and FCPE of the trailing edge of the pump pulse. Furthermore, the SU8 polymer material may have had an instantaneous phase response (with negligible associated TPA) and this could have made an additional contribution to the apparent time delay.

To quantify the trends in Fig. 5.3.5, the point of minimum amplitude, the point of maximum phase change and the relative delay between these points as a function of energy per pump pulse for the 3.6mm long Si nanowire and the 4.9mm long Si nanowire are displayed in Fig. 5.3.6. It can be discerned in Fig. 5.3.6 that there was an almost linear shift of the point of maximum phase shift and the point of minimum amplitude as the energy per pump pulse increased.
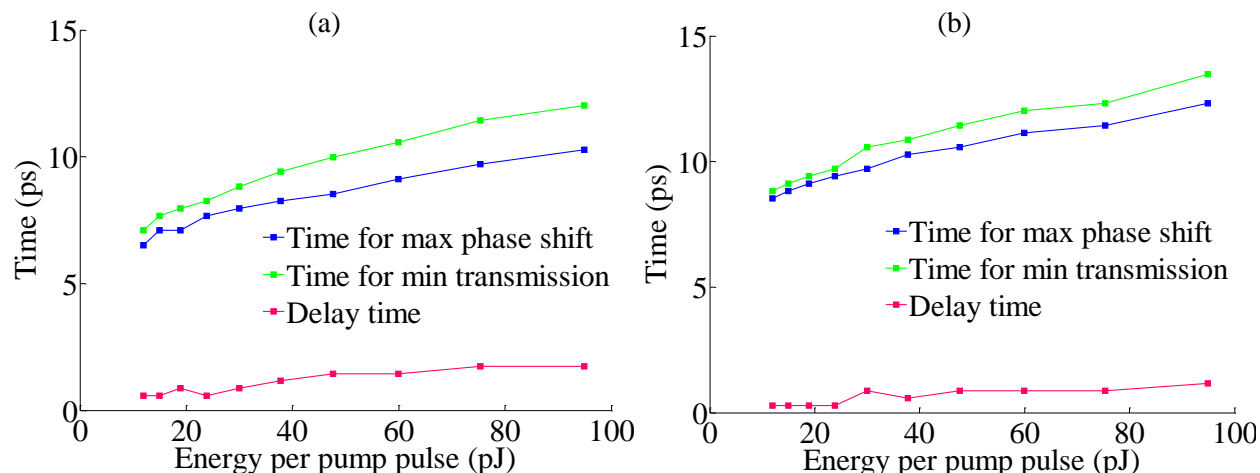
Fig. 5.3.6: Point of minimum amplitude, point of maximum phase change and the relative delay time between these points as a function of energy per pump pulse for (a) 3.6mm long Si nanowire and (b) 4.9mm long Si nanowire.

5.3.3   Self-limiting of optical power

It can be seen in Fig. 5.3.1, Fig. 5.3.3 and Fig. 5.3.4 that the ultrafast TPA amplitude and ultrafast Kerr phase responses began to show signs of saturation as the pump power increased. To quantify this trend, the maximum Kerr effect phase change and maximum change in transmission are plotted as a function of energy per pump pulse in Fig. 5.3.7.
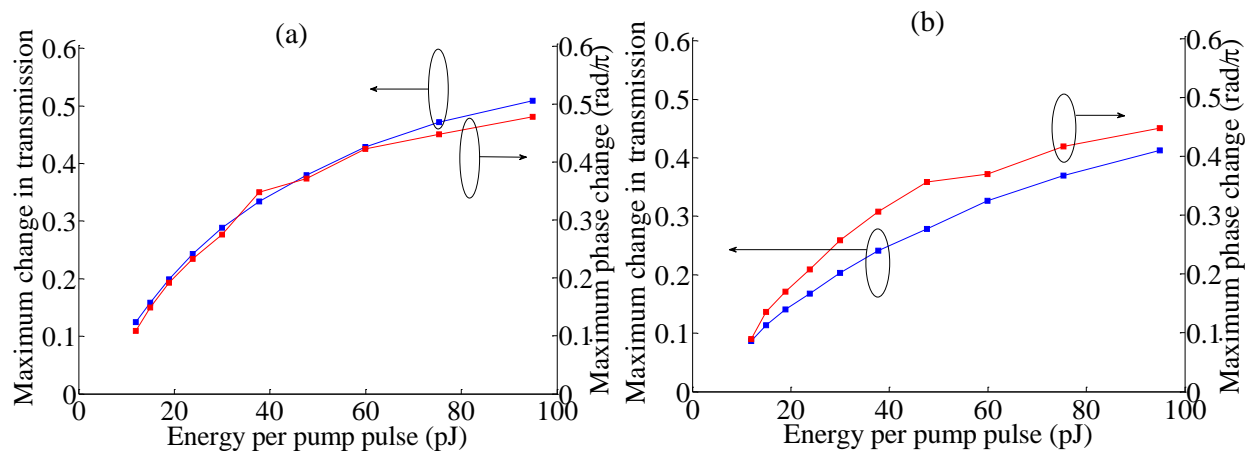
Fig. 5.3.7: Maximum phase change and maximum change in transmission as a function of energy per pump pulse for (a) 3.6mm long Si nanowire and (b) 4.9mm long Si nanowire.

Fig. 5.3.7 shows that the maximum phase shift and the minimum amplitude began to saturate at energy per pump pulse >40pJ for both nanowires. This can be ascribed to the fact that FCA induced by strong pump signals led to absorption of the pump signal itself i.e. self-limiting took

place [77]. The trends in Fig. 5.3.7 are qualitatively similar to the pump saturation visible in graphs which show average output power as a function of average input power presented by R. Dekker *et al* [77] and W. Astar *et al* [334].

The Kerr phase shift φ_{Kerr} is defined by Eq. 5.3.1, where λ is the signal wavelength, L_{eff} is the effective interaction length, z is the propagation distance along the length of the waveguide and $I(z)$ is the lightwave intensity [180].

$$\varphi_{Kerr} = \frac{2\pi n_2}{\lambda} \int_0^{L_{eff}} I(z)dz \qquad (5.3.1)$$

The intensity $I(z)$ is determined by the rate equation Eq. 5.3.2, where α_{lin} is the linear propagation loss, β_{tpa} is the TPA coefficient and α_{fca} is the FCA coefficient [180, 335].

$$\frac{dI(z)}{dz} = -[\alpha_{lin} + \beta_{tpa} I(z) + \alpha_{fca} I^2(z)]I(z) \qquad (5.3.2)$$

The free carrier absorption coefficient α_{fca} is defined by Eq. 5.3.3, where τ_{fc} is the free carrier lifetime, h is Planck's constant and c is the speed of light in a vacuum [335].

$$\alpha_{fca} = 1.45 \times 10^{-21} [m^2] \left(\frac{\lambda}{1.55 \times 10^{-6} [m]} \right)^2 \frac{\beta_{tpa} \tau_{fc} \lambda}{2hc} \qquad (5.3.3)$$

To focus on the influence of FCA on the Kerr phase shift and transmission, Eq. 5.3.1 can be simplified by neglecting both the linear absorption and TPA terms. Solving the resulting equation leads to an expression for the normalized transmission $T(z)$ given by Eq. 5.3.4, where I_0 is the intensity at $z=0$.

$$T(z) = \frac{I(z)}{I_0} = \frac{1}{\sqrt{1 + 2I_0^2 \alpha_{fca} z}} \qquad (5.3.4)$$

Furthermore, $I(z)$ can be substituted into Eq. 5.3.1 to give an expression for φ_{Kerr} (see Eq. 5.3.5).

$$\varphi_{Kerr} = \frac{2\pi n_2}{\lambda I_0 \alpha_{fca}} [\sqrt{1 + 2I_0^2 \alpha_{fca} L_{eff}} - 1] \qquad (5.3.5)$$

It can be inferred from Eq. 5.3.4 and Eq. 5.3.5 that both the Kerr phase shift and the transmission saturate due to FCA as the pump intensity (or power) increases.

5.3.4   Estimation of free carrier lifetime

The FCA recovery time was estimated using the un-normalized probe amplitude power measured by the "PP" photodiode, and this data for the 3.6mm long Si nanowire is displayed in Fig. 5.3.8. It is apparent in Fig. 5.3.8 that when pump pulses at a repetition rate of 665MHz were launched into the Si nanowire, the probe transmission did not return to the steady-state level corresponding to no pump input to the device. This implies that the free carrier density did not fully decay within the pump pulse period (1.5ns) and as a consequence, the amplitude and phase evolutions had sawtooth-like waveforms.
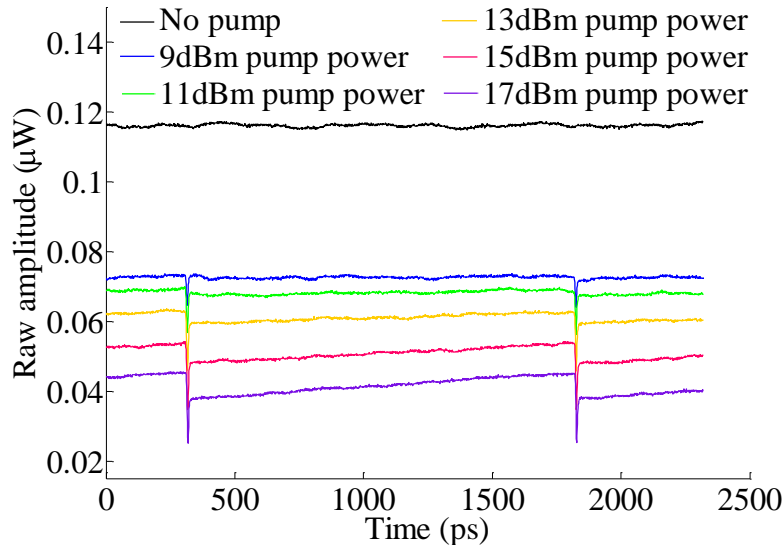
Fig. 5.3.8: Un-normalized transmission power for 3.6mm long Si nanowire, with probe input power set to -27dBm and pump input power varied from 9dBm to 17dBm at the chip input.

To estimate the free carrier lifetime in the Si nanowires, both the steady-state amplitude level when no pump was incident on the nanowire A_0 and the un-normalized amplitude when pump pulses with a given average power were input to the nanowire $A_{pp}(t)$ were plotted on a single graph. The difference between the point t_0 of arrival of the pump pulse and the point t_1 where the

extrapolation of the FCA recovery tail in $A_{pp}(t)$ intersected with A_0 was taken to be equal to the FCA lifetime i.e. $\tau_{fc}=(t_1 - t_0)$, as shown in the schematic in Fig. 5.3.9.
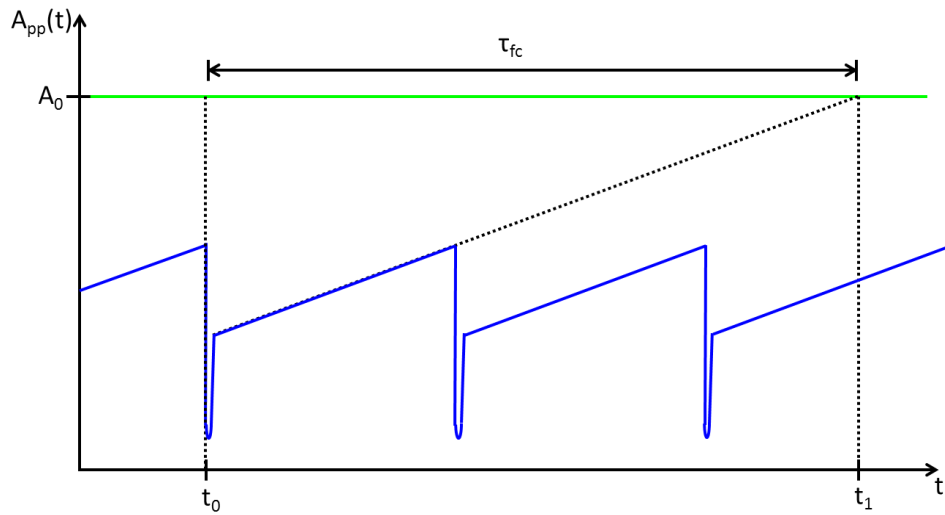
Fig. 5.3.9: Schematic illustration of un-normalized probe transmission power evolution for a Si nanowire (blue line).

The measured un-normalized amplitude data for the 3.6mm long Si nanowire is shown in Fig. 5.3.10. Note that in this figure, the green line refers to the mean un-normalized amplitude level when there is no input pump power, and the red line is the least squares fit to the long FCA recovery tail (the equation of this fitted line is provided in the graph, where t is time in s).

$$y=(5.164\times10^{-18})t+0.0367$$
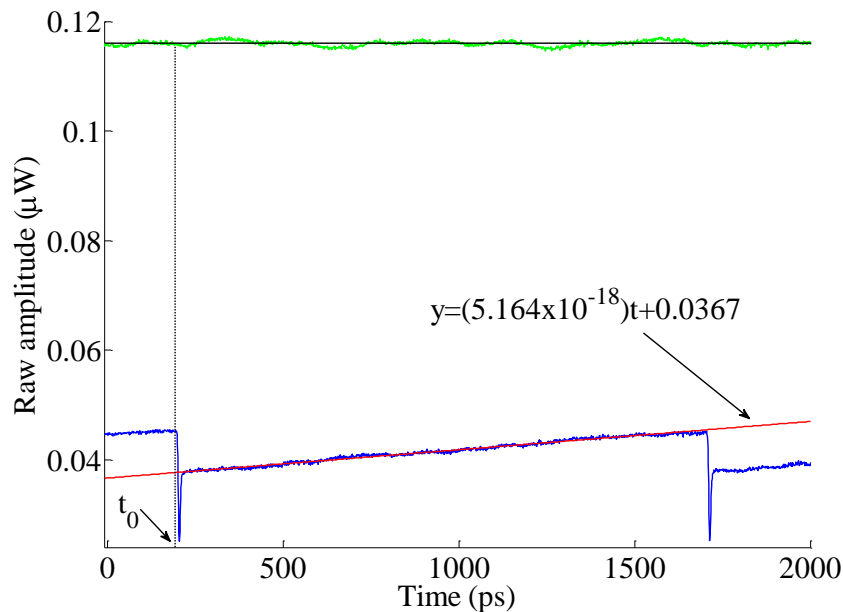
Fig. 5.3.10: Measured un-normalized probe transmission power evolution for 3.6mm long Si nanowire (blue line) for a pump power of 17dBm at the nanowire input.

Using the technique outlined above, the FCA recovery lifetime was determined to be 16.2±0.1ns for the 3.6mm long device, 8.3±0.1ns for the 4.9mm long device and 7.5±0.1ns for the 14.9mm long device. The errors in these values for the free carrier lifetime are based on linear regression analysis of the slope of the start of the long recovery tail. This allowed the uncertainty in t_1 and, by extension, the uncertainty in τ_{fc} to be estimated (it was assumed that the uncertainty in t_0 and the uncertainty in A_0 was negligible) These values for the free carrier lifetime in the Si nanowires embedded in SU8 polymer (~10ns) are slightly longer than the values reported in the literature for Si nanowires embedded in SiO_2 without material modifications and/or the application of a reverse bias (i.e. 0.2 to 3ns) [180, 182, 183]. This comparatively long free carrier lifetime can be attributed to passivation of the surface of the silicon by the SU8 polymer [336, 337]. The disparity in free carrier lifetime for the Si nanowires with different lengths is probably due to variations in the fabrication process for each device.

5.4 Theory and modelling

An impulse response formalism was employed to explain the main features of the amplitude and phase evolution of the Si nanowires, using a similar approach to the impulse response model for carrier dynamics in SOAs described by K.L. Hall *et al* [105]. For the Si nanowire modelling, contributions from TPA, the Kerr effect, FCA and FCPE processes were all taken into consideration because FCA and FCPE became significant at high pump powers (>11dBm). The TPA impulse response and the Kerr impulse response were not represented by instantaneous delta functions, but were instead assumed to be exponential functions with a short lifetime (0.6ps) so as to capture hot carrier relaxation effects [331]. The FCA and FCPE impulse responses were modelled as a step function multiplied by a line with constant slope to simulate sawtooth operation. The TPA and FCA amplitude impulse responses, $R_{ampl,tpa}$ and $R_{ampl,fca}$, were described by Eq. 5.4.1 and Eq. 5.4.2 respectively, where $Q_{ampl,tpa}$ determines the magnitude of the TPA response, τ_{hc} is the hot carrier relaxation time, $\Delta H_{ampl,fca}$ determines the magnitude of the FCA response, $C_{ampl,fca}$ can adjust the slope of the FCA response and τ_{fc} is the free carrier lifetime (16ns for the 3.6mm long Si nanowire).

$$R_{ampl,tpa} = Q_{ampl,tpa} \exp\left(\frac{-t}{\tau_{hc}}\right) \tag{5.4.1}$$

$$R_{ampl,fca} = \Delta H_{ampl,fca} - C_{ampl,fca}\left(\frac{t}{\tau_{fc}}\right) \tag{5.4.2}$$

Similarly the Kerr effect and FCPE impulse responses, $R_{phase,Kerr}$ and $R_{phase,fcpe}$, were described by Eq. 5.4.3 and Eq. 5.4.4 respectively, where $Q_{phase,Kerr}$ determines the magnitude of the Kerr effect response, $\Delta H_{phase,fcpe}$ determines the magnitude of the FCPE response and $C_{phase,fcpe}$ can adjust the slope of the FCPE response.

$$R_{phase,Kerr} = Q_{phase,Kerr} \exp\left(\frac{-t}{\tau_{hc}}\right) \tag{5.4.3}$$

$$R_{phase,fcpe} = -\Delta H_{phase,fcpe} + C_{phase,fcpe}\left(\frac{t}{\tau_{fc}}\right) \tag{5.4.4}$$

To reproduce the modal amplitude and phase change ($g_{conv,pump}(t)$ and $\Delta\varphi_{conv,pump}(t)$ respectively) of the nanowire in response to a pump pulse, the TPA and Kerr impulse responses were initially convolved with a modelled 3.5ps sech^2 pump pulse. This convolution was performed because the ultrafast effects detected by the TOAD loop system were due to non-degenerate TPA of one pump and one probe photon, and the changes in absorption $\Delta\alpha_{tpa}$ and refractive index Δn_{Kerr} due to TPA and the Kerr effect are described by Eq. 5.4.5 and Eq. 5.4.6, where β_{tpa} is the TPA coefficient and n_2 is the Kerr coefficient [338]. Although degenerate TPA of two pump photons occurred, this process was not directly detectable by the TOAD loop system.

$$\Delta\alpha_{tpa} = \beta_{tpa} I_{pump} \tag{5.4.5}$$

$$\Delta n_{Kerr} = n_2 I_{pump} \tag{5.4.6}$$

However, the FCA and FCPE impulse responses were convolved with the modelled 3.5ps sech^2 pump pulse *squared,* because the vast majority of free carriers were generated by degenerate TPA of two pump photons. Therefore, the effects of FCA and FCPE were proportional to the square of the pump intensity. It was necessary to include a relative time delay between the onset of the TPA response and the onset of the Kerr effect response, varying from 0.6 to 1.3ps. The modal amplitude was converted into total amplitude $G_{conv,pump}(t)$ using Eq. 5.4.7.

$$G_{conv,pump}(t) = \exp(-g_{conv,pump}(t)) \tag{5.4.7}$$

As will be outlined further on in this section, the convolutions of the TPA, Kerr effect, FCA and FCPE impulse responses with the pump were translated into reflection and transmission coefficients of the TOAD loop. In turn, these reflection and transmission coefficients were convolved with the probe before finally calculating the modelled amplitude and phase evolutions for the Si nanowire. This method enabled direct comparison between the experimental data and the data derived from the impulse response model.

Both $G_{conv,pump}(t)$ and $\Delta\varphi_{conv,pump}(t)$ when the pump power was 15dBm as well as the modelling parameters are displayed in Fig. 5.4.1. It was only necessary to change the peak pump power parameter and the relative time delay between the onset of TPA and the onset of the Kerr

159

effect for modelling the amplitude and phase evolution of the Si nanowire as the pump power was varied from 9 to 17dBm while all other parameters in the fitting routine remained approximately constant (i.e. they had similar values to those shown in Fig. 5.4.1).
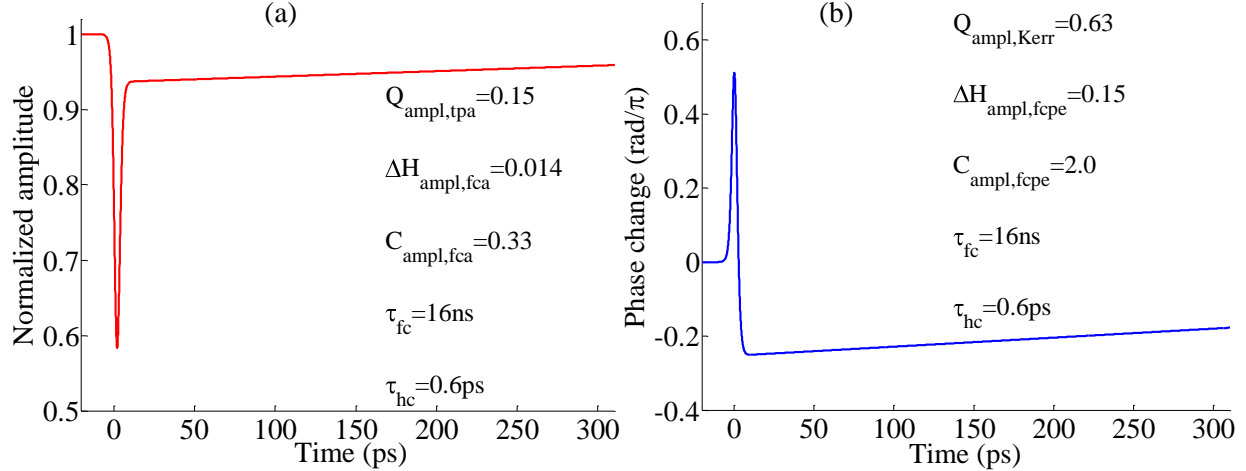
Fig. 5.4.1: (a) Modelled amplitude and (b) phase change dynamics of 3.6mm long Si nanowire in response to input pump pulse (at 15dBm pump power).

As depicted in Fig. 5.4.1(b), the modelled Kerr phase response was positive whereas the modelled FCPE phase response was negative following the injection of a pump pulse [77]. After the calculation of the amplitude and phase dynamics in the 3.6mm long Si nanowire in response to a pump pulse, the reflection and transmission coefficients ($R_{conv,1}$ and $T_{conv,1}$) for the TOAD loop were calculated from $G_{conv,pump}(t)$ and $\Delta\varphi_{conv,pump}(t)$ using equations similar to those described in ref. [153] (see Eq. 5.4.8 and Eq. 5.4.9).

$$R_{conv,1} = d^2k^2 + 2d^2k^2\sqrt{G_{conv,pump}(t)}\cos\theta_0\cos\varphi_{conv,pump}(t) + d^2k^2G_{conv,pump}(t) \qquad (5.4.8)$$

$$T_{conv,1} = d^4 - 2d^2k^2\sqrt{G_{conv,pump}(t)}\cos\theta_0\cos\varphi_{conv,pump}(t) + k^4G_{conv,pump}(t) \qquad (5.4.9)$$

The reflection and transmission coefficients ($R_{conv,1}$ and $T_{conv,1}$) were convolved with a modelled 2.5ps sech^2 probe pulse to produce new values for these coefficients, $R_{conv,2}$ and $T_{conv,2}$, so as to include the effect of the probe. Finally, $R_{conv,2}$ and $T_{conv,2}$ were employed to calculate the amplitude and phase evolutions, which permitted a direct comparison to be made between the measured data and the modelled data (see Fig. 5.4.2). Fig. 5.4.2 shows that there was strong agreement between the modelled and measured data for both the reflection and transmission

coefficients of the TOAD loop, indicating that the impulse response formalism could account for the main features in the reflection and transmission coefficients.
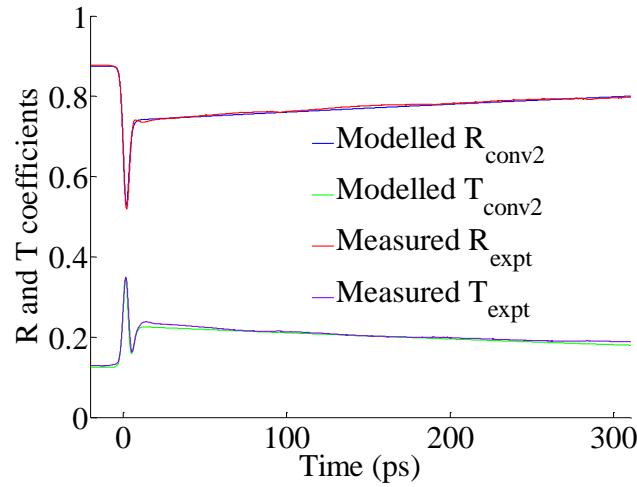
Fig. 5.4.2: Measured reflection (R_{expt}) and transmission (T_{expt}) coefficients compared with the modelled reflection (R_{conv2}) and transmission (T_{conv2}) coefficients for the TOAD loop incorporating the 3.6mm long Si nanowire (at 15dBm input pump power).

In Fig. 5.4.3, the measured amplitude and phase evolutions of the 3.6mm long Si nanowire with an input pump power of 15dBm are compared with the corresponding modelled evolutions. Note that the experimental amplitude evolution shown in Fig. 5.4.3(a) was derived from the TOAD loop reflection and transmission coefficients measured by the "R" and "T" photodiodes, which slightly underestimated the FCA component compared to the amplitude evolution measured by the "PP" photodiode. This underestimation of the FCA recovery tail may have been due to inaccuracies in the calibration of the measurement system.
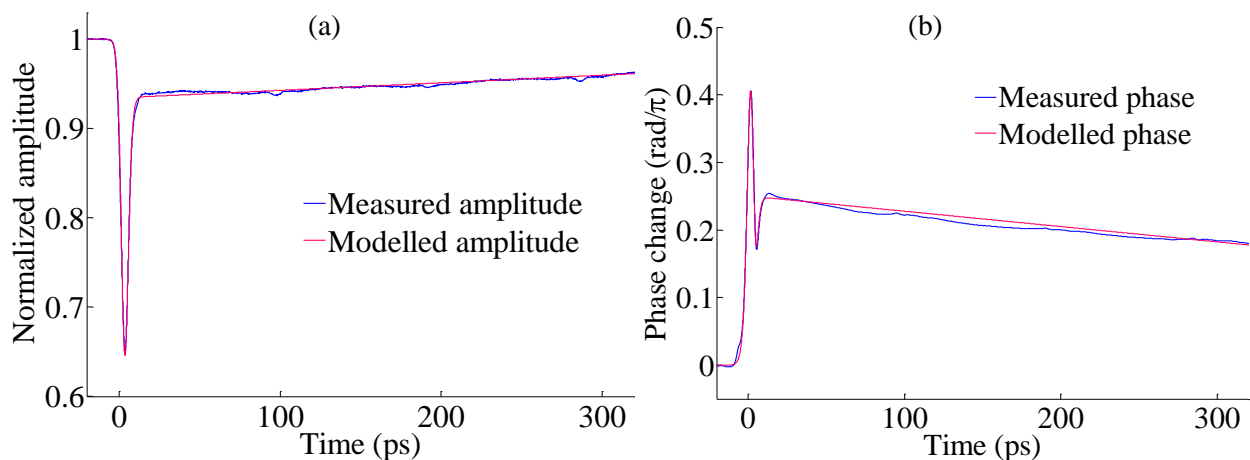
Fig. 5.4.3: Measured and modelled (a) amplitude and (b) phase response of the 3.6mm long Si nanowire (15dBm input pump power).

It can be seen from Fig. 5.4.3 that a close fit between the experimental phase data and the modelled phase curve could be obtained, thereby suggesting that the simple impulse response model which included the effects of TPA, the Kerr effect, FCA and FCPE accounted for the main features in the amplitude and phase evolutions of the Si nanowires as measured by the TOAD loop test-bed. Thus, without the use of complicated rate equations, it was possible to fit the experimental data for a range of input pump powers by only varying the peak pump power parameter, and the relative time delay between the peak of the TPA effect and the peak of the Kerr effect, while all other parameters essentially remained fixed.

Values for the TPA coefficient β_{tpa} and the Kerr coefficient n_2 were estimated using the amplitude and phase impulse responses at low pump powers ($\leq$11dBm). At pump powers below 11dBm, individual pump pulses contributed only a small addition to the mean free carrier population. At low pump powers, the experimental data shows that the FCA can be approximated as a simple addition to the linear propagation loss. This approximation can be used to calculate the normalized probe power transmission T_P and the total phase change $\Delta\varphi_{tot}$ for the Si nanowire at low input powers [323]. The expressions for T_P and $\Delta\varphi_{tot}$ in this reference can be rearranged to give expressions for β_{tpa} and n_2 (see Eq. 5.4.10 and Eq. 5.4.11) [323, 339].

$$\beta_{tpa} = \frac{\left(\frac{1}{\sqrt{T_P}} - 1\right)}{I_{p0}L_{eff}} \tag{5.4.10}$$

$$n_2 = \frac{\lambda_{pump}\Delta\varphi_{tot}}{4\pi \int\limits_0^{L_{wg}} I_{pump}(z)dz} \tag{5.4.11}$$

In Eq. 5.4.10 and Eq. 5.4.11, I_{p0} refers to the pump intensity at the input, λ_{pump} is the pump wavelength, L_{eff} is the typical parameter which refers to the effective interaction length and z is the distance travelled by the pump pulse within the waveguide. For the 3.6mm long Si nanowire, β_{tpa} and n_2 were calculated to be 3×10^{-12}m.W^{-1} and 4×10^{-18}m^2.W^{-1} respectively using λ_{pump}=1555nm, $I_{p,0}$=1.2x10^{13}W.m^{-2}, α_{lin}=4.5dB.cm^{-1}, T_P=0.857 and $\Delta\varphi_{tot}$=0.137π rad (when average pump input power was 9dBm). The same approximate values for β_{tpa} and n_2 were found for the 4.9mm long and 14.9mm long Si nanowires. These calculated values for β_{tpa} and n_2 have the same order of magnitude as the range of values cited in the literature [181, 340-342],

although they were marginally lower than expected, possibly due to uncertainties in determining the waveguide effective area and the taper loss. The FOM for the Si nanowires was 0.9, calculated using the expression defined by M. Dinu *et al* [340] (see Eq. 5.4.12).

$$FOM = \frac{n_2}{\beta_{tpa}\lambda} \qquad (5.4.12)$$

In Table 5.4.1, the free carrier lifetimes, TPA coefficients and FCA coefficients for Si waveguides (without material modifications and not incorporated into a p-i-n diode structure) in the literature are compared with the values for these parameters cited in this thesis to place the research presented in this thesis into a broader context.

Ref.	Type	w (μm)	h (μm)	L (mm)	C.M.	τ_{fc} (ns)	β_{tpa} (m.W^{-1})	n_2 (m^2.W^{-1})	FOM
This work	Nw	0.45	0.24	3.6 – 14.9	SU8	7.5 – 16.2	3×10^{-12}	4×10^{-18}	0.9
[183]	Nw	0.40	0.22	1.4	SiO$_2$	0.2	4.3×10^{-12}	2.0×10^{-18}	0.3
[314]	Nw	0.45	0.22	4.7	SiO$_2$	0.5	-	-	-
[179]	Nw	0.45	0.30	7	SiO$_2$	5	-	-	-
[169]	Rib	1.52	1.45	48.0	SiO$_2$	25	5×10^{-12}	-	-
[343]	Rib	4.0	-	17	SiO$_2$	-	4.5×10^{-12}	6.0×10^{-18}	1.2
[344]	Rib	1.6	0.2	0.3	SiO$_2$	150	9.0×10^{-12}	7.0×10^{-18}	1.8
[323]	Slot	0.18	0.22	2.6	DDMEBT	1.2 (core)	0.5×10^{-12} (cladding)	1.7×10^{-18} (cladding)	2.19
[340]	Bulk Si <110>	-	-	0.48	-	-	7.9×10^{-12}	4.5×10^{-18}	0.37
[340]	Bulk Si <111>	-	-	0.48	-	-	8.8×10^{-12}	4.3×10^{-18}	0.32

Table 5.4.1: Comparison between the results presented in this paper and results reported in the literature (Nw=nanowire, Rib=rib waveguide, Slot=slot waveguide, w=waveguide width, h=waveguide height, L=waveguide length, C.M.=cladding material, and the dash means that the quantity was not reported).

5.5   *Two-copy wavelength conversion using XPM in Si nanowire*

It was outlined in Section 5.1 that wavelength conversion, format conversion, waveform sampling and demultiplexing at bit rates up to 1.28Tb.s^{-1} have already been realized using Si nanowires embedded in SU8 polymer waveguides by utilizing the effect of FWM [227, 345]. However, it would be desirable to explore alternative switching mechanisms to FWM in Si nanowires to avoid the relatively low conversion efficiency associated with FWM e.g. the peak fibre-to-fibre FWM efficiency was determined as -14dB by H. Ji *et al* , as -11dB by K. Yamada *et al* [227, 346] and as -8.5dB by H. Rong *et al* (with the application of a reverse bias of 25V)[189]. However, the typical FWM efficiency in Si nanowires can be as low as -30dB in many experiments involving Si nanowires reported in the literature [221, 325].

The effect of XPM between a pump and a CW beam was exploited in an early demonstration of the switching capability of Si waveguides by O. Boyraz *et al*, but the switching window was limited to 7ns due to free carrier accumulation which could not be avoided because the Si waveguide was placed inside a Mach-Zehnder interferometric configuration [347]. Subsequently, wavelength conversion based on XAM in a Si nanowire was demonstrated at 10Gb.s^{-1} by K. Yamada *et al* [346]. Furthermore, both format conversion (NRZ-OOK to RZ-OOK) and wavelength conversion based on XPM in a Si nanowire at 10Gb.s^{-1} have been reported by W. Astar *et al* [334, 348]. However, the long free carrier lifetime (>1ns) would seem to suggest that XPM is not a viable switching mechanism in Si waveguides at data rates >10Gb.s^{-1} unless a p-i-n diode structure is employed to sweep out the free carriers. However, it will be shown in the following section that it is possible to take advantage of wavelength chirp in an unbiased Si nanowire to carry out wavelength conversion based on XPM at 80Gb.s^{-1}.

After fitting the experimental amplitude and phase data using the impulse response formalism, the wavelength chirp associated with the change in refractive index in the device was calculated using the modelled phase evolution. The relationship between the wavelength shift and the phase change is described by Eq. 5.5.1, where $\Delta\lambda$ is the instantaneous wavelength shift, λ_0 is the centre wavelength, c is the speed of light and $\Delta\varphi$ is the instantaneous phase change [77].

$$\Delta\lambda = -\left(\frac{1}{2\pi}\right)\left(\frac{\lambda_0{}^2}{c}\right)\Delta\omega = -\left(\frac{1}{2\pi}\right)\left(\frac{\lambda_0{}^2}{c}\right)\left(-\frac{d(\Delta\varphi)}{dt}\right) = \left(\frac{1}{2\pi}\right)\left(\frac{\lambda_0{}^2}{c}\right)\frac{d(\Delta\varphi)}{dt} \qquad (5.5.1)$$

The modelled phase change and the corresponding wavelength shift for the 3.6mm long Si nanowire is displayed in Fig. 5.5.1. It can be seen in Fig. 5.5.1(b) that there was an appreciable wavelength shift on both the red and blue sidebands. While these wavelength shifts were similar in magnitude, the blue-shift was always slightly greater than the red-shift e.g. when the average pump power was 17dBm (i.e. the energy per pump pulse was 75pJ), there was a red-shift of 1.0nm and a blue-shift of 1.4nm. The larger blue-shift was due to the accumulation of free carriers in the device at the trailing edge of the pump pulse.
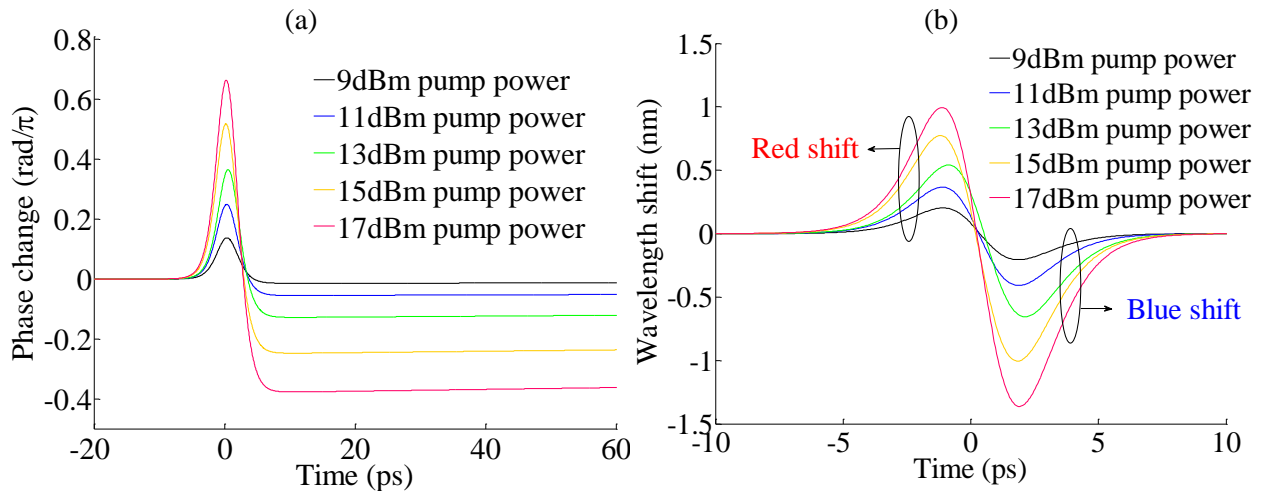
Fig. 5.5.1: (a) Modelled phase change and (b) wavelength shift for the 3.6mm long Si nanowire.

It was found by R. Dekker *et al* that the wavelength shift in Si waveguides embedded in SiO_2 cladding was approximately equal on the red and blue sidebands when the pump pulses had a pulsewidth of 300fs, but that the blue shift was much greater than the red shift when the pump pulses had a pulsewidth of 3.5ps [77, 179]. Thus, in relation to measurements on Si nanowires embedded in SU8 polymer, it was surprising that the magnitude of the wavelength shift on the red and blue sidebands were quite similar when the pump pulses had a pulsewidth of 3.5ps.

This observation served as the inspiration for a demonstration of two-copy wavelength conversion at a bit rate of 80Gb.s[-1] by Hua Ji *et al* [349] using an 8mm long Si nanowire with cross section dimensions of 450nm x 250nm. Although the author was not directly involved in the experiments that are outlined in the following paragraphs, the dynamic characterization of the Si nanowires is able to explain the fact that it was possible to carry out this high speed demonstration of two-copy wavelength conversion.

A train of pump pulses at 1542nm with a pulsewidth of 2ps was emitted by an erbium-doped glass oscillator (ERGO) laser at a repetition rate of 10GHz. These pulses were compressed by passing them through dispersion-flattened highly nonlinear fibre (DF-HNLF) and filtering the output signal using a BPF with a 3dB bandwidth of 3.0nm centred at 1550nm. The pulsewidth of the compressed pulses was 1.7ps. These pulses were encoded with a 2^{31}-1 PRBS using a LiNbO$_3$ MZM to create a 10Gb.s^{-1} RZ-OOK signal. This was passively multiplexed using OTDM bit interleaving to create an 80Gb.s^{-1} serial data signal at 1550nm. This data signal was amplified with a high power EDFA and combined with a CW probe at 1556.5nm using a 2x1 50:50 coupler and the output from this coupler was sent into the Si nanowire.

The average powers of the 80Gb.s^{-1} data signal and the CW probe coupled into the Si nanowire were 16.5dBm and 15.5dBm respectively. The polarization states of the data signal and the CW probe were both aligned to the TE mode of the Si nanowire using PCs. After the Si nanowire, a BPF with 20 nm bandwidth was utilized to partially suppress the original data signal at 1550nm. Two fibre Bragg gratings (FBGs) with a 3dB bandwidth of 0.8nm suppressed the optical carrier at 1556.5nm. A wavelength selective switch (WSS) simultaneously extracted both the blue and red sidebands on the probe output. The filtered output signal was sent into a nonlinear optical loop mirror (NOLM) for demultiplexing the WC line rate signal at 80Gb.s^{-1} to a base rate channel at 10Gb.s^{-1} which was detected by a pre-amplified receiver. For B2B and WC signals, the BER was measured as a function of received power (see Fig. 5.5.2).
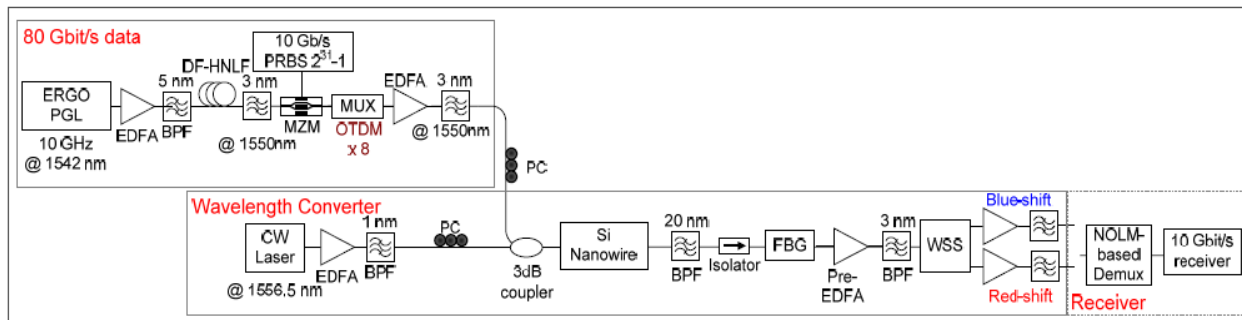
Fig. 5.5.2: Experimental scheme of wavelength conversion using Si nanowire.

Fig. 5.5.3(a) shows the unfiltered spectra measured at both the input and output ports of the Si nanowire and Fig. 5.5.3(b) shows the filtered spectra measured at the NOLM demultiplexer. It can be discerned in Fig. 5.5.3(a) that the CW probe was spectrally broadened due to XPM

between the probe and the original data signal in the Si nanowire. The 80Gb.s^{-1} components are clearly visible in the sidebands of the CW probe spectrum. As shown in Fig. 5.5.3(b), the sidebands that included the information of the original data signal were extracted by wavelength selective filtering at 1557.6nm (red-shifted), and at 1555.4nm and 1555.0nm (both blue-shifted).

(a)   (b)
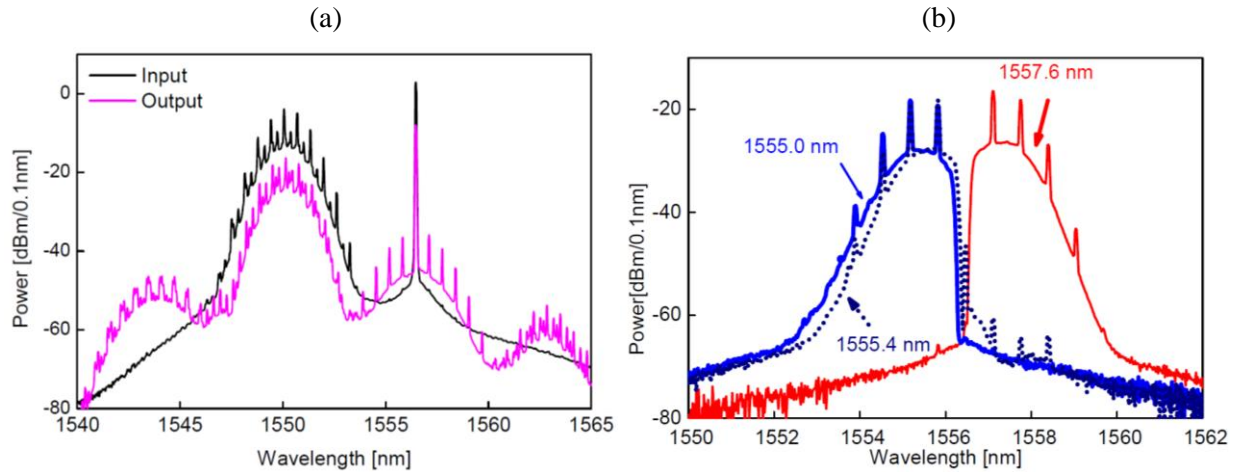
Fig. 5.5.3: (a) Input and output spectra without filtering and (b) the filtered output spectra from the 3.6mm long Si nanowire.

The BER curves as a function of received power for the B2B, 1557.6nm (red-shifted), 1555.4nm (blue-shifted) and 1555.0nm (blue-shifted) signals measured by the receiver are displayed on a single graph in Fig. 5.5.4.
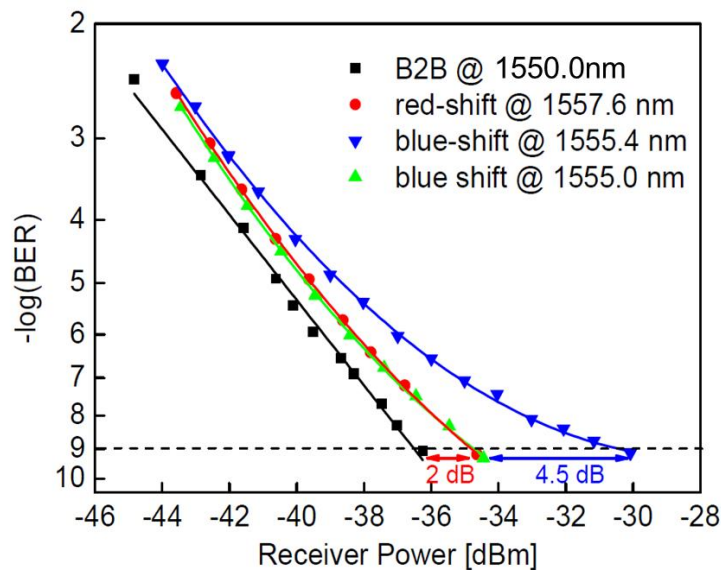
Fig. 5.5.4: BER vs received power for B2B, red-shifted and blue-shifted signals at 80Gb.s^{-1}.

167

As shown in Fig. 5.5.4, a BER of 1×10^{-9} could be achieved for both the red-shifted 1557.6nm signal and the blue-shifted 1555.4nm signal, with a power penalty of 2.0dB and 6.5dB respectively, compared to the B2B signal. However, when the blue-shifted signal was located slightly further away from the carrier (filter centred at 1555.0nm), the BER performance improved significantly and was comparable to BER performance of the red-shifted 1557.6nm signal. This was consistent with the wavelength chirp in the 3.6mm long Si nanowire calculated from the modelled phase evolution data in Fig. 5.5.1(b), where the wavelength shift on the blue side was slightly higher compared to the wavelength shift on the red side, owing to the accumulation of free carriers. The converted data signals at 1557.6nm and 1555.0nm both had a 2dB power penalty with respect to the B2B data signal. This penalty was mainly due to the lower optical signal noise ratio (OSNR) after propagating through the Si nanowire, which had an insertion loss of approximately 6.6dB (including the coupling and propagation losses).

5.6 *Summary*

In this chapter, the amplitude and phase responses for Si nanowires with various lengths (3.6mm to 14.9mm) embedded in a polymer waveguide using a pump-probe test-bed incorporating a TOAD loop interferometer have been presented. The points of maximum ultrafast phase change and minimum ultrafast amplitude shifted in time as a function of pump power, which suggested that carrier heating effects were becoming apparent at high pump powers (>11dBm). A relative time delay between the points of maximum ultrafast phase change and minimum ultrafast amplitude that increased as a function of pump power was observed, which we attribute to a combination of (a) the asymmetry in the phase response due to the fact that free carriers generated by the leading edge of the pump pulse subsequently led to FCA and FCPE of the trailing edge of the pump pulse and (b) an instantaneous phase response in the SU8 polymer.

The amplitude and phase evolutions of the Si nanowires were fitted using a simple impulse response formalism which accounted for TPA, the Kerr effect, FCA and FCPE, without requiring the use of detailed rate equations. Based on this impulse response model, we present values for β_{tpa} and n_2 (3×10^{-12}m.W^{-1} and 4×10^{-18}m^2.W^{-1} respectively) and the TPA FOM was 0.9. The long values for the free carrier lifetime (7.5 to 16.2ns) may have been due to a combination of the relatively low degree of sidewall roughness (which led to a moderate propagation loss of 4.5dB.cm^{-1}) and passivation of the Si nanowire surface by the SU8 polymer [337, 350].

The reversal from a positive phase shift to a negative phase shift at the point when TPA gave way to FCA led to wavelength chirping, where the red and blue shifts had the same order of magnitude. Based on this discovery, an experimental demonstration of 80Gb.s^{-1} wavelength conversion to two copies by simultaneously extracting the blue-shifted and red-shifted sidebands after XPM in a Si nanowire was presented. A BER of 1×10^{-9} was measured for both sidebands, with a receiver sensitivity power penalty of 2dB. It was found that the blue-shifted filter had to be shifted slightly further away from the central carrier wavelength compared to the red-shifted filter to obtain equal performance between the two converted signals. This result was consistent with the characterization of the carrier dynamics in the Si nanowire, where it was found that the magnitude of the blue frequency chirp was slightly greater than the red chirp [349, 351]. It should be possible to extend the exploitation of XPM in Si nanowires embedded in SU8 polymer to functionalities such as format conversion and demultiplexing at high data rates (~100Gb.s^{-1})

EAM with custom epitaxy design incorporating quantum well offsetting

This chapter presents the absorption dynamics of an EAM with a custom epitaxy design which employed three main design features to improve the power handling capability by minimizing the sweepout time. When a moderate reverse voltage bias of 4.5V was applied to the EAM, the 1/e absorption recovery time was as low as 3.0ps. A direct comparison between the absorption dynamics in this custom epitaxy design EAM and a commercially available EAM indicated that the design features in the former led to a dramatic reduction in the sweepout time at a moderate reverse voltage bias. A summary of the experimental and computational data is given and potential applications of this type of EAM are discussed. The research described in this chapter is based on the following publications:

[1] "Sub 10ps carrier response times in electroabsorption modulators using quantum well offsetting," Chris L.M. Daunt, Ciaran S. Cleary, Robert J. Manning, Kevin Thomas, Robert J. Young, Emanuele Pelucchi, Brian Corbett, Frank H. Peters, IEEE *Journal of Quantum Electronics*, vol. 48, pp. 1467-1475 (2012)

[2] "Sub 10ps carrier response times in elecroabsorption modulators using quantum well offsetting," Chris L.M. Daunt, Ciaran S. Cleary, Robert J. Manning, Frank H. Peters, *Proc. Frontiers in Optics (San Jose, USA),* paper PDPC2 (2011)

6.1   Background

MQW EAMs which exploit QCSE are critically important components in the field of optical communications [352]. MQW EAMs offer benefits including low cost, compactness (80 to 300μm in length), low drive voltage (<5V) and compatibility for monolithic integration with a wide variety of devices such as photodetectors, lasers, optical amplifiers, phase shifters, attenuators and passive waveguides on a III-V semiconductor compound platform [158, 353]. Thus, EAMs are ideal candidate components in photonic integrated circuits (PICs) with a high degree of integration (>50 components per chip) [353]. EAMs are frequently employed as external modulators to electrically modulate the intensity and/or phase of an input CW optical

signal [158, 354, 355] but in addition to this application, they can be employed as saturable absorbers to realize functionalities such as pulse generation, wavelength conversion, demultiplexing and signal regeneration [356]. However, EAMs have several disadvantages including limited power handling capability, high insertion losses (typically 10dB), limited optical bandwidth (i.e. they are strongly wavelength dependent), and the fact that it is difficult to encode optical signals with advanced modulation formats using this type of device [357].

By comparison with EAMs, MZMs incorporating $LiNbO_3$ as the active material are bulky, highly sensitive to polarization and difficult to integrate with other components. However, $LiNbO_3$ MZMs have good power handling capability, they are compatible with advanced modulation formats, they have low chirp, and they have broad optical bandwidth [138, 158].

As outlined above, one major disadvantage associated with EAMs is their limited power handling capability owing to the fact that an EAM cannot absorb unlimited optical power [358]. In general, the dynamic extinction ratio of an EAM is compromised due to screening of the externally applied electric field by photogenerated carriers at high optical input powers. As described in Chapter 2, electron-hole pairs are generated in the intrinsic region of an EAM following the arrival of an excite pulse. These charge carriers escape from the quantum wells and drift towards the p-type and n-type contacts. The carriers accumulate at the heterobarriers until they are swept out under the influence of the built-in potential and the applied reverse bias. Thus, an increase in the applied reverse bias leads to a decrease in the sweepout time.

The sweepout time constant is typically of the order of tens of picoseconds [359, 360] but lifetimes below 10ps have been reported in the literature by various research groups. For instance, K. Nishimura *et al* reported a sweepout lifetime of 10ps in an InGaAsP EAM at a moderate reverse bias of 4V [361] and T.H. Wu *et al* reported a sweepout time of less than 10ps in a InGaAsP-AlInGaAs EAM at a high reverse bias of 8V [362]. Similarly, N. El Dahdah *et al* reported a sweepout lifetime of 5ps in an InGaAs-AlInGaAs EAM at a low reverse bias of 2V [167, 363] and R.P. Green *et al* reported a sweepout time of 2.5ps in an AlInGaAs EAM at a moderate reverse bias of 4V [364]. Furthermore, it was found by J. Mork *et al* that there was a two-stage recovery process in an InGaAsP EAM, where the initial recovery process had a lifetime as low as 3ps whereas the subsequent recovery process had a lifetime of 100ps at a high reverse bias of 10V[156, 157]. J. Mork *et al* ascribed the fast initial recovery time to carrier

escape from the quantum wells and the slow subsequent recovery time to carrier sweepout from the intrinsic region into the contacts [156, 157].

In this chapter, we discuss an AlInGaAs EAM with a custom epitaxy design that was designed and fabricated by Dr Chris Daunt in Tyndall National Institute which was specifically designed to minimize carrier pile-up at the heterobarriers. This type of device could potentially be employed as a high speed modulator with good power handling capability or to carry out optical signal processing tasks at high data rates ($\geq 100 \text{Gb.s}^{-1}$). It is important to state at this point that the author was not involved in the fabrication or static characterization of the custom epitaxy design EAM. However, the author was involved in the dynamic characterization and subsequent impulse response modelling of the carrier dynamics in the device. This custom epitaxy design EAM employed three principal design characteristics to reduce the carrier sweepout time:

1.) Quantum well offsetting within the intrinsic region
2.) Carbon doping in p-type layers close to the MQW section
3.) Reduction of the valence band discontinuity at heterobarriers

Each of these design aspects are described in greater depth in the following paragraphs.

Quantum well offsetting

Firstly, the MQW section was spatially offset from the midpoint of the intrinsic region to ensure that the distance between the MQW section and the p-type doped region was less than the distance between the MQW section and the n-type doped region. This was done to equalize the time taken for photo-generated carriers to escape from the quantum wells and travel to the p-doped and n-doped regions while still preserving the total thickness of the intrinsic region so as to avoid increasing the capacitance of the device. Quantum well offsetting means that carrier sweepout for both holes and electrons into the contacts can start at the same time, and this minimizes the build-up of positive charges (i.e. holes) in the intrinsic region. Thus, field screening in the device is reduced and the response time of the EAM decreases.

A theoretical study of the concept of quantum well offsetting using a comprehensive drift-diffusion model of the carrier dynamics in an EAM was undertaken by S. Hojfeldt *et al* [162] and it was found that there was a significant reduction in the recovery time when the MQW

section was offset towards the p-type region. When the MQW region is placed in the centre of the intrinsic region, it takes a longer time for holes to travel to the p-doped region than for electrons to travel to the n-doped region, as holes have greater effective mass and lower carrier mobility than electrons. By contrast, when the MQW section is placed close to the p-type region, this ensures that the holes reach the p-type region at the same time that the electrons reach the n-type region. A schematic diagram of the energy band diagram of the custom epitaxy design EAM is given in Fig. 6.1.1.
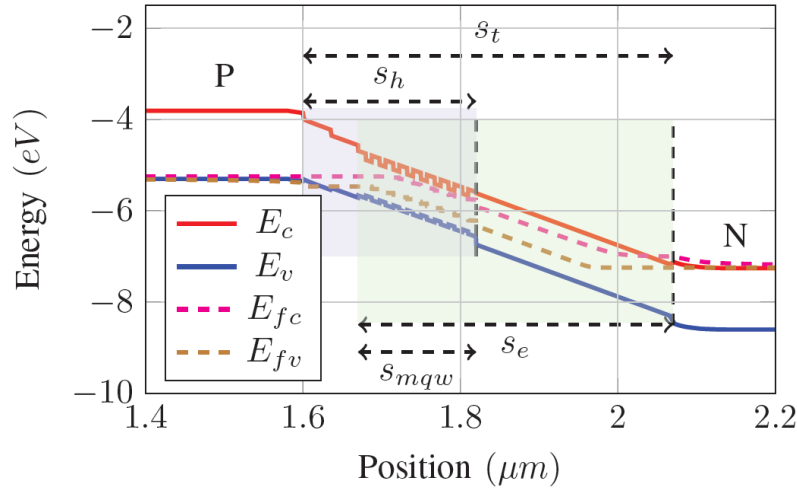
Fig. 6.1.1: Energy band diagram of the custom epitaxy design EAM in the presence of an externally applied electric field.

The maximum distances that the photo-generated holes and electrons had to travel (s_h and s_e respectively) were carefully chosen to ensure that the transit time for the holes to reach the p-type region and the transit time for the electrons to reach the n-type region were equal, without affecting the capacitance of the device (i.e. the total thickness of the intrinsic region s_t remained constant). The relationship between s_h, s_e and s_t is described by Eq. 6.1.1, where s_{mqw} is the width of the MQW section.

$$s_t = s_h + s_e - s_{mqw} \tag{6.1.1}$$

The transit time for holes to travel from the MQW section to the p-type contact $\tau_{t,h}$ and the transit time for electrons to travel from the MQW section to the n-type contact $\tau_{t,e}$ are given by Eq. 6.1.2 and Eq. 6.1.3 respectively, where v_h is the hole drift velocity and v_e is the electron drift velocity.

$$\tau_{t,h} = \frac{s_h}{v_h} \tag{6.1.2}$$

$$\tau_{t,e} = \frac{s_e}{v_e} \tag{6.1.3}$$

The spatial offset ratio γ is defined by Eq. 6.1.4 and this parameter should be greater than unity to compensate for the lower mobility of the holes relative to the electrons.

$$\gamma = \frac{s_e}{s_h} \tag{6.1.4}$$

The optimal offset is achieved when $\tau_{t,h}$ and $\tau_{t,e}$ are equal (see Eq. 6.1.5, Eq. 6.1.6 and Eq. 6.1.7).

$$\tau_{t,h} = \tau_{t,e} \tag{6.1.5}$$

$$\Rightarrow \frac{s_h}{v_h} = \frac{s_e}{v_e} \tag{6.1.6}$$

$$\Rightarrow \gamma_{optimum} = \frac{v_e}{v_h} \tag{6.1.7}$$

As shown in Eq. 6.1.7, the optimal offset is dependent on the ratio of electron drift velocity to hole drift velocity. This relationship can be used to derive the optimum transit time $\tau_{t,optimum}$, as shown in Eq. 6.1.8.

$$\tau_{t,optimum} = \frac{s_t + s_{mqw}}{(v_h + v_e)} \tag{6.1.8}$$

Thus, the total thickness of the intrinsic region and the thickness of the MQW section must be carefully chosen to ensure that the transit time is minimized while ensuring that there is low capacitance (~1pF) and an acceptable extinction ratio (~10dB) in the device [288, 365, 366].

Carbon doping in p-type layers close to the MQW section

Secondly, carbon was chosen as the dopant for the layers close to the MQW section to form the start of the p-type region. By offsetting the MQW section within the intrinsic region, the absorption enhancement caused by room temperature excitons would be eliminated by the diffusion of p-dopants into the MQW region. Due to the fact that carbon has a low diffusion coefficient in III-V semiconductor compounds, carbon doping was selected instead of zinc or beryllium doping for the layers in the p-type region close to the intrinsic region, so as to minimize diffusion of the p-dopant into the MQW section [367-369]. However, as carbon exhibits donor activity in phosphorus-based quaternary alloys, zinc doping was chosen for p-type layers that were not adjacent to the MQW section [370].

Valence band discontinuity minimization

Thirdly, the valence band discontinuity at the heterojunction on the p-type side was minimized by grading the potential in a series of steps, as demonstrated experimentally by research groups such as M. Suzuki *et al* [371] and T.H. Wood *et al* [372], and theoretically investigated by S. Hojfeldt *et al [162, 373]*. Schematic diagrams showing both a one-step heterobarrier and a two-step heterobarrier between the p-type contact and the intrinsic region are shown in Fig. 6.1.2.
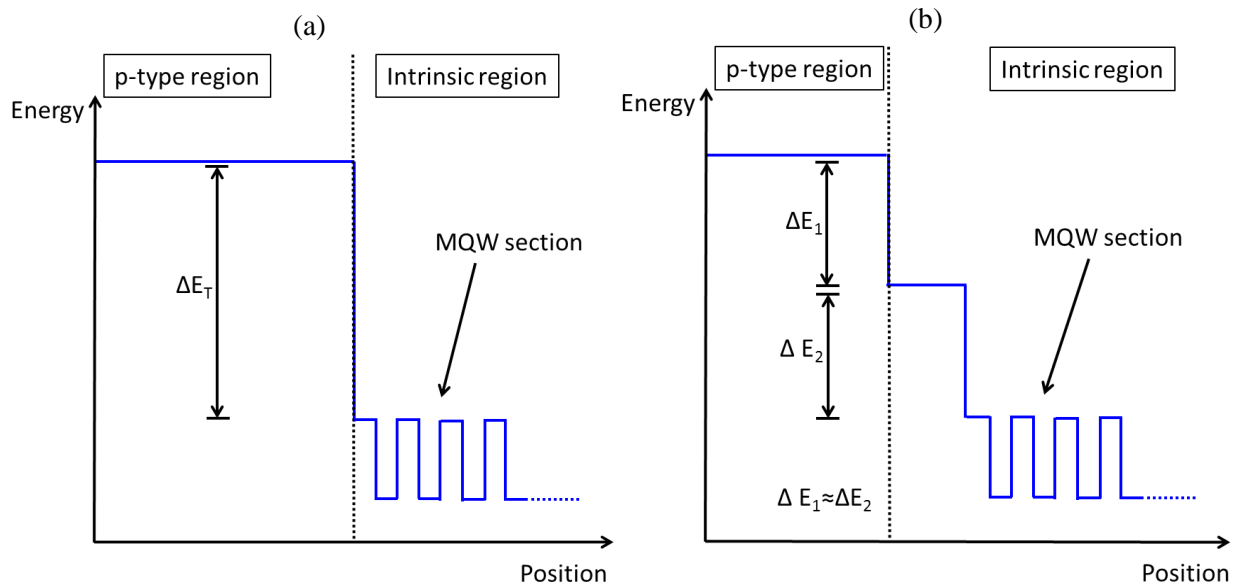
Fig. 6.1.2: (a) One-step potential barrier and (b) two-step graded potential barrier between the p-type region and the intrinsic region (without externally applied electric field).

When carriers reach the heterojunctions between the intrinsic region and the contacts, they accumulate there until they can overcome the potential barriers via a combination of thermionic emission and Fowler-Nordheim tunnelling, although the former is the dominant process [162]. While the carriers are trapped at the heterojunctions, they screen the applied electric field and this further reduces the carrier sweepout rate. A graded potential step between the intrinsic region and the p-type doped region leads to a reduction in the size of each potential barrier that must be overcome by the carriers, and thereby increases the carrier sweepout rate. This technique was only applied to the hole transit region and not to the electron transit region because the heavy hole is the limiting carrier type. Ideally, the steps should be chosen to have equal height to ensure that neither of these steps act as a bottleneck.

The AlInGaAs material system was chosen for the active region rather than the more conventional InGaAsP material system commonly employed in photonic components operating at wavelengths close to 1550nm. The reason for this choice lies in the fact that AlInGaAs has a high conduction band discontinuity [374-376] and this property was exploited to assist the minimization of the valence band discontinuity at the heterojunction on the p-type side.

6.2   Experimental details

The custom epitaxy design EAM was fabricated by Dr Chris Daunt in Tyndall National Institute using the techniques described in ref. [288]. The wafer was grown via metal-organic vapour phase epitaxy (MOVPE) in a commercial MOVPE reactor, using n-doped InP as the substrate and nitrogen as the carrier gas [377]. The MQW section consisted of eight unstrained 7.5nm-thick $Al_{0.03}In_{0.53}Ga_{0.44}As$ quantum wells that were separated by 10nm-thick $Al_{0.17}In_{0.53}Ga_{0.3}As$ barriers. The MQW section was grown on top of a 210nm-thick $In_{0.85}Ga_{0.15}As_{0.32}P_{0.68}$ layer, so as to offset the MQW section from the centre of the intrinsic region. A schematic diagram of a cross-section through the wafer is displayed in Fig. 6.2.1(a) and the material composition of each layer is given in Fig. 6.2.1(b).

(a)

(b)

Repeated	Dopant	Doping (10^{18}) cm^{-3}	Material	λ_g (μm)	Thickness (nm)
1	Zn	10.0	InGaAs	1.7	150
1	Zn	1.5	$In_{0.73}Ga_{0.27}As_{0.59}P_{0.41}$	1.3	50
1	Zn	1.0	InP	1.35	1340
1	C	1.0	$Al_{0.48}In_{0.52}As$	1.47	60
1	uid		$Al_{0.35}In_{0.53}Ga_{0.12}As$	0.97	35
1	uid		$Al_{0.25}In_{0.53}Ga_{0.22}As$	1.1	35
8	uid		$Al_{0.17}In_{0.53}Ga_{0.3}As$	1.24	10
8	uid		$Al_{0.03}In_{0.53}Ga_{0.44}As$	1.55	7.5
1	uid		$Al_{0.17}In_{0.53}Ga_{0.3}As$	1.24	10
1	uid		$In_{0.85}Ga_{0.15}As_{0.32}P_{0.68}$	1.12	210
1	Si	0.2	InP	0.92	80
1	Si	0.5	InP	0.92	70
1	Si	8.0	InP	0.92	920
1	uid		InP	0.92	500

Schematic (a) labels: InGaAs – Zn 7e18; InP – Zn 1e18; AlGaInAs (0.97μm); AlGaInAs (1.55/1.24μm) QWs x 8; 2e17; InP - Si 8e18; InP substrate; AlInAs – C 1e18; AlGaInAs (1.1μm); GaInAsP (1.1μm).

Fig. 6.2.1: (a) Cross-section through the custom epitaxy design EAM and (b) the exact chemical composition of each layer in the device (uid = undoped, λ_g = bandgap wavelength).

A schematic diagram of the energy band diagram around the interface between the p-type region and the intrinsic region is illustrated in Fig. 6.2.2 to show the graded potential step between the two regions.
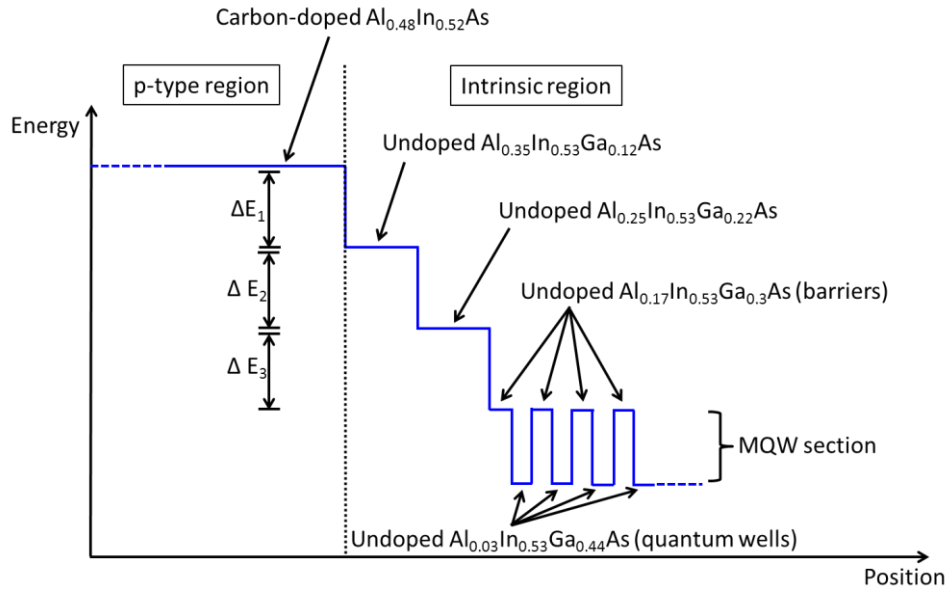
Fig. 6.2.2: Energy band diagram of the interface between the p-type contact and the intrinsic region.

As mentioned in Section 6.1, it was important to ensure that the carbon dopant in the p-type layers adjacent to the intrinsic region did not penetrate into the MQW section. To verify that no carbon dopant had diffused into the MQW section, secondary ion mass spectroscopy (SIMS) was performed on one of the fabricated waveguides and the measured data is illustrated in Fig. 6.2.3 [378]. The SIMS measurement technique measures the composition of material as a function of time (rather than as a function of depth) as the material is analysed from the top-side p-type layers to the bottom-side n-type layers.
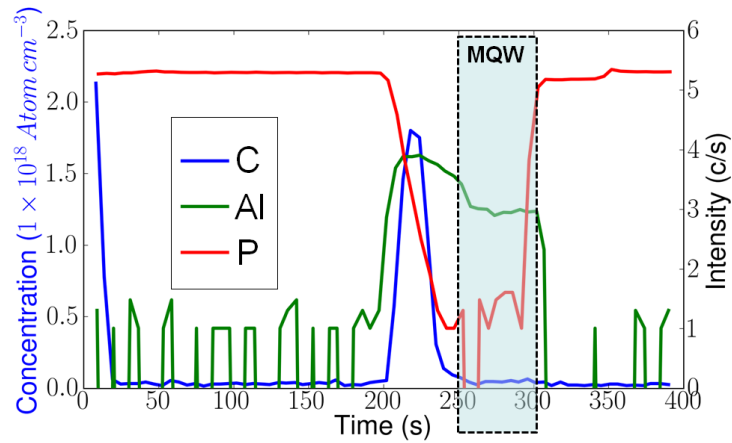
Fig. 6.2.3: SIMS profile of the concentration of carbon, aluminium and phosphorus atoms in the custom epitaxy design EAM, with the presumed location of the MQW section shaded in blue.

As shown in Fig. 6.2.3, there was a localized dip in the aluminium concentration at t=250s, which suggests that this marks the beginning of the MQW section. Similarly, there was a sharp increase in the concentration of phosphorus at t=290s and this indicates the end of the MQW section. As the carbon concentration peak situated at t=225s had almost completely decayed by the time that the local drop in aluminium concentration occurred at t=250s, it can be concluded that penetration of carbon dopants into the MQW section was negligible.

Following growth of the wafer, 1.5µm deep dry etching was employed to create shallow ridge waveguides with a width of 2.5µm. A p-type contact was added to the top-side of the waveguides and the bottom-side of the chip was metallized before the chip was cleaved into 300µm long bars. Static characterization of the fabricated waveguides on the chip was undertaken to determine the viability of each waveguide for use as an EAM. The photocurrent was measured as a function of wavelength following the application of a reverse bias across the waveguides. The photocurrent spectra for the waveguide labelled A0220 at various values for reverse bias are shown in Fig. 6.2.4.
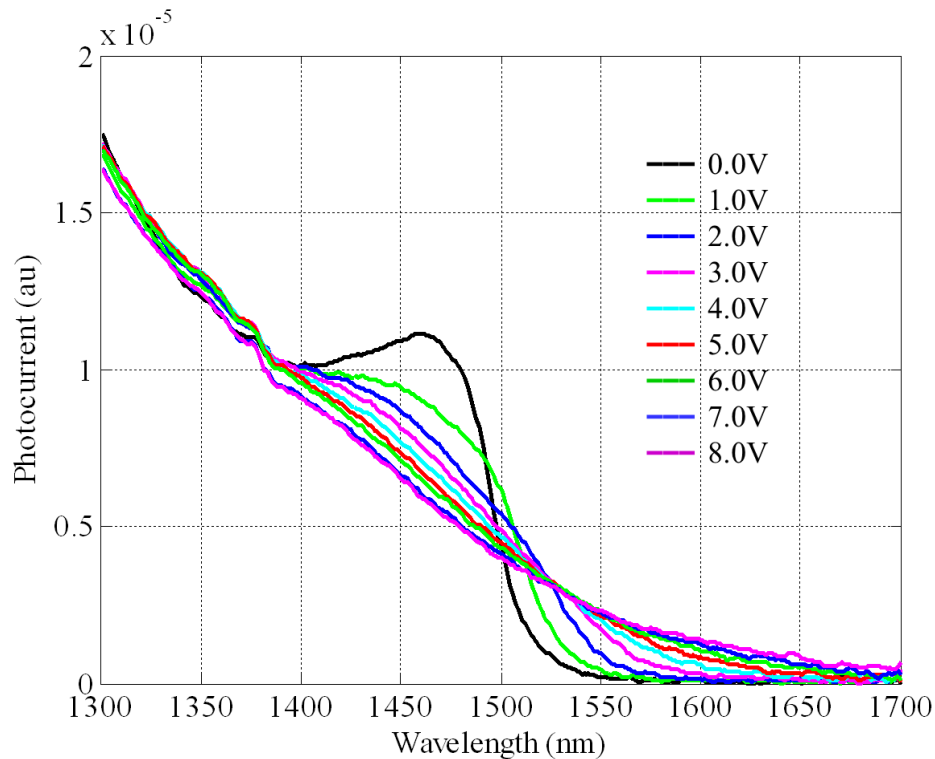
Fig. 6.2.4: Measured photocurrent spectra for EAM A0220, where the applied reverse bias was varied from 0V (black line) to 8V (pink line).

It can be seen in Fig. 6.2.4 that a room temperature excitonic feature was present in the photocurrent spectrum of EAM A0220 at a wavelength of 1470nm when no reverse bias was applied. However, this excitonic feature disappeared as the reverse bias increased.

Dynamic characterization of both EAM A0220 and a commercially available EAM (manufactured by CIP Photonics, serial no. 05045) under identical operation conditions was undertaken by the author in collaboration with Dr Chris Daunt using the TOAD loop test-bed displayed in Fig. 6.2.5. Both EAMs had an active region length of 300μm and a bandgap wavelength of approximately 1500nm. The pump and probe wavelengths were fixed at 1535nm and 1565nm respectively. The average pump power was 5.0dBm (i.e. energy per pump pulse was 4.8pJ) and the average probe power was -20.0dBm (i.e. energy per probe pulse was 15fJ) at the device input port. The pulsewidth was 4.0ps for the pump pulses and 3.0ps for the probe pulses.

Fig. 6.2.5: TOAD loop system for measuring carrier dynamics in the EAM under test.

In principle, it should have been possible to measure both the amplitude and phase dynamics in EAM A0220 and EAM 05045. However, it proved impossible to reliably determine the phase response of EAM A0220 due to a combination of factors including the high coupling loss into the waveguide and the low maximum phase shift of the device (<0.1π rad),. Thus, only amplitude evolutions for EAM A0220 and EAM 05045 are discussed in this chapter.

6.3   *Experimental carrier dynamics*

In Fig. 6.3.1, the amplitude evolutions of EAM A0220 and EAM 05045 under identical operation conditions for various values of applied reverse bias voltage are displayed. All of the graphs in Fig. 6.3.1 are normalized relative to the steady-state amplitude level before the arrival of the excite pulse at a given reverse bias.
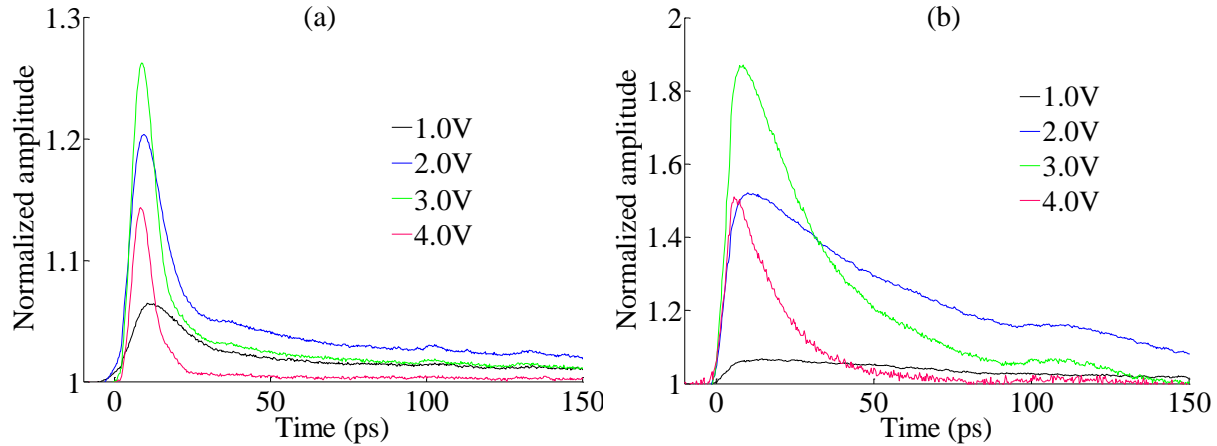
Fig. 6.3.1: Amplitude evolution of EAM A0220 and (b) EAM 05045, normalized relative to the steady-state amplitude just before the arrival of the pump pulse at each given reverse bias.

It is immediately apparent from Fig. 6.3.1 that the recovery time of EAM A0220 was considerably shorter than that of EAM 05045 at the same reverse bias. The direct comparison between the amplitude evolutions for the custom epitaxy design EAM and the commercially available EAM suggests that photo-generated carriers were swept out rapidly into the contacts in EAM A0220 due to the combination of having an offset MQW section within the intrinsic region, using carbon as the p-dopant in layers close to the MQW section and employing a graded potential step at the heterojunction between the p-type region and the intrinsic region.

To further compare the behaviour of EAM A0220 with that of EAM 05045, the amplitude evolutions of both EAMs were re-normalized relative to the maximum transmission for each value of reverse bias, and the steady-state amplitude level was subtracted away. The resulting evolutions are displayed in Fig. 6.3.2 and a substantial difference between the response times of the two devices can be discerned in the figure.
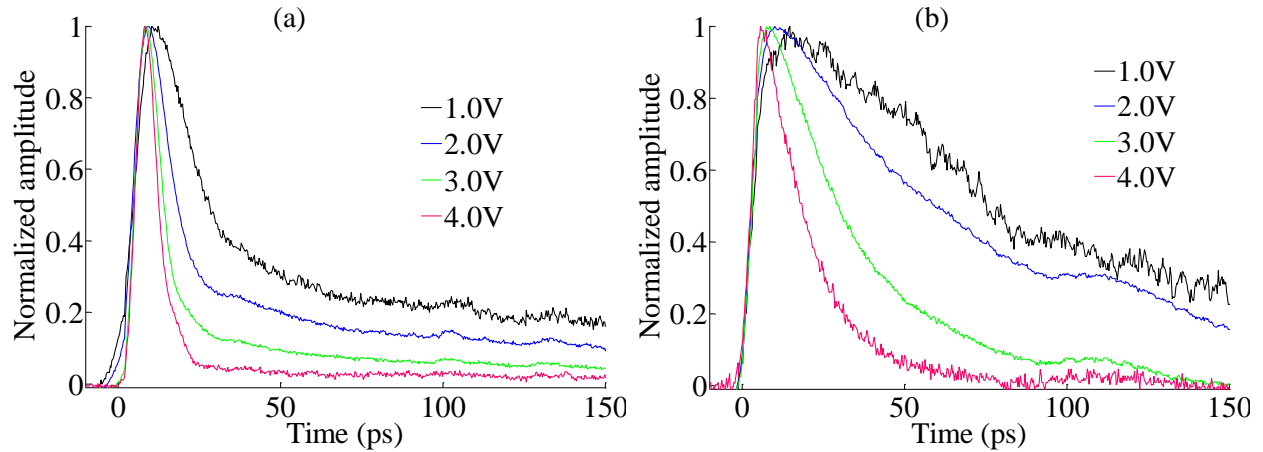
Fig. 6.3.2: Amplitude evolution for (a) EAM A0220 and (b) EAM 05045 normalized relative to the maximum change in transmission at each given reverse bias.

Fig. 6.3.3 shows the 10/90 recovery times as a function of applied reverse bias for both EAM A0220 and EAM 05045. The 10/90 recovery time for EAM A0220 was comparable to that for EAM 05045 at low values for the reverse bias (≤2.0V). However, at higher value for the reverse bias (>2.0V), the 10/90 recovery time for EAM A0220 was shorter than that for EAM 05045.
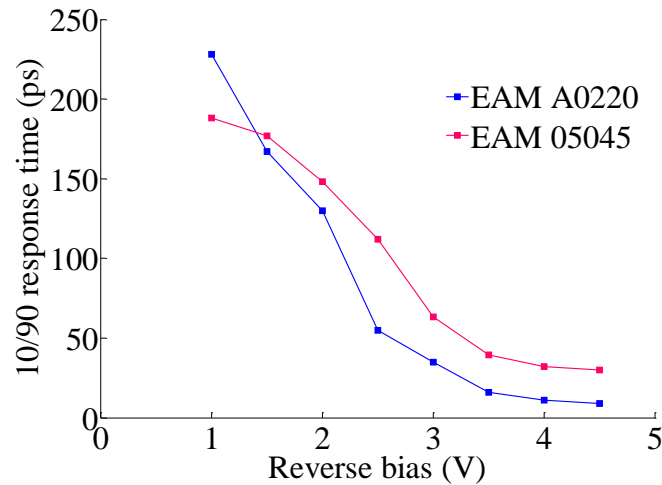
Fig. 6.3.3: Graph of 10/90 recovery time vs reverse bias for EAM A0220 and EAM 05045.

In addition to measuring the amplitude dynamics of EAM A0220, the possibility of operating the device as a photodiode was investigated. A light beam at 1550nm was input to EAM A0220 when a reverse bias of 5V was applied to the device and the photo-generated current was measured as a function of input optical power (see Fig. 6.3.4).
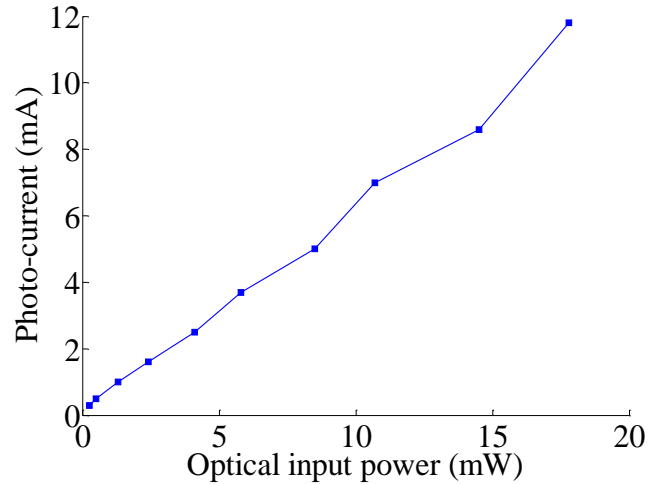
Fig. 6.3.4: Graph of photo-current vs input optical power in EAM A0220 at a wavelength of 1550nm and with a reverse bias of 5V applied to the device.

Fig. 6.3.4 shows that EAM A0220 could potentially be employed as a photodiode as the photocurrent was linearly proportional to the optical input power up to 18mW (equivalent to 12.5dBm). This is comparable to the performance of EAMs with high saturation input powers described in the literature (up to 14dBm input saturation power has been reported) [379-381]. The high input saturation power in EAM A0220 was consistent with fast carrier sweepout.

Furthermore, the extinction ratio of EAM A0220 as a function of reverse bias for various input powers and wavelengths was measured (see Fig. 6.3.5). This figure shows that at a given operating wavelength and reverse bias, the extinction ratio did not change to any significant extent when the input power was varied from 0 to 8dBm, indicating that the device had good power handling capability.
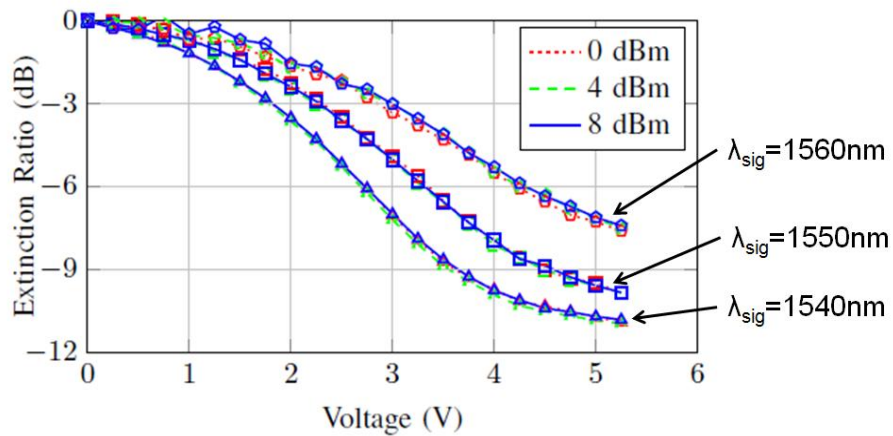
Fig. 6.3.5: Graph of extinction ratio vs applied reverse bias for EAM A0220.

6.4 Impulse response modelling

An impulse response model was developed to determine the lifetimes associated with various stages in the probe transmission evolution of EAM A0220, similar to the impulse response formalism outlined in Chapter 4 for the CSES configuration and Chapter 5 for the Si nanowires embedded in SU8 polymer. The impulse response formalism was chosen over more sophisticated first-principle models [382] as the more simple approach enabled the extraction of the time constants and strengths of various processes in the absorption evolution without the need to estimate various parameters governing the behaviour of the device e.g. the confinement factor, etc. A fitting procedure similar to the method described by J. Mork *et al* was employed, where there was a fast recovery component with a relaxation time of ~10ps followed by a slow recovery component with a relaxation time of ~100ps [156, 157]. However, it was necessary to include an additional fast rise component with a relaxation time of ~10ps to account for the shape of the probe transmission immediately after the arrival of a pump pulse.

A modelled 4.0ps $\sec h^2$ pump pulse, $y_{pump}(t)$, was convolved with the impulse response function of the EAM, $R_{EAM}(t)$, to produce $G_{conv,pump}(t)$ (see Eq. 6.4.1, Eq. 6.4.2 and Eq. 6.4.3). In these equations, A_{pump} determines the magnitude of the pump pulse, τ_{pump} is the pump pulsewidth (4.0ps), $t_{pump,0}$ determines the position in time of the pump pulse relative to the start of the amplitude coefficient impulse response, $A_{EAM,0}$ determines the magnitude of the fast component in the amplitude impulse response, $B_{EAM,0}$ determines the magnitude of the slow component in the amplitude impulse response, $\tau_{rise,fast}$ is the rise time of the fast component, $\tau_{rec,slow}$ is the recovery time of the fast component, and $\tau_{rec,slow}$ is the recovery time of the slow component. The lifetime $\tau_{rise,fast}$ may reflect the differences between the carrier escape times and transit times for electrons and holes or field-induced carrier heating and cooling effects in the EAM, $\tau_{rec,fast}$ can be attributed to carriers escaping from the quantum wells once the field screening had reached a maximum, and $\tau_{rec,slow}$ can be attributed to electrons being swept out into the n-type region and holes being swept out into the p-type region [359, 383].

$$y_{pump}(t) = A_{pump} \sec h^2 \left(\frac{1.7627(t - t_{pump,0})}{\tau_{pump}} \right) \tag{6.4.1}$$

$$R_{EAM}(t) = A_{EAM,0}\left[1 - \exp\left(\frac{-t}{\tau_{rise,fast}}\right)\right]\exp\left(\frac{-t}{\tau_{rec,fast}}\right) + B_{EAM,0}\exp\left(\frac{-t}{\tau_{rec,slow}}\right) \qquad (6.4.2)$$

$$G_{conv,pump}(t) = y_{pump}(t) * R_{EAM}(t) \qquad (6.4.3)$$

For the convolution described by Eq. 6.4.3, it was implicitly assumed that the change in transmission was proportional to the change in carrier density. In general, the change in electric field is proportional to the change in carrier density, but the transmission is a complex function of the electric field. However, for the experiments conducted on EAM A0220, the change in transmission induced by the pump pulses was relatively low (<3dB). For this reason, it was assumed that the change in electric field could be approximated as being directly proportional to the change in transmission.

The convolution of the pump with the amplitude impulse response of the EAM was subsequently convolved with a modelled 3.0ps sech^2 probe pulse (see Eq. 6.4.4), to take the effect of the probe pulse into consideration (see Eq. 6.4.5). In these equations, A_{probe} determines the magnitude of the probe pulse, $t_{probe,0}$ determines the position in time of the probe pulse relative to the start of the amplitude coefficient impulse response and τ_{probe} is the probe pulsewidth (3.0ps).

$$y_{probe}(t) = A_{probe}\ \sec h^2\left(\frac{1.7627(t - t_{probe,0})}{\tau_{probe}}\right) \qquad (6.4.4)$$

$$G_{conv,pump+probe}(t) = y_{probe}(t) * G_{conv,pump}(t) \qquad (6.4.5)$$

The parameters A_{pump}, A_{probe}, $t_{pump,0}$ and $t_{probe,0}$ were fixed while all remaining parameters were varied until a good fit between the measured transmission and the modelled transmission was achieved, as shown in Fig. 6.4.1. All of the graphs in Fig. 6.4.1 have identical scales to facilitate direct comparison between them.
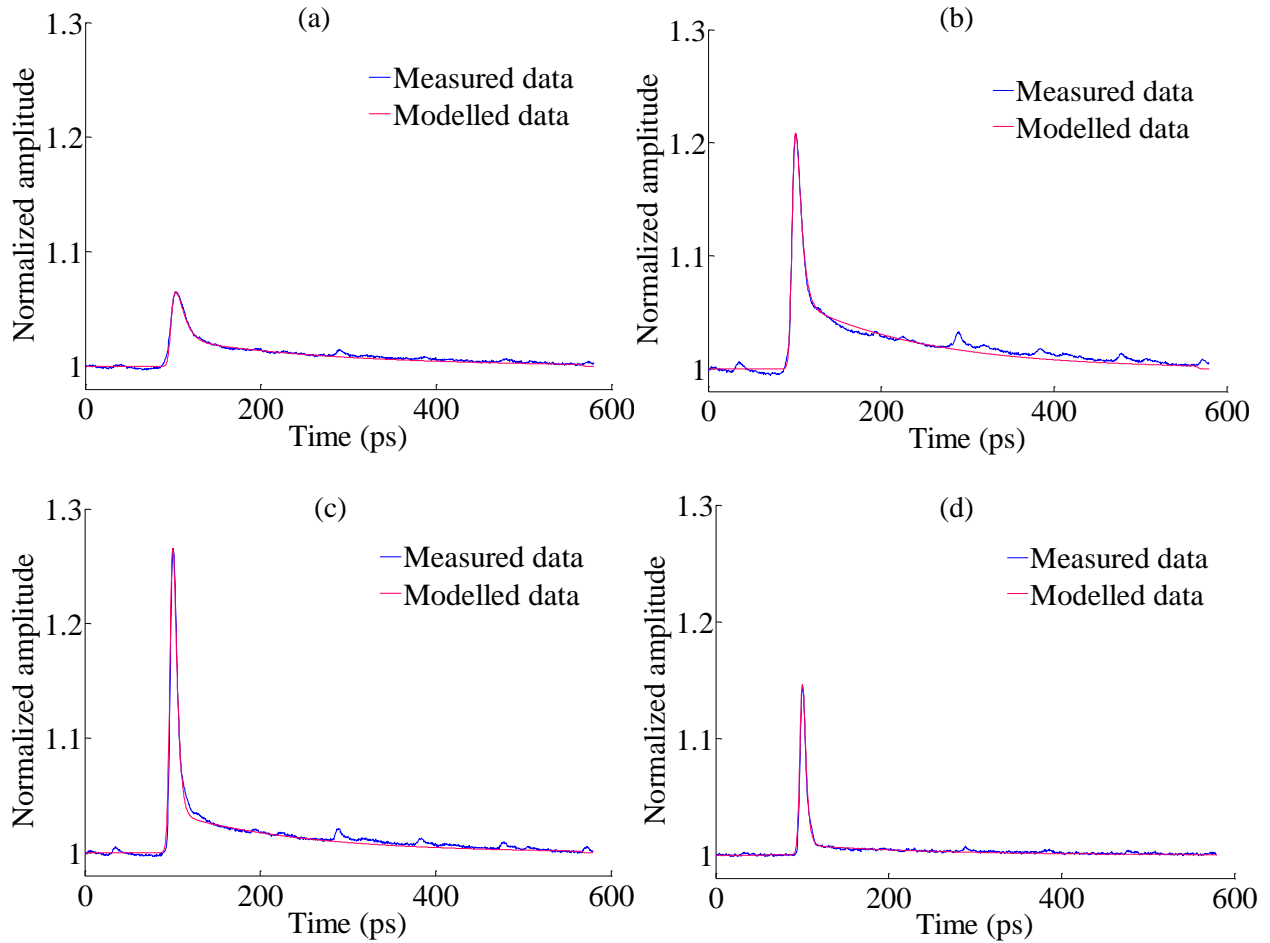
Fig. 6.4.1: Comparison between measured and modelled amplitude evolution of EAM A0220 at a reverse bias of (a) 1.0V, (b) 2.0V, (c) 3.0V and (d) 4.0V.

Using this fitting procedure, it was possible to extract the magnitude and time constants associated with the various components in the impulse response of the EAM. In Fig. 6.4.2, the fast component coefficient $A_{EAM,0}$ and the slow component coefficient $B_{EAM,0}$ are plotted as a function of reverse bias.
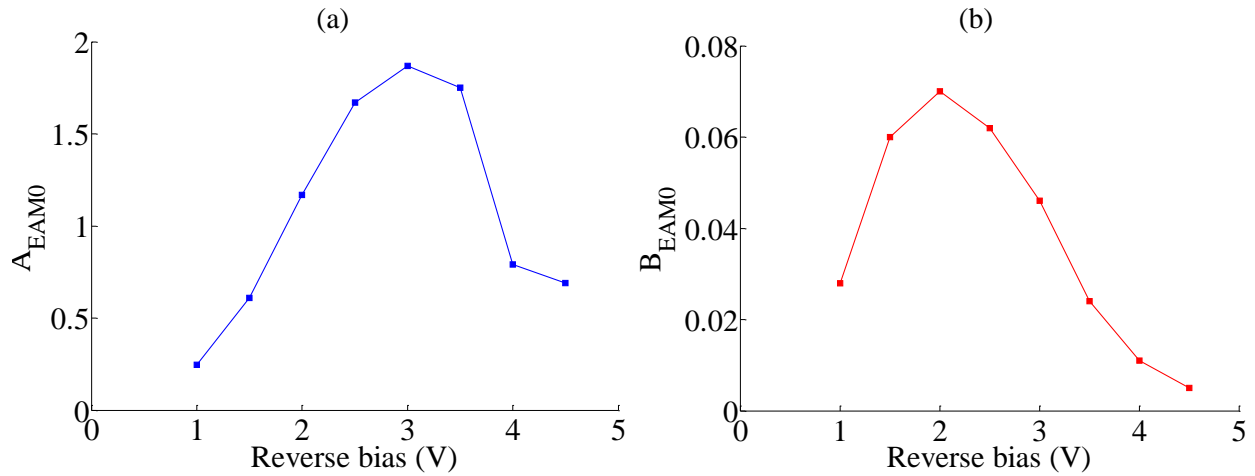
Fig. 6.4.2: Magnitude of (a) the fast component and (b) the slow component in the amplitude evolution of EAM A0220 as a function of reverse bias.

It can be discerned in Fig. 6.4.2(a) that the magnitude of the fast component increased until a reverse bias of 3.0V was reached, after which it began to gradually decrease. Similarly, Fig. 6.4.2(b) shows that the magnitude of the slow component increased until a reverse bias of 2.0V was reached, but rapidly decreased beyond this point. In fact, when the reverse bias was ≥4.0V, the slow recovery component only made a small contribution to the total amplitude response, suggesting that carriers were being efficiently swept out from the intrinsic region under these operation conditions.

In Fig. 6.4.3, the rise time and the recovery time of the fast component coefficient are plotted as a function of reverse bias.
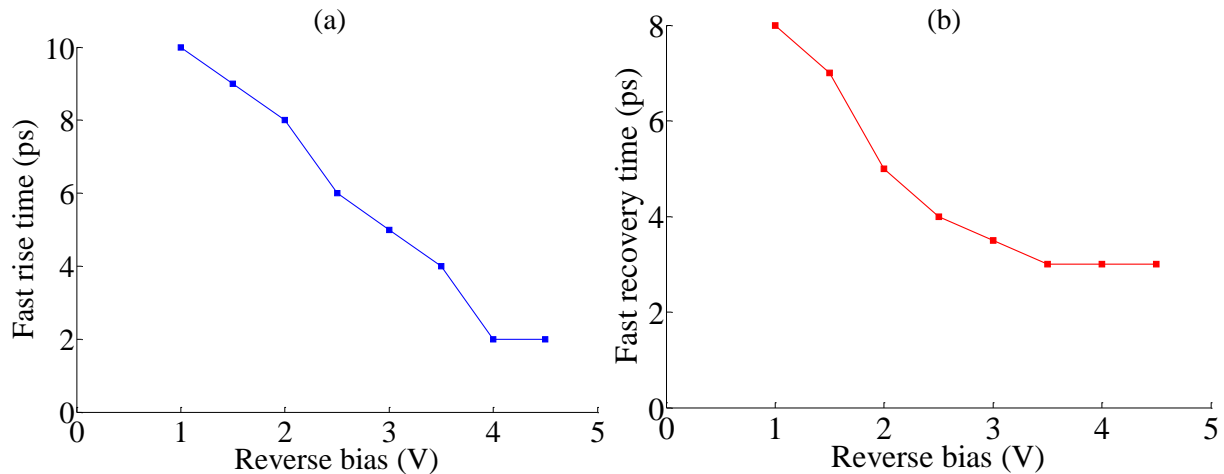
Fig. 6.4.3: (a) Rise time and (b) recovery time of the fast component in the amplitude evolution of EAM A0220 as a function of reverse bias.

It can be discerned in Fig. 6.4.3(a) that the rise time decreased as a function of reverse bias, which can be explained by the fact that the carrier escape time from the quantum wells decreased when the applied reverse bias increased. Also, Fig. 6.4.3(b) shows that the recovery time of the fast component in the amplitude evolution steadily decreased as a function of reverse bias, which can be explained by the fact that electrons were swept out of the intrinsic region faster when the applied reverse bias increased.

The trends in Fig. 6.4.3(a) and Fig. 6.4.3(b) are consistent with the process of thermionic emission of carriers escaping from the quantum wells. The lifetime for carriers escaping from a quantum well via thermionic emission is given by Eq. 6.4.6, where m_i is the mass of the carrier (either electron or hole), L_w is the width of the quantum well, k_B is the Boltzmann constant, T is temperature, e is the charge of an electron, E_b is the barrier height, V_{appl} is the applied reverse bias, V_{bi} is the built-in potential and d is total width of the intrinsic region [364].

$$\tau_{therm} = \sqrt{\frac{2\pi m_i L_w^2}{k_B T}} \exp\left(\frac{E_b - \dfrac{eL_w(V_{appl} - V_{bi})}{2d}}{k_B T}\right) \tag{6.4.6}$$

It can be deduced from Eq. 6.4.6 that the relationship between τ_{therm} and V_{appl} is given by the expression given in Eq. 6.4.7.

$$\ln\left(\frac{1}{\tau_{therm}}\right) \propto V_{appl} \tag{6.4.7}$$

The natural logarithm of the reciprocal of the rise time and the recovery time of the fast component (i.e. $ln(1/\tau_{rise,fast})$ and $ln(1/\tau_{rec,fast})$ respectively) in the amplitude response of EAM A0220 as a function of applied reverse bias is shown in Fig. 6.4.4. It can be seen that there was an approximately linear relationship between these quantities, which demonstrates that thermionic emission was the dominant mechanism through which the carriers escaped from the quantum wells.
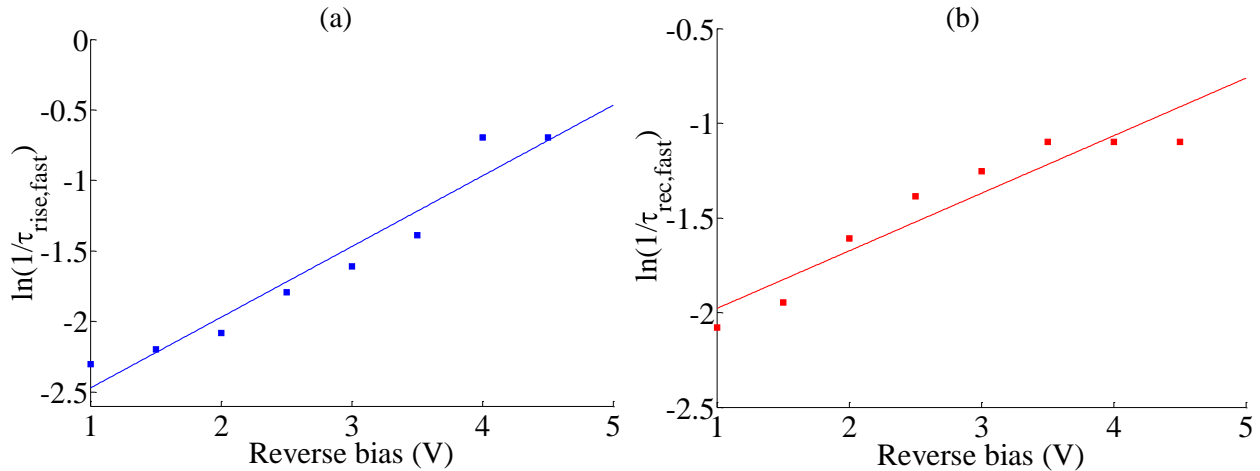
Fig. 6.4.4: (a) ln(1/τ$_{rise,fast}$) and (b) ln(1/τ$_{rec,fast}$) in the amplitude evolution of EAM A0220 as a function of reverse bias.

Similarly, the time constant of the slow recovery component in the amplitude evolution of EAM A0220 as a function of reverse bias is shown in Fig. 6.4.5. Note that the line in Fig. 6.4.5 is not a fitted line but is only meant to act as a guide to the eye.
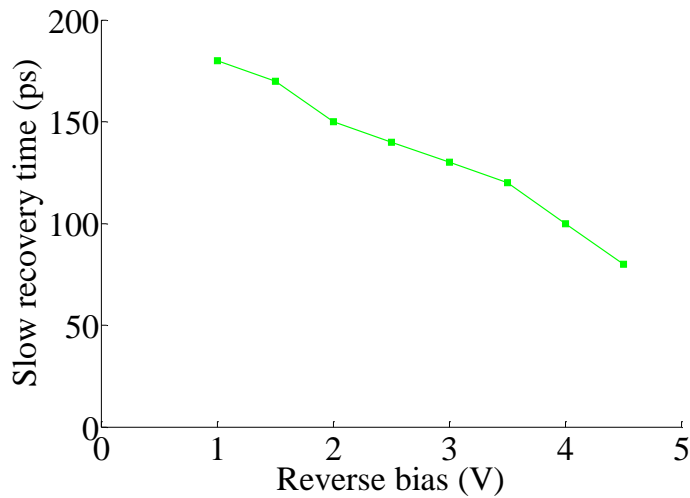
Fig. 6.4.5: Time constant of the slow recovery component in the amplitude evolution of EAM A0220 as a function of reverse bias.

Although the contribution of the slow recovery component to the total transmission diminished as the reverse bias increased, the lifetime of this component was always ≥80ps. Despite the presence of a graded potential step heterojunctions between the p-type region and the intrinsic region, it may have taken a long time (>100ps) for the holes to be swept out completely [384].

6.5   *Summary*

The amplitude dynamics of a custom epitaxy design EAM (waveguide A0220) were investigated and it was found that a 1/e lifetime of 3.0ps for the predominant ultrafast recovery component was attainable at a moderate reverse bias (4.5V), corresponding to a 10/90 recovery time of 9ps. This response time compares favourably with the fastest EAM response times reported in the literature [364, 382, 385]. EAM A0220 had an exceptionally fast response time due to a combination of the quantum wells being offset from the centre of the intrinsic region, the presence of a graded potential step at the heterojunction between the p-doped region and the intrinsic region, and using carbon as the p-dopant in layers close to the quantum wells. The fast sweepout dynamics in the EAM meant that the device had a high saturation input power (18mW), which implies that the device had good power handling capability.

By contrast, the amplitude dynamics of the commercially available EAM 05045 (which did not employ these three techniques to enhance the amplitude response) were significantly slower under the same operation conditions and the shortest 1/e recovery time measured was 9ps (which corresponded to a 10/90 recovery time of 30ps) at a moderate reverse bias (4.5V).

The development of EAMs with fast sweepout dynamics has important implications for the research field of optical signal processing. In Chapter 4, it was described how an EAM could be employed in the CSES configuration to create a high speed all-optical switch. However, unlike the case of the EAM in the CSES configuration where the primary function of the EAM was to act as an intensity filter, an EAM with optimized design features similar to those of EAM A0220 could be used as a standalone all-optical switching element.

The benefits of using a standalone EAM as a photonic switch include its low power consumption, its compact size, its potential for integration with other III-V semiconductor devices, and the fact that it conserves the polarity of the input optical signals i.e. there is no signal inversion. By contrast, devices such as single SOAs, the conventional Turbo-Switch and the CSES configuration consume far more power due to the current bias that must be applied to SOAs for them to operate (≥300mA for each SOA), even when there are no input optical signals. Furthermore, these three types of devices invert data signals and it is necessary to include interferometric arrangements to reverse this signal inversion.

Unfortunately, an EAM is an absorptive device so it requires high input pump powers (energy per pulse >1pJ) to achieve an acceptable OSNR at the output port. If EAMs were cascaded together to build logic gates, it would be necessary to include gain blocks between successive EAMs to counteract the losses experienced in each device [80]. This is a problem which is not shared by SOAs, the Turbo-Switch or the CSES configuration as these devices provide net gain to input signals. However, despite these disadvantages, it should be feasible to employ standalone EAMs with optimized design features to perform a wide range of all-optical switching operations including wavelength conversion, demultiplexing and format conversion at data rates $\geq 100\text{Gb.s}^{-1}$.

Conclusions

This thesis has presented the carrier dynamics of NLO components in a variety of device configurations which exhibited predominantly ultrafast amplitude and/or phase responses under certain specific operation conditions. All of the NLO device configurations have excellent potential for integration on a monolithic chip or a hybrid-integration PLC platform. Furthermore, these device configurations are potentially able to compete with electronics vis-à-vis power consumption and device footprint. As a result, these NLO device configurations could be deployed as high speed photonic switches in next-generation WDM, OTDM and hybrid OTDM/WDM optical networks with minimal patterning of input data signals.

It was outlined in Chapter 1 that electronic signal processing systems currently employed at core internet routers already require huge amounts of power to operate and they may be unable to continue to satisfy the consumer demand for more bandwidth without an inordinate increase in cost, size and/or energy consumption [55, 69, 386, 387]. On that basis, optical signal processing techniques may be suitable for simple tasks such as wavelength conversion, demultiplexing and format conversion at high speed to alleviate the pressure on core router infrastructure based on existing electronic signal processing technology [62, 65]. The deployment of optical signal processing techniques could necessitate fundamental changes in optical communication networks including the need to employ pulsed laser sources to produce RZ data signals that could increase the capacity of each wavelength channel to data rates $>100\text{Gb.s}^{-1}$ [65].

It is important to emphasize here that it is not feasible for optical signal processing to completely replace electronic signal processing due to issues related to energy consumption, device footprint, cost of device fabrication per unit, and the fact that there is no practical counterpart to electronic random access memory (RAM) in the optical domain [388, 389]. Instead, optical signal processing could operate in tandem with electronic signal processing, whereby the former would carry out simple "on-the-fly" tasks at high speed such as demultiplexing and wavelength conversion while the latter would perform more computationally intensive operations such as FEC, electronic equalization (for dispersion compensation),

buffering and clock recovery [10, 390]. Optical signal processing functions have yet to be implemented to a significant extent in commercial optical communication systems. Nevertheless, as the ability of DWDM networks to handle ever increasing volumes of data traffic starts to diminish using existing electronic routing technology, it is conceivable that optical signal processing could be implemented in hybrid OTDM/WDM networks when the data rate per wavelength channel exceeds $100Gb.s^{-1}$.

Experimental and theoretical studies reported in the literature have shown that optical signal processing can deliver a wide range of functionalities at high speed in a variety of NLO devices including SOAs, EAMs, Si nanowires, HNLF, PPLN and chalcogenide glass. However, there are various problems associated with each of these components including excessive energy consumption, device footprint, difficulties with device integration and/or limitations on the switching capability due to nonlinear patterning effects. In this thesis, we have presented four novel NLO device configurations which are capable of addressing most of the problems mentioned in the previous paragraph, owing to the fact that they can be integrated, they are compact, they have low total power consumption and their switching capability can be maximized by careful control of their operation conditions. The carrier dynamics in these four novel device configurations, namely a long SOA, the CSES configuration, Si nanowires embedded in SU8 polymer and an EAM with a unique custom epitaxy design, were studied in detail and this comprised the main body of work.

A comprehensive survey of the gain and phase dynamics of a long SOA was carried out for the first time and it was found that a predominantly ultrafast gain response with a full recovery time as low as 9ps could be achieved under certain operation conditions, although the corresponding full phase recovery time remained quite long (~60ps). These operation conditions include the requirement for a high current bias, the CW probe wavelength had to be close to the small signal gain peak and the pump wavelength had to be blue-shifted relative to the CW probe wavelength. The behaviour of this long SOA can be explained by the carrier density profile along the length of the device, whereby the pump signal experienced gain near the input facet but it was attenuated and filtered out beyond the midpoint of the length of the active region. Furthermore, this explanation is consistent with the fact that the carrier dynamics in this long SOA under optimized conditions were similar to those in the Turbo-Switch configuration. This type of long SOA operating under optimum conditions has several key advantages including its

ease of integration, its small footprint and the fact that it provides net gain to an incoming optical signal. However, there are several disadvantages associated with this type of photonic switch such as the strong wavelength dependence, the high current bias required and the need for a moderate power CW probe beam to be input to the device. Despite these shortcomings, it should be possible to employ this type of long SOA in applications such as demultiplexing and format conversion by operating under optimal conditions and by placing the device into an interferometric arrangement.

The amplitude and phase dynamics of the novel CSES configuration were investigated for the first time and it was found that, under certain operation conditions, they were reminiscent of the carrier dynamics in the Turbo-Switch configuration. It was found that under optimized operation conditions, namely when the pump was blue-shifted as much as possible, the CW probe was red-shifted as much as possible, there was a moderate current bias applied to each SOA ($\geq$200mA) and the EAM reverse bias was around 2.5V, the CSES amplitude response consisted of a predominant ultrafast component with a full recovery time of 10ps without any appreciable overshoot. However, the corresponding phase response remained long (~150ps). It is possible to explain the behaviour of the CSES configuration by taking the interaction of both the pump signal and the modulated CW probe signal with the impulse response in each component in the system (i.e. SOA1, EAM and SOA2) into account. The CSES configuration has several advantages including ease of integration and the fact that it provides net gain. Unfortunately, the CSES has several disadvantages including its strong wavelength dependence and the fact that fine control over the EAM reverse bias is necessary to achieve a fast response. The CSES configuration could be suitable for applications such as demultiplexing and format conversion but, to improve its switching capability, the CSES should be incorporated into an interferometer to circumvent the long phase recovery time.

The amplitude and phase dynamics of Si nanowires embedded in SU8 polymer that were fabricated in DTU Fotonik were determined for the first time and it was found that the free carrier lifetime was quite long due to passivation of the silicon by the SU8 polymer. Values for the TPA coefficient β_{tpa} (3×10^{-12}m.W^{-1}) and the nonlinear refractive index n_2 (4×10^{-18}m^2.W^{-1}) were extracted using an impulse response formalism. The impulse response model indicated that the blue wavelength chirp had the same order of magnitude as the red wavelength chirp for 3.5ps pump pulses. On the basis of this observation, a demonstration of two-copy wavelength

conversion via XPM at a data rate of 80Gb.s^{-1} was realized in Si nanowires embedded in SU8 polymer, although the author was not directly involved in this demonstration. This type of NLO device has a number of key advantages such as its compactness, its potential for integration with other photonic and/or electronic components using well-established CMOS fabrication technology, the fact that no current bias or reverse voltage bias is required, and its limited dependence on input signal wavelength (provided that dispersion engineering of the waveguides is implemented). However, there are several disadvantages with this NLO device such as the fact that it is an absorptive device and the long free carrier lifetime means that the input signal power must be kept within certain limits i.e. the intensity should be sufficiently high to induce an appreciable Kerr effect response without generating too many TPA-induced free carriers. Despite these limitations, it should be possible to exploit XPM in Si nanowires embedded in SU8 polymer for operations such as wavelength conversion, format conversion, demultiplexing and waveform sampling at high data rates ($\geq$100Gb.s^{-1}). Moreover, these devices could be deployed in applications such as on-chip and inter-chip photonic interconnects [391].

Finally, the carrier dynamics in an EAM with a unique custom epitaxy design fabricated in Tyndall National Institute were accurately measured and the device was found to have one of the fastest response times for an EAM ever reported in the literature i.e. the 10/90 recovery time was 9ps under a moderate reverse bias of 4.5V. The EAM had an extremely fast response time due to quantum well offsetting, valence band discontinuity minimization and the use of carbon as a p-type dopant. As a consequence of these fast carrier sweepout dynamics, the device had excellent power handling capability (photocurrent was linearly proportional to optical input power up to 12.5dBm). This type of NLO device has several advantages including its compactness, ease of integration, preservation of signal polarity and low power consumption. However, this type of device is absorptive, high input pump powers are required to achieve an acceptable extinction ratio for the output signal (>10dB) and the phase response is relatively low (<1.0π rad) so the switching capability of the EAM may not be substantially improved by incorporating it into an interferometer. This type of EAM could be employed as a high speed modulator with good power handling capability or it could act as a photonic switching element for operations such as demultiplexing and wavelength conversion.

Future Work

The research work described in this thesis has the potential to be extended in a variety of different ways and a few possible research directions are outlined here. For instance, following the investigation of the carrier dynamics in the long SOA, the CSES configuration, the Si nanowires in SU8 polymer and the custom epitaxy design EAM, naturally the next step would be to demonstrate optical signal processing functionalities such as wavelength conversion and demultiplexing at high bit rates ($\geq$100Gb.s^{-1}) in a variety of modulation formats using these devices to confirm whether or not they would be suitable for deployment as high speed switching elements in next-generation optical networks.

Furthermore, in relation to the CSES configuration, it would be ideal to monolithically integrate the entire system to find out if this leads to an enhanced switching capability due to reduced coupling losses between the SOAs and the EAM. In addition, it might be a valuable exercise to measure the carrier dynamics in a version of the CSES configuration where the EAM has a band edge that is red-shifted relative to the band edge of the EAM employed in the experiments for this thesis. This change in the EAM band edge should increase absorption of the pump signal while decreasing absorption of the CW probe signal at low values for the applied reverse bias (<2V).

Aside from a long SOA and the CSES configuration, it would be interesting to explore more variations on the design of the conventional Turbo-Switch configuration. For instance, an arrayed waveguide grating (AWG) could be employed to act as the filter between SOA1 and SOA2 to block the pump and transmit the modulated CW probe. This approach would be suitable for monolithic integration while avoiding the effects of self-interaction of the modulated CW probe in the EAM. In fact, E. Tangdiongga *et al* have fabricated an optical switch which is capable of wavelength conversion up to 80Gb.s^{-1} by integrating four SOAs with a four-channel AWG acting as a passband filter on an InP substrate [392]. It should be possible to apply this photonic integration technology to construct an SOA-AWG-SOA configuration, which may display carrier dynamics similar to the original Turbo-Switch.

Alternatively, it could be possible to create a modified version of the Turbo-Switch by using a two-bandgap SOA, whereby both pump and CW probe signals would be within the gain regime in SOA1, but the pump would be in the absorption regime and the CW probe would be in the gain regime in SOA2. This type of NLO device has already been studied theoretically by L. Wang *et al* [393]. Moreover, static characterization of an integrated two-bandgap SOA fabricated by K.H. Lee *et al* has been presented in the literature [394]. However, to the author's knowledge, dynamic characterization of a two-bandgap SOA designed to operate in a manner similar to the conventional Turbo-Switch has not been reported to date.

References

[1]   R. W. Tkach, "Scaling optical communications for the next decade and beyond," *Bell Labs Technical Journal,* vol. 14, pp. 3-9, 2010.

[2]   Available: http://www.internetworldstats.com/emarketing.htm

[3]   J. Baliga, K. Hinton, and R. S. Tucker, "Energy consumption of the Internet," in *Optical Internet, 2007 and the 2007 32nd Australian Conference on Optical Fibre Technology. COIN-ACOFT 2007. Joint International Conference on*, 2007, pp. 1-3.

[4]   A. M. Odlyzko, "Internet traffic growth: Sources and implications," in *ITCom 2003*, 2003, pp. 1-15.

[5]   L. G. Roberts, "Beyond Moore's law: Internet growth trends," *Computer,* vol. 33, pp. 117-119, 2000.

[6]   W. Vereecken, W. Van Heddeghem, M. Deruyck, B. Puype, B. Lannoo, W. Joseph, D. Colle, L. Martens, and P. Demeester, "Power consumption in telecommunication networks: overview and reduction strategies," *Communications Magazine, IEEE,* vol. 49, pp. 62-69, 2011.

[7]   Available: http://www.cisco.com/

[8]   W. B. M. Jr., "Perspectives on a Flexible Framework for Global Internet Growth," presented at the ETNO-ITU Workshop, Brussels, Belgium, 2012.

[9]   C. Labovitz, S. Iekel-Johnson, D. McPherson, J. Oberheide, and F. Jahanian, "Internet inter-domain traffic," in *ACM SIGCOMM Computer Communication Review*, 2010, pp. 75-86.

[10]   M. Conti, S. Chong, S. Fdida, W. Jia, H. Karl, Y.-D. Lin, P. Mähönen, M. Maier, R. Molva, and S. Uhlig, "Research challenges towards the Future Internet," *Computer Communications,* vol. 34, pp. 2115-2134, 2011.

[11]   H. Yu, D. Zheng, B. Y. Zhao, and W. Zheng, "Understanding user behavior in large-scale video-on-demand systems," in *ACM SIGOPS Operating Systems Review*, 2006, pp. 333-344.

[12]   Q. Zhang, L. Cheng, and R. Boutaba, "Cloud computing: state-of-the-art and research challenges," *Journal of Internet Services and Applications,* vol. 1, pp. 7-18, 2010.

[13]   P. W. Shumate, "Fiber-to-the-Home: 1977–2007," *Journal of Lightwave Technology,* vol. 26, pp. 1093-1103, 2008.

[14]   D. Gutierrez, K. S. Kim, S. Rotolo, F. T. An, and L. G. Kazovsky, "FTTH standards, deployments and research issues," in *8th Joint Conference on Information Sciences, Salt Lake City, Utah*, 2005, pp. 21-26.

[15]   L. Rainie, "Internet, broadband, and cell phone statistics," *Pew Internet & American Life Project,* 2010.

[16]   P. Zheng and L. M. Ni, "Spotlight: the rise of the smart phone," *Distributed Systems Online, IEEE,* vol. 7, 2006.

[17]   A. Gnauck, G. Charlet, P. Tran, P. Winzer, C. Doerr, J. Centanni, E. Burrows, T. Kawanishi, T. Sakamoto, and K. Higuma, "25.6-Tb/s WDM transmission of polarization-multiplexed RZ-DQPSK signals," *Lightwave Technology, Journal of,* vol. 26, pp. 79-84, 2008.

References

[18]   G. E. Keiser, "A review of WDM technology and applications," *Optical Fiber Technology,* vol. 5, pp. 3-39, 1999.

[19]   A. H. Gnauck, R. Tkach, A. Chraplyvy, and T. Li, "High-capacity optical transmission systems," *Journal of Lightwave Technology,* vol. 26, pp. 1032-1045, 2008.

[20]   R. Mears, L. Reekie, I. Jauncey, and D. Payne, "Low-noise erbium-doped fibre amplifier operating at 1.54 μm," *Electronics Letters,* vol. 23, pp. 1026-1028, 1987.

[21]   M. Wasfi, "Optical Fiber Amplifiers-Review," *International Journal of Communication Networks and Information Security (IJCNIS),* vol. 1, 2011.

[22]   Y. Sun, J. Judkins, A. Srivastava, L. Garrett, J. Zyskind, J. Sulhoff, C. Wolf, R. Derosier, A. Gnauck, and R. Tkach, "Transmission of 32-WDM 10-Gb/s channels over 640 km using broad-band, gain-flattened erbium-doped silica fiber amplifiers," *Photonics Technology Letters, IEEE,* vol. 9, pp. 1652-1654, 1997.

[23]   E. Ip and J. M. Kahn, "Compensation of dispersion and nonlinear impairments using digital backpropagation," *Lightwave Technology, Journal of,* vol. 26, pp. 3416-3425, 2008.

[24]   G. Charlet, J. Renaudier, H. Mardoyan, P. Tran, O. B. Pardo, F. Verluise, M. Achouche, A. Boutin, F. Blache, and J.-Y. Dupuy, "Transmission of 16.4-bit/s capacity over 2550 km using PDM QPSK modulation format and coherent receiver," *Journal of Lightwave Technology,* vol. 27, pp. 153-157, 2009.

[25]   A. Sano, H. Masuda, T. Kobayashi, M. Fujiwara, K. Horikoshi, E. Yoshida, Y. Miyamoto, M. Matsui, M. Mizoguchi, and H. Yamazaki, "Ultra-high capacity WDM transmission using spectrally-efficient PDM 16-QAM modulation and C-and extended L-band wideband optical amplification," *Journal of Lightwave Technology,* vol. 29, pp. 578-586, 2011.

[26]   D. M. Spirit, A. D. Ellis, and P. E. Barnsley, "Optical time division multiplexing: Systems and networks," *Communications Magazine, IEEE,* vol. 32, pp. 56-62, 1994.

[27]   T. Morioka, K. Uchiyama, S. Kawanishi, S. Suzuki, and M. Saruwatari, "Multiwavelength picosecond pulse source with low jitter and high optical frequency stability based on 200 nm supercontinuum filtering," *Electronics Letters,* vol. 31, pp. 1064-1066, 1995.

[28]   R. Ludwig, D. Stefan, A. Ehrhardt, L. Kuller, W. Pieper, and H. G. Weber, "A tunable femtosecond modelocked semiconductor laser for applications in OTDM-systems," *IEICE transactions on electronics,* vol. 81, pp. 140-145, 1998.

[29]   A. Ellis, R. Manning, I. Phillips, and D. Nesset, "1.6 ps pulse generation at 40 GHz in phaselocked ring laser incorporating highly nonlinear fibre for application to 160 Gbit/s OTDM networks," *Electronics Letters,* vol. 35, pp. 645-646, 1999.

[30]   S.-W. Seo, K. Bergman, and P. R. Prucnal, "Transparent optical networks with time-division multiplexing," *Selected Areas in Communications, IEEE Journal on,* vol. 14, pp. 1039-1051, 1996.

[31]   I. Ogura, H. Kurita, T. Sasaki, and H. Yokoyama, "Precise operation-frequency control of monolithic mode-locked laser diodes for high-speed optical communication and all-optical signal processing," *Optical and Quantum Electronics,* vol. 33, pp. 709-725, 2001.

[32]   K. Tamura, H. Haus, and E. Ippen, "Self-starting additive pulse mode-locked erbium fibre ring laser," *Electronics Letters,* vol. 28, pp. 2226-2228, 1992.

[33]   M. O'Mahony, "Optical multiplexing in fiber networks: progress in WDM and OTDM," *Communications Magazine, IEEE,* vol. 33, pp. 82-88, 1995.

References

[34]   P. M. Anandarajah, A. M. Clarke, C. Guignard, L. Bramerie, L. P. Barry, J. D. Harvey, and J. C. Simon, "System-performance analysis of optimized gain-switched pulse source employed in 40-and 80-Gb/s OTDM systems," *Journal of Lightwave Technology,* vol. 25, pp. 1495-1502, 2007.

[35]   Y. Takushima and K. Kikuchi, "10-GHz, over 20-channel multiwavelength pulse source by slicing super-continuum spectrum generated in normal-dispersion fiber," *Photonics Technology Letters, IEEE,* vol. 11, pp. 322-324, 1999.

[36]   I. Morohashi, T. Sakamoto, H. Sotobayashi, T. Kawanishi, I. Hosako, and M. Tsuchiya, "Widely repetition-tunable 200 fs pulse source using a Mach–Zehnder-modulator-based flat comb generator and dispersion-flattened dispersion-decreasing fiber," *Optics letters,* vol. 33, pp. 1192-1194, 2008.

[37]   H. C. H. Mulvad, M. Galili, L. K. Oxenløwe, H. Hu, A. T. Clausen, J. B. Jensen, C. Peucheret, and P. Jeppesen, "Demonstration of 5.1 Tbit/s data capacity on a single-wavelength channel," *Optics Express,* vol. 18, pp. 1438-1443, 2010.

[38]   T. Richter, E. Palushani, C. Schmidt-Langhorst, M. Nölle, R. Ludwig, and C. Schubert, "Single wavelength channel 10.2 Tb/s TDM-data capacity using 16-QAM and coherent detection," in *Optical Fiber Communication Conference*, 2011.

[39]   H. Hansen Mulvad, L. Oxenlwe, M. Galili, A. Clausen, L. Gruner-Nielsen, and P. Jeppesen, "1.28 Tbit/s single-polarisation serial OOK optical data generation and demultiplexing," *Electronics Letters,* vol. 45, pp. 280-281, 2009.

[40]   M. Nakazawa, T. Yamamoto, and K. Tamura, "1.28 Tbit/s-70 km OTDM transmission using third-and fourth-order simultaneous dispersion compensation with a phase modulator," *Electronics Letters,* vol. 36, pp. 2027-2029, 2000.

[41]   R. J. Manning, X. Yang, R. P. Webb, R. Giller, F. C. Garcia Gunning, and A. D. Ellis, "The turbo-switch-a novel technique to increase the high-speed response of SOAs for wavelength conversion," in *Optical Fiber Communications Conference*, 2006.

[42]   K. Uchiyama and T. Morioka, "All-optical signal processing for 160 Gbit/s/channel OTDM/WDM systems," in *Optical Fiber Communication Conference and Exhibit, 2001. OFC 2001*, 2001, pp. ThH2-ThH2.

[43]   X. Liu, A. Vinokurov, and L. G. Mason, "Performance comparison of OTDM and OBS scheduling for agile all-photonic network," in *Proc. IFIP Metropolitan Area Network Conference, Ho Chi Minh City, Vietnam*, 2005.

[44]   B. Zhang, L. Zhang, L.-S. Yan, I. Fazal, J.-Y. Yang, and A. Willner, "Continuously-tunable, bit-rate variable OTDM using broadband SBS slow-light delay line," *Optics Express,* vol. 15, pp. 8317-8322, 2007.

[45]   K. Uchiyama, E. Hashimoto, and Y. Yamabalashi, "Highly precise bit-phase synchronization technique for an optically controlled time-division demultiplexer," *Photonics Technology Letters, IEEE,* vol. 12, pp. 915-917, 2000.

[46]   S. Kieckbusch, S. Ferber, H. Rosenfeldt, R. Ludwig, C. Boerner, A. Ehrhardt, E. Brinkmeyer, and H.-G. Weber, "Automatic PMD compensator in a 160-Gb/s OTDM transmission over deployed fiber using RZ-DPSK modulation format," *Journal of Lightwave Technology,* vol. 23, p. 165, 2005.

[47]   H. Sunnerud, M. Karlsson, C. Xie, and P. A. Andrekson, "Polarization-mode dispersion in high-speed fiber-optic transmission systems," *Lightwave Technology, Journal of,* vol. 20, pp. 2204-2219, 2002.

[48]   Y. Zhang, P. Chowdhury, M. Tornatore, and B. Mukherjee, "Energy efficiency in telecom optical networks," *Communications Surveys & Tutorials, IEEE,* vol. 12, pp. 441-458, 2010.

[49]   A. A. Saleh and J. M. Simmons, "Evolution toward the next-generation core optical network," *Journal of Lightwave Technology,* vol. 24, p. 3303, 2006.

[50]   Q. Zeng, H. Liu, W. Hu, and C. Jiang, "Advances in DWDM Optical Networking Technology."

[51]   R. Takahashi, T. Nakahara, K. Takahata, H. Takenouchi, T. Yasui, N. Kondo, and H. Suzuki, "Ultrafast optoelectronic packet processing for asynchronous, optical-packet-switched networks [Invited]," *Journal of Optical Networking,* vol. 3, pp. 914-930, 2004.

[52]   M. Mellia, E. Leonardi, M. Feletig, R. Gaudino, and F. Neri, "Exploiting OTDM technology in WDM networks," in *INFOCOM 2002. Twenty-First Annual Joint Conference of the IEEE Computer and Communications Societies. Proceedings. IEEE*, 2002, pp. 1822-1831.

[53]   A. A. Aboketaf, L. Cao, D. Adams, A. W. Elshaari, S. F. Preble, M. T. Crowley, L. F. Lester, and P. Ampadu, "Hybrid OTDM and WDM for Multicore Optical Communication."

[54]   H. Sotobayashi, W. Chujo, and T. Ozeki, "Hierarchical hybrid OTDM/WDM network," in *All-Optical Networking: Existing and Emerging Architecture and Applications/Dynamic Enablers of Next-Generation Optical Communications Systems/Fast Optical Processing in Optical Transmission/VCSEL and*, 2002, pp. WF3-47-WF3-48.

[55]   K. Hinton, J. Baliga, M. Feng, R. Ayre, and R. S. Tucker, "Power consumption and energy efficiency in the internet," *Network, IEEE,* vol. 25, pp. 6-12, 2011.

[56]   R. S. Tucker, R. Parthiban, J. Baliga, K. Hinton, R. W. Ayre, and W. V. Sorin, "Evolution of WDM optical IP networks: A cost and energy perspective," *Journal of Lightwave Technology,* vol. 27, pp. 243-252, 2009.

[57]   R. Ramaswami, "Optical networking technologies: What worked and what didn't," *Communications Magazine, IEEE,* vol. 44, pp. 132-139, 2006.

[58]   K. Roberts, D. Beckett, D. Boertjes, J. Berthold, and C. Laperle, "100G and beyond with digital coherent signal processing," *Communications Magazine, IEEE,* vol. 48, pp. 62-69, 2010.

[59]   E. Yamazaki, M. Tomizawa, and Y. Miyamoto, "100-Gb/s optical transport network and beyond employing digital signal processing," *Communications Magazine, IEEE,* vol. 50, pp. s43-s49, 2012.

[60]   J. Baliga, R. Ayre, K. Hinton, and R. Tucker, "Photonic switching and the energy bottleneck," in *Photonics in Switching, 2007*, 2007, pp. 125-126.

[61]   I. Kang, C. Dorrer, L. Zhang, M. Dinu, M. Rasras, L. L. Buhl, S. Cabot, A. Bhardwaj, X. Liu, and M. A. Cappuzzo, "Characterization of the dynamical processes in all-optical signal processing using semiconductor optical amplifiers," *Selected Topics in Quantum Electronics, IEEE Journal of,* vol. 14, pp. 758-769, 2008.

[62]   S. A. Hamilton, B. S. Robinson, T. E. Murphy, S. J. Savage, and E. P. Ippen, "100 Gb/s optical time-division multiplexed networks," *Journal of Lightwave Technology,* vol. 20, p. 2086, 2002.

[63]   H. Hu, E. Palushani, M. Galili, H. C. H. Mulvad, A. Clausen, L. K. Oxenløwe, and P. Jeppesen, "640 Gbit/s and 1.28 Tbit/s polarisation insensitive all optical wavelength conversion," *Optics Express,* vol. 18, pp. 9961-9966, 2010.

[64]   K. Vlachos, N. Pleros, C. Bintjas, G. Theophilopoulos, and H. Avramopoulos, "Ultrafast time-domain technology and its application in all-optical signal processing," *Lightwave Technology, Journal of,* vol. 21, pp. 1857-1868, 2003.

[65]   D. Cotter, R. Manning, K. Blow, A. Ellis, A. Kelly, D. Nesset, I. Phillips, A. Poustie, and D. Rogers, "Nonlinear optics for high-speed digital information processing," *Science,* vol. 286, pp. 1523-1528, 1999.

[66]   R. Stabile and K. Williams, "Photonic Integrated Semiconductor Optical Amplifier Switch Circuits," in *Advances in Optical Amplifiers*, P. P. Urquahart, Ed.: InTech, 2011.

[67]   A. Zapata-Beghelli and P. Bayvel, "Dynamic versus static wavelength-routed optical networks," *Journal of Lightwave Technology,* vol. 26, pp. 3403-3415, 2008.

[68]   X. Wu, W. R. Peng, V. Arbab, J. Wang, and A. Willner, "Tunable optical wavelength conversion of OFDM signal using a periodically-poled lithium niobate waveguide," *Optics Express,* vol. 17, pp. 9177-9182, 2009.

[69]   K. Hinton, J. Baliga, R. Ayre, and R. S. Tucker, "The future Internet-An energy consumption perspective," in *OptoElectronics and Communications Conference, 2009. OECC 2009. 14th*, 2009, pp. 1-2.

[70]   S. Diez, C. Schubert, R. Ludwig, H. J. Ehrke, U. Feiste, C. Schmidt, and H. Weber, "160 Gbit/s all-optical demultiplexing using hybrid gain-transparent SOA Mach-Zehnder interferometer," *Electronics Letters,* vol. 36, pp. 1484-1486, 2000.

[71]   C. Schubert, S. Diez, J. Berger, R. Ludwig, U. Feiste, H. Weber, G. Toptchiyski, K. Petermann, and V. Krajinovic, "160-Gb/s all-optical demultiplexing using a gain-transparent ultrafast-nonlinear interferometer (GT-UNI)," *Photonics Technology Letters, IEEE,* vol. 13, pp. 475-477, 2001.

[72]   X. Yang, A. Mishra, R. Manning, R. Webb, and A. Ellis, "All-optical 42.6 Gbit/s NRZ to RZ format conversion by cross-phase modulation in single SOA," *Electronics Letters,* vol. 43, pp. 890-892, 2007.

[73]   J. Yu, G. K. Chang, J. Barry, and Y. Su, "40Gbit/s signal format conversion from NRZ to RZ using a Mach-Zehnder delay interferometer," *Optics communications,* vol. 248, pp. 419-422, 2005.

[74]   N. Calabretta, H. de Waardt, G. Khoe, and H. Dorren, "Ultrafast asynchronous multioutput all-optical header processor," *Photonics Technology Letters, IEEE,* vol. 16, pp. 1182-1184, 2004.

[75]   R. P. Webb, X. Yang, R. Manning, G. Maxwell, A. Poustie, S. Lardenois, and D. Cotter, "All-Optical Header Processing Using Semiconductor Optical Amplifiers," in *Frontiers in Optics*, 2009.

[76]   J. Leuthold, C. Koos, and W. Freude, "Nonlinear silicon photonics," *Nature photonics,* vol. 4, pp. 535-544, 2010.

[77]   R. Dekker, N. Usechak, M. Först, and A. Driessen, "Ultrafast nonlinear all-optical processes in silicon-on-insulator waveguides," *Journal of physics D: applied physics,* vol. 40, p. R249, 2007.

[78]   G. I. Stegeman and W. E. Torruellas, "Nonlinear materials for information processing and communications," *Philosophical Transactions of the Royal Society of London. Series A: Mathematical, Physical and Engineering Sciences,* vol. 354, pp. 745-756, 1996.

References

[79] R. S. Tucker and K. Hinton, "Energy consumption and energy density in optical and electronic signal processing," *Photonics Journal, IEEE,* vol. 3, pp. 821-833, 2011.

[80] K. Hinton, G. Raskutti, P. M. Farrell, and R. S. Tucker, "Switching energy and device size limits on digital photonic signal processing technologies," *Selected Topics in Quantum Electronics, IEEE Journal of,* vol. 14, pp. 938-945, 2008.

[81] M. J. Connelly, *Semiconductor optical amplifiers*: Springer, 2002.

[82] S. Kitamura, H. Hatakeyama, T. Tamanuki, T. Sasaki, K. Komatsu, and M. Yamaguchi, "Angled-facet S-bend semiconductor optical amplifiers for high-gain and large-extinction ratio," *Photonics Technology Letters, IEEE,* vol. 11, pp. 788-790, 1999.

[83] T. Ito, N. Yoshimoto, K. Magari, and H. Sugiura, "Wide-band polarization-independent tensile-strained InGaAs MQW-SOA gate," *Photonics Technology Letters, IEEE,* vol. 10, pp. 657-659, 1998.

[84] L.-Q. Guo and M. J. Connelly, "Signal-induced birefringence and dichroism in a tensile-strained bulk semiconductor optical amplifier and its application to wavelength conversion," *Journal of Lightwave Technology,* vol. 23, p. 4037, 2005.

[85] A. Bilenca, R. Alizon, V. Mikhelashvili, G. Eisenstein, R. Schwertberger, D. Gold, J. Reithmaier, and A. Forchel, "InAs/InP 1550 nm quantum dash semiconductor optical amplifiers," *Electronics Letters,* vol. 38, pp. 1350-1351, 2002.

[86] M. Sugawara, T. Akiyama, N. Hatori, Y. Nakata, H. Ebe, and H. Ishikawa, "Quantum-dot semiconductor optical amplifiers for high-bit-rate signal processing up to 160 Gb s-1 and a new scheme of 3R regenerators," *Measurement Science and Technology,* vol. 13, p. 1683, 2002.

[87] G. Contestabile, A. Maruta, S. Sekiguchi, K. Morito, M. Sugawara, and K. Kitayama, "160 Gb/s cross gain modulation in quantum dot SOA at 1550 nm," in *Optical Communication, 2009. ECOC'09. 35th European Conference on*, 2009, pp. 1-2.

[88] K. Solis-Trapala, Y. An, R. Notzel, H. J. Dorren, and R. J. Manning, "Gain and Phase Dynamics of an InAs/InGaAsP/InP Quantum-Dot Semiconductor Optical Amplifier at 1.55 μm," in *Nonlinear Photonics*, 2010.

[89] M. Sugawara, H. Ebe, N. Hatori, M. Ishida, Y. Arakawa, T. Akiyama, K. Otsubo, and Y. Nakata, "Theory of optical signal amplification and processing by quantum-dot semiconductor optical amplifiers," *Physical Review B,* vol. 69, p. 235332, 2004.

[90] N. Kim, J. Oh, M. Kim, D. Lee, S. Pyun, W. Jeong, and J. Jang, "Gain characteristics of InAs∕ InGaAsP quantum dot semiconductor optical amplifiers at 1.5 μm," *Applied Physics Letters,* vol. 90, p. 241108, 2007.

[91] Y. Ben-Ezra, M. Haridim, and B. Lembrikov, "Theoretical analysis of gain-recovery time and chirp in QD-SOA," *Photonics Technology Letters, IEEE,* vol. 17, pp. 1803-1805, 2005.

[92] T. Akiyama, M. Sugawara, and Y. Arakawa, "Quantum-dot semiconductor optical amplifiers," *Proceedings of the IEEE,* vol. 95, pp. 1757-1766, 2007.

[93] H. Dorren, D. Lenstra, Y. Liu, M. T. Hill, and G.-D. Khoe, "Nonlinear polarization rotation in semiconductor optical amplifiers: Theory and application to all-optical flip-flop memories," *Quantum Electronics, IEEE Journal of,* vol. 39, pp. 141-148, 2003.

[94] D. Nesset, T. Kelly, and D. Marcenac, "All-optical wavelength conversion using SOA nonlinearities," *Communications Magazine, IEEE,* vol. 36, pp. 56-61, 1998.

[95] C.-F. Lin, Y.-S. Su, C.-H. Wu, and G. S. Shmavonyan, "Influence of separate confinement heterostructure on emission bandwidth of InGaAsP superluminescent

diodes/semiconductor optical amplifiers with nonidentical multiple quantum wells," *Photonics Technology Letters, IEEE,* vol. 16, pp. 1441-1443, 2004.

[96] R. Manning, A. Ellis, A. Poustie, and K. Blow, "Semiconductor laser amplifiers for ultrafast all-optical signal processing," *JOSA B,* vol. 14, pp. 3204-3216, 1997.

[97] C. Su, J. Schlafer, J. Manning, and R. Olshansky, "Measurement of radiative recombination coefficient and carrier leakage in 1.3 μm InGaAsP lasers with lightly doped active layers," *Electronics Letters,* vol. 18, p. 1108, 1982.

[98] G. Talli and M. Adams, "Amplified spontaneous emission in semiconductor optical amplifiers: modelling and experiments," *Optics communications,* vol. 218, pp. 161-166, 2003.

[99] W. Shockley and W. Read Jr, "Statistics of the recombinations of holes and electrons," *Physical Review,* vol. 87, p. 835, 1952.

[100] R. Olshansky, C. Su, J. Manning, and W. Powazinik, "Measurement of radiative and nonradiative recombination rates in InGaAsP and AlGaAs light sources," *Quantum Electronics, IEEE Journal of,* vol. 20, pp. 838-854, 1984.

[101] E. Yablonovitch and E. Kane, "Band structure engineering of semiconductor lasers for optical communications," *Lightwave Technology, Journal of,* vol. 6, pp. 1292-1299, 1988.

[102] J. Dong, X. Zhang, F. Wang, W. Hong, and D. Huang, "Experimental study of SOA-based NRZ-to-PRZ conversion and distortion elimination of amplified NRZ signal using spectral filtering," *Optics communications,* vol. 281, pp. 5618-5624, 2008.

[103] H. N. Tan, M. Matsuura, and N. Kishi, "Enhancement of input power dynamic range for multiwavelength amplification and optical signal processing in a semiconductor optical amplifier using holding beam effect," *Journal of Lightwave Technology,* vol. 28, pp. 2593-2602, 2010.

[104] J. Sakaguchi, R. Suzuki, Y. Ueno, M. L. Nielsen, and J. Mork, "Reduction of Nonlinear Patteming Effects in SOA-based All-Optical Switches using Optical Filtering," in *Optical Fiber Communications Conference*, 2005.

[105] K. Hall, G. Lenz, A. Darwish, and E. Ippen, "Subpicosecond gain and index nonlinearities in InGaAsP diode lasers," *Optics communications,* vol. 111, pp. 589-612, 1994.

[106] W. Z. Lin, R. Schoenlein, J. Fujimoto, and E. Ippen, "Femtosecond absorption saturation studies of hot carriers in GaAs and AlGaAs," *Quantum Electronics, IEEE Journal of,* vol. 24, pp. 267-275, 1988.

[107] B. N. Gomatam and A. P. DeFonzo, "Theory of hot carrier effects on nonlinear gain in GaAs-GaAlAs lasers and amplifiers," *Quantum Electronics, IEEE Journal of,* vol. 26, pp. 1689-1704, 1990.

[108] A. D'Ottavi, E. Iannone, A. Mecozzi, S. Scotti, P. Spano, R. Dall'Ara, G. Guekos, and J. Eckner, "Ultrafast gain and refractive index dynamics of semiconductor amplifiers measured by four-wave mixing," in *Semiconductor Laser Conference, 1994., 14th IEEE International*, 1994, pp. 63-64.

[109] R. Giller, R. J. Manning, and D. Cotter, "Gain and phase recovery of optically excited semiconductor optical amplifiers," *Photonics Technology Letters, IEEE,* vol. 18, pp. 1061-1063, 2006.

[110] L. Westbrook and M. Adams, "Simple expressions for the linewidth enhancement factor in direct-gap semiconductors," 1987, pp. 209-214.

References

[111] C. Schubert, "Interferometric gates for all-optical signal processing," PhD thesis, School of Optics and Photonics, Karlsruhe Institute of Technology, 2004.

[112] J. Wang, A. Maitra, C. G. Poulton, W. Freude, and J. Leuthold, "Temporal dynamics of the alpha factor in semiconductor optical amplifiers," *Journal of Lightwave Technology,* vol. 25, pp. 891-900, 2007.

[113] F. D. Mahad, S. M. Idrus, and D. Forsyth, "Comparative performance testing of SOA wavelength conversion techniques for future all-optical systems," *Optik-International Journal for Light and Electron Optics,* vol. 124, pp. 1254-1269, 2013.

[114] H. Lee, H. Yoon, Y. Kim, and J. Jeong, "Theoretical study of frequency chirping and extinction ratio of wavelength-converted optical signals by XGM and XPM using SOA's," *Quantum Electronics, IEEE Journal of,* vol. 35, pp. 1213-1219, 1999.

[115] H. J. Lee, M. Sohn, K. Kim, and H. G. Kim, "Wavelength dependent performance of a wavelength converter based on cross-gain modulation and birefringence of a semiconductor optical amplifier," *Photonics Technology Letters, IEEE,* vol. 11, pp. 185-187, 1999.

[116] A. Poustie, "Semiconductor devices for all-optical signal processing," in *Optical Communication, 2005. ECOC 2005. 31st European Conference on*, 2005, pp. 475-478.

[117] D. F. Geraghty, R. B. Lee, M. Verdiell, M. Ziari, A. Mathur, and K. J. Vahala, "Wavelength conversion for WDM communication systems using four-wave mixing in semiconductor optical amplifiers," *Selected Topics in Quantum Electronics, IEEE Journal of,* vol. 3, pp. 1146-1155, 1997.

[118] G. Contestabile, L. Banchi, M. Presi, and E. Ciaramella, "Investigation of transparency of FWM in SOA to advanced modulation formats involving intensity, phase, and polarization multiplexing," *Journal of Lightwave Technology,* vol. 27, pp. 4256-4261, 2009.

[119] D. Kong, Y. Li, H. Wang, X. Zhang, J. Zhang, J. Wu, and J. Lin, "All-Optical xor Gates for QPSK Signals Based on Four-Wave Mixing in a Semiconductor Optical Amplifier," *Photonics Technology Letters, IEEE,* vol. 24, pp. 988-990, 2012.

[120] H. Sotobayashi and K. Kitayama, "All-optical simultaneous code and wavelength conversion of 10 Gbit/s BPSK codes by four-wave mixing in semiconductor optical amplifier for optical code division multiplexing," *Electronics Letters,* vol. 35, pp. 1091-1093, 1999.

[121] S. Diez, C. Schmidt, R. Ludwig, H. G. Weber, K. Obermann, S. Kindt, I. Koltchanov, and K. Petermann, "Four-wave mixing in semiconductor optical amplifiers for frequency conversion and fast optical switching," *Selected Topics in Quantum Electronics, IEEE Journal of,* vol. 3, pp. 1131-1145, 1997.

[122] S.-L. Lee, P.-M. Gong, and C.-T. Yang, "Performance enhancement on SOA-based four-wave-mixing wavelength conversion using an assisted beam," *Photonics Technology Letters, IEEE,* vol. 14, pp. 1713-1715, 2002.

[123] R. P. Webb, M. J. Power, and R. J. Manning, " Phase sensitive frequency conversion of quadrature modulated signals " *Optics Express,* vol. 21, pp. 12713-12727, 2013.

[124] L. Zhang, I. Kang, A. Bhardwaj, N. Sauer, S. Cabot, J. Jaques, and D. Neilson, "Reduced recovery time semiconductor optical amplifier using p-type-doped multiple quantum wells," *Photonics Technology Letters, IEEE,* vol. 18, pp. 2323-2325, 2006.

[125] L. Zhang, I. Kang, A. Bhardwaj, N. Sauer, S. Cabot, J. Jaques, and D. Neilson, "Significant reduction of recovery time in semiconductor optical amplifier using p type

modulation doped MQW," in *Optical Communications, 2006. ECOC 2006. European Conference on*, 2006, pp. 1-2.

[126] Y. Liu, E. Tangdiongga, Z. Li, S. Zhang, H. Waardt, G. Khoe, and H. Dorren, "Error-free all-optical wavelength conversion at 160 Gb/s using a semiconductor optical amplifier and an optical bandpass filter," *Journal of Lightwave Technology,* vol. 24, pp. 230-235, 2006.

[127] M. L. Nielsen, B. Lavigne, and B. Dagens, "Polarity-preserving SOA-based wavelength conversion at 40 Gbit/s using bandpass filtering," *Electronics Letters,* vol. 39, pp. 1334-1335, 2003.

[128] G. Talli and M. Adams, "Gain recovery acceleration in semiconductor optical amplifiers employing a holding beam," *Optics communications,* vol. 245, pp. 363-370, 2005.

[129] R. P. Giller, R. J. Manning, and D. Cotter, "Recovery dynamics of the'Turbo-switch'," in *Optical Amplifiers and their Applications*, 2006.

[130] E. Zhou, F. Öhman, C. Cheng, X. Zhang, W. Hong, J. Mørk, and D. Huang, "Reduction of patterning effects in SOA-based wavelength converters by combining cross-gain and cross-absorption modulation," *Optics Express,* vol. 16, pp. 21522-21528, 2008.

[131] M. T. Hill, E. Tangdiongga, H. De Waardt, G. Khoe, and H. Dorren, "Carrier recovery time in semiconductor optical amplifiers that employ holding beams," *Optics letters,* vol. 27, pp. 1625-1627, 2002.

[132] R. Manning and D. Davies, "Three-wavelength device for all-optical signal processing," *Optics letters,* vol. 19, pp. 889-991, 1994.

[133] G. Talli and M. Adams, "Gain dynamics of semiconductor optical amplifiers and three-wavelength devices," *Quantum Electronics, IEEE Journal of,* vol. 39, pp. 1305-1313, 2003.

[134] M. Matsuura, N. Kishi, and T. Miki, "Performances of a widely pulsewidth-tunable multiwavelength pulse generator by a single SOA-based delayed interferometric switch," *Optics Express,* vol. 13, pp. 10010-10021, 2005.

[135] G. Wang, X. Yang, and W. Hu, "All-optical logic gates for 40Gb/s NRZ signals using complementary data in SOA-MZIs," *Optics Communications,* vol. 290, pp. 28-32, 2012.

[136] E. Zhou, X. Zhang, F. Öhman, C. Cheng, J. Mørk, and D. Huang, "Mitigation of patterning effect in wavelength conversion by cascaded semiconductor optical amplifier and electroabsorption modulator," in *Asia Pacific Optical Communications*, 2008, pp. 713607-713607-8.

[137] W. M. Green, M. J. Rooks, L. Sekaric, and Y. A. Vlasov, "Ultra-compact, low RF power, 10 Gb/s silicon Mach-Zehnder modulator," *Optics Express,* vol. 15, pp. 17106-17113, 2007.

[138] E. L. Wooten, K. M. Kissa, A. Yi-Yan, E. J. Murphy, D. A. Lafaw, P. F. Hallemeier, D. Maack, D. V. Attanasio, D. J. Fritz, and G. J. McBrien, "A review of lithium niobate modulators for fiber-optic communications systems," *Selected Topics in Quantum Electronics, IEEE Journal of,* vol. 6, pp. 69-82, 2000.

[139] A. Gnauck, G. Raybon, S. Chandrasekhar, J. Leuthold, C. Doerr, L. Stulz, A. Agarwal, S. Banerjee, D. Grosz, and S. Hunsche, "2.5 Tb/s (64x42. 7 Gb/s) transmission over 40x100 km NZDSF using RZ-DPSK format and all-Raman-amplified spans," in *Optical Fiber Communication Conference*, 2002.

References

[140] N. Dupuis, C. R. Doerr, L. Zhang, L. Chen, N. J. Sauer, P. Dong, L. L. Buhl, and D. Ahn, "InP-based comb generator for optical OFDM," *Lightwave Technology, Journal of,* vol. 30, pp. 466-472, 2012.

[141] K. E. Stubkjaer, "Semiconductor optical amplifier-based all-optical gates for high-speed optical processing," *Selected Topics in Quantum Electronics, IEEE Journal of,* vol. 6, pp. 1428-1435, 2000.

[142] Y. Ueno, S. Nakamura, and K. Tajima, "Nonlinear phase shifts induced by semiconductor optical amplifiers with control pulses at repetition frequencies in the 40–160-GHz range for use in ultrahigh-speed all-optical signal processing," *JOSA B,* vol. 19, pp. 2573-2589, 2002.

[143] S. Nakamura, Y. Ueno, K. Tajima, J. Sasaki, T. Sugimoto, T. Kato, T. Shimoda, M. Itoh, H. Hatakeyama, and T. Tamanuki, "Demultiplexing of 168-Gb/s data pulses with a hybrid-integrated symmetric Mach-Zehnder all-optical switch," *Photonics Technology Letters, IEEE,* vol. 12, pp. 425-427, 2000.

[144] S. Nakamura, Y. Ueno, and K. Tajima, "168-Gb/s all-optical wavelength conversion with a symmetric-Mach-Zehnder-type switch," *Photonics Technology Letters, IEEE,* vol. 13, pp. 1091-1093, 2001.

[145] Y. Ueno, S. Nakamura, K. Tajima, and S. Kitamura, "3.8-THz wavelength conversion of picosecond pulses using a semiconductor delayed-interference signal-wavelength converter (DISC)," *Photonics Technology Letters, IEEE,* vol. 10, pp. 346-348, 1998.

[146] J. Leuthold, C. Joyner, B. Mikkelsen, G. Raybon, J. Pleumeekers, B. Miller, K. Dreyer, and C. Burrus, "100 Gbit/s all-optical wavelength conversion with integrated SOA delayed-interference configuration," *Electronics Letters,* vol. 36, pp. 1129-1130, 2000.

[147] H. Wong, W. Tan, A. Bryce, J. Marsh, J. Arnold, A. Krysa, and M. Sorel, "Current injection tunable monolithically integrated InGaAs-InAlGaAs asymmetric Mach-Zehnder interferometer using quantum-well intermixing," *Photonics Technology Letters, IEEE,* vol. 17, pp. 1677-1679, 2005.

[148] H. Wong, W. Tan, A. Bryce, J. Marsh, J. Arnold, and M. Sorel, "Integrated asymmetric Mach-Zehnder interferometer WDM (de) multiplexer using quantum well intermixing," in *Indium Phosphide and Related Materials, 2005. International Conference on*, 2005, pp. 28-30.

[149] J. Sokoloff, P. Prucnal, I. Glesk, and M. Kane, "A terahertz optical asymmetric demultiplexer (TOAD)," *Photonics Technology Letters, IEEE,* vol. 5, pp. 787-790, 1993.

[150] K. Hall and B. Robinson, "Bit error rate characterization of 100 Gb/s all-optical demultiplexers," in *Lasers and Electro-Optics, 1999. CLEO'99. Summaries of Papers Presented at the Conference on*, 1999, pp. 214-215.

[151] P. Toliver, R. J. Runser, I. Glesk, and P. R. Prucnal, "Comparison of three nonlinear interferometric optical switch geometries," *Optics communications,* vol. 175, pp. 365-373, 2000.

[152] K. Kang, I. Glesk, T. Chang, P. Prucnal, and R. Boncek, "Demonstration of all-optical Mach-Zehnder demultiplexer," *Electronics Letters,* vol. 31, pp. 749-750, 1995.

[153] R. Giller, R. J. Manning, G. Talli, R. P. Webb, and M. J. Adams, "Analysis of the dimensional dependence of semiconductor optical amplifier recovery speeds," *Optics Express,* vol. 15, pp. 1773-1782, 2007.

[154] N. Patel, K. Hall, and K. Rauschenbach, "40-Gbitys cascadable all-optical logic with an ultrafast nonlinear interferometer," *Optics letters,* vol. 21, pp. 1466-1468, 1996.

References

[155] K. Hall and K. Rauschenbach, "100-Gbit/s bitwise logic," *Optics letters,* vol. 23, pp. 1271-1273, 1998.

[156] M. Chacinski, U. Westergren, L. Thylen, R. Schatz, J. Li, A. Djupsjobacka, and B. Stoltz, "Modulation and chirp evaluation of 100 GHz DFB-TWEAM," in *Optical Communication (ECOC), 2010 36th European Conference and Exhibition on*, 2010, pp. 1-3.

[157] J. Mork, F. Romstad, S. Hojfeldt, L. Oxenlowe, K. Yvind, L. Xu, F. Ohman, L. J. Christiansen, A. Tersigni, and K. Hoppe, "Optical signal processing using electro-absorption modulators," in *11th European Conference on Integrated Optics. Proceedings*, 2003, pp. 45-54.

[158] G. Li and P. Yu, "Optical intensity modulators for digital and analog applications," *Lightwave Technology, Journal of,* vol. 21, pp. 2010-2030, 2003.

[159] J. W. Raring, L. A. Johansson, E. J. Skogen, M. N. Sysak, H. N. Poulsen, S. P. DenBaars, and L. A. Coldren, "40-Gb/s widely tunable low-drive-voltage electroabsorption-modulated transmitters," *Lightwave Technology, Journal of,* vol. 25, pp. 239-248, 2007.

[160] Y. Zhuang, W. S. Chang, and P. Yu, "Peripheral-coupled-waveguide MQW electroabsorption modulator for near transparency and high spurious free dynamic range RF fiber-optic link," *Photonics Technology Letters, IEEE,* vol. 16, pp. 2033-2035, 2004.

[161] A. V. Uskov, J. Karin, R. Nagarajan, and J. Bowers, "Dynamics of carrier heating and sweepout in waveguide saturable absorbers," *Selected Topics in Quantum Electronics, IEEE Journal of,* vol. 1, pp. 552-561, 1995.

[162] S. Hojfeldt and J. Mork, "Modeling of carrier dynamics in quantum-well electroabsorption modulators," *Selected Topics in Quantum Electronics, IEEE Journal of,* vol. 8, pp. 1265-1276, 2002.

[163] L. Huo, Y. Yang, Y. Nan, C. Lou, and Y. Gao, "A study on the wavelength conversion and all-optical 3R regeneration using cross-absorption modulation in a bulk electroabsorption modulator," *Lightwave Technology, Journal of,* vol. 24, pp. 3035-3044, 2006.

[164] E. Verdurmen, Y. Liu, G. Khoe, and H. De Waardt, "Study on the limits of all-optical time-domain demultiplexing using cross-absorption modulation in an electroabsorption modulator," in *Optoelectronics, IEE Proceedings-*, 2006, pp. 75-83.

[165] P. S. Cho, D. Mahgerefteh, and J. Coldhar, "All-optical 2R regeneration and wavelength conversion at 20 Gb/s using an electroabsorption modulator," *Photonics Technology Letters, IEEE,* vol. 11, pp. 1662-1664, 1999.

[166] H. Murai, M. Kagawa, H. Tsuji, and K. Fujii, "All-optical 3R-signal regeneration at 80 Gbit/s using high-speed electro-absorpsion modulator," in *Optical Amplifiers and Their Applications*, 2003.

[167] N. E. Dahdah, J. Decobert, A. Shen, S. Bouchoule, C. Kazmierski, G. Aubin, B.-E. Benkelfat, and A. Ramdane, "New design of InGaAs-InGaAlAs MQW electroabsorption modulator for high-speed all-optical wavelength conversion," *Photonics Technology Letters, IEEE,* vol. 16, pp. 2302-2304, 2004.

[168] A. M. Fox, D. A. Miller, G. Livescu, J. Cunningham, and W. Y. Jan, "Quantum well carrier sweep out: relation to electroabsorption and exciton saturation," *Quantum Electronics, IEEE Journal of,* vol. 27, pp. 2281-2295, 1991.

References

[169] A. Liu, H. Rong, M. Paniccia, O. Cohen, and D. Hak, "Net optical gain in a low loss silicon-on-insulator waveguide by stimulated Raman scattering," *Optics Express,* vol. 12, pp. 4261-4268, 2004.

[170] E. Dulkeith, Y. A. Vlasov, X. Chen, N. C. Panoiu, and R. M. Osgood Jr, "Self-phase-modulation in submicron silicon-on-insulator photonic wires," *Optics Express,* vol. 14, pp. 5524-5534, 2006.

[171] K. Yamada, T. Tsuchizawa, T. Watanabe, J. I. Takahashi, H. Fukuda, M. Takahashi, T. Shoji, S. Uchiyama, E. Tamechika, and S. I. Itabashi, "Silicon wire waveguiding system: fundamental characteristics and applications," *Electronics and Communications in Japan (Part II: Electronics),* vol. 89, pp. 42-55, 2006.

[172] R. Soref, "The past, present, and future of silicon photonics," *Selected Topics in Quantum Electronics, IEEE Journal of,* vol. 12, pp. 1678-1687, 2006.

[173] X. Chen, N. C. Panoiu, and R. M. Osgood Jr, "Theory of Raman-mediated pulsed amplification in silicon-wire waveguides," *Quantum Electronics, IEEE Journal of,* vol. 42, pp. 160-170, 2006.

[174] H. Takahashi, Y. Hibino, and I. Nishi, "Polarization-insensitive arrayed-waveguide grating wavelength multiplexer on silicon," *Optics letters,* vol. 17, pp. 499-501, 1992.

[175] M. Uenuma and T. Motooka, "Temperature-independent silicon waveguide optical filter," *Optics letters,* vol. 34, pp. 599-601, 2009.

[176] J. Leuthold, W. Freude, J. M. Brosi, R. Baets, P. Dumon, I. Biaggio, M. L. Scimeca, F. Diederich, B. Frank, and C. Koos, "Silicon organic hybrid technology—A platform for practical nonlinear optics," *Proceedings of the IEEE,* vol. 97, pp. 1304-1316, 2009.

[177] D. Miller, "Device requirements for optical interconnects to silicon chips," *Proceedings of the IEEE,* vol. 97, pp. 1166-1185, 2009.

[178] T. Barwicz, H. Byun, F. Gan, C. Holzwarth, M. Popovic, P. Rakich, M. Watts, E. Ippen, F. Kärtner, and H. Smith, "Silicon photonics for compact, energy-efficient interconnects [Invited]," *Journal of Optical Networking,* vol. 6, pp. 63-73, 2007.

[179] R. Dekker, A. Driessen, T. Wahlbrink, C. Moormann, J. Niehusmann, and M. Först, "Ultrafast Kerr-induced all-optical wavelength conversion in silicon waveguides using 1.55 µm femtosecond pulses," *Optics Express,* vol. 14, pp. 8336-8346, 2006.

[180] A. C. Turner-Foster, M. A. Foster, J. S. Levy, C. B. Poitras, R. Salem, A. L. Gaeta, and M. Lipson, "Ultrashort free-carrier lifetime in low-loss silicon nanowaveguides," *Optics Express,* vol. 18, pp. 3582-3591, 2010.

[181] R. Osgood Jr, N. Panoiu, J. Dadap, X. Liu, X. Chen, I. W. Hsieh, E. Dulkeith, W. Green, and Y. Vlasov, "Engineering nonlinearities in nanoscale optical systems: physics and applications in dispersion-engineered silicon nanophotonic wires," *Advances in Optics and Photonics,* vol. 1, pp. 162-235, 2009.

[182] S. Suda, T. Ogasawara, Y. Shoji, K. Kintaka, H. Kawashima, T. Hasama, and H. Ishikawa, "Femtosecond index dynamics in silicon wire waveguides," in *Group IV Photonics, 2009. GFP'09. 6th IEEE International Conference on*, 2009, pp. 98-100.

[183] S. Suda, T. Ogasawara, Y. Shoji, K. Kintaka, H. Kawashima, T. Hasama, and H. Ishikawa, "Optical Nonlinear Properties and Carrier Plasma Effect at Low Carrier Density in Silicon Wire Waveguides," *Quantum Electronics, IEEE Journal of,* vol. 47, pp. 1208-1213, 2011.

References

---

[184] L. Jia, M. Geng, L. Zhang, L. Yang, P. Chen, Y. Liu, Q. Fang, and M. Yu, "Effects of waveguide length and pump power on the efficiency of wavelength conversion in silicon nanowire waveguides," *Optics letters,* vol. 34, pp. 3502-3504, 2009.

[185] R. Soref and B. Bennett, "Electrooptical effects in silicon," *Quantum Electronics, IEEE Journal of,* vol. 23, pp. 123-129, 1987.

[186] R. Ludwig, U. Feiste, C. Schmidt, C. Schubert, J. Berger, E. Hilliger, M. Kroh, T. Yamamoto, C. Weinert, and H. Weber, "Enabling transmission at 160 Gbit/s," in *Optical Fiber Communication Conference and Exhibit, 2002. OFC 2002*, 2002, pp. 1-2.

[187] V. R. Almeida, C. A. Barrios, R. R. Panepucci, and M. Lipson, "All-optical control of light on a silicon chip," *Nature,* vol. 431, pp. 1081-1084, 2004.

[188] D. Dai, S. He, and H.-K. Tsang, "Bilevel mode converter between a silicon nanowire waveguide and a larger waveguide," *Journal of Lightwave Technology,* vol. 24, p. 2428, 2006.

[189] H. Rong, Y. H. Kuo, A. Liu, M. Paniccia, and O. Cohen, "High efficiency wavelength conversion of 10 Gb/s data in silicon waveguides," *Optics Express,* vol. 14, pp. 1182-1188, 2006.

[190] P. Apiratikul, A. M. Rossi, and T. E. Murphy, "Nonlinearities in porous silicon optical waveguides at 1550 nm," *Optics Express,* vol. 17, pp. 3396-3406, 2009.

[191] Y. Shoji, T. Ogasawara, T. Kamei, Y. Sakakibara, S. Suda, K. Kintaka, H. Kawashima, M. Okano, T. Hasama, and H. Ishikawa, "Ultrafast nonlinear effects in hydrogenated amorphous silicon wire waveguide," *Optics Express,* vol. 18, pp. 5668-5673, 2010.

[192] B. Kuyken, H. Ji, S. Clemmen, S. Selvaraja, H. Hu, M. Pu, M. Galili, P. Jeppesen, G. Morthier, and S. Massar, "Nonlinear properties of and nonlinear processing in hydrogenated amorphous silicon waveguides," *Optics Express,* vol. 19, pp. B146-B153, 2011.

[193] N. Wright, D. Thomson, K. Litvinenko, W. Headley, A. Smith, A. Knights, J. Deane, F. Gardes, G. Mashanovich, and R. Gwilliam, "Free carrier lifetime modification for silicon waveguide based devices," *Optics Express,* vol. 16, pp. 19779-19784, 2008.

[194] M. Waldow, T. Plötzing, M. Gottheil, M. Först, J. Bolten, T. Wahlbrink, and H. Kurz, "25ps all-optical switching in oxygen implanted silicon-on-insulator microring resonator," *Optics Express,* vol. 16, pp. 7693-7702, 2008.

[195] M. Yoshizawa, A. Yasuda, and T. Kobayashi, "Ultrafast optical response in polydiacetylenes and polythiophenes," *Applied Physics B: Lasers and Optics,* vol. 53, pp. 296-307, 1991.

[196] C. Koos, P. Vorreau, T. Vallaitis, P. Dumon, W. Bogaerts, R. Baets, B. Esembeson, I. Biaggio, T. Michinobu, and F. Diederich, "All-optical high-speed signal processing with silicon–organic hybrid slot waveguides," *Nature photonics,* vol. 3, pp. 216-219, 2009.

[197] S. Watanabe, "Optical signal processing using nonlinear fibers," *Journal of Optical and Fiber Communications Research,* vol. 3, pp. 1-24, 2006.

[198] S. Watanabe and F. Futami, "All-optical signal processing using highly-nonlinear optical fibers," *IEICE Transactions on Electronics,* vol. 84, pp. 553-563, 2001.

[199] M. Onishi, T. Okuno, T. Kashiwada, S. Ishikawa, N. Akasaka, and M. Nishimura, "Highly nonlinear dispersion-shifted fibers and their application to broadband wavelength converter," *Optical Fiber Technology,* vol. 4, pp. 204-214, 1998.

[200] P. Petropoulos, T. M. Monro, H. Ebendorff-Heidepriem, K. Frampton, R. C. Moore, H. N. Rutt, and D. J. Richardson, "Soliton-self-frequency-shift effects and pulse

compression in an anomalously dispersive high nonlinearity lead silicate holey fiber," in *Optical Fiber Communications Conference, 2003. OFC 2003*, 2003, pp. PD3-1-3 vol. 3.

[201] N. Sugimoto, T. Nagashima, T. Hasegawa, and S. Ohara, "Bismuth-based optical fiber with nonlinear coefficient of 1360 $W^{-1}km^{-1}$," in *Optical Fiber Communication Conference* 2004, p. 3 pp. vol. 2.

[202] M. D. Pelusi, V. G. Ta'eed, L. Fu, E. Magi, M. R. E. Lamont, S. Madden, D. Y. Choi, D. A. P. Bulla, B. Luther-Davies, and B. J. Eggleton, "Applications of highly-nonlinear chalcogenide glass devices tailored for high-speed all-optical signal processing," *Selected Topics in Quantum Electronics, IEEE Journal of,* vol. 14, pp. 529-539, 2008.

[203] G. Meloni, M. Scaffardi, P. Ghelfi, A. Bogoni, L. Poti, and N. Calabretta, "Ultrafast all-optical ADD-DROP multiplexer based on 1-m-long bismuth oxide-based highly nonlinear fiber," *Photonics Technology Letters, IEEE,* vol. 17, pp. 2661-2663, 2005.

[204] C. Langrock, S. Kumar, J. E. McGeehan, A. Willner, and M. Fejer, "All-optical signal processing using $\chi^{(2)}$ nonlinearities in guided-wave devices," *Lightwave Technology, Journal of,* vol. 24, pp. 2579-2592, 2006.

[205] A. Bogoni, X. Wu, I. Fazal, and A. Willner, "All-optical 160Gb/s half-addition half-subtraction and AND/OR function exploiting pump depletion and nonlinearities in a PPLN waveguide," in *European Conference on Optical Communication*, 2008, pp. 1-2.

[206] A. Bogoni, X. Wu, I. Fazal, and A. E. Willner, "Photonic processing of 320 Gbits/s based on sum-/difference-frequency generation and pump depletion in a single PPLN waveguide," *Optics letters,* vol. 34, pp. 1825-1827, 2009.

[207] W. Sohler, H. Hu, R. Ricken, V. Quiring, C. Vannahme, H. Herrmann, D. Büchter, S. Reza, W. Grundkötter, and S. Orlov, "Integrated optical devices in lithium niobate," *Optics and Photonics News,* vol. 19, pp. 24-31, 2008.

[208] M. D. Pelusi, V. G. Ta'eed, L. Fu, E. Magi, M. R. Lamont, S. Madden, D.-Y. Choi, D. A. Bulla, B. Luther-Davies, and B. J. Eggleton, "Applications of highly-nonlinear chalcogenide glass devices tailored for high-speed all-optical signal processing," *Selected Topics in Quantum Electronics, IEEE Journal of,* vol. 14, pp. 529-539, 2008.

[209] M. Galili, J. Xu, H. C. Mulvad, A. T. Clausen, P. Jeppesen, B. Luther-Davies, S. Madden, A. Rode, D.-Y. Choi, and M. Pelusi, "Breakthrough switching speed with an all-optical chalcogenide glass chip: 640 Gbit/s demultiplexing," *Optics Express,* vol. 17, pp. 2182-2187, 2009.

[210] V. G. Ta'Eed, L. Fu, M. Pelusi, M. Rochette, I. C. Littler, D. J. Moss, and B. J. Eggleton, "Error free all optical wavelength conversion in highly nonlinear As-Se chalcogenide glass fiber," *Optics Express,* vol. 14, pp. 10371-10376, 2006.

[211] V. Ta'Eed, N. J. Baker, L. Fu, K. Finsterbusch, M. R. Lamont, D. J. Moss, H. C. Nguyen, B. J. Eggleton, D.-Y. Choi, and S. Madden, "Ultrafast all-optical chalcogenide glass photonic circuits," *Optics Express,* vol. 15, pp. 9205-9221, 2007.

[212] Y. Luo and N. Ansari, "Restoration with wavelength conversion in WDM networks," *Electronics Letters,* vol. 38, pp. 900-901, 2002.

[213] Y. Hirota and K. MURAKAMI, "A simple and speedy routing with reduced resource information in large-capacity optical WDM networks," *IEICE transactions on communications,* vol. 94, pp. 884-893, 2011.

[214] C. N. Jessop, R. B. Jenkins, and R. J. Voigt, "Routing in an optical local area network using wavelength conversion," in *Avionics Fiber-Optics and Photonics, 2006. IEEE Conference*, 2006, pp. 24-25.

References

[215] T. Hatta, T. Miyahara, Y. Miyazaki, K. Takagi, K. Matsumoto, T. Aoyagi, K. Motoshima, K. Mishina, A. Maruta, and K. Kitayama, "Polarization-Insensitive Monolithic 40-Gbps SOA–MZI Wavelength Converter With Narrow Active Waveguides," *Selected Topics in Quantum Electronics, IEEE Journal of,* vol. 13, pp. 32-39, 2007.

[216] G.-K. Chang, J. Yu, Y.-K. Yeo, A. Chowdhury, and Z. Jia, "Enabling technologies for next-generation optical packet-switching networks," *Proceedings of the IEEE,* vol. 94, pp. 892-910, 2006.

[217] M. Pu, H. Hu, M. Galili, H. Ji, C. Peucheret, L. K. Oxenlowe, K. Yvind, P. Jeppesen, and J. M. Hvam, "15-THz tunable wavelength conversion of picosecond pulses in a silicon waveguide," *Photonics Technology Letters, IEEE,* vol. 23, pp. 1409-1411, 2011.

[218] T. Durhuus, B. Mikkelsen, C. Joergensen, S. Lykke Danielsen, and K. E. Stubkjaer, "All-optical wavelength conversion by semiconductor optical amplifiers," *Lightwave Technology, Journal of,* vol. 14, pp. 942-954, 1996.

[219] Y.-H. Kuo, H. Rong, V. Sih, S. Xu, M. Paniccia, and O. Cohen, "Demonstration of wavelength conversion at 40 Gb/s data rate in silicon waveguides," *Optics Express,* vol. 14, pp. 11721-11726, 2006.

[220] H. Hu, H. Ji, M. Galili, M. Pu, H. C. Hansen Mulvad, L. Oxenløwe, K. Yvind, J. M. Hvam, and P. Jeppesen, "320 Gb/s phase-transparent wavelength conversion in a silicon nanowire," in *Optical Fiber Communication Conference*, 2011.

[221] H. Hu, H. Ji, M. Galili, M. Pu, H. C. Hansen Mulvad, L. Oxenløwe, K. Yvind, J. M. Hvam, and P. Jeppesen, "Silicon chip based wavelength conversion of ultra-high repetition rate data signals," in *Optical Fiber Communication Conference*, 2011.

[222] H. Hu, H. Suche, R. Ludwig, B. Huettl, C. Schmidt-Langhorst, R. Nouroozi, W. Sohler, and C. Schubert, "Polarization insensitive all-optical wavelength conversion of 320 Gb/s RZ-DQPSK data signals," in *Optical Fiber Communication-incudes post deadline papers, 2009. OFC 2009. Conference on*, 2009, pp. 1-3.

[223] M. Pelusi, F. Luan, S. Madden, D.-Y. Choi, D. Bulla, B. Luther-Davies, and B. Eggleton, "CW Pumped wavelength conversion of 40 Gb/s DPSK and 160 Gb/s OOK signals in a chalcogenide glass chip," in *OptoElectronics and Communications Conference, 2009. OECC 2009. 14th*, 2009, pp. 1-2.

[224] M. Galili, L. Oxenlowe, H. H. Mulvad, A. T. Clausen, and P. Jeppesen, "Optical wavelength conversion by cross-phase modulation of data signals up to 640 Gb/s," *Selected Topics in Quantum Electronics, IEEE Journal of,* vol. 14, pp. 573-579, 2008.

[225] Y. Liu, E. Tangdiongga, Z. Li, H. De Waardt, A. Koonen, G. Khoe, H. Dorren, X. Shu, and I. Bennion, "Error-free 320 Gb/s SOA-based wavelength conversion using optical filtering," in *Optical Fiber Communication Conference, 2006 and the 2006 National Fiber Optic Engineers Conference. OFC 2006*, 2006, pp. 1-3.

[226] K. Nishimura, R. Inohara, M. Usami, and S. Akiba, "All-optical wavelength conversion by electroabsorption modulator," *Selected Topics in Quantum Electronics, IEEE Journal of,* vol. 11, pp. 278-284, 2005.

[227] H. Ji, M. Galili, H. Hu, M. Pu, L. K. Oxenløwe, K. Yvind, J. M. Hvam, and P. Jeppesen, "1.28-Tb/s demultiplexing of an OTDM DPSK data signal using a silicon waveguide," *Photonics Technology Letters, IEEE,* vol. 22, pp. 1762-1764, 2010.

[228] H. Ji, M. Pu, H. Hu, M. Galili, L. K. Oxenlowe, K. Yvind, J. M. Hvam, and P. Jeppesen, "Optical waveform sampling and error-free demultiplexing of 1.28 Tb/s serial data in a

nanoengineered silicon waveguide," *Lightwave Technology, Journal of,* vol. 29, pp. 426-431, 2011.

[229] F. Gomez-Agis, C. Okonkwo, A. Albores-Mejia, E. Tangdiongga, and H. Dorren, "320-to-10 Gbit/s all-optical demultiplexing using sum-frequency generation in PPLN waveguide," *Electronics Letters,* vol. 46, pp. 1008-1009, 2010.

[230] M. Saruwatari, "All-optical signal processing for terabit/second optical transmission," *Selected Topics in Quantum Electronics, IEEE Journal of,* vol. 6, pp. 1363-1374, 2000.

[231] E. Tangdiongga, Y. Liu, H. De Waardt, G. Khoe, A. Koonen, H. Dorren, X. Shu, and I. Bennion, "All-optical demultiplexing of 640 to 40 Gbits/s using filtered chirp of a semiconductor optical amplifier," *Optics letters,* vol. 32, pp. 835-837, 2007.

[232] H.-F. Chou, Y.-J. Chiu, J. E. Bowers, L. Rau, S. Rangarajan, and D. J. Blumenthal, "Standing-wave Enhanced Electroabsorption Modulator for 80Gb/s to 10Gb/s OTDM Demultiplexing," in *Optical Communication, 2002. ECOC 2002. 28th European Conference on*, 2002, pp. 1-2.

[233] J. Dong, X. Zhang, J. Xu, D. Huang, S. Fu, and P. Shum, "40 Gb/s all-optical NRZ to RZ format conversion using single SOA assisted by optical bandpass filter," *Optics Express,* vol. 15, pp. 2907-2914, 2007.

[234] I. Kang, M. Rasras, L. Buhl, M. Dinu, S. Cabot, M. Cappuzzo, L. Gomez, Y. Chen, S. Patel, and N. Dutta, "Generation of 173-Gbits/s single-polarization QPSK signals by all-optical format conversion using a photonic integrated device," in *European Conference on Optical Communication*, 2009, pp. 1-2.

[235] G.-W. Lu and T. Miyazaki, "Optical phase erasure based on FWM in HNLF enabling format conversion from 320-Gb/s RZDQPSK to 160-Gb/s RZ-DPSK," *Optics Express,* vol. 17, pp. 13346-13353, 2009.

[236] H. Christian, H. Mulvad, E. Palushani, H. Hu, H. Ji, M. Lillieholm, M. Galili, A. T. Clausen, M. Pu, and K. Yvind, "Ultra-high-speed optical serial-to-parallel data conversion by time-domain optical Fourier transformation in a silicon nanowire," *Optics Express,* vol. 19, pp. B825-B835, 2011.

[237] F. Wang, E. Xu, Y. Yu, and Y. Zhangc, "All-optical 40 Gbit/s data format conversion between RZ and NRZ using a fiber delay interferometer and a single SOA," in *Asia Communications and Photonics Conference and Exhibition*, 2011.

[238] J. M. Dailey, R. P. Webb, and R. J. Manning, "All-optical technique for modulation format conversion from on-off-keying to alternate-mark-inversion," *Optics Express,* vol. 18, pp. 21873-21882, 2010.

[239] X. Yang, A. Mishra, R. Manning, and R. Giller, "All-optical 40 Gbit/s NRZ to RZ format conversion by nonlinear polarisation rotation in SOAs," *Electronics Letters,* vol. 43, pp. 469-471, 2007.

[240] M. Westlund, H. Sunnerud, M. Karlsson, and P. A. Andrekson, "Software-synchronized all-optical sampling for fiber communication systems," *Lightwave Technology, Journal of,* vol. 23, pp. 1088-1099, 2005.

[241] H. Ji, H. Hu, M. Galili, M. Pu, K. Yvind, J. Hvam, L. K. Oxenlowe, and P. Jeppesen, "Optical waveform sampling and error-free demultiplexing of 1.28 Tbit/s serial data in a silicon nanowire," in *National Fiber Optic Engineers Conference*, 2010.

[242] J. Van Erps, F. Luan, M. D. Pelusi, T. Iredale, S. Madden, D.-Y. Choi, D. A. Bulla, B. Luther-Davies, H. Thienpont, and B. J. Eggleton, "High-Resolution Optical Sampling of 640-Gb/s Data Using Four-Wave Mixing in Dispersion-Engineered Highly Nonlinear

As2S3 Planar Waveguides," *Journal of Lightwave Technology,* vol. 28, pp. 209-215, 2010.

[243]   A. O. Wiberg, C.-S. Bres, B.-P. Kuo, J. M. C. Boggio, N. Alic, and S. Radic, "Multicast parametric synchronous sampling of 320-Gb/s return-to-zero signal," *Photonics Technology Letters, IEEE,* vol. 21, pp. 1612-1614, 2009.

[244]   T. Mori, A. Otani, and T. Otani, "All-optical sampling using cross-absorption modulation in electroabsorption modulator for optical performance monitor," in *Optical Communication, 2008. ECOC 2008. 34th European Conference on*, 2008, pp. 1-2.

[245]   N. Yamada, S. Nogiwa, and H. Ohta, "640-Gb/s OTDM signal measurement with high-resolution optical sampling system using wavelength-tunable soliton pulses," *Photonics Technology Letters, IEEE,* vol. 16, pp. 1125-1127, 2004.

[246]   S. Fischer, M. Bitter, M. Caraccia, M. Dülk, E. Gamper, W. Vogt, E. Gini, H. Melchior, and W. Hunziker, "All-optical sampling with a monolithically integrated Mach–Zehnder interferometer gate," *Optics letters,* vol. 26, pp. 626-628, 2001.

[247]   H. Dorren, M. Hill, Y. Liu, N. Calabretta, A. Srivatsa, F. Huijskens, H. De Waardt, and G. Khoe, "Optical packet switching and buffering by using all-optical signal processing methods," *Lightwave Technology, Journal of,* vol. 21, pp. 2-12, 2003.

[248]   D. K. Hunter and I. Andonovic, "Approaches to optical Internet packet switching," *Communications Magazine, IEEE,* vol. 38, pp. 116-122, 2000.

[249]   N. Calabretta, H.-D. Jung, J. Herrera, E. Tangdiongga, T. Koonen, and H. Dorren, "1 x 4 all-optical packet switch at 160 Gb/s employing optical processing of scalable in-band address labels," in *National Fiber Optic Engineers Conference*, 2008.

[250]   H. Teimoori, J. D. Topomondzo, C. Ware, and D. Erasme, "Optical packet header processing using time-to-wavelength mapping in semiconductor optical amplifiers," *Journal of Lightwave Technology,* vol. 25, pp. 2149-2158, 2007.

[251]   J. P. Wang, B. S. Robinson, S. A. Hamilton, and E. P. Ippen, "Demonstration of 40-Gb/s packet routing using all-optical header processing," *Photonics Technology Letters, IEEE,* vol. 18, pp. 2275-2277, 2006.

[252]   N. Calabretta, H. Jung, E. Tangdiongga, A. Koonen, and H. Dorren, "160 Gb/s all-optical packet switching with label wewriting," in *Optical Communication, 2008. ECOC 2008. 34th European Conference on*, 2008, pp. 1-2.

[253]   H. Dorren, J. Herrera, O. Raz, E. Tangdiongga, Y. Liu, J. Marti, F. Ramos, G. Maxwell, A. Poustie, and H. H. Mulvad, "All-optical devices for ultrafast packet switching," in *Lasers and Electro-Optics Society, 2007. LEOS 2007. The 20th Annual Meeting of the IEEE*, 2007, pp. 729-730.

[254]   A. Bogoni, X. Wu, S. R. Nuccio, and A. E. Willner, "640 Gb/s All-Optical Regenerator Based on a Periodically Poled Lithium Niobate Waveguide," *Journal of Lightwave Technology,* vol. 30, pp. 1829-1834, 2012.

[255]   T. Vivero, N. Calabretta, I. T. Monroy, G. CarvalhoKassar, F. Ohman, K. Yvind, A. Gonzalez-Marcos, and J. Mork, "10 Gb/s-NRZ Optical 2R-regeneration in two-section SOA-EA chip," in *Lasers and Electro-Optics Society, 2007. LEOS 2007. The 20th Annual Meeting of the IEEE*, 2007, pp. 806-807.

[256]   R. Salem, M. A. Foster, A. C. Turner, D. F. Geraghty, M. Lipson, and A. L. Gaeta, "Signal regeneration using low-power four-wave mixing on silicon chip," *Nature Photonics,* vol. 2, pp. 35-38, 2007.

References

[257] P. Ghelfi, A. Bogoni, M. Scaffardi, F. Ponzini, C. Porzi, and L. Potì, "320 Gbit/s all-optical regeneration for OTDM signals," in *European Conference on Optical Communication*, 2004.

[258] Y. Ueno, S. Nakamura, and K. Tajima, "Penalty-free error-free all-optical data pulse regeneration at 84 Gbps with Symmetric-Mach-Zehnder-type regenerator," in *Optical Fiber Communication Conference and Exhibit, 2001. OFC 2001*, 2001, pp. MG5-MG5.

[259] T. Mizuochi, Y. Miyata, T. Kobayashi, K. Ouchi, K. Kuno, K. Kubo, K. Shimizu, H. Tagami, H. Yoshida, and H. Fujita, "Forward error correction based on block turbo code with 3-bit soft decision for 10-Gb/s optical communication systems," *Selected Topics in Quantum Electronics, IEEE Journal of,* vol. 10, pp. 376-386, 2004.

[260] F. Li, T. Vo, C. Husko, M. Pelusi, D. Xu, A. Densmore, R. Ma, S. Janz, B. Eggleton, and D. Moss, "All-optical XOR logic gate for 40Gb/s DPSK signals via FWM in a silicon nanowire," *Optics Express,* vol. 19, pp. 20364-20371, 2011.

[261] J. Wang, Q. Sun, and J. Sun, "All-optical 40 Gbit/s CSRZ-DPSK logic XOR gate and format conversion using four-wave mixing," *Optics Express,* vol. 17, pp. 12555-12563, 2009.

[262] J. Wang, J. Sun, X. Zhang, D. Huang, and M. Fejer, "Ultrafast all-optical three-input Boolean XOR operation for differential phase-shift keying signals using periodically poled lithium niobate," *Optics letters,* vol. 33, pp. 1419-1421, 2008.

[263] X. Yang, R. Manning, and R. Webb, "All-optical 85Gb/s XOR using dual ultrafast nonlinear interferometers and turbo-switch configuration," in *European Conference on Optical Communications*, 2006, pp. 1-2.

[264] G. Berrettini, A. Simi, A. Malacarne, A. Bogoni, and L. Poti, "Ultrafast integrable and reconfigurable XNOR, AND, NOR, and NOT photonic logic gate," *Photonics Technology Letters, IEEE,* vol. 18, pp. 917-919, 2006.

[265] Z. Li, Y. Liu, S. Zhang, H. Ju, H. De Waardt, G. Khoe, H. Dorren, and D. Lenstra, "All-optical logic gates using semiconductor optical amplifier assisted by optical filter," *Electronics Letters,* vol. 41, pp. 1397-1399, 2005.

[266] K. Chan, C.-K. Chan, L. K. Chen, and F. Tong, "Demonstration of 20-Gb/s all-optical XOR gate by four-wave mixing in semiconductor optical amplifier with RZ-DPSK modulated inputs," *Photonics Technology Letters, IEEE,* vol. 16, pp. 897-899, 2004.

[267] F. Ginovart, J. Simon, and I. Valiente, "Gain recovery dynamics in semiconductor optical amplifier," *Optics communications,* vol. 199, pp. 111-115, 2001.

[268] M. Asghari, I. H. White, and R. V. Penty, "Wavelength conversion using semiconductor optical amplifiers," *Lightwave Technology, Journal of,* vol. 15, pp. 1181-1190, 1997.

[269] F. Girardin, G. Guekos, and A. Houbavlis, "Gain recovery of bulk semiconductor optical amplifiers," *Photonics Technology Letters, IEEE,* vol. 10, pp. 784-786, 1998.

[270] X. Yang, D. Lenstra, G. Khoe, and H. Dorren, "Nonlinear polarization rotation induced by ultrashort optical pulses in a semiconductor optical amplifier," *Optics Communications,* vol. 223, pp. 169-179, 2003.

[271] T. Liu, K. Obermann, K. Petermann, F. Girardin, and G. Guekos, "Effect of saturation caused by amplified spontaneous emission on semiconductor optical amplifier performance," *Electronics Letters,* vol. 33, pp. 2042-2043, 1997.

[272] W. Mathlouthi, F. Vacondio, P. Lemieux, and L. A. Rusch, "SOA gain recovery wavelength dependence: simulation and measurement using a single-color pump-probe technique," *Optics Express,* vol. 16, pp. 20656-20665, 2008.

References

[273] T. Katayama and H. Kawaguchi, "Measurement of ultrafast cross-gain saturation dynamics of a semiconductor optical amplifier using two-color pump-probe technique," *Photonics Technology Letters, IEEE,* vol. 16, pp. 855-857, 2004.

[274] F. Ginovart, M. Amaya, and A. Sharaiha, "Wavelength dependence of semiconductor optical amplifier gain recovery time with optical injection at the transparency wavelength," in *Information and Communication Technologies, 2006. ICTTA'06. 2nd*, 2006, pp. 2073-2078.

[275] X. Li, M. Adams, D. Alexandropoulos, and I. Lealman, "Gain recovery in semiconductor optical amplifiers," *Optics Communications,* vol. 281, pp. 3466-3470, 2008.

[276] Y. An, "12 Month Progress Report for PhD project," unpublished.

[277] S. Schneider, "MSc thesis internship report," unpublished.

[278] L. Xu, N. Chi, L. Oxenlowe, K. Yvind, J. Mork, P. Jeppesen, and J. Hanberg, "Optical label encoding using electroabsorption modulators and investigation of chirp properties," *Lightwave Technology, Journal of,* vol. 21, pp. 1763-1769, 2003.

[279] R. Gutiérrez-Castrejón, L. Schares, L. Occhi, and G. Guekos, "Modeling and measurement of longitudinal gain dynamics in saturated semiconductor optical amplifiers of different length," *Quantum Electronics, IEEE Journal of,* vol. 36, pp. 1476-1484, 2000.

[280] J. Leuthold, M. Mayer, J. Eckner, G. Guekos, H. Melchior, and C. Zellweger, "Material gain of bulk 1.55 μm InGaAsP/InP semiconductor optical amplifiers approximated by a polynomial model," *Journal of Applied Physics,* vol. 87, pp. 618-620, 2000.

[281] J. Minowa and Y. Fujii, "Dielectric multilayer thin-film filters for WDM transmission systems," *Lightwave Technology, Journal of,* vol. 1, pp. 116-121, 1983.

[282] G. Castagno, F. Demichelis, and E. Minetti-Mezzetti, "Design method for multilayer interference filters," *Applied optics,* vol. 19, pp. 386-388, 1980.

[283] T. Vivero, N. Calabretta, I. Tafur Monroy, G. Kassar, F. Öhman, K. Yvind, A. González-Marcos, and J. Mørk, "2R-Regeneration in a monolithically integrated four-section SOA–EA chip," *Optics communications,* vol. 282, pp. 117-121, 2009.

[284] F. Ohman, S. Bischoff, B. Tromborg, and J. Mork, "Noise properties and cascadability of SOA-EA regenerators," in *Lasers and Electro-Optics Society, 2002. LEOS 2002. The 15th Annual Meeting of the IEEE*, 2002, pp. 895-896.

[285] L. J. Christiansen, L. Xu, K. Yvind, F. Öhman, L. Oxenløwe, and J. Mørk, "2R regeneration in concatenated semiconductor optical amplifiers and electroabsorbers," in *European Conference on Optical Communication*, 2004, pp. 30-31.

[286] J. M. Roth, K. Dreyer, B. C. Collings, W. H. Knox, and K. Bergman, "Actively mode-locked 1.5-μm 10-GHz picosecond fiber laser using a monolithic semiconductor optical amplifier/electroabsorption modulator," *Photonics Technology Letters, IEEE,* vol. 14, pp. 917-919, 2002.

[287] J.-H. Seo, C.-S. Choi, Y.-S. Kang, Y.-D. Chung, J. Kim, and W.-Y. Choi, "Conversion efficiency characteristics of cascaded SOA-EAM frequency up/down-converters," in *Microwave Photonics, 2005. MWP 2005. International Topical Meeting on*, 2005, pp. 107-110.

[288] C. L. Daunt, J. O'Callaghan, K.-H. Lee, H. Yang, R. J. Young, K. Thomas, E. Pelucchi, B. Corbett, and F. H. Peters, "Compact electroabsorption modulators for photonic integrated circuits, using an isolated pedestal contact scheme," *Photonics Technology Letters, IEEE,* vol. 24, pp. 356-358, 2012.

[289] D. Smith, I. Lealman, X. Chen, D. Moodie, P. Cannard, J. Dosanjh, L. Rivers, C. Ford, R. Cronin, and T. Kerr, "Colourless 10Gb/s reflective SOA-EAM with low polarization sensitivity for long-reach DWDM-PON networks," in *European Conference on Optical Communication*, 2009, pp. 1-2.

[290] G. Talli and P. D. Townsend, "Hybrid DWDM-TDM long-reach PON for next-generation optical access," *Journal of Lightwave Technology,* vol. 24, p. 2827, 2006.

[291] C. S. Cleary, M. J. Power, S. Schneider, R. P. Webb, and R. J. Manning, "Fast gain recovery rates with strong wavelength dependence in a non-linear SOA," *Optics Express,* vol. 18, pp. 25726-25737, 2010.

[292] L. Occhi, Y. Ito, H. Kawaguchi, L. Schares, J. Eckner, and G. Guekos, "Intraband gain dynamics in bulk semiconductor optical amplifiers: measurements and simulations," *Quantum Electronics, IEEE Journal of,* vol. 38, pp. 54-60, 2002.

[293] A. Bilenca, R. Alizon, V. Mikhelashhvili, D. Dahan, G. Eisenstein, R. Schwertberger, D. Gold, J. Reithmaier, and A. Forchel, "Broad-band wavelength conversion based on cross-gain modulation and four-wave mixing in InAs-InP quantum-dash semiconductor optical amplifiers operating at 1550 nm," *Photonics Technology Letters, IEEE,* vol. 15, pp. 563-565, 2003.

[294] M. Hofmann, K. Frojdh, S. Brorson, and J. Mork, "Temporal and spectral dynamics in multiquantum-well semiconductor saturable absorbers," *Photonics Technology Letters, IEEE,* vol. 9, pp. 622-624, 1997.

[295] J. Karin, R. Helkey, D. J. Derickson, R. Nagarajan, D. Allin, J. Bowers, and R. Thornton, "Ultrafast dynamics in field-enhanced saturable absorbers," *Applied Physics Letters,* vol. 64, pp. 676-678, 1994.

[296] S. Hojfeldt, "Modeling of carrier dynamics in electroabsorption modulators," PhD thesis, COM Technical University of Denmark, 2002.

[297] D. A. Reid, A. M. Clarke, X. Yang, R. Maher, R. P. Webb, R. J. Manning, and L. P. Barry, "Characterization of a turbo-switch SOA wavelength converter using spectrographic pulse measurement," *Selected Topics in Quantum Electronics, IEEE Journal of,* vol. 14, pp. 841-848, 2008.

[298] F.-Z. Lin, T.-H. Wu, and Y.-J. Chiu, "Novel monolithic integration scheme for high-speed electroabsorption modulators and semiconductor optical amplifiers using cascaded structure," *Optics Express,* vol. 17, pp. 10378-10384, 2009.

[299] E. K. MacHale, G. Talli, P. D. Townsend, A. Borghesani, I. Lealman, D. G. Moodie, and D. W. Smith, "Signal-induced Rayleigh noise reduction using gain saturation in an integrated R-EAM-SOA," in *Optical Fiber Communication Conference*, 2009.

[300] M. J. Heck, E. A. Bente, Y. Barbarin, A. Fryda, H.-D. Jung, Y.-S. Oei, R. Notzel, D. Lenstra, and M. K. Smit, "Characterization of a monolithic concatenated SOA/SA waveguide device for picosecond pulse amplification and shaping," *Quantum Electronics, IEEE Journal of,* vol. 44, pp. 360-369, 2008.

[301] F. Ohman, R. Kjær, L. J. Christiansen, K. Yvind, and J. Mork, "Steep and adjustable transfer functions of monolithic SOA-EA 2R regenerators," *Photonics Technology Letters, IEEE,* vol. 18, pp. 1067-1069, 2006.

[302] G. B. Morrison, J. W. Raring, C. S. Wang, E. J. Skogen, Y. C. Chang, M. Sysak, and L. Coldren, "Electroabsorption modulator performance predicted from band-edge absorption spectra of bulk, quantum-well, and quantum-well-intermixed InGaAsP structures," *Solid-state electronics,* vol. 51, pp. 38-47, 2007.

References

[303]   K. Nishimura, R. Inohara, and M. Usami, "100 Gbit/s wavelength conversion using MQW-EAM blueshifted absorption edge," in *Optical Fiber Communication Conference*, 2004, p. 3 pp. vol. 2.

[304]   J. A. Lázaro, V. Polo, B. Schrenk, F. Bonada, I. Cano, E. Lopez, C. Kazmierski, G. de Valicourt, R. Brenot, and J. Bauwelinck, "Optical subsystems for next generation access networks," in *Access Networks and In-house Communications*, 2011.

[305]   B. Schrenk, J. Fabrega, C. Kazmierski, J. Lazaro, and J. Prat, "SOA/REAM as vector modulator for QAM upstream," in *Optical Fiber Communication Conference and Exposition (OFC/NFOEC), 2011 and the National Fiber Optic Engineers Conference*, 2011, pp. 1-3.

[306]   E. Zhou, X. Yu, X. Zhang, W. Xue, Y. Yu, J. Mørk, and I. T. Monroy, "Photonic generation of ultrawideband monocycle and doublet pulses by using a semiconductor-optical-amplifier-based wavelength converter," *Optics Letters,* vol. 34, pp. 1336-1338, 2009.

[307]   B. Wu, J. Wu, K. Xu, X. Hong, J. Zhang, and J. Lin, "Photonic ultra-wideband monocycle pulses generation using semiconductor optical amplifier and electro-absorber in parallel," *Chinese Optics Letters,* vol. 8, pp. 902-905, 2010.

[308]   W. Zhang, J. Sun, J. Wang, C. Cheng, and X. Zhang, "Ultra-wideband pulse train generation based on turbo-switch structures," *Photonics Technology Letters, IEEE,* vol. 21, pp. 271-273, 2009.

[309]   G. T. Reed and A. P. Knights, *Silicon photonics*: Wiley Online Library, 2008.

[310]   Q. Lin, O. J. Painter, and G. P. Agrawal, "Nonlinear optical phenomena in silicon waveguides: modeling and applications," *Optics Express,* vol. 15, pp. 16604-16644, 2007.

[311]   L. Tsybeskov, D. J. Lockwood, and M. Ichikawa, "Silicon Photonics: CMOS Going Optical [Scanning the Issue]," *Proceedings of the IEEE,* vol. 97, pp. 1161-1165, 2009.

[312]   H. Rong, A. Liu, R. Jones, O. Cohen, D. Hak, R. Nicolaescu, A. Fang, and M. Paniccia, "An all-silicon Raman laser," *Nature,* vol. 433, pp. 292-294, 2005.

[313]   R. Espinola, J. Dadap, R. Osgood Jr, S. McNab, and Y. Vlasov, "C-band wavelength conversion in silicon photonic wire waveguides," *Optics Express,* vol. 13, pp. 4341-4349, 2005.

[314]   I. W. Hsieh, X. Chen, J. I. Dadap, N. C. Panoiu, R. M. Osgood Jr, S. J. McNab, and Y. A. Vlasov, "Cross-phase modulation-induced spectral and temporal effects on co-propagating femtosecond pulses in silicon photonic wires," *Optics Express,* vol. 15, pp. 1135-1146, 2007.

[315]   R. Claps, D. Dimitropoulos, and B. Jalali, "Stimulated Raman scattering in silicon waveguides," *Electronics Letters,* vol. 38, pp. 1352-1354, 2002.

[316]   H. Hu, H. Ji, M. Galili, M. Pu, C. Peucheret, H. Christian H Mulvad, K. Yvind, J. M. Hvam, P. Jeppesen, and L. K. Oxenløwe, "Ultra-high-speed wavelength conversion in a silicon photonic chip," *Optics Express,* vol. 19, pp. 19886-19894, 2011.

[317]   H. Hu, C. Peucheret, M. Pu, H. Ji, M. Galili, K. Yvind, J. M. Hvam, P. Jeppesen, and L. K. Oxenløwe, "Wavelength conversion with large signal-idler separation using discrete four-wave mixing in a silicon nanowire," in *CLEO: Science and Innovations*, 2012.

[318]   Y. Liu and H. Tsang, "Nonlinear absorption and Raman gain in helium-ion-implanted silicon waveguides," *Optics letters,* vol. 31, pp. 1714-1716, 2006.

References

[319] K. Preston, P. Dong, B. Schmidt, and M. Lipson, "High-speed all-optical modulation using polycrystalline silicon microring resonators," *Applied Physics Letters,* vol. 92, pp. 151104-151104-3, 2008.

[320] A. Liu, H. Rong, R. Jones, O. Cohen, D. Hak, and M. Paniccia, "Optical amplification and lasing by stimulated Raman scattering in silicon waveguides," *Journal of Lightwave Technology,* vol. 24, p. 1440, 2006.

[321] L. Yin and G. P. Agrawal, "Impact of two-photon absorption on self-phase modulation in silicon waveguides," *Optics Letters,* vol. 32, pp. 2031-2033, 2007.

[322] M. D. Kelzenberg, D. B. Turner-Evans, B. M. Kayes, A. Michael, M. C. Putnam, N. S. Lewis, and H. A. Atwater, "Photovoltaic measurements in single-nanowire silicon solar cells," *Nano letters,* vol. 8, pp. 710-714, 2008.

[323] T. Vallaitis, S. Bogatscher, L. Alloatti, P. Dumon, R. Baets, M. L. Scimeca, I. Biaggio, F. Diederich, C. Koos, and W. Freude, "Optical properties of highly nonlinear silicon-organic hybrid (SOH) waveguide geometries," *Optics Express,* vol. 17, pp. 17357-17368, 2009.

[324] H. Hu, H. Ji, M. Galili, M. Pu, H. H. Mulvad, K. Yvind, J. M. Hvam, P. Jeppesen, L. Oxenlowe, and L. Oxenløwe, "All-optical wavelength conversion of a high-speed RZ-OOK signal in a silicon nanowire," in *IEEE Photonics Conference*, 2011, pp. 595-596.

[325] H. H. Mulvad, E. Palushani, H. Hu, H. Ji, M. Galili, A. Clausen, M. Pu, K. Yvind, J. M. Hvam, and P. Jeppesen, "Ultra-high-speed optical serial-to-parallel data conversion in a silicon nanowire," in *European Conference on Optical Communication*, 2011, pp. 1-3.

[326] L. Wang, P. Estrela, E. Huq, P. Li, S. Thomas, P. K. Ferrigno, D. Paul, P. Adkin, and P. Migliorato, "Fabrication of BioFET linear array for detection of protein interactions," *Microelectronic Engineering,* vol. 87, pp. 753-755, 2010.

[327] R. Giller, "Ultrafast effects in semiconductor optical amplifiers and ther exploitation for all-optical logic," PhD thesis, Department of Physics, University College Cork, Cork, 2007.

[328] A. Riordan, "Real-time Sampling Measurement of Gain, Phase and Alpha Factor Dynamics of Semiconductor Optical Amplifiers on a Picosecond Time-Scale," MSc thesis, Department of Physics, University College Cork, Cork, 2008.

[329] N. Matsuda, R. Shimizu, Y. Mitsumori, H. Kosaka, A. Sato, H. Yokoyama, K. Yamada, T. Watanabe, T. Tsuchizawa, and H. Fukuda, "All-optical phase modulations in a silicon wire waveguide at ultralow light levels," *Applied Physics Letters,* vol. 95, pp. 171110-171110-3, 2009.

[330] Q. Xu and M. Lipson, "All-optical logic based on silicon micro-ring resonators," *Optics Express,* vol. 15, pp. 924-929, 2007.

[331] T. Sjodin, H. Petek, and H. L. Dai, "Ultrafast carrier dynamics in silicon: A two-color transient reflection grating study on a (111) surface," *Physical review letters,* vol. 81, pp. 5664-5667, 1998.

[332] M. Harb, R. Ernstorfer, T. Dartigalongue, C. T. Hebeisen, R. E. Jordan, and R. D. Miller, "Carrier relaxation and lattice heating dynamics in silicon revealed by femtosecond electron diffraction," *The Journal of Physical Chemistry B,* vol. 110, pp. 25308-25313, 2006.

[333] H. Renner, "Nonlinear distortion of optical pulses by self-produced free carriers in short or highly lossy silicon-based waveguides," *Optics Express,* vol. 20, pp. 25718-25743, 2012.

References

[334] W. Astar, J. B. Driscoll, X. Liu, J. I. Dadap, W. M. Green, Y. A. Vlasov, G. M. Carter, and R. Osgood, "All-Optical Format Conversion of NRZ-OOK to RZ-OOK in a Silicon Nanowire Utilizing Either XPM or FWM and Resulting in a Receiver Sensitivity Gain of 2.5dB," *Selected Topics in Quantum Electronics, IEEE Journal of,* vol. 16, pp. 234-249, 2010.

[335] R. Claps, V. Raghunathan, D. Dimitropoulos, and B. Jalali, "Influence of nonlinear absorption on Raman amplification in Silicon waveguides," *Opt. Express,* vol. 12, pp. 2774-2780, 2004.

[336] H. Kim, E. Plis, A. Khoshakhlagh, S. Myers, N. Gautam, Y. Sharma, L. Dawson, S. Krishna, S. Lee, and S. Noh, "Performance improvement of InAs/GaSb strained layer superlattice detectors by reducing surface leakage currents with SU-8 passivation," *Applied Physics Letters,* vol. 96, pp. 033502-033502-3, 2010.

[337] N. K. Rajan, D. A. Routenberg, and M. A. Reed, "Optimal signal-to-noise ratio for silicon nanowire biochemical sensors," *Applied Physics Letters,* vol. 98, pp. 264107-264107-3, 2011.

[338] C. Manolatou and M. Lipson, "All-optical silicon modulators based on carrier injection by two-photon absorption," *Journal of Lightwave Technology,* vol. 24, p. 1433, 2006.

[339] T. Vallaitis, *Ultrafast nonlinear silicon waveguides and quantum dot semiconductor optical amplifiers*: KIT Scientific Publishing.

[340] M. Dinu, F. Quochi, and H. Garcia, "Third-order nonlinearities in silicon at telecom wavelengths," *Applied Physics Letters,* vol. 82, pp. 2954-2956, 2003.

[341] H. Rong, A. Liu, R. Nicolaescu, M. Paniccia, O. Cohen, and D. Hak, "Raman gain and nonlinear optical absorption measurements in a low-loss silicon waveguide," *Applied Physics Letters,* vol. 85, pp. 2196-2198, 2004.

[342] T. Liang and H. Tsang, "Role of free carriers from two-photon absorption in Raman amplification in silicon-on-insulator waveguides," *Applied Physics Letters,* vol. 84, pp. 2745-2747, 2004.

[343] H. K. Tsang, C. Wong, T. Liang, I. Day, S. Roberts, A. Harpin, J. Drake, and M. Asghari, "Optical dispersion, two-photon absorption and self-phase modulation in silicon waveguides at 1.5microns," *Applied Physics Letters,* vol. 80, pp. 416-418, 2002.

[344] G. W. Rieger, K. S. Virk, and J. F. Young, "Nonlinear propagation of ultrafast 1.5 μm pulses in high-index-contrast silicon-on-insulator waveguides," *Applied Physics Letters,* vol. 84, pp. 900-902, 2004.

[345] L. Oxenlowe, H. Ji, M. Galili, M. Pu, H. Hu, H. C. H. Mulvad, K. Yvind, J. M. Hvam, A. T. Clausen, and P. Jeppesen, "Silicon photonics for signal processing of Tbit/s serial data signals," *Selected Topics in Quantum Electronics, IEEE Journal of,* vol. 18, pp. 996-1005, 2012.

[346] K. Yamada, H. Fukuda, T. Watanabe, T. Tsuchizawa, H. Shinojima, T. Tanabe, M. Takahashi, and S. Itabashi, "All-optical wavelength conversion using silicon photonic wire waveguide," in *Group IV Photonics, 2006. 3rd IEEE International Conference on*, 2006, pp. 237-239.

[347] O. Boyraz, P. Koonath, V. Raghunathan, and B. Jalali, "All optical switching and continuum generation in silicon waveguides," *Optics Express,* vol. 12, pp. 4094-4102, 2004.

[348] W. Astar, J. B. Driscoll, X. Liu, J. I. Dadap, W. M. Green, Y. Vlasov, G. M. Carter, and R. M. Osgood, "Tunable wavelength conversion by XPM in a silicon nanowire, and the

potential for XPM-multicasting," *Lightwave Technology, Journal of,* vol. 28, pp. 2499-2511, 2010.

[349] H. Ji, C. S. Cleary, J. M. Dailey, J. Wang, H. Hu, R. P. Webb, R. J. Manning, M. Galili, P. Jeppesen, and M. Pu, "Two-Copy Wavelength Conversion of an 80 Gbit/s Serial Data Signal Using Cross-Phase Modulation in a Silicon Nanowire and Detailed Pump-Probe Characterisation," in *European Conference and Exhibition on Optical Communication*, 2012.

[350] A. Agarwal, K. Buddharaju, I. Lao, N. Singh, N. Balasubramanian, and D. Kwong, "Silicon nanowire sensor array using top–down CMOS technology," *Sensors and Actuators A: Physical,* vol. 145, pp. 207-213, 2008.

[351] H. J. Ciaran S. Cleary, James M. Dailey, Roderick P.Webb, Robert J. Manning, M. Galili, Palle Jeppesen, Minhao Pu, Kresten Yvind, Leif K. Oxenlowe, "Dynamic characterization of silicon nanowires using a terahertz optical asymmetric demultiplexer based pump-probe scheme," presented at the IEEE Photonics Conference, Burlingame, USA, 2012.

[352] B. Mason, A. Ougazzaden, C. W. Lentz, K. G. Glogovsky, C. L. Reynolds, G. J. Przybylek, R. E. Leibenguth, T. L. Kercher, J. W. Boardman, and M. T. Rader, "40-Gb/s tandem electroabsorption modulator," *Photonics Technology Letters, IEEE,* vol. 14, pp. 27-29, 2002.

[353] R. Nagarajan, C. H. Joyner, R. P. Schneider Jr, J. S. Bostak, T. Butrie, A. G. Dentai, V. G. Dominic, P. W. Evans, M. Kato, and M. Kauffman, "Large-scale photonic integrated circuits," *Selected Topics in Quantum Electronics, IEEE Journal of,* vol. 11, pp. 50-65, 2005.

[354] C. R. Doerr, L. Zhang, A. L. Adamiecki, N. J. Sauer, J. H. Sinsky, and P. J. Winzer, "Compact EAM-based InP DQPSK modulator and demonstration at 80 Gb/s," in *Optical Fiber Communication Conference*, 2007.

[355] C. Doerr, "Compact Advanced Modulation Format InP Modulators and Receivers," in *Integrated Photonics and Nanophotonics Research and Applications*, 2008.

[356] S. Hojfeldt, F. Romstad, and J. Mork, "Absorption recovery in strongly saturated quantum-well electroabsorption modulators," *Photonics Technology Letters, IEEE,* vol. 15, pp. 676-678, 2003.

[357] P. J. Winzer and R.-J. Essiambre, "Advanced optical modulation formats," *Proceedings of the IEEE,* vol. 94, pp. 952-985, 2006.

[358] F. Devaux, S. Chelles, A. Ougazzaden, A. Mircea, and J. Harmand, "Electroabsorption modulators for high-bit-rate optical communications: a comparison of strained InGaAs/InAIAs and InGaAsP/InGaAsP MQW," *Semiconductor science and technology,* vol. 10, p. 887, 1999.

[359] S. Hojfeldt, S. Bischoff, and J. Mork, "All-optical wavelength conversion and signal regeneration using an electroabsorption modulator," *Lightwave Technology, Journal of,* vol. 18, pp. 1121-1127, 2000.

[360] N. Cheng and J. Cartledge, "Measurement-based model for cross-absorption modulation in an MQW electroabsorption modulator," *Lightwave Technology, Journal of,* vol. 22, pp. 1805-1810, 2004.

[361] K. Nishimura, M. Tsurusawa, and M. Usami, "Delayed-interferometric wavelength converter using electroabsorption modulator with optimized bandgap wavelength," in *European Conference on Optical Communication*, 2002, pp. 1-2.

[362] T.-H. Wu, J.-P. Wu, and Y.-J. Chiu, "Field-driven all-optical wavelength converter using novel InGaAsP/InAlGaAs quantum wells," *Optics Express,* vol. 19, pp. 26645-26650, 2011.

[363] N. E. Dahdah, R. Coquille, B. Charbonnier, E. Pincemin, C. Kazmierski, J. Decobert, A. Vedadi, G. Aubin, and A. Ramdane, "All-optical wavelength conversion by EAM with shifted bandpass filter for high bit-rate networks," *Photonics Technology Letters, IEEE,* vol. 18, pp. 61-63, 2006.

[364] R. P. Green, M. Haji, L. Hou, G. Mezosi, R. Dylewicz, and A. E. Kelly, "Fast saturable absorption and 10 GHz wavelength conversion in Al-quaternary multiple quantum wells," *Optics Express,* vol. 19, pp. 9737-9743, 2011.

[365] M. Aoki, M. Suzuki, H. Sano, T. Kawano, T. Ido, T. Taniwatari, K. Uomi, and A. Takai, "InGaAs/InGaAsP MQW electroabsorption modulator integrated with a DFB laser fabricated by band-gap energy control selective area MOCVD," *Quantum Electronics, IEEE Journal of,* vol. 29, pp. 2088-2096, 1993.

[366] G. Mak, C. Rolland, K. Fox, and C. Blaauw, "High-speed bulk InGaAsP-InP electroabsorption modulators with bandwidth in excess of 20 GHz," *Photonics Technology Letters, IEEE,* vol. 2, pp. 730-733, 1990.

[367] C. Abernathy, S. Pearton, F. Ren, W. Hobson, T. Fullowan, A. Katz, A. Jordan, and J. Kovalchick, "Carbon doping of III–V compounds grown by MOMBE," *Journal of crystal growth,* vol. 105, pp. 375-382, 1990.

[368] B. Cunningham, L. Guido, J. Baker, J. Major, N. Holonyak, and G. Stillman, "Carbon diffusion in undoped, n-type, and p-type GaAs," *Applied Physics Letters,* vol. 55, pp. 687-689, 1989.

[369] E. Schubert, "Delta doping of III–V compound semiconductors: fundamentals and device applications," *Journal of Vacuum Science & Technology A: Vacuum, Surfaces, and Films,* vol. 8, pp. 2980-2996, 1990.

[370] S. Pearton, U. Chakrabarti, C. Abernathy, and W. Hobson, "Carbon implantation in InP," *Applied Physics Letters,* vol. 55, pp. 2014-2016, 1989.

[371] M. Suzuki, H. Tanaka, and S. Akiba, "Effect of hole pile-up at heterointerface on modulation voltage in GaInAsP electroabsorption modulators," *Electronics Letters,* vol. 25, pp. 88-89, 1989.

[372] T. H. Wood, J. Z. Pastalan, C. A. Burrus, B. C. Johnson, B. I. Miller, J. L. Demiguel, U. Koren, and M. G. Young, "Electric field screening by photogenerated holes in multiple quantum wells: A new mechanism for absorption saturation," *Applied Physics Letters,* vol. 57, pp. 1081-1083, 1990.

[373] S. Hojfeldt and J. Mork, "Modeling of carrier transport in multi-quantum-well pin modulators," *Physica Scripta,* vol. 2002, p. 161, 2002.

[374] Y.-h. Kuo, H.-W. Chen, and J. E. Bowers, "High speed hybrid silicon evanescent electroabsorption modulator," *Optics Express,* vol. 16, pp. 9936-9941, 2008.

[375] R. Kazarinov and G. Belenky, "Novel design of AlGaInAs-InP lasers operating at 1.3 μm," *Quantum Electronics, IEEE Journal of,* vol. 31, pp. 423-426, 1995.

[376] W.-C. Liu, W.-C. Wang, H.-J. Pan, J.-Y. Chen, S.-Y. Cheng, K.-W. Lin, K.-H. Yu, K.-B. Thei, and C.-C. Cheng, "Multiple-route and multiple-state current-voltage characteristics of an InP/AlInGaAs switch for multiple-valued logic applications," *Electron Devices, IEEE Transactions on,* vol. 47, pp. 1553-1559, 2000.

References

[377] S. Pellegrino and L. Tarricone, "MOVPE growth and study of InP-based materials: opportunities and challenges," *Materials chemistry and physics,* vol. 66, pp. 189-196, 2000.

[378] A. Benninghoven, F. Rudenauer, and H. W. Werner, "Secondary ion mass spectrometry: basic concepts, instrumental aspects, applications and trends," 1987.

[379] Y. J. Chiu, H. F. Chou, V. Kaman, P. Abraham, and J. E. Bowers, "High extinction ratio and saturation power traveling-wave electroabsorption modulator," *Photonics Technology Letters, IEEE,* vol. 14, pp. 792-794, 2002.

[380] G. Li, S. Pappert, P. Mages, C. Sun, W. Chang, and P. Yu, "High-saturation high-speed traveling-wave InGaAsP-InP electroabsorption modulator," *Photonics Technology Letters, IEEE,* vol. 13, pp. 1076-1078, 2001.

[381] F. Devaux, J. Harmand, I. Dias, T. Guettler, O. Krebs, and P. Voisin, "High power saturation, polarisation insensitive electroabsorption modulator with spiked shallow wells," *Electronics Letters,* vol. 33, pp. 161-163, 1997.

[382] B. Wu, Y. Cheng, S. Fu, J. Wu, C. Yao, S. Wei, L. Li, Y. Dai, and P. Shum, "Investigation of InGaAsP Quantum-Well EAM Based Pump-Probe Configuration for Ultrafast Optical Signal Processing," *Quantum Electronics, IEEE Journal of,* vol. 47, pp. 1113-1122, 2011.

[383] A. Uskov, J. McInerney, J. Karin, and J. Bowers, "Intraband carrier kinetics and picosecond pulse shaping in field-enhanced bulk semiconductor absorbers," *Optics Letters,* vol. 23, pp. 376-378, 1998.

[384] H. Kurita, I. Ogura, and H. Yokoyama, "Ultrafast all-optical signal processing with mode-locked semiconductor lasers," *IEICE transactions on electronics,* vol. 81, pp. 129-139, 1998.

[385] N. El Dahdah, G. Aubin, J.-C. Harmand, A. Ramdane, A. Shen, F. Devaux, A. Garreau, and B.-E. Benkelfat, "Ultrafast InGaAs/InGaAlAs multiple-quantum-well electro-absorption modulator for wavelength conversion at high bit rates," *Applied Physics Letters,* vol. 84, pp. 4268-4270, 2004.

[386] P. Winzer, G. Raybon, C. Doerr, M. Duelk, and C. Dorrer, "107-Gb/s optical signal generation using electronic time-division multiplexing," *Journal of Lightwave Technology,* vol. 24, p. 3107, 2006.

[387] G. Grasso, M. Romagnoli, and A. Melloni, "Silicon Photonics: The Enabling Technology for Green Optical Processing," in *Photonics in Switching*, 2010.

[388] M. J. O'Mahony, D. Simeonidou, D. K. Hunter, and A. Tzanakaki, "The application of optical packet switching in future communication networks," *Communications Magazine, IEEE,* vol. 39, pp. 128-135, 2001.

[389] R. Tucker, K. Hinton, and G. Raskutti, "Energy consumption limits in high-speed optical and electronic signal processing," *Electronics Letters,* vol. 43, pp. 906-908, 2007.

[390] W. Rosenkranz, C. Hebebrand, and A. Ali, "Signal Processing in High-Speed Optical Communications and Impact on Electronic Subsystems."

[391] C. Batten, A. Joshi, J. Orcutt, A. Khilo, B. Moss, C. W. Holzwarth, M. A. Popovic, H. Li, H. I. Smith, and J. L. Hoyt, "Building many-core processor-to-DRAM networks with monolithic CMOS silicon photonics," *Micro, IEEE,* vol. 29, pp. 8-21, 2009.

[392] E. Tangdiongga, Y. Liu, J. Den Besten, M. van Geemert, T. Van Dongen, J. Binsma, H. De Waardt, G. Khoe, M. Smit, and H. Dorren, "Monolithically integrated 80-Gb/s AWG-

based all-optical wavelength converter," *Photonics Technology Letters, IEEE,* vol. 18, pp. 1627-1629, 2006.

[393] L. Wang, M. Wang, S. Lou, and W.-P. Huang, "Pattern Effect Mitigation in High-Speed All-Optical Switch Based on Cross-Gain Modulation in Two SOAs with Different Bandgaps," *Modern Physics Letters B,* vol. 24, pp. 2031-2040, 2010.

[394] K. Lee, R. P. Webb, R. J. Manning, B. Roycroft, J. O'Callaghan, F. H. Peters, and B. Corbett, "Two-bandgap semiconductor optical amplifier integrated using quantum well intermixing," in *Compound Semiconductor Week (CSW/IPRM), 2011 and 23rd International Conference on Indium Phosphide and Related Materials*, 2011, pp. 1-4.